UNIVERSITY OF SOUTHAMPTON

FACULTY OF PHYSICAL SCIENCES AND ENGINEERING

Optoelectronics Research Centre

Waveguide Enhanced Raman Spectroscopy (WERS): Principles, Performance, and Applications

By

Zilong Wang, BEng

Thesis for the degree of Doctor of Philosophy

October 2016

UNIVERSITY OF SOUTHAMPTON

ABSTRACT

FACULTY OF PHYSICAL SCIENCES AND ENGINEERING

Doctor of Philosophy

Thesis for the degree of Doctor of Philosophy

Waveguide Enhanced Raman Spectroscopy (WERS): Principles, Performance, and Applications

By Zilong Wang

Integrated optics is set to revolutionise the translation of laboratory-based, bulky, and expensive spectroscopy instruments to miniaturised, low-cost, automated yet powerful analytical instruments, which will be utilised to tackle challenges faced in a multiplicity of applications from food safety, environmental monitoring, security, personal medicine, pharmacogenetics and rapid point-of-care diagnostics. Waveguides, as the most fundamental integrated optics component, were utilised to replace bulky and alignment-critical free space optics in conventional spectroscopy. Raman spectroscopy, which provides the fingerprint of the analyte, was incorporated into the waveguide platform to be waveguide-enhanced Raman spectroscopy (WERS). The optical confinement provided by waveguide gives rise of the enhancement. The goal of this project is to push the limit of conventional waveguide-enhanced Raman spectroscopy with significantly improved performance while minimising utilisation of costly materials, components and techniques.

Electromagnetic models were established to obtain optimised 2D slab waveguide design for maximising Raman excitation. The fabricated waveguide samples made of Ta_2O_5 on fused silica substrates were in excellent agreement with the design parameters. WERS of bulk toluene liquid and polystyrene film were successfully measured from the conventional configuration of the collection, which was at the waveguide surface. Optimised 110 nm thick Ta_2O_5 waveguides on fused silica substrates excited at a wavelength of 637 nm were shown experimentally to yield overall system power conversion efficiency of $\sim 5\times10^{-12}$ from the pump power in the waveguide to the collected Raman power in the 1002 cm^{-1} Raman line of toluene. For the first time, a power budget analysis of WERS was reported, which aided comparisons of intrinsic WERS performance between different waveguide designs and shed light on the improvements needed for collection efficiency.

The spontaneous emission characteristic of an emitted molecule on the presence of a waveguide was analysed. In particular, the spatial radiation distributions were calculated for near-field and far-field radiations. It was found that near-field radiation dominated for the 110 nm thick Ta_2O_5 waveguide at an excitation wavelength of 633 nm. The emission patterns of both near-field and far-field radiations showed angular characteristic that were different to that from the free-space, which explained the low collection efficiency observed at the waveguide surface, and suggested that collection configuration played a critical role in efficient Raman collection.

For the first time, Raman collection from the waveguide front edge showed experimentally 2-3 orders of enhancement in comparison with that from the waveguide surface for bulk liquid toluene and polystyrene film under TM excitation. Theoretical analysis of spatial distributions of an emitted dipole located at the waveguide surface showed features of asymmetric emission for both near-field and far-field radiations. Notably, the waveguide front edge received 71.6% more near-field emission than that at the back edge. By summing up contributions of near-field and far-field radiations, collection from the waveguide front edge compared to that from the waveguide surface had a radiative enhancement factor of 7.2 and area enhancement factor of 7.7, hence a total theoretical collection enhancement factor of 55.

For the first time, WERS measurements of monolayers of trichloro(phenyl)silane and *p*-tolyltrichlorosilane with multiple Raman features were successfully shown by using the simplest all-dielectric slab waveguides. The structural difference of the methyl group between PTCS and TTCS was clearly shown, which validated the measurements. Polarised Raman measurements of TTCS on WERS platform were successfully performed, which resulted in depolarisability ratio being calculated. The tensor nature of Raman polarisability was utilised to calculate the relationship between the depolarisability ratio and the tilt angle of monolayer molecules on waveguide surface. Based on that, tilt angle was predicted to be 30^0 with the assumptions of randomly oriented molecules in the azimuthal and rotational plane.

Table of Contents

List of tables

List of figures

Declaration of Authorship

I, Zilong Wang declare that this thesis and the work presented in it are my own and has been generated by me as the result of my own original research.

Waveguide enhanced Raman spectroscopy (WERS): principles, performance, and applications

I confirm that:

1. This work was done wholly or mainly while in candidature for a research degree at this University;
2. Where any part of this thesis has previously been submitted for a degree or any other qualification at this University or any other institution, this has been clearly stated;
3. Where I have consulted the published work of others, this is always clearly attributed;
4. Where I have quoted from the work of others, the source is always given. With the exception of such quotations, this thesis is entirely my own work;
5. I have acknowledged all main sources of help;
6. Where the thesis is based on work done by myself jointly with others, I have made clear exactly what was done by others and what I have contributed myself;
7. Either none of this work has been published before submission, parts of this work have been published as [please see List of Publications]:

Signed:...

Date: ....

Acknowledgements

First of all, I would like to send my sincere appreciations to my primary supervisor James S Wilkinson, who gave me enormous patience and encouragements during my PhD studies, guided me through at each stage, and above all gave me this opportunity to research such an interesting topic. Also, I would like to thank my second supervisor Phil N Bartlett, who always provided insightful perspectives during discussions, gave instant feedbacks to me whenever I asked for, and encouraged me constantly. In addition, I would like to thank Michalis N. Zervas for his contributions in discussing the theory and experimental results, and for his constant encouragements.

I had wonderful memories with members in the Integrated Photonic Devices Group. Their rich characters lighted up my days in ORC, and made me learn a lot. I would like to express great gratitude towards them: Dr. Senthil Ganapathy, Dr. Ping Hua, Dr. Alina Karabchevsky, Dr. David Rowe, Jonathan Butement, Vinita Mittal, Ali Masoudi, Armen Aghajani, Mohd Narizee Mohd Nasir, Amy Sen Kay Tong, Shahab Gorajoobi and Neil Sessions. One of greatest joys of doing a multidisciplinary research was to have collaborations with people from other fields. Not only did they provide many helps for me to successfully operate in another field, but also open my minds about many things through their personalities, skills and stories. Therefore, I would like to say great thanks to Yung-Chun Lin (Chemistry) for showing me Renishaw Raman microscopy, Dr. David Cook (Chemistry) for teaching me how to operate in nitrogen-filled glove box, Youngho Jung (KAIST) for demonstrating me the use of Lumerical FDTD, and Dr. Christopher Cave-Ayland (Chemistry) for operating Gaussian calculations for me. Tremendous thanks to all cleanroom technicians and office secretaries for accommodating me in ORC. Doing this PhD required quite a lot of efforts. Warm chats and funny jokes between colleagues were great snacks to quickly fuel up my working energy. Thanks for colleagues, such as Ausra Cerkauskaite, Giulio Negri and Pablo Cencillo, who accompanied me with these in many late office hours.

A special thanks goes to my girlfriend, who said she was my only loyal fan to celebrate every little achievement of mine. This really echoes to my PhD research experience, which was to keep building up 'invisible' (unpublished) achievements until something novel was achieved, and from then onwards it became a lot easier. I feel truly blessed to have her celebrate with me for 'offstage' achievements. Although she was not physically by my side in these four years, I felt that she was next to me. Wholeheartedly, I would like to express my gratitude to my parents. To my mother, who devoted tremendous love to me for my upbringing, I want to say to you that in the past I always felt your love, but now I gradually understand. To my father, who made me believe no matter what happened it will not be the end of the world, I want to share my thought with him that more tests to this belief are coming soon.

Finally, I am grateful to be funded by the European Union's Seventh Framework Programme (FP7/2007-2013) ERC grant agreement no. 291216 "Wideband Integrated Photonics for Accessible Biomedical Diagnostics" for four years.

Abbreviations

AFM – Atomic Force Microscopy

ATR – Attenuated Total Reflection

CARS – Coherent Anti-Stokes Raman Spectroscopy

CCD – Charge-Coupled Device

CVD – Chemical Vapour Deposition

DFT – Density Function Theory

DI water– Deionised water

FDTD – Finite-Difference Time-domain

FPGA – Field-Programmable Gate Array

FTIR – Fourier Transform Infrared Spectroscopy

IR – Infrared Absorption

IPA – Isopropyl alcohol

LB film– Langmuir-Blodgett film

LED – Light Emitted Diode

LIB – Laser-Induced-Breakdown

LPCVD – Low Pressure Chemical Vapour Deposition

LSPP – Localised Surface Plasmon-Polaritons

NA – Numerical Aperture

NIR – Near Infrared

PARS – Photo-Acoustic Raman Spectroscopy

PC – Personal Computer

PECVD – Plasma Enhanced Chemical Vapour Deposition

PML – Perfectly Matched Layer

PSPP – Propagating Surface Plasmon-Polaritons

PTCS – Trichloro(phenyl)silane

PVD – Physical Vapour Deposition

RF – Radio Frequency

RPM – Rotations Per Minute

RR – Resonance Raman

SAM – Self-Assembled Monolayer

SERS – Surface Enhanced Raman Spectroscopy

SRS – Stimulated Raman Scattering

SPP – Surface Plasmon-Polaritons

TTCS – *p*-tolyltrichlorosilane

WERS – Waveguide Enhanced Raman Spectroscopy

UV – Ultraviolet

XPS – X-ray Photoelectron Spectroscopy

XRD – X-Ray Diffraction

2D – Two Dimensional

3D – Three Dimensional

List of Publications

Journals

Z Wang, M. N. Zervas, P. N. Bartlett, and J. S. Wilkinson, "*Surface and waveguide collection of Raman emission in waveguide-enhanced Raman spectroscopy,*" Opt. Lett. 41, 4146-4149 (2016).

Z Wang, S. J. Pearce, Y-C. Lin, M. N. Zervas, P. N. Bartlett, and J. S. Wilkinson, "*Power Budget Analysis for Waveguide-Enhanced Raman Spectroscopy,*" Appl. Spectrosc.70, 1384-1391 (2016).

Conferences

Z. Wang, S. J. Pearce, Y. C. Lin, M. N. Zervas, P. N. Bartlett, J. S. Wilkinson, *"Enhancement of waveguide-enhanced Raman spectroscopy (WERS) end measurement"*, Euro(p)trode XIII Graz, Austria, 2016.

Z. Wang, S. J. Pearce, Y. C. Lin, M. N. Zervas, P. N. Bartlett, J. S. Wilkinson, *"Power budget analysis for waveguide-enhanced Raman spectroscopy",* Optical wave and waveguide theory and numerical modelling workshop, London, UK, 2015.

CHAPTER 1 Introduction

1.1 Background

The rise of Homo sapiens (Latin for “wise person”) among other species in the natural world started nearly 200,000 years ago, coinciding with the invention of ‘tools’ by Homo sapiens. These tools provided Homo sapiens with ‘enhanced’ abilities to tackle challenges in order to adapt to the environment, which eventually led to its current supremacy in the earth. In the last few hundred years, the design and making of new ‘tools’ have greatly expanded Homo sapiens’ knowledge of the world, as is reflected in the vast developments of science, and vice versa. The advances of science and technology help Homo sapiens to successfully tackle many great challenges. For example, as compared with the period at few hundred years ago, when Homo sapiens were very vulnerable to devastating pandemics, such as the Black Death; pandemics nowadays are much more preventable and treatable thanks to advances in understanding of the causes of diseases, and consequent improvements in diagnostic techniques and treatments such as vaccines. This transition over centuries would not be possible without the invention of the optical microscope in the 17th century, which revealed the fascinating microscopic world that was invisible to the naked eye [1]. The development of the optical microscope, especially coupled with spectroscopy, led the modern human to observe microorganisms (e.g. bacteria), tissues, cells, molecules, etc, which resulted in great advances in biology, chemistry, and medicine [2]. Following scientific and technological transitions, Homo sapiens’ life style continues to transform from surviving to better living. In fact, the life expectancy of Homo sapiens has increased rapidly since the Enlightenment and now that no country in the world has a lower life expectancy than the countries with the highest life expectancy in 1800 [3]. This brings some new challenges in many levels of society, especially for health care and the environment. In developing countries, there is an urgent need to provide more affordable and accessible healthcare services to the general public especially for the people with lower incomes or living in rural areas. In addition, while economic development increases the living standards of people, the environmental impacts from industrialization impose challenging pollution issues on them. In developed countries with universal healthcare, an aging population poses the challenge of meeting their healthcare demands within constrained budgets, and leads to pressure to reform the current healthcare system with more cost-effective, equitable, easy-to-access and rapid health services, as well as growing services in areas such as personalised healthcare and preventive healthcare [4].

Technological ‘tools’ will continue to play a critical role in tackling these challenges. The access to chemical or the biochemical information in media, ranging from water samples, blood samples, etc., is a prerequisite for all the scenarios of the above challenges, such as environmental monitoring and medical diagnostics. Optical spectroscopy techniques have already been widely employed in obtaining chemical or biochemical information by exploiting rich light-matter interactions. For example, fluorescence spectroscopy, which analyses the emitted light (fluorescence) of certain compounds excited by using an excitation beam of light, has been utilised in virtually every discipline of the medical and biological sciences, from detecting cancers [5], revealing causes for neurodegenerative diseases [6], to membrane and protein studies [7]. Indeed, the versatility of optical spectroscopy techniques is deeply rooted in the universality of the light-matter interaction. However, these extremely powerful analytical techniques especially spectroscopic techniques have been mostly utilised in research and clinical laboratories. Despite the urgent need, there is a gap in translating these powerful analytical techniques from the laboratories to point-of-use application scenarios. Indeed, spectroscopic techniques in laboratories mostly require bulky expensive equipment with operations by experienced personnel; whereas widespread local application demands systems that are portable (miniaturised), automated and low-cost.

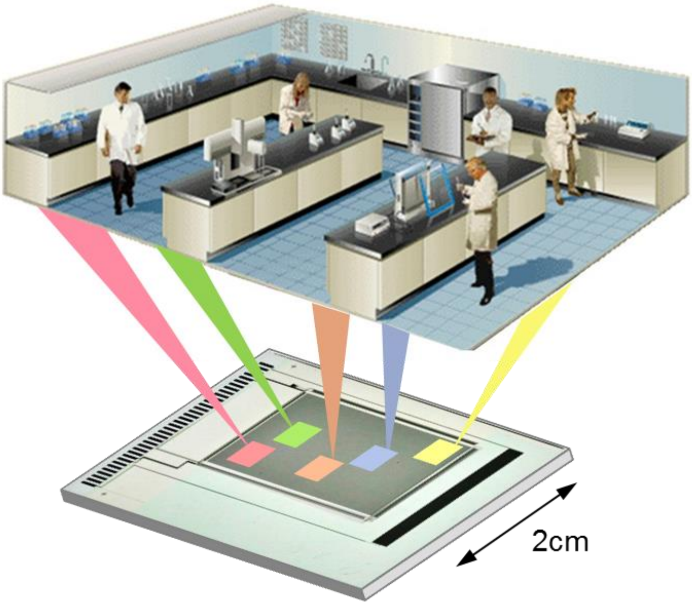

Figure 1.1 Illustration of translating bulky analytical equipment from laboratory to a chip. Retrieved from: http://www.sle.sharp.co.uk/sharp/apps/sle-web/research/health_medical/lab-on-a-chip.png

Integrated optics, combining a system of light-controlling components into a single device, is set to revolutionise the translation of laboratory-based bulky but powerful spectroscopy equipment to miniaturised, robust, low-cost chips, as illustrated schematically in Figure 1.1. In a sense, integrated optics are to the photonics industry just as integrated circuits are to the electronics industry. Inspirations and implications for this revolution can be drawn from the electronics industry. Since the 1950s, the invention and development of integrated circuits have enabled the translation of room-size, highly expensive computers to portable, low-cost and even more powerful personal computers, laptops, mobile phones, tablets, etc. As a result, computing power and information flow that used to be ‘centralised’ in laboratories, big corporations, and governments have been redistributed to the general public, which forever changes the society of Homo sapiens. Similarly, the ubiquitous access to chemical and biochemical information will help people to increase awareness and understanding of the environment and themselves, which can lead to solutions for better environments and better well-being. This will rely on the success of this revolution, which is set to be offered by integrated optics. By exploiting advanced micro (or nano)-fabrication techniques, many complex optical functionalities can be realised on a single chip in a mass-producible manner. While spectroscopic techniques have analytical capability for detection and quantification of a wide range of chemical species, integrated optics offer universality of applications by adding on different functionalities and interfacing with different system components on a common platform. Therefore, the powerful combination of spectroscopic techniques and integrated optics is suitable for a multiplicity of applications from food safety, water quality, security, personal and preventative medicine, pharmacogenetics and rapid point-of-care diagnostics.

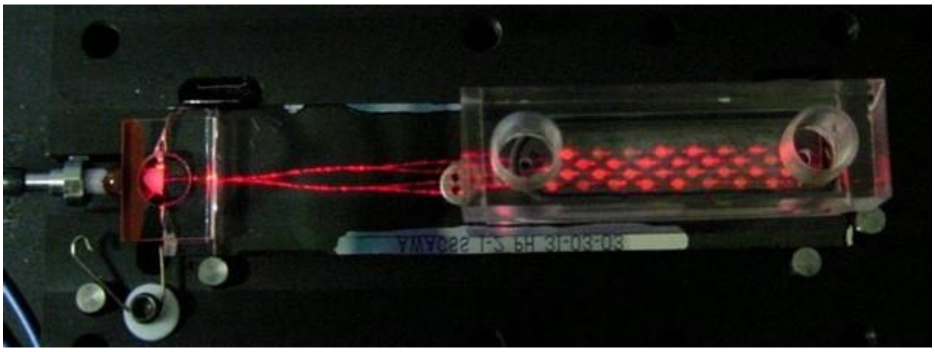

Figure 1.2 A fluorescence multi-sensor chip realised based on optical waveguide technologies. Acknowledgement to Dr. Ping Hua

The planar waveguide is the key component to bring conventional spectroscopy onto a chip. Planar waveguides are to integrated optics just as wires are to integrated circuits, and are the most fundamental components. Formed by a core film sandwiched by cladding films with lower refractive indices, the planar waveguide is utilised to guide and manipulate light. Conventional spectroscopy often comprises of three key units: a laser source, a sample, and a spectrometer. The sample is excited by the laser beam coming from a laser source, and emitted light is analysed by a spectrometer. In between these three units, the manipulation of light is achieved in free-space, which depends on strict alignment of bulky optical components such as mirrors and lenses. Because of this, the equipment needs to be placed on a stabilised surface that is free from any movement. By replacing these free-space components, the planar waveguide can be utilised to transport light, excite the sample, and potentially collect the emitted light, which results in a robust and miniaturised unit without the need for complex adjustments, as shown in Figure 1.2. In addition, conventional spectroscopy requires a focussed beam incident onto the sample, in order to achieve the desired sensitivity. The planar waveguide effectively squeezes the light within a scale of dimension as small as approximately half of the wavelength of the excitation light, and maintains this over a long propagation range. This results in a significant enhancement on light intensity within the waveguide structure, which makes the planar waveguide ultrasensitive to many kinds of optical measurements [8]. Because of these advantages, incorporation of spectroscopic techniques with planar waveguides have been previously demonstrated in waveguide enhanced absorption spectroscopy [9], waveguide enhanced fluorescence spectroscopy [10], and waveguide enhanced Raman spectroscopy (WERS) [11]. Despite these early efforts, there is still a gap in performance between the demonstrated works and application requirements, especially in the case of the relatively new field of waveguide enhanced Raman spectroscopy.

Raman spectroscopy, which provides a molecular fingerprint of the analyte, has many great advantages over other spectroscopic techniques. For examples, it offers much better molecular specificity than fluorescence spectroscopy. Unlike in fluorescence spectroscopy where costly and complicated labelling is often required, Raman spectroscopy requires trivial or no sample preparation. In addition, the Raman spectral features are narrow bands with the use of a narrow line laser, which makes Raman spectroscopy attractive for multiplexed measurements. Similar to Raman spectroscopy, IR absorption spectroscopy provides molecular fingerprints. However, IR absorption spectroscopy suffers from troubling background absorption in water, while Raman spectroscopy is much more readily suitable for aqueous measurements. Nevertheless of all these benefits offered by Raman spectroscopy, Raman spectroscopy suffers from a severe sensitivity issue, as the efficiency of Raman scattering is extremely low. Although the planar waveguide can provide a significant enhancement, waveguide enhanced Raman spectroscopy is still hindered by low sensitivity to date in order to realise its potentials in a wide range of applications. Literature reviews of WERS from different perspectives will be given in Chapter 2 and Chapter 4. While the incorporation of the laser source and the spectrometer have already been demonstrated on a chip [12], the focus is now on significantly improving the efficiency of optical transduction on chip such as the excitation and collection of waveguide enhanced Raman scattering, in order to realise a compact, low-cost, mass-producible spectroscopy-on-a-chip with performance matching or even surpassing the conventional spectroscopy.

The basic principle of WERS is illustrated in Figure 1.3. While the majority of light is guided in the core of the waveguide, there is a certain amount of light penetrating to the cladding in a manner of exponential decay, i.e. the evanescent field. It is through the interaction between analyte molecules and the evanescent field of the waveguide that Raman is excited and part of its emission is collected by the waveguide. The Raman emission can be collected in different configurations such as collection from the waveguide surface and the waveguide front edge, as illustrated in Figure 1.3.

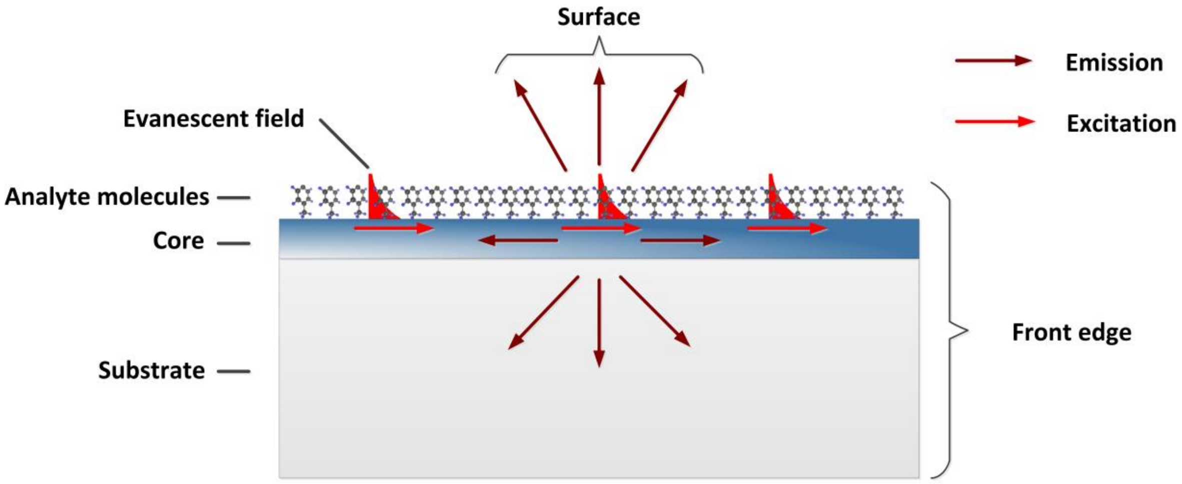

Figure 1.3 Illustration of WERS configuration for Raman excitation and collection of its emission.

Besides, the interaction between analyte molecules and light in the core region has been exploited in liquid-core waveguides [13], in which analyte molecules in solution form the waveguide core. Normally, the highest optical intensity is located in the waveguide core, which leads to the highest light-matter interaction. However, the highest intensity can be also located at the waveguide surface by exploiting different waveguide designs, such as metal-dielectric-metal slab waveguides [14]. Moreover, the requirement of filling the core with liquid puts limits on realising waveguide with small core dimension, hence compromising the waveguide design of maximum excitation. Furthermore, compared to liquid-core waveguides, waveguides based on evanescent excitation avoid suffering severe non-specific interference from the analyte due to the short penetration depth of evanescent field. Therefore, the focus of the topic will be on WERS based upon evanescent excitation.

1.2 Project development

This section will 1) state the goal of this project; 2) describe under what scope the goal being pursued; 3) explain the scientific approaches taken in order to achieve the final goal; and finally 4) briefly highlight original achievements.

The goal of this project is to revolutionise WERS by significantly boosting its sensitivity while minimising costly materials, components and procedures. The successful completion of this project aims to establish necessary scientific principles backed up by concrete experimental and theoretical evidence, which advances the future realisation of spectroscopy-on-a-chip. The experimental demonstrations of representative applications are expected to inspire many other applications.

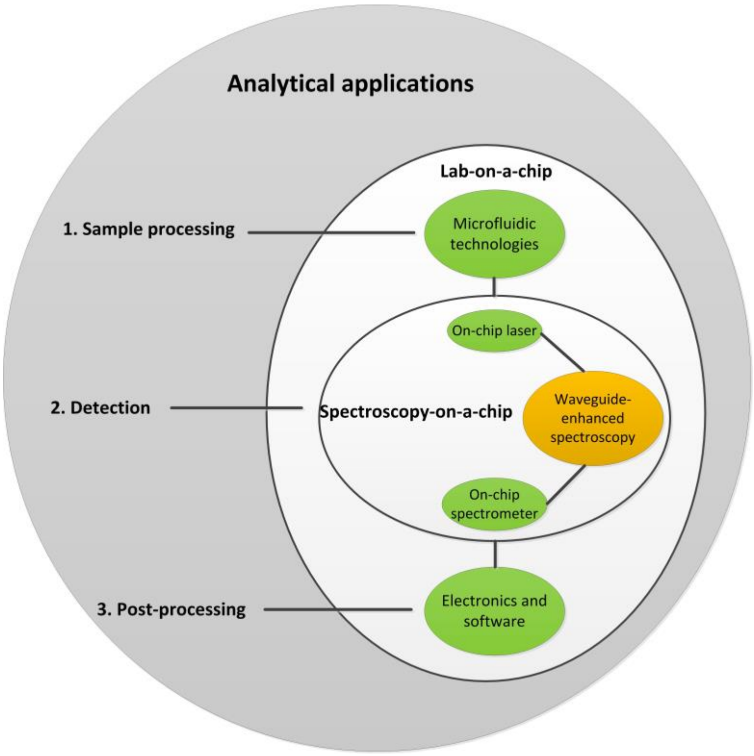

Figure 1.4 Block diagram illustrating project scope as part of an overall vision. The project scope is highlighted in orange colour.

The project scope is illustrated in Figure 1.4. Beyond the goal of this project, the ultimate goal is to realise a miniaturised, low-cost, automated lab-on-chip system suitable for a range of analytical applications. For analytical applications, this generally involves three stages: sample processing, detection, and post-processing. The purpose of sample processing stage is to separate the analyte from indiscernible environment, and present the analyte for the detection system. This stage can include several steps such as centrifugal separation, washing, filtering or capturing by selectively bindings, etc. In conventional laboratory environments, this stage is often very time-consuming, costly, and demands bulky equipment and experienced personnel. Similar to what integrated optics is set to do for bulky spectroscopy equipment, microfluidic technologies aim to perform for sample processing in a miniaturised chip with networks of channels, which have dimensions from tens to hundreds of micrometers. In this project, the realisation of sample processing in a microfluidic chip is not the goal; therefore all sample processing have been performed off the chip. However, the integration of microfluidic technologies and optical waveguides have been successfully demonstrated elsewhere [15], [16]. The detection stage involves a transducer to convert the analyte information into detectable signals, which intrinsically determines the maximum sensitivity and the richness of analyte information to be measured. While Raman spectroscopy provides rich information on analytes, this project focuses on increasing the sensitivity aspect of the detection. In specific, the miniaturised detection can be achieved by spectroscopy-on-a-chip, which has the laser source, the waveguide enhanced spectroscopy, and the spectrometer all on a single chip. For maximum flexibilities, compact diode laser and commercial spectrometer have been chosen instead of on-chip ones while this project will focus on the waveguide-enhanced spectroscopy part, as highlighted in a different background compared with others in Figure 1.4. As for post-processing, it deals with signal processing in order to extract useful information from the measured data and present results to the user. For convenience, this step will be performed in a personal computer (PC). For the ultimate lab-on-a-chip or spectroscopy-on-a-chip, this step can be easily performed by a microcontroller or a field-programmable gate array (FPGA) chip with embedded programs for signal processing, results display and other user interface functions.

This project has focussed on expanding the understanding of WERS, developing necessary technologies, and demonstrating their performances through some representative examples, thus providing a technological tool box of WERS for future application developments. For this reason, no specific application is aimed at in this project although some potential applications will be discussed. Nevertheless, the generic approach taken and waveguide platform realised in this project provide results applicable to a wide range of applications.

A systematic approach was taken to achieve the project goal, as the project can be divided into different stages. The purpose of the first stage is to establish the necessary ‘infrastructures’ including software models, fabrication protocols and experimental apparatus, which will be utilised for the later stages of the project. In the first stage of the project, significant effort has been put into 1) establishing a series of electromagnetic models for waveguide design and optimisation based upon established knowledge; 2) establishing protocols for fabricating low-loss waveguide with ultra-thin film(s) on a glass substrate; 3) designing and constructing an experimental apparatus for WERS measurements. The success of the first stage will be indicated through a fabricated waveguide with optimised design (based upon established knowledge) successfully working on the experimental apparatus.

In the second stage, the state-of-the-art design was employed in a proof-of-concept experiment for bulk analyte. A power budget analysis will be given, which sheds lights on where improvements may be best focussed in order to significantly improve the WERS performance. Building on the insights drawn from this power budget analysis, a theory of waveguide Raman collection will be given, which indicates improvements to be made. Based on that, a new WERS configuration will be investigated. The performance of the new WERS configuration will be put in direct comparison with the previous state-of-the-art. A dramatic enhancement from the new WERS configuration will be shown. A theoretical analysis will be given to explain the experimental result. To conclude, the success of the second stage is evaluated based on 1) a power budget analysis of the state-of-the-art, which reveals potentials for future improvements; 2) a new WERS configuration with a much better performance; and 3) a rigorous theory to reveal the performance mechanisms.

In the third stage, the new WERS configuration was employed for a performance-demanding test – monolayer measurement, for which the previous state-of-the-art found little success. Again, the performance from the new WERS configuration will be discussed and compared with the literature. Moreover, the WERS will be employed in an even more performance-demanding application, which will demonstrate the capability of the device and inspire future developments.

To summarise, in this thesis a detailed theoretical analysis and experimental implementations of optimised WERS spectroscopy are given, leading to future promise in delivering analytical applications.

1.3 Thesis structure

In this section, the thesis structure will be briefly explained.

In Chapter 2, principles of Raman spectroscopy will be explained. In particular, the elegance and challenge of Raman spectroscopy will be clearly revealed, by comparisons with other common spectroscopic techniques. Methods utilised to tackle the challenge of Raman spectroscopy in particular its low signal strength will be reviewed, with an emphasis on unique advantages provided by WERS.

In Chapter 3, necessary building blocks for a successful WERS measurement will be explained, which include an electromagnetic model, a fabrication protocol, waveguide characterisations, and a prism coupler. As for the electromagnetic model, it models a 2D multilayer waveguide structure; numerically solves for its mode(s); and simulates the waveguide performance against design parameters such as waveguide core thickness, top layer index, wavelength, etc., with surface intensity as its figure-of-merit. The fabrication techniques for thin-film slab waveguide will be discussed. A fabrication protocol to achieve the low-loss thin-film waveguide will be explained. The characterisation part will describe what methods were utilised to confirm the waveguide parameters such as core thickness. The final part of this Chapter is to discuss the methods utilised to couple light into the waveguide. The design and realisation of a prism coupler will be explained.

In Chapter 4, WERS with optimised excitation will be firstly demonstrated for bulk measurements in order to validate the concept. After that, a power budget analysis will be given in order to aid the comparison between different WERS approaches. Also, it provides an important insight that the Raman collection of conventional WERS from the top surface of the waveguide is extremely inefficient.

In Chapter 5, a theory of waveguide Raman collection will be established through evaluating the emission routes of an excited dipole on waveguide surface. Theories and simulation methods will be explained. The results indicate that collection from the waveguide front edge should lead to a much better WERS performance than that from the waveguide surface.

In Chapter 6, WERS with collection from the waveguide front edge will be demonstrated experimentally. A dramatic increase of the WERS performance will be shown by putting it in direct comparison with the result obtained from the conventional configuration. A theoretical analysis will be given to quantitatively explain the enhancement mechanism.

In Chapter 7, with the much improved performance, WERS is utilised for demanding monolayer measurements. The first part of this Chapter will focus on monolayer fabrication, characterisation and its detection by WERS. Then in the second part, polarised WERS measurements of monolayer will be demonstrated, and then the molecular orientation on the waveguide surface will be determined with the help of Raman tensor theory.

1.4 Novel contributions

The key novel contributions are summarised below:

- A power budget analysis for conventional WERS configuration, which aids comparisons between different WERS designs and provides important insight on where to improve.
- A theory established for waveguide Raman collection with accounts of its emission routes.
- A first experimental and theoretical comparison made between waveguide Raman collection from the waveguide surface and edge.
- A first demonstration of asymmetric coupling of elliptically polarised dipole in WERS.
- A first demonstration of the significant role that the waveguide substrate plays in waveguide Raman collection.
- A first demonstration of monolayer detection by WERS with multiple Raman features on slab waveguide – the simplest waveguide structure.
- A demonstration of polarised Raman measurements on monolayer with Raman tensor analysis for determining the molecular orientation on the waveguide surface.

1.5 References

[1] R. Hooke, *Micrographia*. London, 1665.

[2] B. R. Masters, “A Brief History of the Microscope and Its Significance in the Advancement of Biology and Medicine,” in *Confocal Microscopy and Multiphoton Excitation Microscopy*, 1000 20th Street, Bellingham, WA 98227-0010 USA: SPIE, 2006, pp. 3–17.

[3] M. Roser, “Life Expectancy,” 2016. [Online]. Available: https://ourworldindata.org/life-expectancy/. [Accessed: 07-Oct-2016].

[4] J. Tooke, “Future of healthcare in Europe,” London, UK, 2015.

[5] G. A. Wagnieres, W. M. Star, and B. C. Wilson, “In Vivo Fluorescence Spectroscopy and Imaging for Oncological Applications,” *Photochem. Photobiol.*, vol. 68, no. 5, pp. 603–632, Nov. 1998.

[6] R. F. Laine, G. S. Kaminski Schierle, S. van de Linde, and C. F. Kaminski, "From single-molecule spectroscopy to super-resolution imaging of the neuron: a review," *Methods Appl. Fluoresc.*, vol. 4, no. 2, p. 22004, Jun. 2016.

[7] O. Ryzhova, K. Vus, V. Trusova, E. Kirilova, G. Kirilov, G. Gorbenko, and P. Kinnunen, "Novel benzanthrone probes for membrane and protein studies," *Methods Appl. Fluoresc.*, vol. 4, no. 3, p. 34007, Sep. 2016.

[8] K. Schmitt, K. Oehse, G. Sulz, and C. Hoffmann, "Evanescent field Sensors Based on Tantalum Pentoxide Waveguides – A Review," *Sensors*, vol. 8, no. 2, pp. 711–738, Jan. 2008.

[9] W.-C. Lai, S. Chakravarty, X. Wang, C. Lin, and R. T. Chen, "On-chip methane sensing by near-IR absorption signatures in a photonic crystal slot waveguide," *Opt. Lett.*, vol. 36, no. 6, pp. 984–986, 2011.

[10] P. Hua, J. Hole, J. Wilkinson, G. Proll, J. Tschmelak, G. Gauglitz, M. Jackson, R. Nudd, H. Griffith, R. Abuknesha, J. Kaiser, and P. Kraemmer, "Integrated optical fluorescence multisensor for water pollution.," *Opt. Express*, vol. 13, no. 4, pp. 1124–30, 2005.

[11] J. S. Kanger, C. Otto, M. Slotboom, and J. Greve, "Waveguide Raman Spectroscopy of Thin Polymer Layers and Monolayers of Biomolecules Using High Refractive Index Waveguides," *J. Phys. Chem.*, vol. 100, no. 8, pp. 3288–3292, Jan. 1996.

[12] Z. Xia, A. A. Eftekhar, M. Soltani, B. Momeni, Q. Li, M. Chamanzar, S. Yegnanarayanan, and A. Adibi, "High resolution on-chip spectroscopy based on miniaturised microdonut resonators.," *Opt. Express*, vol. 19, no. 13, pp. 12356–12364, 2011.

[13] P. Measor, L. Seballos, D. Yin, J. Z. Zhang, E. J. Lunt, A. R. Hawkins, and H. Schmidt, "On-chip surface-enhanced Raman scattering detection using integrated liquid-core waveguides," *Appl. Phys. Lett.*, vol. 90, no. 21, pp. 1–4, 2007.

[14] Y. C. Jun, R. D. Kekatpure, J. S. White, and M. L. Brongersma, "Nonresonant enhancement of spontaneous emission in metal-dielectric-metal plasmon waveguide structures," *Phys. Rev. B - Condens. Matter Mater. Phys.*, vol. 78, no. 15, pp. 1–4, 2008.

[15] S. Balslev, A. M. Jorgensen, B. Bilenberg, K. B. Mogensen, D. Snakenborg, O. Geschke, J. P. Kutter, and A. Kristensen, "Lab-on-a-chip with integrated optical transducers," *Lab Chip*, vol. 6, no. 2, pp. 213–217, 2006.

[16] R. Osellame, V. Maselli, R. M. Vazquez, R. Ramponi, and G. Cerullo, "Integration of optical waveguides and microfluidic channels both fabricated by femtosecond laser irradiation," *Appl. Phys. Lett.*, vol. 90, no. 23, p. 231118, 2007.

CHAPTER 2 Principles of Raman spectroscopy

2.1 Motivation

In WERS, the information of molecular structure or the molecule fingerprint is provided by Raman spectroscopy. In this chapter, principles of Raman spectroscopy will be explained. In comparison to other common techniques such as fluorescence and near-infrared spectroscopy, the beauty and the challenge of Raman spectroscopy will be revealed. Many techniques have been invented to enhance Raman signals. Among them, surface-enhanced Raman spectroscopy (SERS) is probably the most popular technique, which has attracted huge amounts of research effort since its discovery in early 1970s by Fleischmann *et al.* at the University of Southampton [1]. The basic principle of SERS will be explained. After that, the development of WERS and its principle will be explained. The chapter will end by briefly explaining other enhanced technologies for Raman spectroscopy.

2.2 What is Raman spectroscopy

This section will describe Raman spectroscopy in order to clarify 1) what is the Raman effect; 2) why the Raman spectrum provides a fingerprint of the molecule; 3) what is the major challenge for this technique; 4) what are the advantages and disadvantages of this technique.

2.2.1 Raman scattering

The effect of Raman scattering was published by C. V. Raman in 1928 [2]. During his work, he focussed sunlight into either a pure liquid or its dust-free vapour, and found the ‘existence of a modified scattered radiation’, which was later known as the anti-Stokes Raman scattering. In a scattering process, incident photons are deflected by scatterers. Most of the emitted photons have the same frequency as the incident photons, and this is described as *elastic scattering*. For molecules, this scattering process is often called Rayleigh scattering. In contrast, a small number of emitted photons (of order one in 10^{10}) possess different frequencies to the incident photons, and this is known as *inelastic scattering*. This is the discovery of Raman scattering. An intuitive way to think of these two processes is depicted in Figure 2.1. The diagram is called a Jablonski diagram, which will be very useful later to illustrate the difference between optical processes such as absorption, fluorescence and Raman scattering.

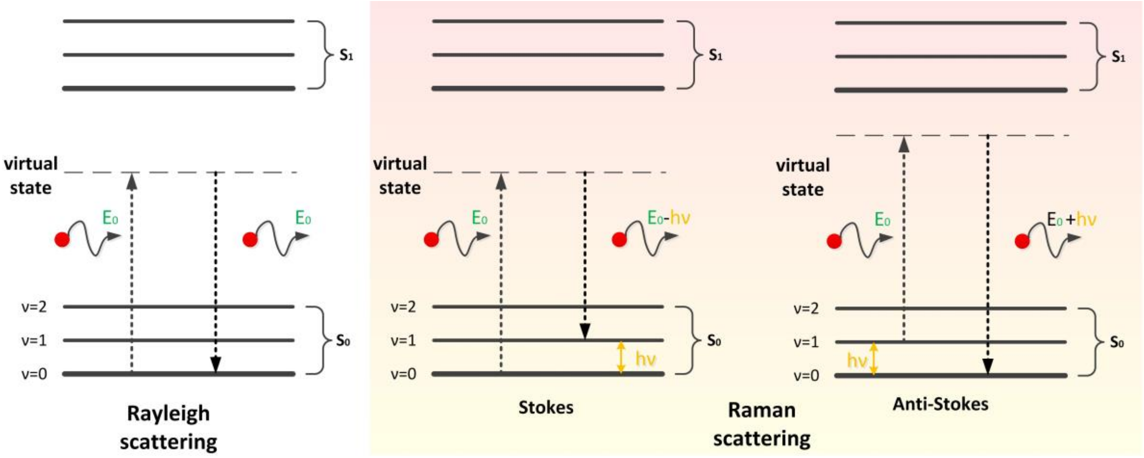

Figure 2.1 Simplified Jablonski diagrams of Rayleigh and Raman scattering (Stokes and anti-Stokes).

For both Rayleigh and Raman scattering, the incident photon energy is not large enough to cause an electron transition to a electronic higher state. Instead, it reaches a virtual state that is below the first possible transition S_1, and simultaneously returns to S_0. For Rayleigh scattering, there is no energy gain or loss, whereas for Raman scattering, the electron returns to one of the vibrational states that are closely spaced in S_0. Depending on the vibrational mode i, the electron returns to a certain vibrational state v_i. In this process of Raman scattering, there is an energy exchange between the incident light and the molecule. As a result, the molecule vibration changes and the emitted photons lose or gain energy compared to the incident photons. By observing in the spectrum, emitted photons shift in frequency (wavenumber) as compared to the incident photons. Each spectral location of a Raman peak corresponds to a vibrational mode of the molecule and the magnitude of that peak indicates how strong that mode is. Therefore, Raman spectrum provides a fingerprint of the molecule. The Stokes process corresponds to energy loss of the emitted photons therefore Raman peaks shift to longer wavelengths whereas the anti-Stokes process corresponds to energy gain of the emitted photons with Raman peaks shifting to shorter wavelengths. They are symmetrical in frequency about the excitation wavelength, however Stokes peaks are generally stronger than anti-Stokes peaks. As Figure 2.1 shows, in an anti-Stokes process the molecule starts in a higher energy vibrational state as compared to the Stokes process. The populations of these states follow the Boltzmann distribution ($N \propto \exp(-\frac{E}{k_B T})$) so that there are exponentially fewer molecules in the higher energy vibrational states. This explains why Stokes lines are generally stronger than anti-Stokes lines.

2.2.2 Classical treatment of Raman scattering theory

Next, the classical description of Raman scattering will be introduced in order to quantitatively understand the effect and be able to interpret the Raman spectrum. An oscillating electric field of the incident light induces a polarisation in the molecule:

$$\boldsymbol{p} = \alpha \cdot \boldsymbol{E}$$ Equation 2.1

where $\boldsymbol{p}$ is the electrical dipole moment induced in the molecule, α is the polarisability of the molecule that determines how easily electrons of the molecule can be moved in response to an external field, $\boldsymbol{E}$ is the electric field of the incident light that can be further described as:

$$\boldsymbol{E} = \boldsymbol{E_0} \cdot \cos(2\pi\nu_0 t) \qquad \text{Equation 2.2}$$

with ν_0 the frequency of the incident light.

The polarisability tensor α in Equation 2.1 depends on the shape and dimensions of the chemical bonds, which change during molecular vibrations [3]. The molecular vibrations are characterised by the normal modes Q_j of the molecule, of which there are 3N-6 (or 3N-5 for a linear molecule) in a molecule with N atoms. In a first approximation, the normal mode oscillates according to the harmonic oscillator:

$$Q_j = Q_{j0} \cdot \cos(2\pi\nu_j t) \qquad \text{Equation 2.3}$$

with Q_{j0} the amplitude of the normal vibration and ν_j the characteristic harmonic frequency of the *j*th normal mode. The relationship between the polarisability tensor α and the normal mode Q_j of the molecule can be expressed as a Taylor series:

$$\alpha = \alpha_0 + \sum_{\boldsymbol{j}} \left(\frac{\boldsymbol{\delta\alpha}}{\boldsymbol{\delta Q_j}}\right) \cdot Q_j + \cdots \qquad \text{Equation 2.4}$$

with α_0 the inherent polarisability of the molecule. Equation 2.4 is in a first approximation by assuming that different vibrations are totally independent. Substitution of Equation 2.4 into Equation 2.1 gives:

$$\boldsymbol{p} = \alpha_0 E_0 \cdot \cos(2\pi\nu_0 t) + \left(\frac{\delta\alpha}{\delta Q_j}\right) \cdot Q_{j0} E_0 \cdot \cos(2\pi\nu_j t)\cos(2\pi\nu_0 t) \qquad \text{Equation 2.5}$$

By applying the trigonometric formula:

$$\mathrm{cosA} \cdot \mathrm{cosB} = 1/2 \times [\cos(\mathrm{A}+\mathrm{B}) + \cos(\mathrm{A}-\mathrm{B})] \qquad \text{Equation 2.6}$$

Equation 2.5 can be written as:

$$\begin{gathered} \boldsymbol{p} = \alpha_0 E_0 \cdot \cos(2\pi\nu_0 t) + \\ 1/2 \times \left(\frac{\delta\alpha}{\delta Q_j}\right) \cdot Q_{j0} E_0 \cdot \cos[2\pi(\nu_0 + \nu_j)t] + \\ 1/2 \times \left(\frac{\delta\alpha}{\delta Q_j}\right) \cdot Q_{j0} E_0 \cdot \cos[2\pi(\nu_0 - \nu_j)t] \end{gathered} \qquad \text{Equation 2.7}$$

Some insights can be drawn from Equation 2.7. Firstly, the induced dipole moment can be split into three components, each with its own frequency dependence. The first term in Equation 2.7 is Rayleigh scattering, which has the same frequency as the incident light. The second term is the anti-Stokes component of the Raman scattering, which has a frequency of $\nu_0 + \nu_j$, while the third term is the Stokes component of the Raman scattering, which has a frequency of $\nu_0 - \nu_j$. Therefore, by associating with the vibration mode ν_j of the molecule, the Raman shift (or peak position) of each mode can then be calculated. Secondly, the second and third terms show that Raman scattering occurs only for vibrations that change the polarisability, i.e. $\frac{\delta\alpha}{\delta Q_j} \neq 0$, which is the basis of the primary *selection rule* for Raman scattering [4]. The importance of this selection rule will be illustrated later when comparison is made between Raman scattering and infrared absorption. Moreover, for different molecules and for different modes in a given molecule, $\frac{\delta\alpha}{\delta Q_j}$ can vary significantly, eventually resulting in variations in Raman scattering intensity, i.e. variations in Raman feature height in the Raman spectrum. The magnitude of $\frac{\delta\alpha}{\delta Q_j}$ is generally much smaller than α_0, which results in Raman scattering being much weaker than Rayleigh scattering.

The intensity of the dipole radiation is given as [5]:

$$I = \frac{\pi^2 c_0 \nu_s^4 p_0^2 sin^2\theta}{2\varepsilon_0} \qquad \text{Equation 2.8}$$

where I is the time-averaged power per unit solid angle, $\nu_s = \nu_0 \pm \nu_j$ is the radiation frequency, p_0 is the amplitude of induced dipole moment that is given in Equation 2.7, θ is the angle between the observation and the axis of the dipole, c_0 is the light velocity in vacuum and ε_0 is the permittivity in vacuum. The substitution of Equation 2.7 into Equation 2.8 shows that both Rayleigh and Raman intensities I are linear with the incident light intensity, i.e. $I \propto E_0^2$. Although nonlinear Raman scattering can be induced at high values of E_0, it is not within the scope of this work and in the following discussion a linear relationship between the Raman scattering intensity and the incident light intensity is always assumed. In addition, the Raman intensity is proportional to the fourth order of the incident light frequency ν_0, which indicates that a shorter wavelength gives larger Raman signal. However, the choice of incident light wavelength also involves assessing additional factors and will be discussed later in Chapter 3.

The classical treatment has sufficiently described how the interaction of an incident light and a molecule gives rise to Raman scattering. It links the frequency of the incident light and vibrational frequency of a particular mode to the Raman radiation frequency, which determines the location of each Raman feature in the spectrum. It also correctly predicts the existence of both Stokes and anti-Stokes scattering. However, it doesn’t yield the correct magnitude of the Stokes Raman polarisability because the spontaneous creation of a vibration is ignored. For further explanation on limitations of the classical treatment and corresponding solutions, references [6] and [5] are good sources of reading. Nevertheless, the classical treatment given in this section is sufficient for the scope of this work.

2.2.3 Raman cross-section

From Section 2.2.2, it is known that the Raman intensity per solid angle (I) is proportional to the incident light intensity. By introducing a cross-section term, a direct relationship between those two is established as followed [6]:

$$P = \sigma \cdot S_{Inc}$$ Equation 2.9

with P the total power of Raman radiation of one molecule, σ the Raman cross-section of that molecule in unit of m^2, S_{Inc} the incident power density in unit of W/m^2. Raman cross-section is a man-made concept used to describe the efficiency of the Raman scattering process but it does not necessarily has any physical meaning. Nevertheless, the concept can be visualised as a homogeneous incident beam going through a circle, for which the light passing through the circle corresponds to the Raman radiation light. The effective area of that circle determines the efficiency of this process, hence is the Raman cross-section. The involvement of Raman cross-section greatly simplifies the relationship given in Equation 2.8 by reducing all molecule related terms to a single term. It makes comparison much easier between different molecules, for the same process and different processes such as fluorescence and Raman scattering.

In fact, for most Raman measurements, only a fraction of the Raman radiation is collected, depending on the collection cone. Therefore, it is useful to know how many photons are scattered in a specific direction. For this purpose, a differential Raman scattering cross-section is introduced as $\frac{d\sigma}{d\Omega}$ in unit of m^2·sr^{-1}. For example, by knowing the solid angle of the collection is $\Delta\Omega_{Det}$, the collected Raman power is then:

$$P = \frac{d\sigma}{d\Omega} \cdot \Delta\Omega_{Det} \cdot S_{Inc}$$ Equation 2.10

2.2.4 Comparison of Raman spectroscopy with other commonly used techniques

In the field of spectroscopy, there are many other commonly used techniques for material identification and molecule detection, such as infrared absorption (IR) and fluorescence. The former is often implemented as Fourier Transform Infrared spectroscopy (FTIR), which has been widely used for material analysis. The latter is probably one of the most popular analytical techniques in life science. Since Raman spectroscopy is also an analytical tool in those areas, a comparison with these two techniques helps to clarify the advantages and disadvantages of the Raman spectroscopy as well as strengthen the understanding of this technique. The theoretical aspects of the Raman scattering established in the previous sections aid understanding of the analysis in this section.

2.2.4.1 Infrared absorption (IR)

Similarly to Raman scattering, infrared absorption also occurs owing to the incident light inducing molecular vibrations. However, they are two different optical processes as their names imply: scattering and absorption. As illustrated in Figure 2.2, in infrared absorption, the incident photon is absorbed by the molecule and excites it to a higher vibrational state, usually from the ground state S_0. In contrast to electronic absorption where the incident photon excites the molecule from ground state S_0 to S_1, the energy required for infrared absorption is much smaller, and the wavelength of the incident light lies in the infrared or far infrared (3-100 µm). Therefore, it is called infrared absorption.

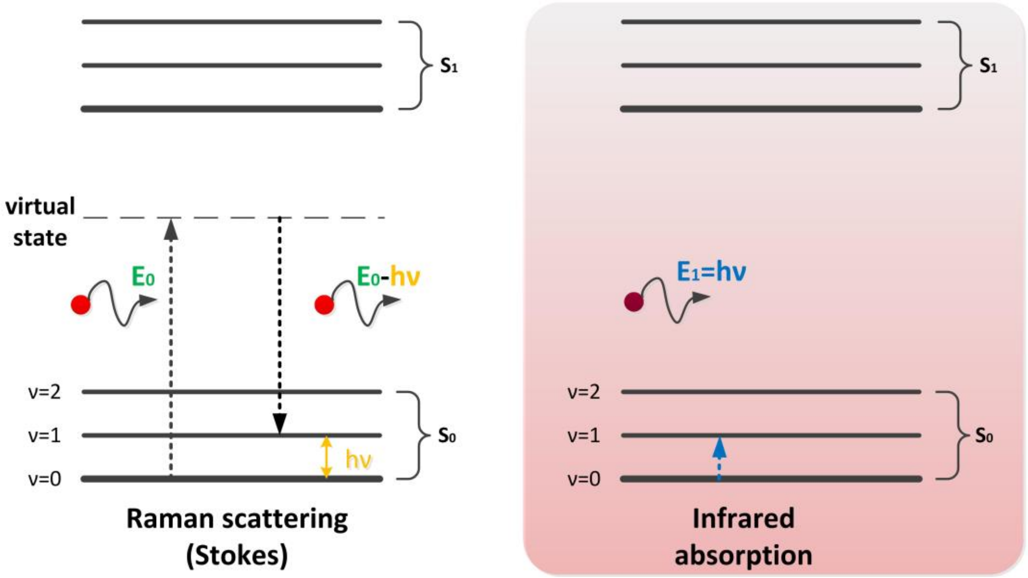

Figure 2.2 Jablonski diagrams illustrate Raman scattering (Stokes) and Infrared absorption.

Since both Raman scattering and infrared absorption probe the vibrational states of the molecule, the location of a spectral feature that corresponds to the same vibrational mode should be at the same frequency. However, the magnitude of them can be very different, as it is often found that one spectral feature is strong in one process but weak in the other, because they have different selection rules. As stated in the previous section, the selection rule for Raman scattering is that the 'polarisability' must change during the molecular vibration; the selection rule for infrared absorption requires that the 'dipole moment' must change during the molecular vibration. While polarisability is a scalar, the dipole moment is a vector. As this implies, certain vibrational modes cause a change of polarisability while others cause a change of dipole moment, as shown in the following examples.

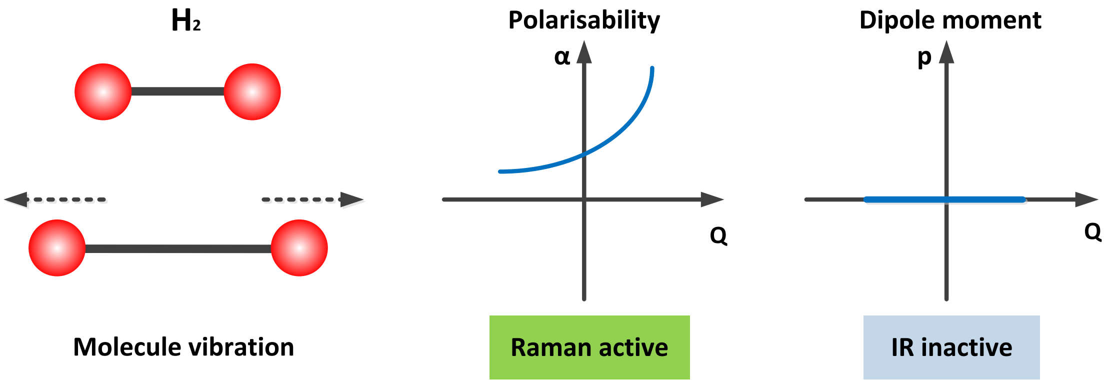

Figure 2.3. The molecule vibration of H_2 and its corresponding polarisability and dipole moment change with respect to the normal coordinate.

Figure 2.3 shows how the polarisability and dipole moment change with respect to the normal coordinate as the molecule H_2 vibrates. The vibration makes the separation between the atoms larger, and the electron cloud becomes less bounded by the atom. It means that the electron cloud tends to be more distorted when applying an external electric field, hence the polarisability becomes larger. Therefore, the vibration illustrated in Figure 2.3 is Raman active and should be shown as a Raman peak in the Raman spectrum. As for dipole moment, the molecule is symmetrical all the time during the vibration, hence the net molecular polarity is zero all the time, i.e. the dipole moment is zero. This vibration mode is then IR inactive and should not exist as a spectral feature in the IR spectrum. In fact, the above analysis is still valid when it extends to homonuclear diatomic molecules, such as O_2, N_2 etc. Therefore, Raman spectroscopy definitely is better than IR for homonuclear diatomic molecules detection. Now, the analysis will be extended to a simple polyatomic molecule - CO_2 - in order to further reveal that Raman spectroscopy and IR spectroscopy are complementary techniques.

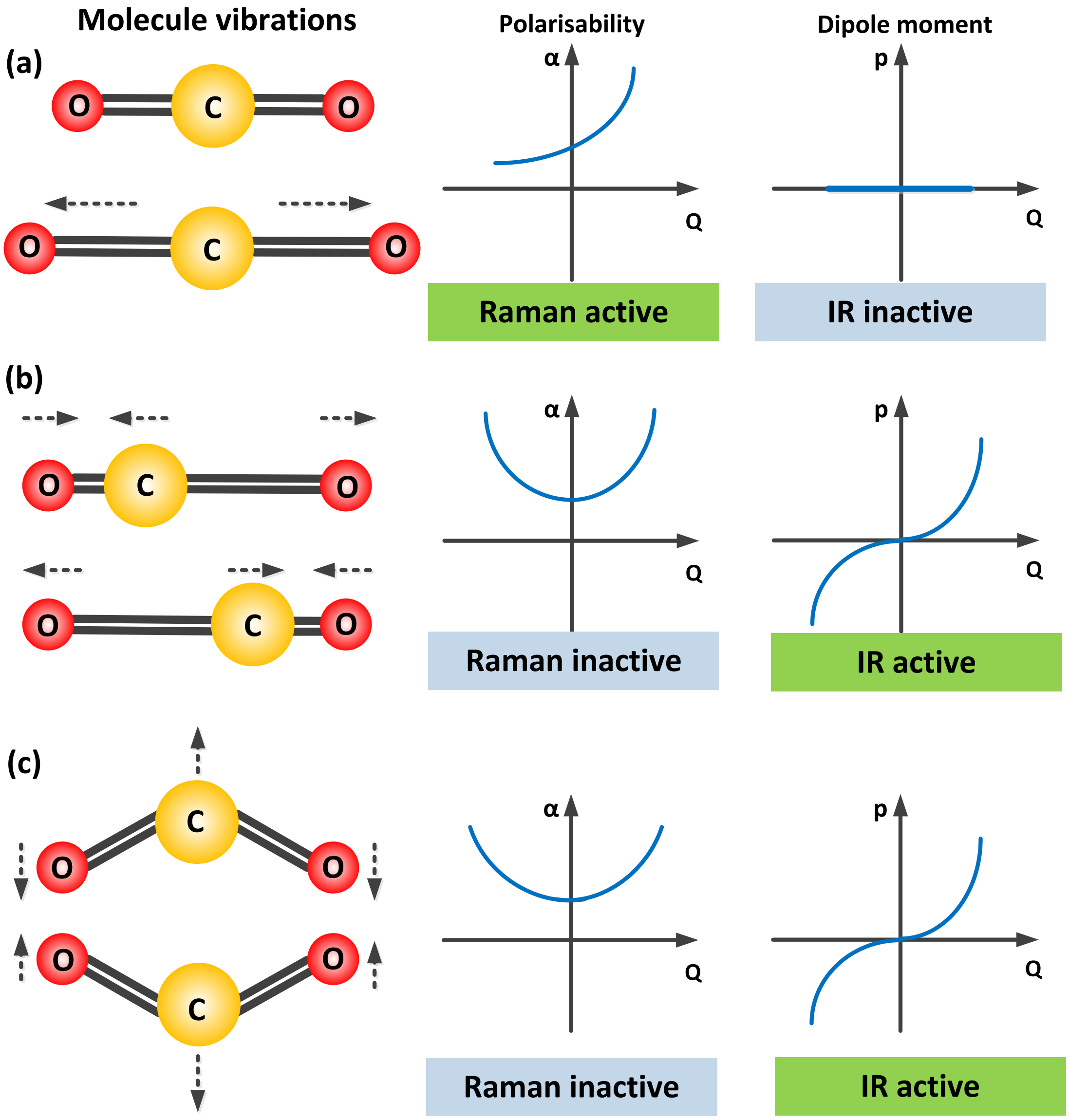

Figure 2.4. Polarisability and dipole moment variations during different molecular vibrations.

For a linear symmetric molecule like CO_2, there are four vibrational modes: a symmetric stretching mode (Figure 2.4a), an asymmetric stretching mode (Figure 2.4b), and two bending modes (Figure 2.4c) that have the same vibrational frequency [5]. For polyatomic molecules, the total molecular polarisability is the sum of contributions from polarisabilities of individual bonds while the total dipole moment is the 'vector' summation of each heteronuclear bond that has a non-zero bond dipole derivative. The length of the bond in Figure 2.4 is an indication of the magnitude of polarisability while the illustration of dipole moment is less obvious. For the symmetric stretching mode, the polarisability becomes larger during the molecular vibration as the atomic separation becomes larger whereas the net molecular polarity is always zero as the non-zero bond dipole derivative between C=O cancel each other. Therefore, this mode is Raman active and IR inactive. For the asymmetric stretching mode, as the polarisability of one bond becomes smaller the other becomes larger accordingly so that the total polarisability is the same. While the magnitude of the dipole moment remains the same, the shift of the carbon atom from one oxygen atom towards the other makes the dipole moment change its direction. Thus, this asymmetric stretching mode is Raman inactive and IR active. A similar analysis can be applied to the bending modes. To summarise, for those molecules with a center of symmetry, vibrational modes that are Raman active must be IR inactive, and vice versa. This rule of mutual exclusion proves to be very useful in distinguishing two alternative configurations of a molecule as well as providing structural information on an asymmetric molecule made of symmetric bands. The combined use of Raman spectroscopy and FTIR provides full and rich structural information of the molecule.

In aqueous media, IR spectroscopy is very vulnerable to high background absorption. In addition, Mid-IR light cannot penetrate many common optical materials, thus requiring nontrivial sample preparation for many applications. The use of near infrared (NIR) light, in the range of 1 to 2.5 µm, can effectively overcome these issues despite the fact that water still absorbs in this range. However, NIR is based on the overtones of FTIR fundamentals, which are not only weaker and broader than FTIR bands but also lack the structural specificity provided in the fingerprint region of FTIR. Under these circumstances, Raman spectroscopy combines the advantages of FTIR in terms of molecular specificity and the advantages of NIR in terms of trivial or no sample preparation, and most importantly is suitable for aqueous detection. Although Raman spectroscopy is a very attractive analytical tool, its use is hindered by low sensitivity due to inherently low Raman cross-sections. For example, Raman scattering is roughly 10^{-10} as likely as the corresponding mid-IR absorption [4]. In the next section, the implication of this drawback will be further explained.

2.2.4.2 Fluorescence

Fluorescence is a two-step process, which involves absorption and emission. As Figure 2.5 shows, an incident photon with energy E_0 excites an electron from ground state S_0 to excited state S_1. The electron then relaxes down the vibrational states of S_1 to the lowest energy level of S_1, on a timescale of the order of 0.1-10 ps [7]. From there, there are two types of transitions from S_1 to S_0, spontaneous emission (radiative transition) and non-radiative transition. Fluorescence relies on spontaneous emission, for which the electron relaxes down to a vibrational state of S_0, with an average lifetime of the order of 1-100 ns. At the same time, a photon is emitted with energy $E_1 < E_0$, where the difference is known as the Stokes shift. This Stokes shift determines the sensitivity of the fluorescence technique as it isolates the interference of excitation photons. The larger the shift the better the sensitivity is. The magnitude of the fluorescence emission is proportional to the magnitude of the excitation. Noting that the absorption can be triggered as long as the photon energy is sufficient, therefore the fluorescence can be excited at different wavelengths. In addition, for one specific molecule, the fluorescence emission is always the same no matter the excitation wavelength.

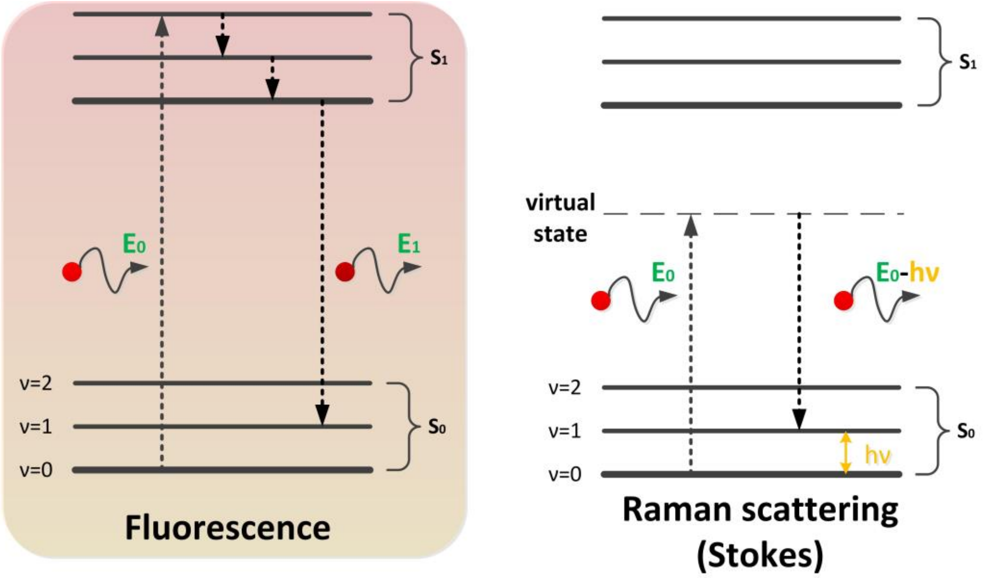

Figure 2.5. Jablonski diagram of fluorescence and Raman Stokes scattering.

Visible fluorescence can only occur in certain molecules, called fluorophores or fluorescent dyes. This limits the range of intrinsic molecule detection. Many applications require nontrivial sample preparation steps such as binding fluorescent dyes to certain molecules. Furthermore, the fluorescent spectrum doesn’t provide as rich structural information of the detected molecule as FTIR and Raman spectroscopy does. Unless photobleaching happens, in which fluorophore is irreversibly destroyed in the excited state, the same fluorophore can be repeatedly excited and generate fluorescence emission. Therefore, fluorescence is a highly sensitivity technique, which makes it attractive for a wide range of applications [8]. In contrast, the Raman cross-section is six to eight orders of magnitude less than that of the fluorescence [4]. Furthermore, the choice of a shorter excitation wavelength for more efficient Raman scattering is much hindered by the resultant generation of an overwhelmingly large fluorescence background that totally submerges the Raman signals. As a result, background fluorescence is one of the main reasons for the limited use of Raman spectroscopy historically. Nevertheless, the molecular specificity provided by Raman spectroscopy together with other advantages such as being label-free provide strong motivations for the development of Raman spectroscopy. Thanks to the development of lasers with many available wavelengths to choose from in the visible and near-IR region, a careful choice of the excitation wavelength can effectively suppress the fluorescence background, and hence increase the signal-to-noise ratio of the Raman signals. Moreover, many researchers have been working on enhancing the Raman signals in order to offer the sufficient sensitivity that many applications require. In the next section, a short introduction to these various techniques will be given with an emphasis on waveguide enhanced Raman spectroscopy.

2.3 Surface-enhanced Raman spectroscopy (SERS)

2.3.1 History

In 1974, Fleischmann *et al.* from the University of Southampton firstly reported a remarkable phenomenon in which the Raman scattering intensity was observed to be surprisingly strong from pyridine adsorbed on an electrochemically roughened silver electrode [1]. Considering that the Raman scattering is extremely weak (1 in 10^{10} photons), the observation of clear Raman spectra from a monolayer of pyridine molecules was unprecedented. From the last section, it is known that the power of the Raman signal is proportional to the number of Raman scatters; therefore for molecules adsorbed on a surface, larger surface area leads to more Raman signal power due to more Raman scatters. Even though the surface area was increased due to the surface roughness, the many orders of magnitude increase in the Raman signal could not be solely accounted for by this. A few years later, Jeanmarie and Van Duyne [9] and Albrecht and Creighton [10] confirmed the effect in the pyridine-on-silver system with an enhancement factor of 10^5 to 10^6, and proposed enhancement mechanism based on electromagnetic and chemical effects, respectively. Later, the SERS acronym was coined by Van Duyne [11]. Since then, a vast number of publications have contributed to this area. A detailed account of the discovery of surface-enhanced Raman scattering by McQuillan, one of Fleischmann's co-workers, can be found in [12].

2.3.2 Basic principles of SERS

Despite some early debates on the enhancement mechanism of SERS, it is now generally agreed that an electromagnetic enhancement and a chemical enhancement constitute the total enhancement. The electromagnetic enhancement relies on confining the electromagnetic field of an exciting laser light at the surface (in nano scale), which leads to a large increase of magnitude of surface intensity. While for the chemical enhancement, the molecular orbitals of the adsorbed molecule overlap with the orbitals of the metal surface to form new electronic levels, which are in resonance with the exciting laser light leading to enhancement in the strength of the Raman scattering for the adsorbed molecule. Of the two, the electromagnetic enhancement is the dominant force, for which both the incident (in-coupling) and scattered light (out-coupling) are influenced by this field enhancement, resulting in a total Raman signal enhancement proportional to E^4 [12], [13]:

$$I_{SERS}(\omega_{sc}) \propto \left|\frac{E_{local}(\omega_0)}{E_{inc}(\omega_0)}\right|^2 \cdot \left|\frac{E_{local}(\omega_{sc})}{E_{inc}(\omega_{sc})}\right|^2 \cdot \sum_{\rho,\sigma} \left|\left(\alpha_{\rho,\sigma}\right)_{f,i}\right|^2 \cdot I_{inc}(\omega_0)$$

Equation 2.11

where $I_{SERS}(\omega_{sc})$ is the SERS intensity at emitted frequency ω_{sc} and $I_{inc}(\omega_0)$ the incident light intensity at frequency ω_0, and E_{inc} is the incident and E_{local} the local field strength. In Equation 2.11, the first two terms describe the electromagnetic enhancement while the summation term contains the chemical enhancement contribution. Noting that the in-coupling and out-coupling enhancement are at different frequencies therefore E^4 is actually a simplification to describe the electromagnetic enhancement. Under the current context, field enhancement is of particular interest hence the discussion of electromagnetic enhancement of SERS will be emphasised.

The origin of electromagnetic enhancement is from coupling incident light into surface plasmon-polaritons (SPP) at the metal-dielectric interface where the energy is confined in the short range of the surface, thus resulting in field enhancement. In this SERS effect, the metal plays a crucial role. The free conduction electrons in a metal oscillate in a background of fixed positive ions, which ensures an overall neutrality to form a *plasma*. In the presence of an optical field, the charge density of the plasma will oscillate, which governs the optical response of the metal. The elementary excitation, or mode, of the oscillations of the plasma charge density is called a *plasmon*. In a sense, a plasmon (charge density oscillation) is to the free plasma charge density is what photons (electromagnetic modes) are to the electromagnetic field. Surface plasmon-polaritons correspond to mixed modes where the energy is shared between the surface plasmon at the metal-dielectric interface and the electromagnetic wave in the medium. These SPPs effectively squeeze the energy at the interface thanks to the non-radiative nature of these SPPs and their short lengths of evanescent decay (penetration depth) from the interface, which is the physical reason behind the field enhancement at the metal-dielectric interface. However, this field enhancement by SPPs will not be achieved without meeting the stringent coupling condition, in which the energy of the incident light is efficiently transferred to the SPPs. The momentum matching requirement of the coupling condition indicates that incident light from the air cannot excite SPPs. Instead, two common methods have been employed to excite SPPs, the grating method and the attenuated reflection (ATR) method [14].

There are two kinds of SPPs, propagating SPPs (PSPPs) and localized SPPs (LSPPs). PSPPs often exist on planar surfaces with propagation along the surface. The propagation length is limited since the energy is decaying due to the ‘lossy’ nature of the metal. Based on this property, a waveguide surface plasmon resonance sensor was previously developed by Harris and James at the University of Southampton [15]. For a surface geometry with micro- and nano-structures or nano-particles, SPPs can be highly localised around the structures (cavities), which can result in a much larger field enhancement than that offered by PSPPs. This enhancement can be so large that even single-molecule detection is possible [16], [17]. The prospect of achieving ultra-sensitive SERS devices, useful for a range of applications [18]–[21], drives significant efforts in designing and fabricating a variety of nanostructures [22] and nanoparticles [23]. Notably, researchers across the University of Southampton have made numerous contributions: SERS substrates based upon spherical nanovoids [24] fabricated by using the templated electrodeposition process [25]; and semiconductor lithographic techniques fabricated nanostructured inverted gold pyramids, which have been successfully commercialized to become the famously known ‘Klarite’ substrate [26].

2.3.3 Challenges

Historically, SERS based upon nanostructures or nanoparticles suffers from fabrication reproducibility issues and measurement repeatability issues, which hinder its wide uses. Significant efforts have been made in producing rational designed and well-controlled nano(micro)structures, such as the ‘Klarite’ substrates. However, the benefits offered have to be analysed on an application by application basis. In addition, SERS requires the use of noble metals such as gold and silver, which often make the production of SERS substrates expensive. Moreover, the uses of SERS substrates are often accompanied by using conventional Raman microscopy, which puts limits to the use out of the laboratory. Having said these, the SERS field is still developing to solve all these issues, which should be checked regularly in order to grasp the state-of-the-art.

2.4 Waveguide enhanced Raman spectroscopy (WERS)

Optical waveguide sensors take advantage of guided wave optics such as circularly shaped fibers and planar waveguides, which integrate the light transportation, light-medium interaction and sometimes collection together in a miniaturised manner. As the light propagates in the waveguide structure, a number of light properties can be modulated during the light-analyte interaction depending the application. Specifically, the motivation of applying waveguide technologies to Raman spectroscopy relies not only on those generic advantages such as miniaturisation and low cost but also on its inherent ability of enhancing the Raman scattering by maintaining a high optical intensity at a long length. Both optical fibers and planar waveguides have been applied for Raman spectroscopy [27]–[35]. While the former is exploited for 1) its needle-like sampling capability in biomedical research such as in vivo probing of tissue [35] and 2) its ability to guide light over a long distance in distributed sensing [36], [37]; the latter, known as integrated optics, is more compatible with 1) established silicon chip fabrication technologies and 2) surface modification techniques, which provide potential for achieving sensor chips with a wide range of applications [38]–[40]. In this section, the scope of discussion will be limited to waveguide enhanced Raman spectroscopy. Moreover, depending on which part of the guided wave is utilised, the light-medium interaction can happen in the waveguide core and/or its cladding, as explained in Chapter 1. It is the latter that is compatible with surface modification techniques for a wider range of applications, and is utilised in this project.

In the next section, the basic principle of waveguide enhanced Raman spectroscopy will be explained, followed by a literature review that highlights the main developments in the field. The aims are to 1) explain the motivation for waveguide enhanced Raman spectroscopy and 2) establish the background of the field in order to demonstrate the significance of the work in later chapters.

2.4.1 Principle of WERS

When light travels from a high refractive index layer A to a layer B with lower refractive index, there is a critical angle of incidence above which light get totally reflected at the interface A/B. If in the reflected direction there is another layer C with lower refractive index, then light is totally reflected again at the interface B/C. As a result, light rays bounce back and forth between the two interfaces, and travel in this structure, known as a waveguide. While the exact wave guiding condition will be explained in Section 3.2.1, the above is intended to illustrate the basic idea of waveguide operation. Though light is totally internally reflected, there is an exponentially decaying evanescent wave at the core/cladding interface 'penetrating' into the cladding. When the sensing medium is in the cladding, it is through the interaction between the evanescent wave and the detected molecules that Raman scattering is excited in WERS.

The magnitude of the Raman excitation, determined by the interface intensity and number of excited molecules, is closely related to the waveguide dimension. The waveguide core thickness can be in a range from less than half of the light wavelength to multiple wavelengths. So, for guided light in the visible to near infrared range (390 nm – 1.4 µm), the waveguide core thickness is only a few hundred nanometres. Guided light reflected back and forth in such a small dimension leads to the equivalent of around 10^3 – 10^6 reflections/cm, depending upon which waveguide mode the light travels in. Compared to the conventional Raman spectroscopy configuration, where light is incident and reflected only once, these multiple reflections essentially contribute to the large intensity on the waveguide surface (interface). Furthermore, light is always focussed in conventional Raman spectroscopy, resulting in a much smaller spot size, which on one hand increases the light intensity, but on the other hand reduces the number of excited molecules (proportional to excitation area). In contrast, light confined into a small dimension by the waveguide structure not only gets effectively 'focussed', which leads to a similar level of high intensity, but also maintains this high intensity over a much longer range (10^3-10^4 more by assuming low loss propagation in a few centimeters), which is proportional to the number of excited molecules for a surface uniformly covered with analyte. Equation 2.9 shows that total Raman scattered power is proportional to the optical intensity at the molecule and the number of 'excited' molecules. Therefore, high intensity and large sampling area in WERS boost the Raman scattered power on the waveguide surface, which are the main reasons for the 'enhancement' in WERS.

In addition, the penetration depth of waveguide evanescent field is only of the order of a few hundred nanometres for light in the visible to near-infrared. Therefore, molecules that are not close enough to the surface are not detected, which makes waveguide-enhanced Raman spectroscopy a surface sensitive technique. This is advantageous compared to the conventional Raman spectroscopy, as in many cases of the latter, there are significant background interferences due to the relatively large depth of focus (~few tens µm).

2.4.2 Development of WERS

The early development of waveguide Raman spectroscopy from 1970s to 1980s was motivated towards probing thin films from a few micro-meter down to sub-micro-meter. To put this into perspective, IR spectroscopy at that time required film thickness of at least 3 µm. Levy and his colleagues incorporated a polymeric film as thin as 0.3 µm as the waveguide core to form an asymmetric waveguide, and Raman spectra were successfully obtained. The higher optical field intensity achieved by waveguide confinement (10^3 enhancement) and increased scattering volume were stated as the two main sources of enhancement by making a comparison to the back scattering configuration of conventional Raman spectroscopy [31], [32]. However, it was found that considerable spectral interference, attributable to the substrate, put constraints on applying the technique to sub-micron thin films. Rabolt and Swalen further improved the technique by altering the optical field intensity distribution inside the waveguide structure through selection of different waveguide modes, resulting in higher optical field intensity in the desired material layer hence better signal to noise ratio. In addition, a careful choice of the substrate helped reduce the background interference [41]. The motivation of studying a polymer/polymer interface brought them to use the waveguide evanescent wave that penetrates into the layer (PVA) under investigation [42]. By incorporating resonance enhanced Raman scattering, Raman spectra of an around 3 nm thick dye monolayer were successfully obtained. Changes in the spectra such as Raman peak shifts compared to that from bulk measurement provided information on the surface adhesive bonding interactions at the surface [43]. Moreover, it was found that different combinations of excitation light polarisation and detection orientation revealed two-dimensional orientation information of a thin film on a substrate [33], [44]–[47]. For example, the extent of order in Langmuir-Blodgett film was studied as a function of temperature and compared with that of the bulk [45]. Later, Schlotter applied WERS for studying diffusion of small molecules in glassy polymer films by noting the technique's novel features including the simultaneous monitoring of all the molecular species involved in the experiment and the collection of in situ 'real time' data [48]. The unique advantages offered by WERS for thin film and interface characterisation were subsequently demonstrated through different test systems from iron phosphate thin films [49], protein films [50], [51], and coordination compounds [52], to silver nanoparticles [53]. Further development of the technique was made by Kanger in the 1990s as he and his colleagues optimised an asymmetric waveguide for highest surface intensity through 1) selecting the fundamental mode, 2) choosing a high index contrast material system (ZnO on SiO_2) and 3) choosing the optimum core thickness. This was demonstrated through detecting an 8 nm polystyrene film, protein bovine albumin and a Langmuir-Blodgett monolayer [30]. However, interference from ZnO limits the range of detection and the signal to noise ratio was only good enough to show the strong C-H stretching mode at around 3000 cm^{-1}.

For nearly all of the above examples, Raman spectra were collected through surface collection by imaging the streak of light of the waveguide surface onto the entrance slit of the spectrometer. WERS enhancement due to the high optical intensity and large scattering volume were generally not sufficient to show monolayer or even sub-monolayer detection with good signal to noise ratio. Although the Raman spectrum of monolayer biomolecules was detected by Kanger, the signal to noise ratio was only sufficient to allow detecting of one Raman feature, which limits its potential for molecular detection [30]. In order to provide additional enhancements, some other well-known Raman related enhancement methods such as resonance Raman spectroscopy [43], [50], coherent Stokes Raman scattering [54], stimulated Raman spectroscopy [34], surface enhanced Raman spectroscopy (SERS) [55]–[57], surface enhanced resonance Raman spectroscopy [52], [58], have been incorporated with WERS. Moreover, improvements have been made in the waveguide design. Qi intensified the evanescent wave by manipulating the refractive index of the waveguide superstrate with test molecules sitting at the core/superstrate interface [59]. Dhakal made waveguides of various lengths (max. 8.1 cm) into spirals and measured the Raman spectra of isopropyl alcohol (IPA) from the waveguide end [60]. From the same group, channel waveguides with different design parameters have been investigated and showed better performance of Raman excitation and collection than typical strip and slot waveguide of similar dimensions [61].

Despite all of the above developments, the sensitivity of WERS above has not been demonstrated to be sufficient for monolayer detection with rich spectral information. The integration of enhancement methods mentioned above and WERS are only applicable to certain molecules, and therefore have limited use.

2.5 Other enhanced Raman spectroscopy techniques

In this section, numerous other enhanced Raman spectroscopy techniques will be briefly mentioned. Resonance Raman (RR) scattering occurs when the incident photon matches an electronic transition of the molecule, which leads to increases of Raman scattering intensity by factors of 10^2- 10^6. However, the corresponding incident wavelengths coincide with exciting background fluorescence in the UV-visible range. Stimulated Raman scattering (SRS) occurs by injecting both pump and Stokes photons so that their frequency difference matches a molecular vibrational mode, which results in an increase of Raman emission rate. In this non-linear effect, the intensity of the emitted Raman signal is proportional to the multiplication of the intensity of pump and Stokes light. Similar to SRS, coherent anti-Stokes Raman spectroscopy (CARS) requires the injection of both pump light and Stokes light, with their frequency difference equal to a molecular vibrational mode. Unlike SRS, another probe light needs to be incident in order to generate anti-Stokes Raman scattering, as illustrated in Figure 2.6.

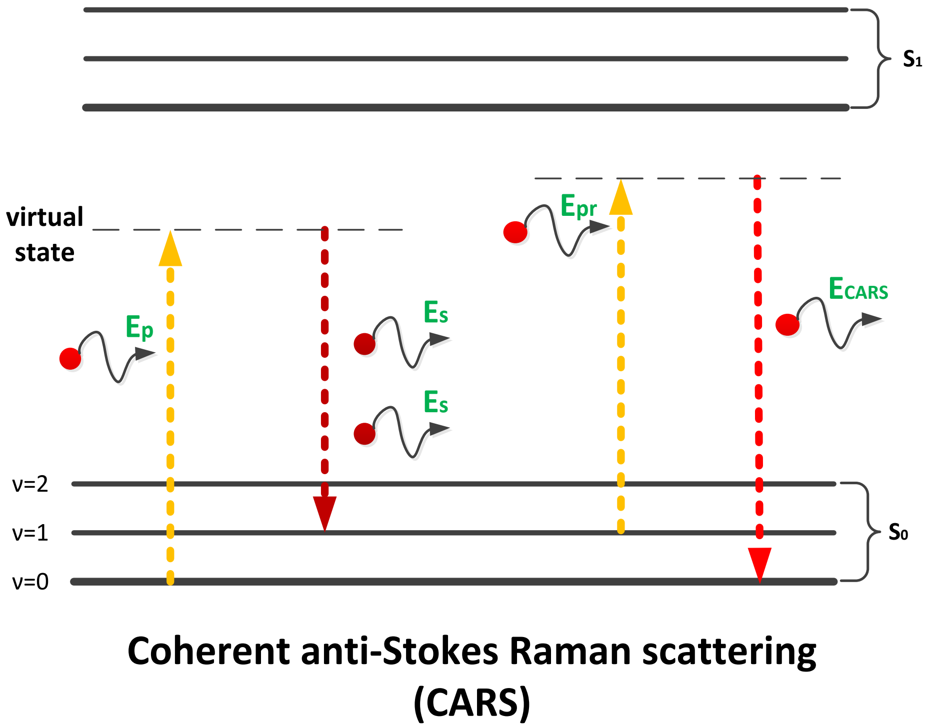

Figure 2.6 Illustration of CARS in Jablonski diagram. E_p represents pump photon energy, E_s represents Stokes photon energy, E_{CARS} represents CARS photon energy. ν indicates vibrational mode of the molecule.

The resultant Raman emission intensity is proportional to the multiplication of all three incident light intensities. This often leads to a much enhanced Raman signal as compared to that from the spontaneous Raman scattering. However, CARS can be hampered by a strong non-resonant background.

Tip-enhanced Raman spectroscopy combines SERS and atomic force microscopy (AFM) by coating the probe tip of AFM with SERS active metals or nanoparticles. When the probe tip with less than 100 nm end radius gets in contact with the surface, ‘hot spots’ with highly localized optical energy can be formed around the probe tip. AFM enables the movement of tip along the surface, thus obtaining Raman signals from molecules or regions of interest. However, the bulky and sophisticated instruments of TERS are very unsuitable for portable system.

The same limitation applied to time-resolved Raman spectroscopy, which suppresses the background fluorescence from Raman signals by taking the fact that Raman scattering occurs in much less than a picosecond whereas fluorescence occurs in nanosecond scale. Short and intense laser pulses are utilised to excite the sample with the measurement taken during the pulses, in a so called time gated measurement [62], [63].

Photo-acoustic Raman spectroscopy (PARS) overcomes the low sensitivity issue of Raman spectroscopy by measuring the acoustic response from the laser illuminated sample. Excitations of molecules generate thermal expansions, which releases acoustic waves to be detected by a sensitive microphone [64]. The advantage of the technology relies on the relatively better photo-acoustic response of the measured substance, as compared with the background. For example, the technology has been applied to glucose detection since blood has better photo-acoustic responses than that of the water, which makes it easier to distinguish hydrocarbons and glucose. However, the technology is sensitive to interference from temperature fluctuations and pressure changes. In addition, the instrumentation is expensive and sensitive to environmental parameters [65].

Electron-enhanced Raman spectroscopy is based on a laser-induced-breakdown (LIB) process, in which an intense laser pulse is focussed in the substance. In a few picoseconds, the number of electrons is dramatically increased, which results in a transient Raman cross-section increase [66]. The requirement of having large optical power density, in an order of 10^{11} W·cm^{-2}, limits the application of the technology for biological samples.

From the brief descriptions above, it is clear that each method has its own strength and weakness with certain applications. Progress have been made to combine these methods in order to deliver optimal performance for targeted applications, for example the combination of resonance Raman scattering and WERS for monolayer detection [43], SERS and CARS for imaging of molecular monolayers [67], SERS and WERS for monolayer detection [56]. It still opens up opportunities for integration of these technologies.

2.6 Conclusion

In this chapter, principles of Raman spectroscopy have been explained. As compared to many other spectroscopic techniques, Raman spectroscopy has advantages as it provides molecular specificity, has low absorption in aqueous environment, and requires trivial or no sample preparations. However, the application of Raman spectroscopy is hindered due to inherently low Raman cross-sections. Many technologies have been developed to tackle this issue. SERS with the help of SPPs on a nanostructured surface or nanoparticles can dramatically increase the Raman intensity by an order of more than 10^6. However, SERS substrates often suffer from issues of fabrication reproducibility and measurement repeatability. The requirement of using noble metals increase the production cost. This puts obstacles on the road of SERS becoming a versatile analytical tool. WERS not only has the capability of integrating many functionalities on a miniaturised device but also enhances the Raman signal due to high intensity maintained over a long length. Although WERS has been successfully employed to investigate thin films, there is a burning demand to have a larger sensitivity so that monolayer detection with multiple Raman features can be achieved.

2.7 References

[1] M. Fleischmann, P. J. Hendra, and A. J. McQuillan, “Raman spectra of pyridine adsorbed at a silver electrode,” *Chem. Phys. Lett.*, vol. 26, no. 2, pp. 163–166, May 1974.

[2] C. V. Raman and K. S. Krishnan, “A new type of secondary Radiation,” *Nature*, vol. 121, no. 3048, pp. 501–502, 1928.

[3] P. Vandenabeele, *Practical Raman Spectroscopy - An Introduction*, First Edit. Chichester, UK: John Wiley & Sons, Ltd, 2013.

[4] R. L. McCreery, *Raman Spectroscopy for Chemical Analysis*. Hoboken, NJ, USA: John Wiley & Sons, Inc., 2000.

[5] D. A. Long, *The Raman Effect*, vol. 8. Chichester, UK: John Wiley & Sons, Ltd, 2002.

[6] P. E. Le Ru and P. G. Etchegoin, *Principles of Surface-Enhanced Raman Spectroscopy: and Related Plasmonic Effects*, 1st editio. Elsevier, 2009.

[7] B. Valeur, *Molecular Fluorescence: Principles and Applications*. Wiley-VCH Verlag GmbH, 2001.

[8] S. T. Hess, S. Huang, A. A. Heikal, and W. W. Webb, “Biological and chemical applications of fluorescence correlation spectroscopy: A review,” *Biochemistry*, vol. 41, no. 3. pp. 697–705, 2002.

[9] D. L. Jeanmaire and R. P. Van Duyne, “Surface Raman spectroelectrochemistry,” *J. Electroanal. Chem. Interfacial Electrochem.*, vol. 84, no. 1, pp. 1–20, Nov. 1977.

[10] M. G. Albrecht and J. A. Creighton, “Anomalously intense Raman spectra of pyridine at a silver electrode,” *J. Am. Chem. Soc.*, vol. 99, no. 15, pp. 5215–5217, Jun. 1977.

[11] R. P. Van Duyne, “Laser Excitation of Raman Scattering from Adsorbed Molecules on Electrode Surfaces,” in *Chemical and Biochemical Applications of Lasers*, C. B. Moore, Ed. Elsevier, 1979, pp. 101–185.

[12] A. J. McQuillan, “The discovery of surface-enhanced Raman scattering,” *Notes Rec. R. Soc.*, vol. 63, no. 1, pp. 105–109, Mar. 2009.

[13] P. Bartlett and S. Mahajan, “Raman Spectroscopy of Biomolecules at Electrode Surfaces,” in *Bioelectrochemistry*, Wiley-VCH Verlag GmbH & Co. KGaA, 2012, pp. 269–334.

[14] J. M. Pitarke, V. M. Silkin, E. V Chulkov, and P. M. Echenique, “Theory of surface plasmons and surface-plasmon polaritons,” *Rep. Prog. Phys.*, vol. 1, no. 1, p. 54, 2006.

[15] R. D. Harris and J. S. Wilkinson, “Waveguide surface plasmon resonance sensors,” *Sensors Actuators B Chem.*, vol. 29, no. 1–3, pp. 261–267, 1995.

[16] K. Kneipp, Y. Wang, H. Kneipp, L. T. Perelman, I. Itzkan, R. R. Dasari, and M. S. Feld, “Single Molecule Detection Using Surface-Enhanced Raman Scattering (SERS),” *Phys. Rev. Lett.*, vol. 78, no. 9, pp. 1667–1670, Mar. 1997.

[17] S. Nie and S. R. Emory, “Probing Single Molecules and Single Nanoparticles by Surface-Enhanced Raman Scattering,” *Science*, vol. 275, no. 5303, pp. 1102–1106, 1997.

[18] G. McNay, D. Eustace, W. E. Smith, K. Faulds, and D. Graham, “Surface-enhanced Raman scattering (SERS) and surface-enhanced resonance raman scattering (SERRS): A review of applications,” *Appl. Spectrosc.*, vol. 65, no. 8, pp. 825–837, 2011.

[19] S. C. Luo, K. Sivashanmugan, J. Der Liao, C. K. Yao, and H. C. Peng, “Nanofabricated SERS-active substrates for single-molecule to virus detection in vitro: A review,” *Biosens. Bioelectron.*, vol. 61, pp. 232–240, 2014.

[20] D. Cialla, A. März, R. Böhme, F. Theil, K. Weber, M. Schmitt, and J. Popp, “Surface-enhanced Raman spectroscopy (SERS): Progress and trends,” *Analytical and Bioanalytical Chemistry*, vol. 403, no. 1. pp. 27–54, 2012.

[21] B. Sharma, R. R. Frontiera, A. Henry, E. Ringe, and R. P. Van Duyne, “SERS: Materials, applications, and the future,” *Mater. Today*, vol. 15, no. 1–2, pp. 16–25, Jan. 2012.

[22] R. J. C. Brown and M. J. T. Milton, “Nanostructures and nanostructured substrates for surface-enhanced Raman scattering (SERS),” *Journal of Raman Spectroscopy*, vol. 39, no. 10. pp. 1313–1326, 2008.

[23] J. Xie, Q. Zhang, J. Y. Lee, and D. I. C. Wang, “The synthesis of SERS-active gold nanoflower tags for in vivo applications,” *ACS Nano*, vol. 2, no. 12, pp. 2473–2480, 2008.

[24] S. Cintra, M. E. Abdelsalam, P. N. Bartlett, J. J. Baumberg, T. A. Kelf, Y. Sugawara, and A. E. Russell, “Sculpted substrates for SERS.,” *Faraday Discuss.*, vol. 132, pp. 1–9, 2006.

[25] P. N. Bartlett, “Electrodeposition of Nanostructured Films Using Self-Organizing Templates,” *Electrochem. Soc. Interface*, vol. 13, no. 4, pp. 28–33, 2004.

[26] “EU project delivers new possibilities for SERS sensors.” [Online]. Available: http://www.renishaw.com/en/eu-project-delivers-new-possibilities-for-sers-sensors--24460. [Accessed: 04-May-2016].

[27] P. C. Ashok, G. P. Singh, K. M. Tan, and K. Dholakia, “Fiber probe based microfluidic raman spectroscopy.,” *Opt. Express*, vol. 18, no. 8, pp. 7642–9, 2010.

[28] S. O. Konorov, C. J. Addison, H. G. Schulze, R. F. B. Turner, and M. W. Blades, “Hollow-core photonic crystal fiber-optic probes for Raman spectroscopy.,” *Opt. Lett.*, vol. 31, no. 12, pp. 1911–1913, 2006.

[29] R. L. McCreery, “Fiber-Optic Raman Sampling,” in *Raman Spectroscopy for Chemical Analysis*, Hoboken, NJ, USA: John Wiley & Sons, Inc., 2005, pp. 333–371.

[30] J. S. Kanger, C. Otto, M. Slotboom, and J. Greve, “Waveguide Raman Spectroscopy of Thin Polymer Layers and Monolayers of Biomolecules Using High Refractive Index Waveguides,” *J. Phys. Chem.*, vol. 100, no. 8, pp. 3288–3292, Jan. 1996.

[31] Y. Levy, C. Imbert, J. Cipriani, S. Racine, and R. Dupeyrat, “Raman scattering of thin films as a waveguide,” *Opt. Commun.*, vol. 11, no. 1, pp. 66–69, 1974.

[32] J. Cipriani, S. Racine, R. Dupeyrat, H. Hasmonay, M. Dupeyrat, Y. Levy, and C. Imbert, “Raman scattering of Langmuir-Blodgett barium stearate layers using a total reflection method,” *Opt. Commun.*, vol. 11, no. 1, pp. 70–73, 1974.

[33] J. S. Kanger and C. Otto, “Orientation Effects in Waveguide Resonance Raman Spectroscopy of Monolayers,” *Appl. Spectrosc.*, vol. 57, no. 12, pp. 1487–1493, Dec. 2003.

[34] J. S. Kanger, C. Otto, and J. Greve, “Stimulated Raman Gain Spectroscopy of Thin Layers Using Dielectric Waveguides,” vol. 3654, no. 96, pp. 16293–16297, 1996.

[35] M. G. Shim, B. C. Wilson, E. Marple, and M. Wach, “Study of fiber-optic probes for in vivo medical Raman spectroscopy,” *Appl. Spectrosc.*, vol. 53, no. 6, pp. 619–627, 1999.

[36] J. P. Dakin, D. J. Pratt, G. W. Bibby, and J. N. Ross, “Distributed optical fiber Raman temperature sensor using a semiconductor light source and detector,” *Electron. Lett.*, vol. 21, no. 13, p. 569, 1985.

[37] M. A. Farahani and T. Gogolla, “Spontaneous Raman scattering in optical fibers with modulated probe light for distributed temperature Raman remote sensing,” *J. Light. Technol.*, vol. 17, no. 8, pp. 1379–1391, 1999.

[38] R. A. Potyrailo, S. E. Hobbs, and G. M. Hieftje, “Optical waveguide sensors in analytical chemistry: today’s instrumentation, applications and trends for future development,” *Fresenius. J. Anal. Chem.*, vol. 362, no. 4, pp. 349–373, 1998.

[39] R. E. Dessy, “Waveguides as chemical sensors,” *Anal. Chem.*, vol. 61, no. 19, p. 1079A–1094A, Oct. 1989.

[40] T. E. Plowman, S. S. Saavedra, and W. M. Reichert, “Planar integrated optical methods for examining thin films and their surface adlayers,” *Biomaterials*, vol. 19, no. 4–5, pp. 341–355, 1998.

[41] J. F. Rabolt, R. Santo, and J. D. Swalen, “Raman Spectroscopy of Thin Polymer Films Using Integrated Optical Techniques.,” *Appl. Spectrosc.*, vol. 33, no. 6, pp. 549–551, 1979.

[42] J. D. Swalen, N. E. Schlotter, R. Santo, and J. F. Rabolt, “Raman Spectroscopy of Laminated Polymer Films by Integrated Optical Techniques,” *The Journal of Adhesion*, vol. 13, no. 2. pp. 189–194, 1981.

[43] J. F. Rabolt, R. Santo, and J. D. Swalen, “Raman Measurements on Thin Polymer Films and Organic Monolayers.,” *Appl. Spectrosc.*, vol. 34, no. 5, pp. 517–521, 1980.

[44] N. E. Schlotter and J. F. Rabolt, “Raman spectroscopy in polymeric thin film optical waveguides. 1. Polarised measurements and orientational effects in two-dimensional films,” *J. Phys. Chem.*, vol. 16, no. 4, pp. 2062–2067, 1984.

[45] J. Rabe, J. Swalen, and J. Rabolt, “Order-disorder transitions in Langmuir-Blodgett films. III. Polarised Raman studies of cadmium arachidate usign integrated optical techniques,” *J. Chem. Phys.*, vol. 86, no. May 2015, p. 1601, 1987.

[46] R. Santo, N. E. Schlotter, and J. D. Swalen, “Integrated Optics and Raman Scattering : Molecular Orientation in Thin Polymer Films and Langmuir-Blodgett Monolayers,” *IBM J. Res. Dev.*, vol. 26, no. 2, 1982.

[47] J. F. Rabolt, N. E. Schlotter, and J. D. Swalen, “Spectroscopic studies of thin film polymer laminates using Raman spectroscopy and integrated optics,” *J. Phys. Chem.*, vol. 85, no. 26, pp. 4141–4144, Dec. 1981.

[48] N. E. Schlotter, “Diffusion of small molecules in glassy polymer thin films studied by waveguide Raman techniques,” *J. Phys. Chem.*, vol. 94, no. 4, pp. 1692–1699, 1990.

[49] T. Mitsuhata, S. Fujii, K. Itoh, K. Itoh, and M. Murabayashi, “Tapered velocity coupling method for optical waveguide Raman scattering spectroscopy: application to iron(III) phosphate thin films,” *J. Phys. Chem.*, vol. 96, no. 22, pp. 8813–8817, 1992.

[50] D. Walker, H. Hellinga, S. Saavedra, and W. Reichert, “Integrated optical waveguide attenuated total reflection spectrometry and resonance Raman spectroscopy of adsorbed cytochrome c,” *J. Phys. Chem.*, vol. 97, no. Number 39, p. 10217, 1993.

[51] A. Pope, A. Schulte, Y. Guo, L. K. Ono, B. R. Cuenya, C. Lopez, K. Richardson, K. Kitanovski, and T. Winningham, “Chalcogenide waveguide structures as substrates and guiding layers for evanescent wave Raman spectroscopy of bacteriorhodopsin,” *Vib. Spectrosc.*, vol. 42, no. 2, pp. 249–253, 2006.

[52] S. Ellahi and R. E. Hester, “Enhanced waveguide Raman spectroscopy with thin films. Plenary lecture,” *The Analyst*, vol. 119, no. 4. pp. 491–495, 1994.

[53] M. Ferrari, F. Gonella, M. Montagna, and C. Tosello, “Waveguide Raman spectroscopy as a tool for the detection of aanometric metallic particles in glasses,” *J. Raman Spectrosc.*, vol. 27, no. 10, pp. 793–797, 1996.

[54] W. M. Hetherington, G. I. Stegeman, R. M. Fortenberry, N. E. Van Wyck, and E. W. Koenig, “Observation of coherent Raman scattering in thin-film optical waveguides,” *Opt. Lett.*, vol. 9, no. 3, p. 88, Mar. 1984.

[55] Y. Gu, S. Xu, H. Li, S. Wang, M. Cong, J. R. Lombardi, and W. Xu, “Waveguide-enhanced surface plasmons for ultrasensitive SERS detection,” *J. Phys. Chem. Lett.*, vol. 4, no. 18, pp. 3153–3157, 2013.

[56] S. J. Pearce, M. E. Pollard, S. Z. Oo, R. Chen, and M. D. B. Charlton, “Nanostructured surface enhanced Raman scattering sensor platform with integrated waveguide core,” *Appl. Phys. Lett.*, vol. 181101, no. May, 2014.

[57] F. Peyskens, A. Dhakal, P. Van Dorpe, N. Le Thomas, and R. Baets, “Surface enhanced Raman spectroscopy using a single mode nanophotonic-plasmonic platform,” *ACS Photonics*, vol. 3, no. 1, pp. 102–108, Jan. 2016.

[58] S. B. Ellahi and R. E. Hester, “Waveguide surface-enhanced resonance Raman spectroscopy of $Ru(bpy)_3{}^{2}+$,” *Anal. Chem.*, vol. 67, no. 1, pp. 108–113, Jan. 1995.

[59] D. Hu and Z. Qi, “Refractive-index-enhanced Raman spectroscopy and absorptiometry of ultrathin film overlaid on an optical waveguide,” *J. Phys. Chem. C*, vol. 117, no. 31, pp. 16175–16181, Aug. 2013.

[60] A. Dhakal, A. Z. Subramanian, P. Wuytens, F. Peyskens, N. Le Thomas, and R. Baets, “Evanescent excitation and collection of spontaneous Raman spectra using silicon nitride nanophotonic waveguides,” *Opt. Lett.*, vol. 39, no. 13, pp. 4025–4028, 2014.

[61] A. Dhakal, A. Raza, F. Peyskens, A. Z. Subramanian, S. Clemmen, N. Le Thomas, and R. Baets, “Efficiency of evanescent excitation and collection of spontaneous Raman scattering near high index contrast channel waveguides.,” *Opt. Express*, vol. 23, no. 21, pp. 27391–404, 2015.

[62] P. Matousek, M. Towrie, C. Ma, W. M. Kwok, D. Phillips, W. T. Toner, and A. W. Parker, “Fluorescence suppression in resonance Raman spectroscopy using a high-performance picosecond Kerr gate,” *J. Raman Spectrosc.*, vol. 32, no. 12, pp. 983–988, 2001.

[63] J. Kostamovaara, J. Tenhunen, M. Kögler, I. Nissinen, J. Nissinen, and P. Keränen, “Fluorescence suppression in Raman spectroscopy using a time-gated CMOS SPAD.,” *Opt. Express*, vol. 21, no. 25, pp. 31632–31645, 2013.

[64] J. J. Barrett and M. J. Berry, “Photoacoustic Raman spectroscopy (PARS) using cw laser sources,” *Appl. Phys. Lett.*, vol. 34, no. 2, pp. 144–146, 1979.

[65] C. F. So, K. S. Choi, T. K. S. Wong, and J. W. Y. Chung, “Recent advances in noninvasive glucose monitoring,” *Med. Devices Evid. Res.*, vol. 5, no. 1, pp. 45–52, 2012.

[66] H. Yui, “Electron-enhanced Raman scattering: A history of its discovery and spectroscopic applications to solution and interfacial chemistry,” *Anal. Bioanal. Chem.*, vol. 397, no. 3, pp. 1181–1190, 2010.

[67] C. Steuwe, C. F. Kaminski, J. J. Baumberg, and S. Mahajan, “Surface Enhanced Coherent Anti-Stokes Raman Scattering on Nanostructured Gold Surfaces,” *Nano Lett.*, vol. 11, no. 12, pp. 5339–5343, Dec. 2011.

CHAPTER 3 Design, fabrication and characterisation of slab waveguides for WERS

3.1 Motivation

From the previous chapter, it was learned that Raman scattering was a very weak process therefore significant care should be put onto the design and fabrication of waveguides for WERS in order to achieve maximum performance. An electromagnetic model has been established to model the multilayer waveguide structure, solve for its modes and set up a 'venue' for a series of optimisations to be done. First of all, a classic matrix method was utilised to formulate mode equation of multi-layered waveguide. Then, Muller's method was applied to solve for its multiple modes. The results were checked against the literature for validation. Once a mode was solved, a vast amount of information can be obtained such as the surface intensity and penetration depth. Here, the excitation and the collection of Raman scattering are discussed separately. The excitation part will be discussed in this chapter whereas the collection part of theory will be discussed at later chapters, depending on the collection configuration. As a result, the primary figure of merit for excitation was defined as surface intensity. A series of figures will be shown for the figure of merit against different waveguide design parameters, and an optimised design of waveguide for WERS will be proposed.

In section on fabrication, the techniques used to form thin film waveguide structures will be discussed. Due to the very sensitive nature of the waveguide surface, significant efforts must be put into sample preparation techniques to ensure that low loss waveguide samples optimised for maximising waveguide Raman excitation can be obtained.

In section on characterisation, the thickness and index of the deposited film were measured and compared to the design. The deposited film needs to be amorphous therefore the crystallinity was measured by X-Ray Diffraction (XRD) technique. In order to couple light into the thin film waveguide, prism coupling method was used among others for experimental flexibility and practicality. An apparatus was designed and realised in order to successfully and repeatedly couple light into the waveguide, which enabled Raman measurements required in Chapters 4, 6, and 7.

3.2 Design of waveguides for WERS

3.2.1 Basic principles of slab waveguides

The simplest optical waveguides are dielectric slabs, also called planar waveguides, as shown in Figure 3.1A. They are often used as study models in order to gain an understanding of the waveguide properties of more complicated waveguides such as rib waveguides, as shown in Figure 3.1B. The core has a refractive index (n_1) larger than that of the substrate (n_2) and the cladding (n_3) in order to achieve confined waveguiding. Imagining a plane wave bouncing back and forth between the cladding-core and core-substrate interfaces, it is confined in the core region when the total internal reflection condition is met. However, it does not mean that any plane wave will be confined as long as that condition is met. In fact, only discrete angles for plane waves are associated with guided modes. Light travelling 'coherently' in multilayer media corresponds to a mode [1].

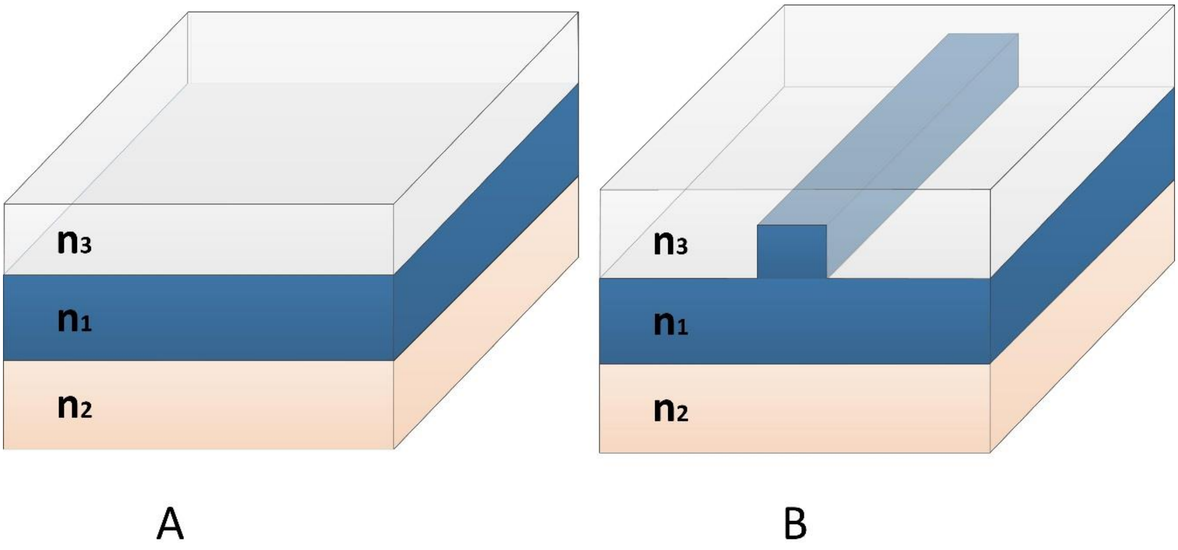

Figure 3.1 Schematic examples of A. Slab waveguide and B. Rib waveguide

As illustrated in Figure 3.2, when a plane wave travels in the direction θ, the dotted lines correspond to the phase fronts of the plane wave for which all points on the same phase front must be in phase. Thus, the phase difference Φ_1 occurring during travelling over the optical path AB and CD must be a multiple of 2π. Phase change is not only accumulated in traveling the physical distance (AB and CD) but in addition, phase changes occurs due to the total internal reflections at the interfaces.

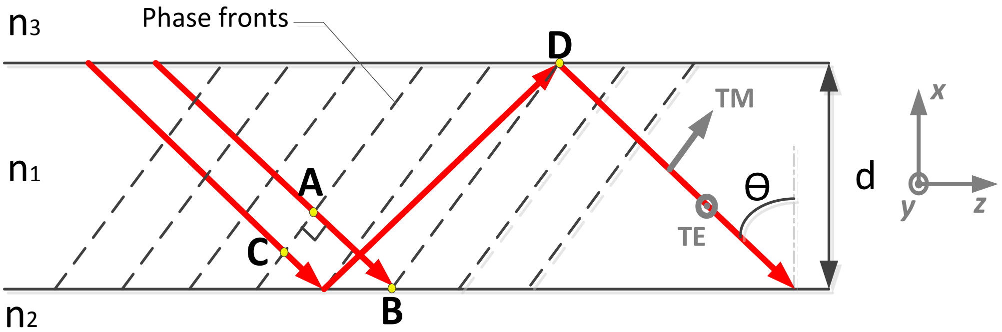

Figure 3.2 Illustration of light rays of a plane wave travels with their corresponding phase condition.

For example, the ray CD has two phase changes caused by the total internal reflection, one (Φ_2) is at the cladding-core (n_3-n_1) interface and the other (Φ_3) is at the core-substrate (n_1-n_2) interface. The eigenvalue equation then can be written as

$$\Phi_1 + \Phi_2 + \Phi_3 = 2N\pi \qquad \text{Equation 3.1}$$

Phases Φ are functions of plane wave traveling angle θ, refractive index of each layer and thickness of the core, which are given as:

$$\Phi_1 = 2dkn_1 \cos\theta$$ Equation 3.2

$$\Phi_2 = 2tan^{-1}\left[\frac{\sqrt{(sin^2\theta - n_3{}^2/n_1{}^2)}}{\cos\theta}\right](TE)\ or\ 2tan^{-1}\left[\frac{\sqrt{(sin^2\theta - n_3{}^2/n_1{}^2)}}{n_3{}^2/n_1{}^2\cos\theta}\right](TM)$$ Equation 3.3

$$\Phi_3 = 2tan^{-1}\left[\frac{\sqrt{(sin^2\theta - n_2{}^2/n_1{}^2)}}{\cos\theta}\right](TE)\ or\ 2tan^{-1}\left[\frac{\sqrt{(sin^2\theta - n_2{}^2/n_1{}^2)}}{n_2{}^2/n_1{}^2\cos\theta}\right](TM)$$ Equation 3.4

where $k = \frac{2\pi}{\lambda}$ is the propagation factor in free space, and TM and TE are polarisations that indicates the electric field direction as shown in Figure 3.2. In different polarisations, phases Φ are different, hence resulting in different eigenvalue equations. The above eigenvalue equation (Equation 3.1) essentially describes that for a plane wave to be guided within the waveguide structure, the transverse component of the wave needs to have an integral multiple of 2π, as it moves from one interface to the other then back to the beginning interface. The solutions (θ) of the eigenvalue equation correspond to confined modes, which can be characterised by effective index or propagation constant.

Ray optics as described above is intuitive to understand the concept of waveguide mode. In order to obtain a complete description of the modes of dielectric waveguides, Maxwell's equations must be solved. By assuming the magnetic permeability is everywhere the same as that of free space μ_0, Maxwell's equations are written in terms of the refractive index n_j (j=1,2,3) of the three layers as:

$$\nabla \times \mathbf{H} = n_j{}^2 \varepsilon_0 \frac{d\mathbf{E}}{dt}$$ Equation 3.5

$$\nabla \times \mathbf{E} = -\mu_0 \frac{d\mathbf{H}}{dt}$$ Equation 3.6

$$\nabla \cdot \mathbf{E} = 0$$ Equation 3.7

$$\nabla \cdot \mathbf{H} = 0$$ Equation 3.8

Where **H** is the magnetic field vector, **E** is the electric field vector, ε_0 is the electric permittivity of free space. By applying curl operator to Equation 3.3 and after some mathematical operations, it leads to the equation below:

$$\nabla^2 \mathbf{E} = \mu_0 \varepsilon_0 n_j{}^2 \frac{d^2\mathbf{E}}{dt^2}$$ Equation 3.9

Assuming $\mathbf{E} \propto e^{-i\omega t}$, $\frac{d^2\mathbf{E}}{dt^2}$ can be simplified to be $\omega^2\mathbf{E}$. Together with $k = \frac{\omega}{c}$ and $c = \frac{1}{\sqrt{\mu_0\varepsilon_0}}$, equation 3.6 can be written as:

$$\nabla^2\mathbf{E} + \mathrm{k}^2{\mathrm{n_j}}^2\mathbf{E} = 0$$ Equation 3.10

Equation 3.7 is known as the wave equation for a uniform dielectric medium with refractive index $\mathrm{n_j}$. Since slab waveguides are only two dimensional confined, field distributions of the modes are uniform throughout the *y*-direction, i.e. all derivatives with respect to *y* are zero. In addition, the *z*-dependence of **E** is in the form of $\mathrm{e}^{-\mathrm{i}\beta z}$, where β is the propagation constant in the *z*-direction. As a result, the wave equation in each layer $\mathrm{n_j}$ (j=1,2,3) can be written as [2]:

$$\frac{\partial^2\mathbf{E_j}}{\partial x^2} + \left({\mathrm{k_j}}^2 - \beta^2\right)\cdot\mathbf{E_j} = 0$$ Equation 3.11

$\mathrm{k_j}$ is the propagation constant in medium $\mathrm{n_j}$ (j=1,2,3) and is given by $\mathrm{k_j} = \mathrm{k}\cdot\mathrm{n_j}$. Equation 3.8 is in the form of the second order ordinary differential equation, therefore the solution E_y for TE polarisation in each layer can be easily obtained as:

Region 3:	$\mathrm{A}\cdot\mathrm{e}^{-\sqrt{\beta^2-{\mathrm{k_3}}^2}\cdot x}$	Equation 3.12
Region 1:	$\mathrm{B}\cdot\cos\left(\sqrt{{\mathrm{k_1}}^2-\beta^2}\cdot x\right) + \mathrm{C}\cdot\sin\left(\sqrt{{\mathrm{k_1}}^2-\beta^2}\cdot x\right)$	Equation 3.13
Region 2:	$\mathrm{D}\cdot\mathrm{e}^{\sqrt{\beta^2-{\mathrm{k_2}}^2}\cdot(x)}$	Equation 3.14

For TE polarisation, the only nonzero field components are E_y, H_x and H_z. The boundary condition requires that tangential components E_y and H_z (parallel to the interface) should be continuous at each interface. By linking E_y of each layer at the interface, the amplitude coefficient B and D can be expressed in terms of A and C:

Interface 3-1	$\mathrm{B} = \mathrm{A}$	Equation 3.15
Interface 1-2	$\mathrm{D} = \left[\mathrm{B}\cdot\cos\left(\sqrt{{\mathrm{k_1}}^2-\beta^2}\cdot\mathrm{d}\right) - \mathrm{C}\cdot\sin\left(\sqrt{{\mathrm{k_1}}^2-\beta^2}\cdot\mathrm{d}\right)\right]\cdot\mathrm{e}^{\sqrt{\beta^2-{\mathrm{k_2}}^2}\cdot(\mathrm{d})}$	Equation 3.16

By writing Equation 3.3 explicitly, H_x and H_z can be expressed in terms of E_y:

$$\mathrm{H}_x = -\frac{\beta}{\omega\mu_0}\mathrm{E}_y$$ Equation 3.17

$$\mathrm{H}_z = -\frac{\mathrm{i}}{\omega\mu_0}\cdot\frac{\partial\mathrm{E}_y}{\partial x}$$ Equation 3.18

Hence H_z can be expressed as

Region 3:

$$\frac{i}{\omega\mu_0}\cdot\sqrt{\beta^2-{k_3}^2}\cdot A\cdot e^{-\sqrt{\beta^2-{k_3}^2}\cdot x}$$

Equation 3.19

Region 1:

$$\frac{i}{\omega\mu_0}\cdot\sqrt{{k_1}^2-\beta^2}\cdot\left[A\cdot\sin\left(\sqrt{{k_1}^2-\beta^2}\cdot x\right)-C\cdot\cos\left(\sqrt{{k_1}^2-\beta^2}\cdot x\right)\right]$$

Equation 3.20

Region 2:

$$\frac{-i}{\omega\mu_0}\cdot\sqrt{\beta^2-{k_2}^2}\cdot\left[A\cdot\cos\left(\sqrt{{k_1}^2-\beta^2}\cdot d\right)-C\cdot\sin\left(\sqrt{{k_1}^2-\beta^2}\cdot d\right)\right]\cdot e^{\sqrt{\beta^2-{k_2}^2}\cdot(x+d)}$$

Equation 3.21

The boundary condition requires that:

Interface 3-1

$$\sqrt{\beta^2-{k_3}^2}\cdot A=-\sqrt{{k_1}^2-\beta^2}\cdot C$$

Equation 3.22

Interface 1-2

$$\sqrt{{k_1}^2-\beta^2}\cdot\left[A\cdot\cos\left(\sqrt{{k_1}^2-\beta^2}\cdot d\right)+C\cdot\sin\left(\sqrt{{k_1}^2-\beta^2}\cdot d\right)\right]=\sqrt{\beta^2-{k_2}^2}\cdot\left[A\cdot\cos\left(\sqrt{{k_1}^2-\beta^2}\cdot d\right)-C\cdot\sin\left(\sqrt{{k_1}^2-\beta^2}\cdot d\right)\right]$$

Equation 3.23

The amplitude coefficients can be eliminated after mathematical manipulation, resulting in the eigenvalue equation for TE modes:

$$\tan\left(\sqrt{{k_1}^2-\beta^2}\cdot d\right)=\frac{\sqrt{{k_1}^2-\beta^2}\cdot\left(\sqrt{\beta^2-{k_2}^2}+\sqrt{\beta^2-{k_3}^2}\right)}{({k_1}^2-\beta^2)-\sqrt{\beta^2-{k_2}^2}\cdot\sqrt{\beta^2-{k_3}^2}}$$

Equation 3.24

The same approach applied to the case of TM polarisation, the eigenvalue equation can be obtained as:

$$\tan\left(\sqrt{{k_1}^2-\beta^2}\cdot d\right)=\frac{{n_1}^2\cdot\sqrt{{k_1}^2-\beta^2}\cdot\left({n_3}^2\cdot\sqrt{\beta^2-{k_2}^2}+{n_2}^2\cdot\sqrt{\beta^2-{k_3}^2}\right)}{{n_2}^2\cdot{n_3}^2\cdot({k_1}^2-\beta^2)-{n_1}^4\cdot\sqrt{\beta^2-{k_2}^2}\cdot\sqrt{\beta^2-{k_3}^2}}$$

Equation 3.25

As shown above, the derivation of the eigenvalue equation for a simple 3 layer dielectric waveguide is quite complex. As the number of layer increases, it becomes even more difficult to derive. Therefore, it is necessary to have a generic approach for formulating the eigenvalue equation of a multi-layered waveguide easily.

3.2.2 Matrix method: formulate the mode equation of a multi-layer waveguide

One can imagine based on the illustration in Section 3.2.1, as the number of layers increase, the complexity of getting the analytical expression of eigenvalue equation becomes dramatically larger. Matrix method is powerful to easily formulate mode equation no matter how many layers the structure has [3]. This section will introduce what the matrix method is and how it can be utilised to formulate the mode equations of any arbitrary two-dimensional multilayer structure.

Electric fields are expressed at each interface as superposition of a forward travelling wave (A) and a backward travelling wave (B), as illustrated in Figure 3.3. The amplitude coefficients can be linked through boundary conditions at each interface.

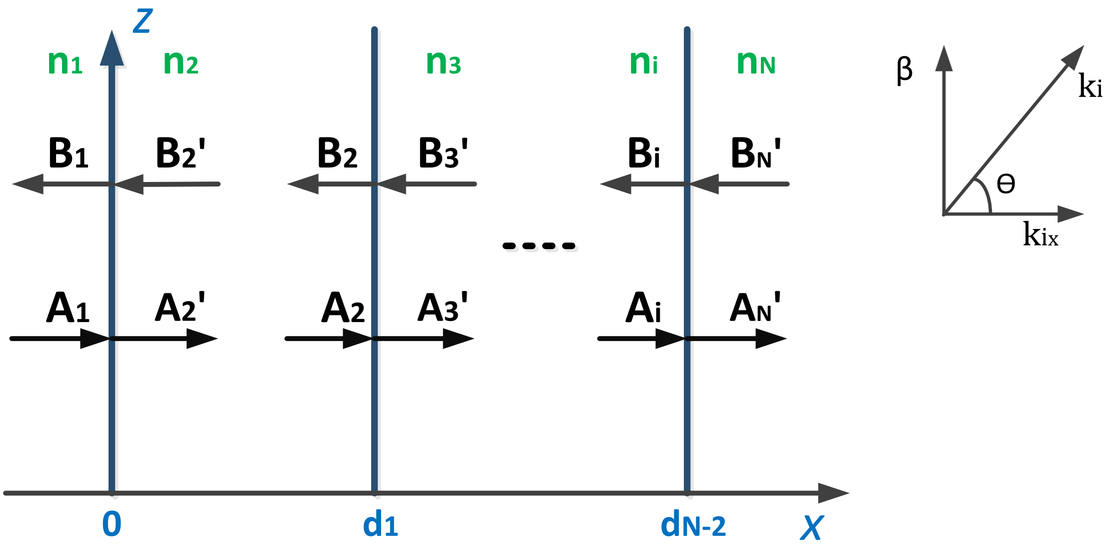

Figure 3.3 Illustration of waves in multilayer mediums represented by forward travelling wave (A) and backward travelling wave (B).

The electric field can be written as [3]

$$\mathrm{E_i}(x) = \mathrm{A_i}(x) + \mathrm{B_i}(x) = \mathrm{R} \cdot \mathrm{e}^{\mathrm{j k_{ix}} x} + \mathrm{L} \cdot \mathrm{e}^{-\mathrm{j k_{ix}} x}$$ **Equation 3.26**

(i indicates which medium layer the waves travels, R, L are amplitude coefficient of forward and backward travelling waves, respectively) by ignoring time dependant and *z*-dependant terms. k_{ix} is the propagation constant in the *x*-direction, which can be expressed as

$$\mathrm{k}_{ix} = \mathrm{k_0} \cdot \sqrt{\mathrm{n_i}^2 - \mathrm{n_{eff}}^2}$$ **Equation 3.27**

Or

$$\mathrm{k}_{\mathrm{i}x} = \sqrt{{\mathrm{k}_{\mathrm{i}}}^2 - \beta^2}$$

k_0	k -vector in vacuum equal to $\frac{2\pi}{\lambda}$, λ is the wavelength of the light guided in the waveguide.
n_{i}	Refractive index in layer i
$\mathrm{n}_{\mathrm{eff}}$	Effective index of the mode
k_{i}	k -vector in layer i equal to $\frac{2\pi}{\lambda} \cdot \mathrm{n}_{\mathrm{i}}$
β	Mode propagation constant

For TE modes, by applying boundary conditions, fields at the interface can be linked together as followed

$$\mathrm{A}_1(x) + \mathrm{B}_1(x) = {\mathrm{A}_2}'(x) + {\mathrm{B}_2}'(x)$$

Equation 3.28

$$\mathrm{n}_1 \cdot \cos(\theta_1) \cdot \mathrm{A}_1(x) - \mathrm{n}_1 \cdot \cos(\theta_1) \cdot \mathrm{B}_1(x) = \mathrm{n}_2 \cdot \cos(\theta_2) \cdot {\mathrm{A}_2}'(x) - \mathrm{n}_2 \cdot \cos(\theta_2) \cdot {\mathrm{B}_2}'(x)$$

Equation 3.29

Where θ_{i} is the ray angle to the normal plane of the interface in layer i. Then, it can be expressed in terms of propagation vectors as

$$\cos(\theta_{\mathrm{i}}) = \frac{\mathrm{k}_{\mathrm{i}x}}{\mathrm{k}_{\mathrm{i}}} \text{ or } \sqrt{1 - \frac{\beta^2}{{\mathrm{k}_{\mathrm{i}}}^2}}$$

Equation 3.30

These equations then can be written as

$$\mathrm{D}_1 \cdot \begin{pmatrix} \mathrm{A}_1 \\ \mathrm{B}_1 \end{pmatrix} = \mathrm{D}_2 \cdot \begin{pmatrix} \mathrm{A}'_2 \\ \mathrm{B}'_2 \end{pmatrix}$$

Equation 3.31

Where

$$\mathrm{D}_{\mathrm{i}} = \begin{pmatrix} 1 & 1 \\ \mathrm{n}_{\mathrm{i}} \cdot \cos\theta_{\mathrm{i}} & -\mathrm{n}_{\mathrm{i}} \cdot \cos\theta_{\mathrm{i}} \end{pmatrix}$$

Equation 3.32

is called a transfer matrix. Applying boundary conditions for TM modes, the transfer matrix is found to be:

$$\mathrm{D}_{\mathrm{i}} = \begin{pmatrix} \mathrm{n}_{\mathrm{i}} & \mathrm{n}_{\mathrm{i}} \\ \cos\theta_{\mathrm{i}} & -\cos\theta_{\mathrm{i}} \end{pmatrix}$$

Equation 3.33

In addition, when the light travels from one end of the medium layer to the other, light will change its phase and this can be described in terms of matrix by the following

$$P_2 \cdot \begin{pmatrix} A_2' \\ B_2' \end{pmatrix} = \begin{pmatrix} A_2 \\ B_2 \end{pmatrix} \quad \text{Equation 3.34}$$

where

$$P_2 = \begin{pmatrix} e^{i \cdot \varphi_2} & 0 \\ 0 & e^{-i \cdot \varphi_2} \end{pmatrix} \quad \text{Equation 3.35}$$

φ_i is the phase generated when the light propagates in the medium i and in the above case is given as:

$$\varphi_2 = k_{2x} \cdot d_2 \quad \text{Equation 3.36}$$

As a result, the fields at each interface can be represented by the fields at one end of the structure, which in this case is $E_1(x)$. And each amplitude coefficient can be calculated in the following:

$$\begin{pmatrix} A_N' \\ B_N' \end{pmatrix} = D_N^{-1} \left[\prod_{i=N}^{2} D_i P_i D_i^{-1} \right] D_1 \cdot \begin{pmatrix} A_1 \\ B_1 \end{pmatrix} \quad \text{Equation 3.37}$$

Or

$$\begin{pmatrix} A_N' \\ B_N' \end{pmatrix} = M_N \cdot \begin{pmatrix} A_1 \\ B_1 \end{pmatrix} \quad \text{Equation 3.38}$$

Where

$$M_N = D_N^{-1} \left[\prod_{i=N}^{2} D_i P_i D_i^{-1} \right] D_1 = \begin{pmatrix} M_{N11} & M_{N12} \\ M_{N21} & M_{N22} \end{pmatrix} \quad \text{Equation 3.39}$$

Then we can explicitly link the amplitude coefficient $\begin{pmatrix} A_N' \\ B_N' \end{pmatrix}$ in the last layer to the amplitude coefficient in the first layer $\begin{pmatrix} A_1 \\ B_1 \end{pmatrix}$.

$$A_N' = M_{N11} \cdot A_1 + M_{N12} \cdot B_1 \quad \text{Equation 3.40}$$

$$B_N' = M_{N21} \cdot A_1 + M_{N22} \cdot B_1 \quad \text{Equation 3.41}$$

In order to confine the light in the waveguide, it requires no exponentially growing field components in the cladding and substrate. Therefore, B_1 and A_N' must equal to zero. These guidance conditions then lead to the following condition that must to be met for a modal solution:

$$M_{N11} \cdot A_1 = 0 \quad \text{Equation 3.42}$$

As A_1 is not zero, therefore M_{N11} must be equal to zero. The following Equation 3.40 is the mode equation or eigenvalue equation.

$$\mathrm{M}_{\mathrm{N}11} = 0 \qquad \text{Equation 3.43}$$

The solution of the mode equation gives the mode characterised by a propagation constant (β) or effective index ($\mathrm{n}_{\mathrm{eff}}$). It can then be substituted back to Equation 3.34 to obtain all the amplitude coefficients. All these values will also need to be normalised to the power confined in the waveguide. In this process, A_1 is assigned to be any arbitrary number such as one initially. Once all the amplitude coefficients are calculated through Equation 3.34, the time-averaged power flow in the waveguide can then be calculated by integrating over the guide cross-section of the z-component of the Poynting vector (S_z):

$$\mathrm{P}_0 = \int_{-\infty}^{+\infty} \mathrm{S}_z \mathrm{d}x = \frac{1}{2}\int_{-\infty}^{+\infty} \mathrm{Re}(\mathrm{E} \times \mathrm{H}^*)_z \mathrm{d}x \qquad \text{Equation 3.44}$$

For TE modes, S_z is given by

$$\mathrm{S}_z = -\frac{1}{2}\mathrm{E}_y {\mathrm{H}_x}^* = \frac{\beta}{2\omega\mu_0}\left|\mathrm{E}_y\right|^2 \qquad \text{Equation 3.45}$$

For TM modes, S_z is given by

$$\mathrm{S}_z = \frac{1}{2}{\mathrm{H}_y}^*\mathrm{E}_x = \frac{\beta}{2\omega {\mathrm{n}_\mathrm{i}}^2 \varepsilon_0}\left|\mathrm{H}_y\right|^2 \qquad \text{Equation 3.46}$$

The ratio between the ‘real’ power confined in the waveguide, denoted as P_{in} and the one based on assigned value P_0 gives a scaling factor, which should be multiplied by the initial A_1 in order to get the ‘real’ $\mathrm{A}_1{}'$:

$$\mathrm{A}_1{}' = \mathrm{A}_1 \cdot \frac{\mathrm{P}_{\mathrm{in}}}{\mathrm{P}_0} \qquad \text{Equation 3.47}$$

The substitution of $\mathrm{A}_1{}'$ back to the Equation 3.34 finally gives all the ‘real’ amplitude coefficients of field in each layer for power P_{in} propagating in the waveguide.

3.2.3 Muller’s method

The mode equation is usually in a very complicated non-linear form; solving it analytically is usually not possible. Numerical methods that find numerical approximations to the solutions of non-linear equation are therefore chosen to solve for the mode equation. There are many numerical methods can be chosen to solve non-linear equations, popular ones include bisection, secant and Newton – Raphson. All these methods always start with some ‘guesses’ or ‘starting points’ either randomly or carefully chosen. Then, in each iteration the method gives an iteration solution to the equation, which is often wrong. Actually numerical methods will never give exactly true solutions but only good solutions that are ‘close enough’ to the true ones. It is through each iteration that the solution gets closer and closer to the true one until it is so close to be nearly true. And there is a criteria to that closeness, which is often determined by the error tolerance of the solutions. Once this criteria is met, the algorithm then stops and that solution provided in the latest iteration is the answer.

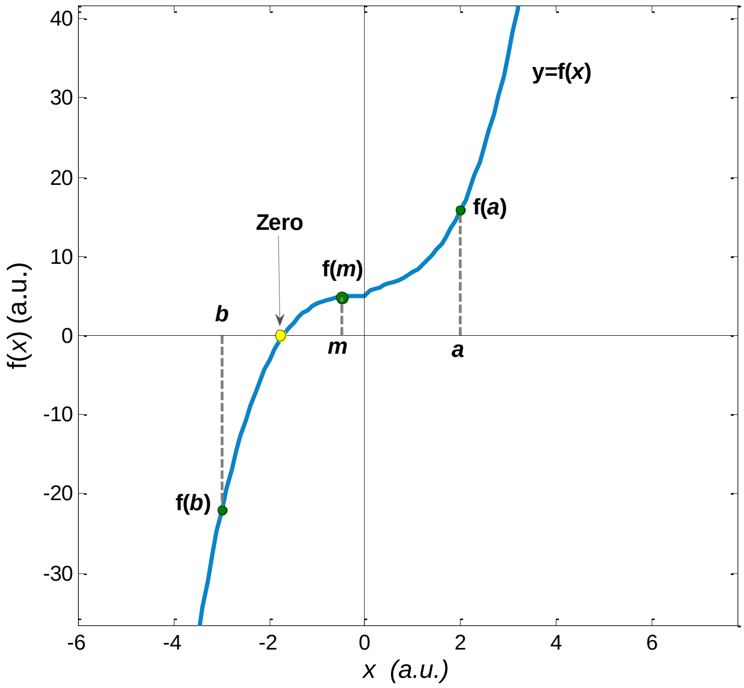

Figure 3.4 Illustration of bisection method.

As illustrated in Figure 3.4, the bisection method is to firstly choose an interval [*a*, *b*] in which the true solution sits in, which means f(*a*)·f(*b*)<0 must be true. Then, the iteration solution *m* is at the center of *a* and *b*, i.e. $m = (a+b)/2$. It is wrong as it does not meet the closeness criteria, i.e. not close enough to the true solution. However, it gets closer to it than the initial two values *a* and *b*. The next iteration then goes on with a new interval [a_1, b_1], where $a_1 = m$ and f(a_1)·f(b_1)<0. It will not be demonstrated here how the final solution is found but one can imagine how in each iteration the solution converges to the ‘true’ one. It will stop when the closeness criteria is met, i.e. f(*m*)<w.

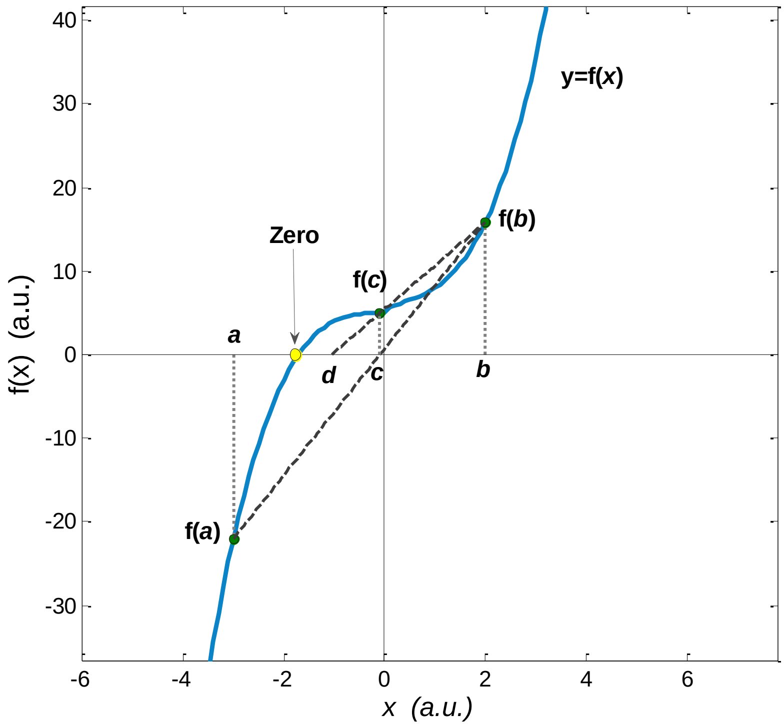

Figure 3.5 Illustration of secant method.

Unlike the bisection method, secant method converges to the solution by drawing a straight line passing through the two points (*a,* f(*a*)) and (*b,* f(*b*)) of the problem curve, as shown in Figure 3.5. The cross point (*c*) between the line and the *x*-axis is the solution in each iteration. Then, the next iteration starts with a new straight line passing through the points (*b,* f(*b*)) and (*c,* f(*c*)).

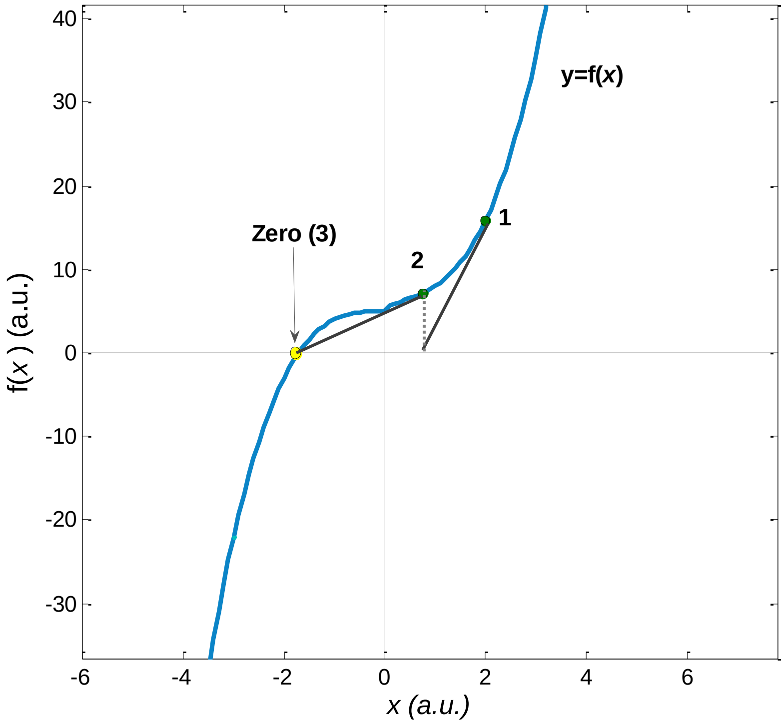

Figure 3.6 Illustration of Newton-Raphson's method.

As for Newton-Raphson's method, it starts with a good initial guess, as shown in Figure 3.6. By drawing a tangent line passing the function value of this guess (point 1), the solution in each iteration is the cross point between the tangent and the x-axis. If the iteration solution value does not meet the closeness criteria, the next iteration then starts at the point (2) corresponding to the last iteration solution. In the case above, the solution is then found at the second iteration, which gives solution (3).

As explained above, different methods have their own unique ways of converging in order to find out the solutions. Depending on the equation to be solved, one method may be more powerful than the others. It can be said that each method has its own territory so that for certain type of equations it may not be able to solve. In order to focus on the topic, it will not be explained in details and fully discussed of the use territory of each of these methods, but discuss it in the scope of the problems to be solved in this research project. Detailed information of each of their uses can be found in references [4], [5].

There are certain limitations to the above three methods. The former two need roots to be bracketed firstly before solving, i.e. locate the solution in a range. For one dimensional problem, this could be relatively easy as the function can be plotted and regions with functions crossing zeros can then be found. However, this can be extremely difficult as well as time consuming for the mode equation to be solved as it is usually very complicated in the complex plane. Newton–Raphson’s method is regarded as the most celebrated of all one-dimensional root-finding routines due to its strong convergence property [4]. Yet, it needs calculation of the first derivative of the function, which can be hugely difficult to do in some cases. Moreover, it needs a ‘good’ initial guess that is close enough to the root. For mode equations of multilayer metal-clad waveguides, it can be very difficult to evaluate its first derivative; and the nature that multiple roots in the complex plane demands more to give good initial guesses. To summarise, these methods fail to effectively solve the mode equation in terms of feasibility, use of convenience and time consumption. Muller’s method is satisfactory since it can be used to find any prescribed number of zeros, real or complex, of an arbitrary function. For most concerns, it usually does not need a good initial guess and it converges quadratically.

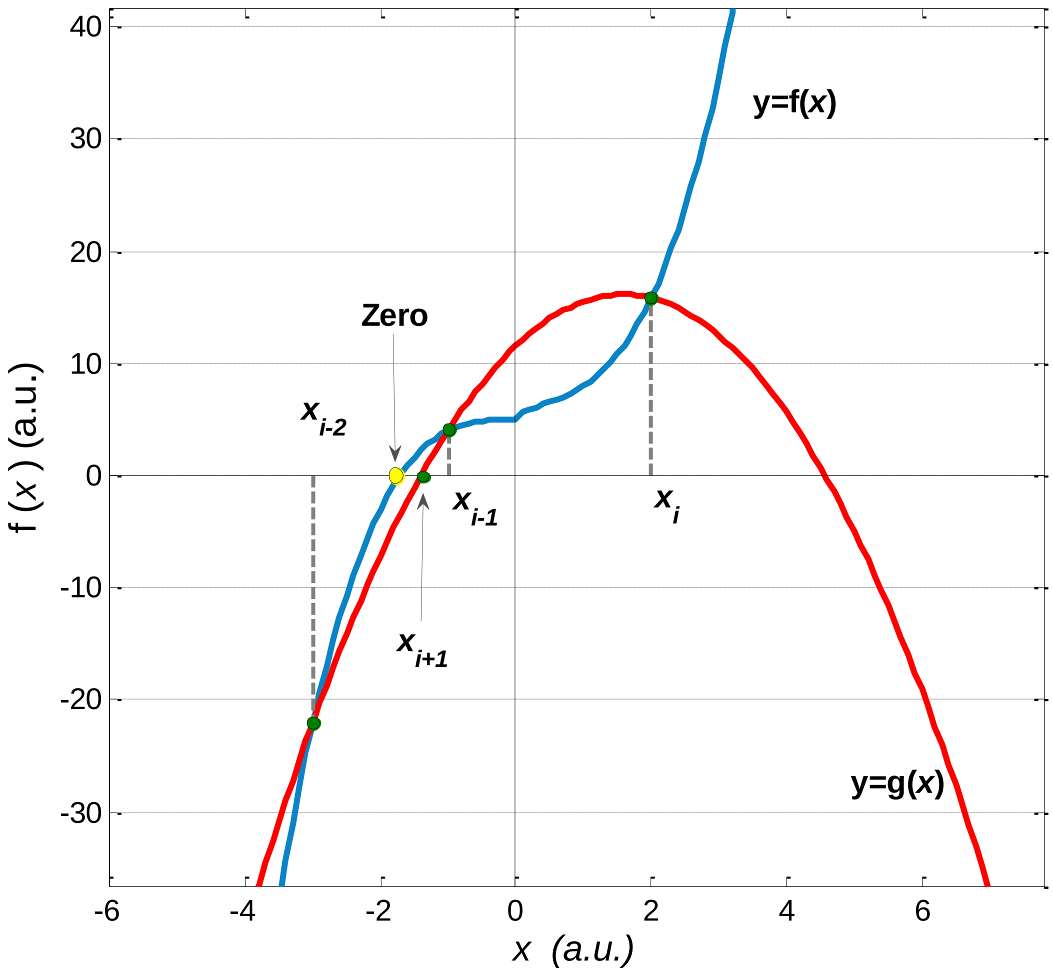

Figure 3.7 Illustration of Muller's method converging quadratically to find the zero.

The working mechanism of Muller's method is very similar to the secant method. Whereas in the secant method linear interpolation is used between two points, Muller's method uses quadratic interpolation by fitting a parabola through three points. The iterations can be started with any three values of x, for example x_{i-2}, x_{i-1} and x_i in Figure 3.7. The red line g(x) is the unique parabola that passes through these three points, (x_{i-2}, f(x_{i-2})), (x_{i-1}, f(x_{i-1})) and (x_i, f(x_i)). The solution or the next iteration point will be the one among two cross points that is at the x-axis. The formulas that produces these two intercepts are given as the below:

$$\mathrm{A} \equiv \frac{\mathrm{f}(x_i) - \mathrm{f}(x_{i-1})}{x_i - x_{i-1}}$$ **Equation 3.48**

$$\mathrm{B} \equiv \frac{\mathrm{f}(x_{i-1}) - \mathrm{f}(x_{i-2})}{x_{i-1} - x_{i-2}}$$ **Equation 3.49**

$$\mathrm{C} \equiv \frac{\mathrm{A} - \mathrm{B}}{x_i - x_{i-2}}$$ **Equation 3.50**

Then the parabola is given by:

$$\mathrm{g(x)} = \mathrm{a}_2 x^2 + \mathrm{a}_1 x + \mathrm{a}_0 \qquad \text{Equation 3.51}$$

Where

$$\mathrm{a}_2 = \mathrm{C} \qquad \text{Equation 3.52}$$

$$\mathrm{a}_1 = \mathrm{A} - (x_i + x_{i-1}) \cdot \mathrm{a}_2 \qquad \text{Equation 3.53}$$

$$\mathrm{a}_0 = \mathrm{f}(x_i) - x_i \cdot (\mathrm{A} - x_{i-1} \cdot \mathrm{a}_2) \qquad \text{Equation 3.54}$$

Through the function f(x) and the three initial points, A, B and C can be calculated from Equation 3.45 – 3.47, hence a_0 a_1 and a_2 can be obtained through Equations 3.49 – 3.51. Finally, the solutions to the parabola are determined through the equation:

$$x = \frac{2\mathrm{a}_0}{-\mathrm{a}_1 \pm \sqrt{{\mathrm{a}_1}^2 - 4\mathrm{a}_0\mathrm{a}_2}} \qquad \text{Equation 3.55}$$

The ± sign in the denominator of Equation 3.52 is chosen so that the denominator is the larger of the two. In the case illustrated in Figure 3.7, the left cross point is assigned to be the iteration solution or the next iteration point. According to [5], for reasons of accuracy and convenience, Muller proposed a somewhat different but equivalent procedure for obtaining the next approximation, x_{i+1}. The procedure as well as the implementation of this procedure in Matlab can be found in the Appendix A.

3.2.4 Validation

After explaining the matrix method that formulates the eigenfunction of multi-layer waveguides and Muller's method that numerically solves it, in this section, these two methods are applied to solve for the modes of multilayer waveguides. They are validated by comparing the results to the literature.

Firstly, a six-layer dielectric waveguide structure is solved. The six-layer structure rather than three-layer structure leads to more complicated eigenvalue function therefore makes it more difficult to solve. In Table 3.1, the modes of this structure in both TE and TM polarisation were obtained by the above methods and the results were presented as effective index. The closeness to zero criterion was set to 10^{-20}, which determines the accuracy of the results. The comparison between reference values and results obtained from waveguide design tool shows that they have no difference to the sixth decimal place, which validates the waveguide design tool for solving the modes of multilayer dielectric waveguides.

Table 3.1 Numerically calculated modes of six-layer dielectric waveguide structure, with structure terms defined in Figure 3.3

Waveguide system

n_1=1.0; n_2=1.66; n_3=1.53; n_4=1.60; n_5=1.66; n_6=1.50

d_1= 50 nm; d_2 = 50 nm; d_3 = 50 nm; d_4 = 50 nm

λ= 632.8 nm

Mode	Reference [6]	Waveguide design tool (Closeness to zero criteria: 10^{-20})
TM_0	1.620031	1.620031
TM_1	1.594788	1.594788
TM_2	1.554981	1.554981
TM_3	1.501818	1.501818
TE_0	1.622729	1.622729
TE_1	1.605276	1.605276
TE_2	1.557136	1.557136
TE_3	1.503587	1.503587

Not only multilayer dielectric waveguides but also multilayer metal-clad waveguides are of great interests as in the case of conventional surface-enhanced Raman spectroscopy that requires metal to support a surface plasmon. Unlike the structures comprised of all dielectric layers, the structure that has metal layer lead to a complex eigenvalue equation, which can fail many numerical methods but not Muller’s method as described in Section 3.2.3. Therefore, the waveguide design tool requires the validation of solving multilayer metal-clad waveguides. In one example provided by reference [7], the five-layer metal-clad waveguide shown in Table 3.2 has been solved for its five TE modes. The results obtained by waveguide design tool are shown in the right column, and are given by showing one more digit of the decimal in a purpose of giving more accuracy. For all these five modes, there are no difference at all for the real parts of the effective indices. Only slight differences are spotted for the imaginary parts of TE_3 and TE_4, and the difference are 0.05% and 0.09% respectively, which are negligible. From this example, it validates the efficacy of the waveguide design tool in solving multilayer metal-clad waveguides.

Table 3.2 Comparison of waveguide design tool implemented by Muller's method to the reference, with structure terms defined in Figure 3.3

Waveguide system

n_1=1.0; n_2=3.591-0.084j; n_3=3.211; n_4=3.166; n_5=3.15

d_1= 1.502 µm; d_2 = 0.74 µm; d_3 = 3.5 µm

λ=1550 nm

Mode	Reference [7]	Waveguide design tool
TE_0	$3.5628 + 8.4013 \times 10^{-2}j$	$3.56283 + 8.40134 \times 10^{-2}j$
TE_1	$3.4779 + 8.3771 \times 10^{-2}j$	$3.47792 + 8.37710 \times 10^{-2}j$
TE_2	$3.3360 + 8.1407 \times 10^{-2}j$	$3.33600 + 8.14066 \times 10^{-2}j$
TE_3	$3.1633 + 5.2852 \times 10^{-3}j$	$3.16328 + 5.28236 \times 10^{-3}j$
TE_4	$3.1594 + 3.4370 \times 10^{-3}j$	$3.15939 + 3.44010 \times 10^{-3}j$

To summarise, the waveguide design tool, developed by using the matrix method to formulate the eigenvalue equation of multilayer waveguides and Muller's method to solve for their modes, has been validated through two examples. There are no or negligible difference between the reference and the waveguide design tool produced results. Therefore, it proves that the waveguide design tool can be used to successfully solve for multilayer waveguides no matter they are all dielectric or metal-clad, which is the foundation to any design discussed in later sections.

One thing to note is that though Muller's method is very effective to solve the mode equation of multilayer waveguide structure, there are many other methods that can solve the problem quite productively as well. One example mentioned here is the Laguerre's method [8].

3.2.5 Performance and optimisation

The purpose of building the waveguide design tool is to study the behaviour of the figure of merit for WERS excitation in response to a series of design parameters such as waveguide core thickness, excitation wavelength and index contrast. After successful validation of the waveguide design tool in the last section, this section will focus on demonstrating and discussing how the figure of merit of waveguide Raman excitation changes with respect to those design parameters, in order to achieve maximum waveguide Raman excitation.

Since the evanescent field of the waveguide is utilised to detect molecules, the detected region is in the vicinity of the waveguide surface. Depending on the penetration depth of the evanescent field, this region is usually about few hundred nanometers. However, the most sensitive part of this region is at the waveguide surface with the maximum intensity. For applications that require high sensitivity such as monolayer detection, it is the surface intensity that determines the performance of waveguide Raman excitation. On the other hand, the total Raman excitation is proportional to the number of excited molecules, which is then approximately proportional to the excited area. Since the excited area is determined by the beam width of the laser and propagation length, it is more or less the same for different slab waveguide designs. Therefore, the primary figure of merit of the waveguide Raman excitation is the surface intensity. The normalised surface intensity, defined as the surface intensity divided by the power per unit width in the waveguide, has been utilised to eliminate the experimental details about pump power and beam width inside the waveguide [9]. Fused silica is chosen as the substrate as 1) it has low refractive index at visible wavelengths in order to achieve high index contrast; 2) it is transparent in the visible that opens window for collection at different locations of the waveguide; 3) its Raman cross-section are usually much smaller compared to the substance to be detected therefore its Raman signals do not block the observation; and 4) it has low fluorescence background. In addition to the choice of the substrate, there are other design parameters that are worth considering in order to maximise the surface intensity. In the following sections how design parameters such as core material, excitation wavelength, core thickness and analyte medium affect the surface intensity will be discussed, hence justifying the decision made for the design used for Raman experiments described in the following Chapters.

3.2.5.1 Surface intensity vs. index contrast

Based on the choice of the substrate, the core material needs to be chosen. It has been found that the index contrast ϕ, defined by the ratio of the core index and the substrate index, determines the refractive index change sensitivity [10] and fluorescence excitation efficiency [11] of the waveguide sensor for an optimised waveguide geometry and given analyte index. In this section, the relationship between the index contrast and the waveguide surface intensity will be investigated.

Figure 3.8A shows a three-layer dielectric waveguide structure with fused silica as the substrate and water as the top layer. The core material is set to be the variable that is due to be investigated. The excitation wavelength is 632.8 nm, which will be justified in the next Section 3.2.5.2. The various plots of normalized surface intensity against the core thickness with respect to different index contrast are shown in Figure 3.8B. Tantalum pentoxide (Ta_2O_5) and common glass materials LASF9, BAF10, BAK1, and Corning glass are chosen for this investigation. The refractive indices of the core span from 1.51 to 2.12. For each one of the plots, characterised by a different colour, there is a maximum surface intensity. It can be seen that this maximum surface intensity drops as the index contrast decreases for both TE and TM polarisations. The maximum surface intensity in the lowest index case (Corning glass) is only about 1/10th of that in the highest index case (Ta_2O_5) for both polarisations. Moreover, the rate of the fall in maximum surface intensity decreases as the index contrast becomes close to 1. In addition, the corresponding core thickness for maximum surface intensity becomes increasingly larger as the index contrast decreases. From an economical point of view, a high index contrast surely helps the reduction of the material use, although the total material cost needs to take into account the material cost per unit volume. Despite the inefficiency of achieving the high surface intensity in the case of low index contrast, the surface intensity is relatively insensitive to the variation of the core thickness, i.e. insensitive to fabrication errors. However, the fabrication error in terms of thin film thickness tends to be around few nanometers, which means that even in the case of high index contrast, the maximum surface intensity also remains without sharp change. All of these indicate that a high index contrast between the core and the substrate results in a significantly larger surface intensity than the correspondence in the case of low index contrast. For this reason, Ta_2O_5 is the best choice among the others. Moreover, it is optically transparent, compatible to silicon process, and has low attenuation below 3 dB/cm [10]. Therefore, Ta_2O_5 was chosen as the core material for waveguide enhanced Raman spectroscopy in this project.

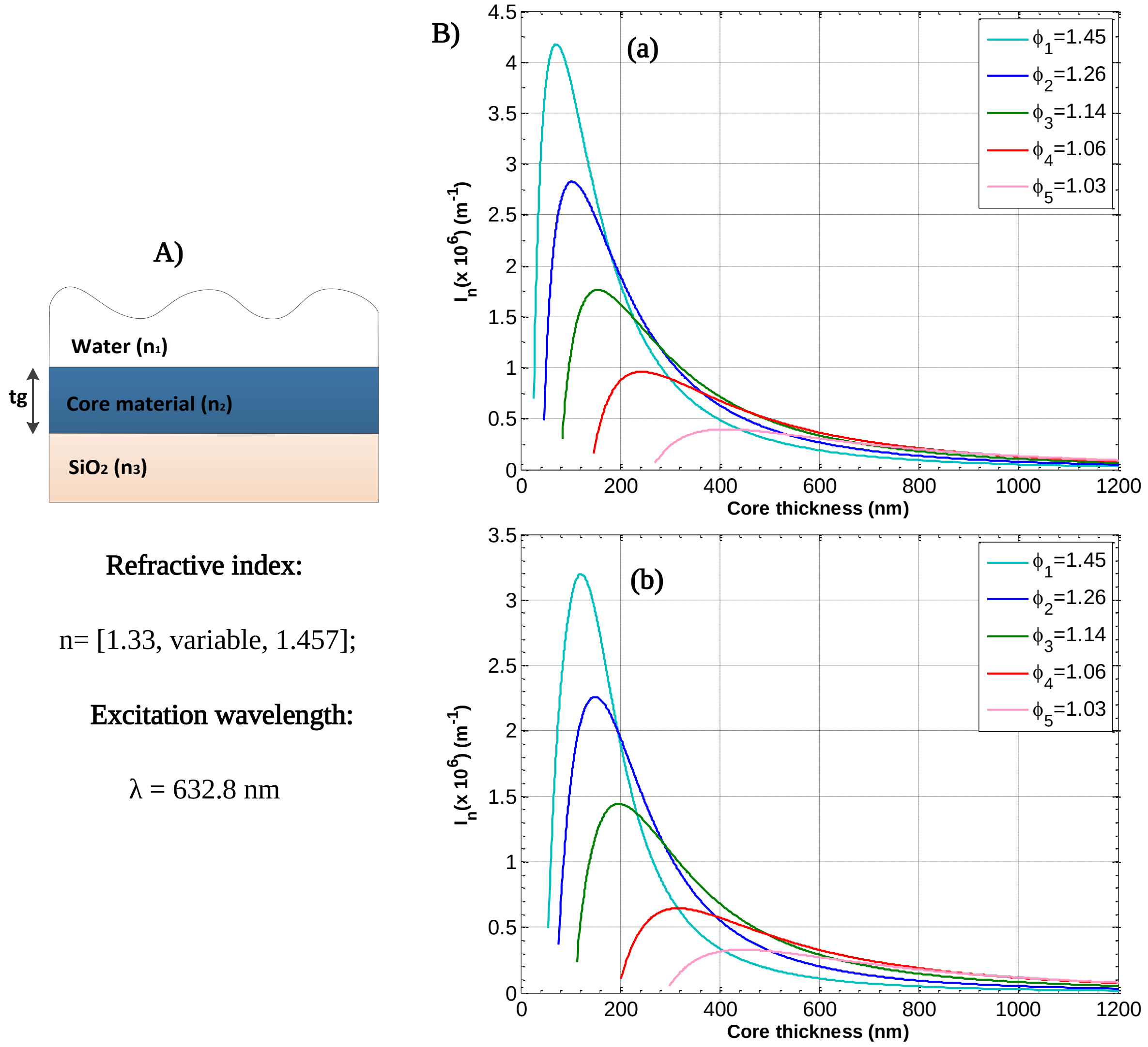

Figure 3.8 Index contrast varied plots of normalised surface intensity against the core thickness. A) 3 layer dielectric waveguide and its excitation wavelength; B) plots of normalized surface intensity against the core thickness under different index contrast. (a) TE case and (b) TM case. ϕ_1 corresponds to core material of Ta_2O_5 with refractive index 2.12. ϕ_2 corresponds to core material of LASF9 with refractive index 1.84. ϕ_3 corresponds to core material of BAF10 with refractive index 1.67. ϕ_4 corresponds to core material of BAK1 with refractive index 1.56. ϕ_5 corresponds to core material of Corning glass with refractive index 1.51.

3.2.5.2 Surface intensity vs. wavelength

The excitation wavelength (λ) is a very crucial factor to be carefully considered. First of all, it is closely related to the Raman cross-section (σ) of detected molecules as shown in Equation 3.56. As the wavelength decreases, the Raman cross-section becomes larger. Therefore, a shorter excitation wavelength is favourable for stronger Raman signal.

$$\sigma \propto \frac{1}{\lambda^4} \qquad \text{Equation 3.56}$$

However, another factor needs to be considered, which is the background fluorescence. Compared to Raman scattering, fluorescence is a much stronger process. Therefore, background fluorescence needs to be suppressed as much as it can be in order to successfully observe desired Raman signals. At shorter wavelength, there is a higher chance of exciting fluorescence due to higher photon energy. As a result, the excitation wavelength has to be chosen at a compromise of achieving less Raman signals in order to suppress the background fluorescence. Furthermore, the Charge-Coupled Device (CCD) in the majority of spectrometers used today is silicon based, which has low quantum efficiency at wavelength near to near-IR, hence low sensitivity. The low efficiency of exciting Raman can be compensated by having a large laser power. However, the aim of the project is for low-cost and miniaturised systems, which put limits on using bulky and expensive high-power laser. It is the efficiency of Raman excitation rather than purely absolute measure of Raman signals that counts in the design goal. Despite all the discussion above, it needs to be answered what the efficiency of 'waveguide' Raman excitation is with respect to the excitation wavelength.

Figure 3.9 shows how normalized surface intensity against core thickness curve varies with excitation wavelength. First of all, shorter excitation wavelength gives higher surface intensity regardless of the core thickness, for both TE and TM polarisations. Secondly, the rate of intensity changes with respect to the core thickness becomes lower as the excitation wavelength becomes longer, which means that it is not always true that shorter excitation wavelength leads to higher surface intensity therefore more efficient waveguide Raman excitation. For an example, at the core thickness of around 120 nm, the change of excitation wavelength between 532 nm, 632.8 nm and 785 nm has nearly no effect on the surface intensity in TE. Of course, if one takes into account the fourth order inversely proportional relationship between the excitation wavelength and Raman cross-section, as illustrated in Equation 3.56, the same 'waveguide' Raman excitation means that the shorter excitation wavelength gives an edge in total excited Raman scattering signals. Nevertheless, it is still necessary to point out that shorter excitation wavelength does not necessarily mean a higher waveguide Raman excitation for a fixed core thickness.

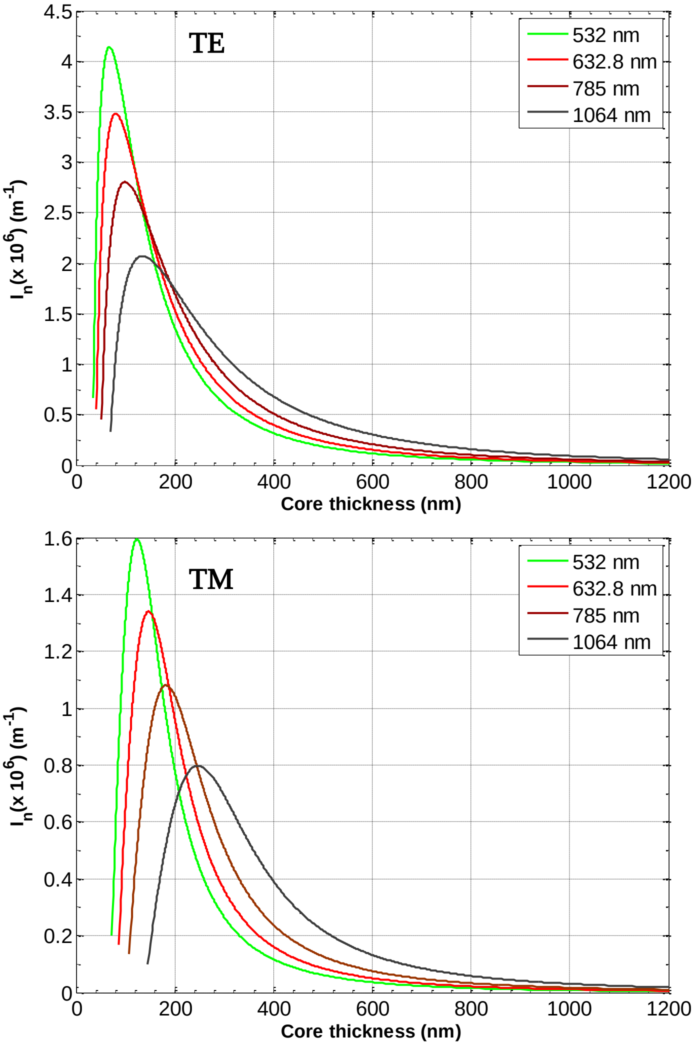

Figure 3.9 Excitation wavelength varied plots of normalised surface intensity against core thickness.

For design purpose, choosing a shorter excitation wavelength at its optimum core thickness surely will give a much more waveguide excited Raman scattering signals in both TE and TM polarisations. By taking into account the purpose of suppressing fluorescence, 632.8 nm is chosen to be the excitation wavelength.

3.2.5.3 Surface intensity vs. waveguide core thickness

Once the excitation wavelength and materials are chosen, then the next question is that how thick the waveguide core film should be in order to achieve the maximum surface intensity for monolayer and other close-to-surface detections. In this section, a more detailed examination of core thickness will be given.

As shown in Figure 3.10 below, the modelled three layer dielectric waveguide comprises of Ta_2O_5 core, fused silica substrate and air top layer. The excitation wavelength is 632.8 nm. The normalised surface intensity against various core thickness is plotted for mode number 0, 1 and 2 in both TE and TM polarisations.

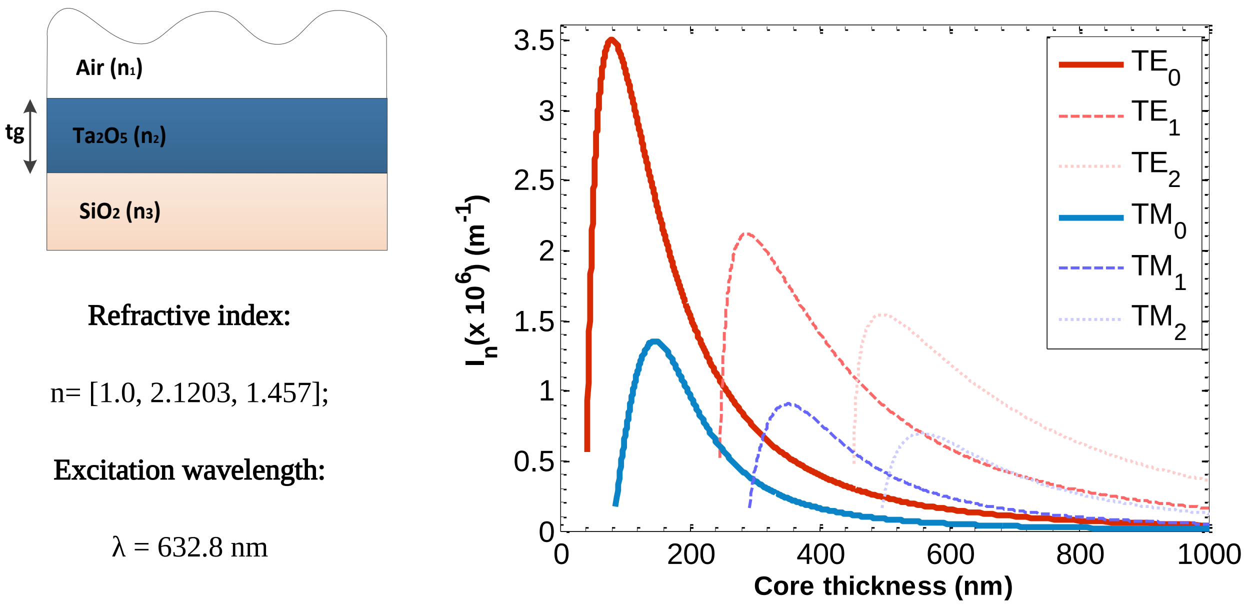

Figure 3.10 Normalised surface intensity I_n vs. core thickness in different orders of both polarisation TE and TM.

First of all, the normalised surface intensity does not linearly respond as the core thickness varies as it firstly increases sharply then drops in a lower rate until it vanishes with increasing core thickness. In this trend, there is a peak surface intensity for which the corresponding core thickness is the optimum. It can be seen that the optimum core thickness in TE and TM are different, where the optimum core is always thicker in TM than that in TE for the same order mode. In addition, the peak of the surface intensity is always larger in TE than that in TM for the same order mode. As the core thickness increases, the number of supported modes increases. However, the peak of the normalised surface intensity is lower for higher order modes since more power is confined in the waveguide core, and therefore less light penetrates into the air top layer. Not only the peak but for a range of the core thicknesses, their corresponding surface intensities are also higher than the peak of that in the higher order modes. To summarise, the monomode waveguide that has a thin core and supports only the fundamental mode(s), gives the optimum performance in terms of achieving the maximum surface intensity, hence the maximum waveguide Raman excitation, given the waveguide structure and the excitation wavelength. Once the optimum core thickness is found, the waveguide can then be fabricated and tested.

3.2.5.4 Surface intensity vs. analyte medium index

Once the waveguide core is deposited, the waveguide structure is mostly fixed except for the top layer, which in the above modelling cases is air. However, this can be varied in different applications such as sensing in aqueous environment will put a higher index medium than air on the waveguide structure. Not only the reason that it is good to know the performance of waveguide excitation in different sensing medium, i.e. different applications, but also during the experiment it provides another parameter to tune the performance of waveguide Raman excitation. For these two main reasons, the surface intensity changes with respect to the change of top layer index, i.e. analyte medium, will now be discussed.

The modelled waveguide structure is Ta_2O_5 on fused silica with the top layer index as the parameter to be tuned. The excitation wavelength was chosen to be 632.8 nm. The choice of top layer medium relies on the fact that in most cases the sensing medium is either aqueous environment or air. The targeted molecules in the vicinity (few nm) of the waveguide surface cause the local medium index to change. However, this effect is negligible compared to the index of the bulk medium that these molecules are in. Therefore, water and air superstrates are good choices for this modelling.

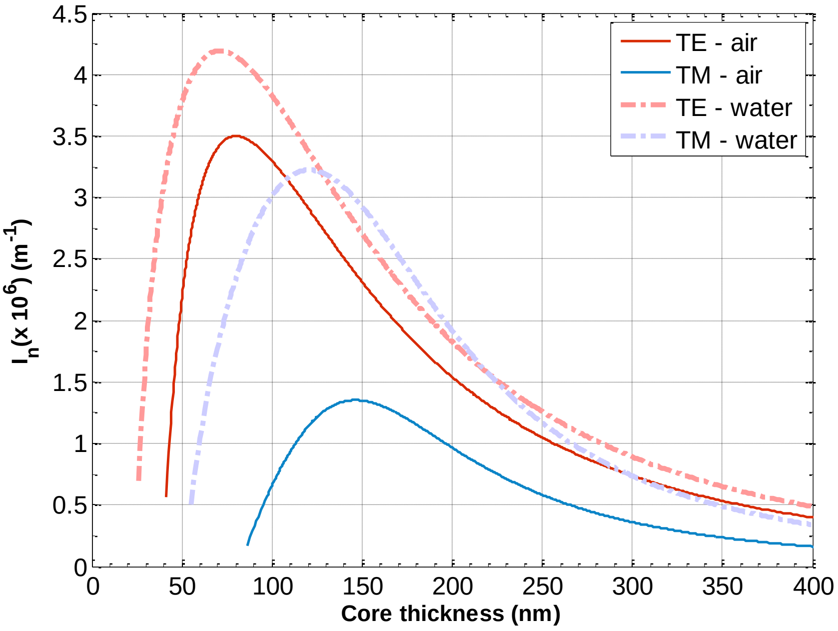

Figure 3.11 Normalised surface intensity against different core thickness with air and water as top layer, respectively.

Figure 3.11 shows how the change of the superstrate layer from air to water affects the normalised surface intensity with respect to the waveguide core thickness. For both TE and TM polarisation of the excitation light, the change of top layer medium from air to water increases the surface intensity for all waveguide core thickness. In particular, the surface intensity is more than doubled in the TM case for most of the waveguide core thicknesses. On the other hand, a small shift of the curve towards the thinner core thickness can be seen, which means that the corresponding core thickness for the maximum surface intensity is thinner for a water superstrate no matter the polarisation. What all these findings imply is that the waveguide Raman excitation has better performance in higher-index solution. It will become useful in monolayer detection when air is by default the top layer, and by replacing air with water or other aqueous Raman-inactive solutions the surface intensity hence the waveguide Raman excitation can be enhanced, which will be demonstrated in Chapter 7.

3.2.5.5 Conclusion to waveguide design

In summary, the surface intensity of the waveguide has been chosen as the figure of merit for waveguide Raman excitation. A series of investigations have been carried out in order to design a waveguide that gives the maximum performance. A higher index contrast between the waveguide core and substrate gives higher surface intensity, therefore a high-index material Ta_2O_5 has been chosen. The selection of Raman excitation wavelength has been discussed as a compromise between large Raman cross-section, large waveguide Raman excitation and low fluorescence background. 632.8 nm was chosen as it has better performance than 532 nm in suppressing the fluorescence background without compromising much in maintaining a relatively large Raman cross-section of the detected molecules and large waveguide Raman excitation. Moreover, 632.8 nm is red light in the visible that makes it easier to operate with in experiments. Having decided the core material and the excitation wavelength, the core thickness must be chosen. It is very important to choose an appropriate core thickness in order to maximise the performance of waveguide Raman excitation; otherwise the above benefits provided by the deliberately choosing the core material and the excitation wavelength will not be realised. Lastly, the refractive index of analyte medium can play a significant role for efficient waveguide Raman excitation. Comparison between two most important media – air and water shows that water with a higher refractive index leads to higher surface intensity, which can be useful in increasing the Raman scattering during experiments. Here, a thorough justification of the waveguide design for maximising the waveguide Raman excitation has been given.

3.3 Fabrication of Ta_2O_5 slab waveguides

In the last section, the design of a three-layer dielectric slab waveguide has been discussed with the goal of maximising the waveguide surface intensity, in order to maximise waveguide Raman excitation for molecules on waveguide surface. In this section, the fabrication of the designed waveguide with core material Ta_2O_5 on fused silica substrate will be explained.

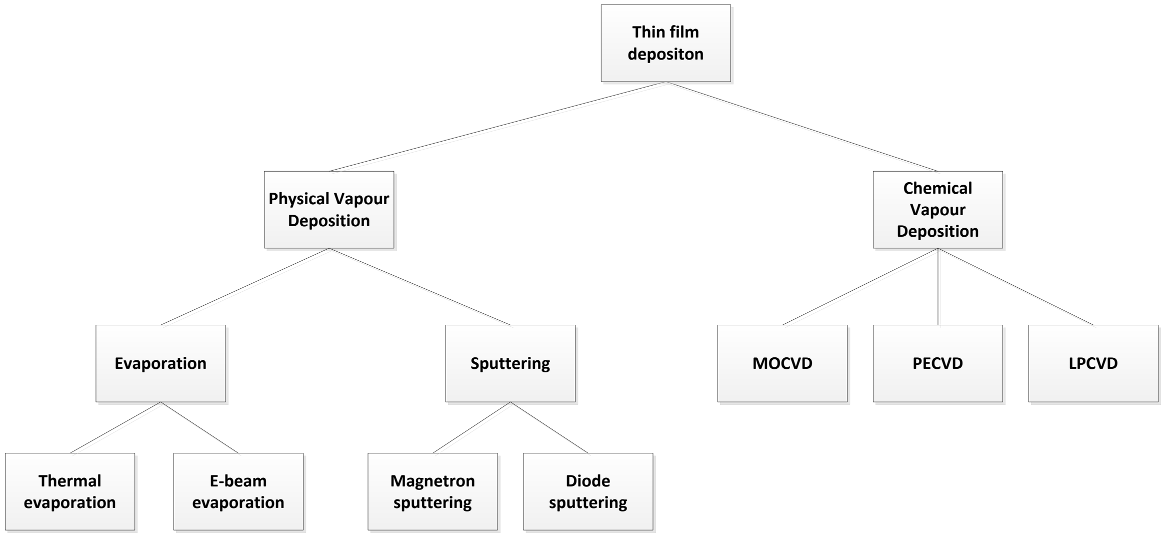

Figure 3.12 Branch diagram of fabrication techniques for thin film deposition.

The category of thin film deposition from the gas phase can be divided into Physical Vapour Deposition (PVD) and Chemical Vapour Deposition (CVD), as illustrated in Figure 3.12. PVD is a physical process where layers of atoms or molecules from the source material are deposited onto a solid substrate in a vacuum chamber. There are mainly two ways to achieve this kind of deposition. One is evaporation, either thermal evaporation or electron beam evaporation, which melts the source material into the vapour phase and then transports this and deposits it onto a solid substrate. The other one is sputtering, where source materials are bombarded with plasma, then eroded, and finally injected in the form of atoms or molecules. It starts in a low pressure chamber with an opposed parallel-place electrodes inside. When applying electrical potentials to the electrodes, free electrons will accelerate away from the cathode, which is usually located behind the target material. If now the chamber is filled with argon gas, for example the collisions between accelerating electrons and argon atoms cause the ionization of argon atoms. One ionisation process produces two free electrons and one positively charged argon ion. This positively charged ion is then accelerated into the negatively charged cathode therefore bombarding the target material. The resultant neutral target atoms or molecules go to the substrate and are deposited on it. However, there are two issues for this process known as diode sputtering. One is a low deposition rate and the other is extensive substrate bombardment by free electrons, which causes substrate damages. The use of a magnetron behind cathode and source material confines the electrons directly above the source surface, which essentially solves two issues imposed by the diode sputtering. Compared to evaporation, sputtering is preferable in many applications due to a wider choice of materials, better uniformity, and better adhesion to the substrate, which make sputtering more common in industrial production [12].

CVD is a chemical process where constituents of a vapour phase ‘react’ and deposit a solid film on a hot surface that is typically higher than 300 ^{0}C. Depending on applications as well as operational pressures and temperatures, there are many different types of CVD processes such as Low Pressure CVD (LPCVD), Plasma Enhanced CVD (PECVD) and Metal Organic CVD (MOCVD) [12]. These three CVD processes have been successfully demonstrated in depositing Ta_2O_5 [10]. The film deposition achieved through CVD methods has features of high degree of purity, control, and economy, which embeds in the fact that it is used extensively in the semiconductor industry.

The main goal is to deposit thickness controlled, pure, uniform Ta_2O_5 film on fused silica substrate with the resultant waveguide possessing low loss. The choice making between the above techniques is based on their performance in achieving this target as well as their ease of use, on-site availability, time and economy. It is more preferable to use PVD than CVD in this project since PVD techniques are cheaper, easy to operate and easy to get access to. In PVD techniques, sputtering is a better choice than evaporation as it gives denser film, better adhesion, better controlled thickness and better uniformity. Therefore magnetron sputtering technique was utilised for depositing Ta_2O_5 film on the fused silica substrate. This has achieved 0.4 dB/cm low loss Ta_2O_5 slab waveguides using a Plasmalab 400 sputtering machine with an optimised process for Ta_2O_5 [13], and this process was adopted in this work. Specifically, waveguides were fabricated by RF sputtering onto 50 mm square, 1 mm thick, silica substrates at a temperature of 200 ^{0}C from a 150 mm diameter powder-pressed pure Ta_2O_5 target with an RF power of 300 W, oxygen flow of 5 sccm and argon flow of 20 sccm. The inclusion of oxygen with argon rather than pure argon is to mitigate the oxygen deficiency issue occurring when sputtering metal oxides, which happens even if the desired deposited material is used as the target [14]. The chamber was maintained at a pressure of 10 mTorr. The deposition rate was around 3 nm/s, which changed occasionally. After the sputtering, carrying out an annealing step in oxygen has been found crucial in order to produce low loss waveguides [13], [14]. Samples were placed in a furnace at ambient pressure and an oxygen flow of 2L/min. The temperature was ramped up to 550 ^{0}C at a rate of 5^{0}C/min; then dwelled for 2 hours before it was ramped down to room temperature 20 ^{0}C at a rate of 2^{0}C/min.

In addition to what has described above, special cares must be taken in sample preparation stage before the sputtering process, in which handling tools need to be cleaned at each time to be used, washing up step should be accompanied with ‘large’ quantity of running DI water, drying step should have nitrogen gas blow the center of the sample.

3.4 Characterisation of slab Ta_2O_5 waveguides

The purpose of characterising the deposited Ta_2O_5 thin films is to 1) evaluate important parameters including Ta_2O_5 film thickness, refractive index, waveguide loss and crystallinity, and 2) feedback the measured values to the theoretical model established in Section 3.3, in order to have a more accurate prediction of the Ta_2O_5 waveguide performance in waveguide Raman excitation.

3.4.1 Thickness and refractive index measurements of Ta_2O_5 films

The thickness and refractive index of the deposited Ta_2O_5 films were measured using a Metricon Prism Coupler 2010/M. The sample to be measured was put in contact with the base of a high index coupling prism by means of pneumatically-operated coupling head, which created a small air gap between the deposited film and the prism, shown in Figure 3.13.

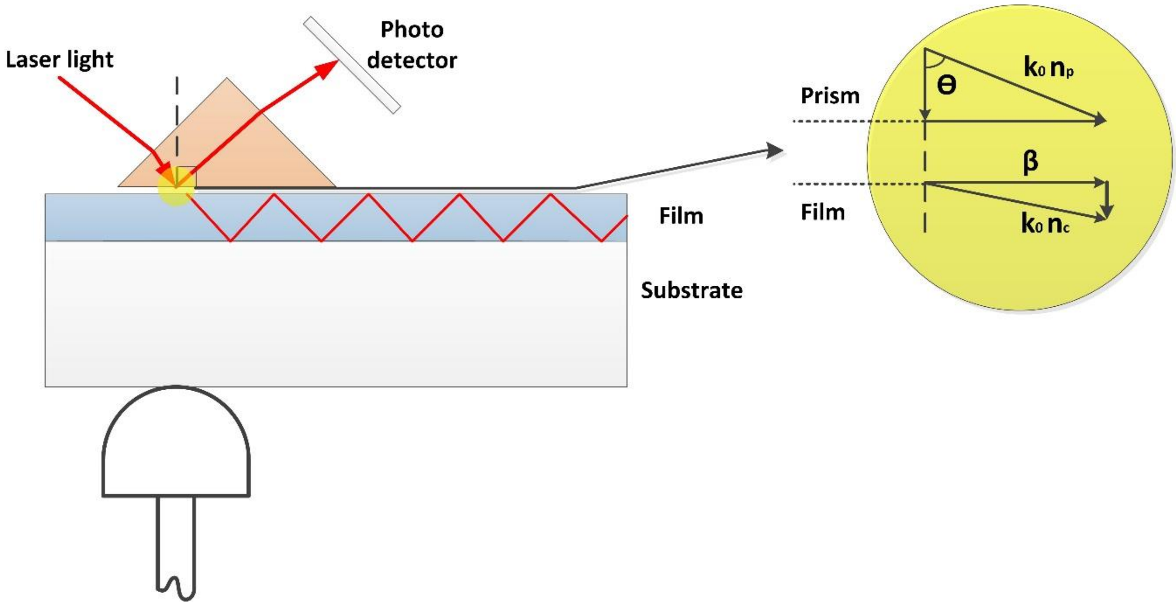

Figure 3.13 Prism coupler and its principle

The monochromatic laser light strikes at the prism base and is totally internally reflected. The reflected laser power is measured by a photodetector. As the incident angle of the laser beam changes, only at certain discrete incident angles that enables phase matching between the incident laser beam and the guided modes of the sample, photons will tunnel across the gap and travel in the guided modes of the sample, which is known as frustrated total internal reflection. By observing reference power meanwhile, a sharp drop in reflected light power is observed at the phase-matching angle. Therefore, after a full sweep of incident angles, the resultant reflected light spectrum of the photodetector clearly indicates the exact locations (angles) where light coupling between the prism and the sample occurs. The software of the system takes in these coupling angles together with the known parameters such as prism index and wavelength of the laser, and calculates the thickness and the refractive index of the thin film. The underlying principles of this calculation are briefly explained as below.

$$k_{in} \cdot \sin\theta = \beta$$ Equation 3.57

Equation 3.57 gives the phase matching relationship, in which k_{in} is the propagation vector of the incident laser beam inside the prism, θ is the incident angle between the incident laser beam and the prism base, and β is the propagation vector of the sample supported guided mode. By simplifying Equation 3.57, it is easy to obtain $n_{prism} \cdot \sin\theta = n_{eff}$, where n_{prism} is the refractive index of the prism and n_{eff} is the effective index of a guided mode supported by the sample. With a known value of prism refractive index (n_{prism}) and incident angle of the laser beam (θ), the effective index can be easily calculated. As can be seen from this equation, incident angle is the variable whose accuracy determines the accuracy of calculated effective index. The prism coupler system offers high accuracy that gives routine index resolution of $\pm5\times10^{-4}$. In the next section, calculation of the thickness and the refractive index of the thin film based on the calculated mode effective index will be discussed.

In Section 3.2.1, it was shown that the mode equation of a three-layer slab waveguide was a function of effective index, core thickness, the indices of all three layers, and the excitation wavelength. The known parameters are, the index of fused silica substrate, air superstrate, and the excitation wavelength. Therefore, only the core thickness and index are unknown. Two unknown variables need two equations to be solved. For thin film waveguides that support more than one mode, more than two equations can readily be formulated, each for one specific mode, hence both the core thickness and the index of the measured film can be calculated. However, this is not possible for a waveguide that supports only the fundamental mode. Nevertheless, it is possible to avoid this issue by measuring the fundamental mode in both TE and TM polarisations, hence providing two equations with two unknown variables. The only assumption behind this method is that all layers of the sample structure must have no birefringence, i.e. their refractive indices do not change with respect to polarisation. This assumption is valid for both amorphous Ta_2O_5 and fused silica. Therefore, the measurement of film thickness and refractive index of Ta_2O_5 on fused silica substrate can be done with high accuracy, using prism coupler.

3.4.1.1 Film thickness

Multiple sites on the same sample as well as multiple samples with the same designed thickness have been measured to obtain an average value of the film thickness. Table 3.3 gives measured thicknesses for two thicknesses of the three-layer slab Ta_2O_5 waveguide mentioned in Section 3.2, 153.5 nm and 190.4 nm, which correspond to the maximum surface intensities for two excitation wavelength 632.8 nm and 785 nm, respectively.

Table 3.3 Theoretical film thickness and averaged characterised film thickness for 5 samples each.

Thickness to be fabricated [nm]	Averaged characterised film thickness [nm]	Error percentage
153.5	155.4	1.24%
190.4	189.7	0.37%

It can be seen that the measured film thicknesses are very consistent with the target values with marginal discrepancy, which validates the effective thickness control of the sputtering system.

3.4.1.2 Film index

Measurements taken using the Metricon Prism coupler were used to obtain an average value of the deposited Ta_2O_5 film index for measuring at five different positions of the sample. This average result is 2.143 ± 0.001 for an excitation wavelength of 633 nm, whereas the averaged literature value for Ta_2O_5 is 2.128 [15], [16]. The difference between them is no more than 1%, which indicates excellent composition of Ta_2O_5.

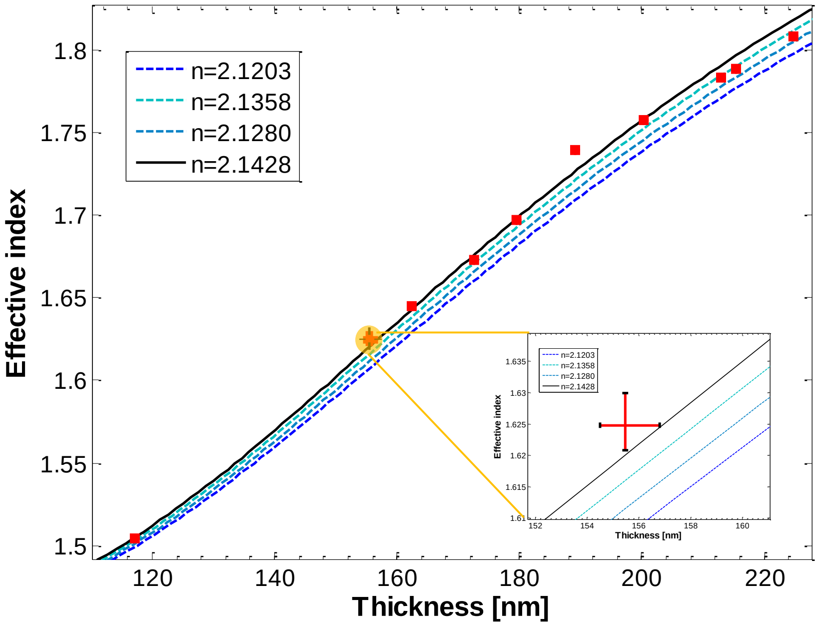

Figure 3.14 Effective index of TM fundamental mode vs. Ta_2O_5 core thickness curve fits with different Ta_2O_5 refractive indices. Each line represents a fitted refractive index value. Inset: error bars of deposited core thickness and effective index of the mode for four samples.

To further validate the characterisation results, the thicknesses and effective indices of these samples are plotted in the Figure 3.14, and to be compared with theoretical plots based on different refractive index of Ta_2O_5. By generating a series of theoretical effective index against Ta_2O_5 core thickness plots in response to different Ta_2O_5 refractive indices by using the electromagnetic models in Section 3.2, the value of Ta_2O_5 refractive index can be validated. Curves with dotted line correspond to calculation based on literature provided Ta_2O_5 refractive indices and their average value. The solid black curve corresponds to the average Ta_2O_5 refractive index from the Metricon measurements reported here. When the thickness is below 200 nm, black curve fits the best to the measured data among the all. However, blue curve with index 2.1358 fits better to samples with thicknesses more than 200 nm. Therefore, an appropriate refractive index value should be selected based on the obtained waveguide thickness. With the justified model, it is very convenient to fit the measured data with different Ta_2O_5 refractive index, hence finding the best value. The above discussion shows an excellent agreement between the fabrication results and expectations.

3.4.2 Waveguide loss

The waveguide loss was also measured by using the Metricon prism coupler. When the light was coupled into the waveguide by the prism coupler, the surface scattering along the propagation path resulted in a streak of light. By scanning an optical fiber along the propagation path, the intensity of the surface scattering was measured. The assumption was made that the surface scattering intensity was proportional to the power confined by the waveguide. Therefore, the propagation loss of the waveguide can be known by measuring the intensity drop of the surface scattering along the propagation path. The waveguide loss of the fabricated monomode waveguides are in the range of 3-4 dB for TM and 6 – 7 dB for TE polarisations. The loss is believed to be mainly caused by surface roughness. A higher loss for TE polarisation is due to a higher surface intensity, which results in more surface scattering, hence loss.

3.4.3 Degree of crystallinity

The major difference between crystalline and amorphous solid in this context is that the properties of amorphous solids are isotropic whereas they are anisotropic in crystalline solid. The measurement of a solid’s crystallinity can be performed by X-ray Diffraction (XRD). In XRD measurements, crystalline solids show multiple peaks in the spectra but for amorphous solids there are no sharp peaks. Figure 3.15 shows XRD spectra of different Ta_2O_5 coated fused silica samples. There are no significant sharp peaks in the spectra, confirming that the solids are amorphous.

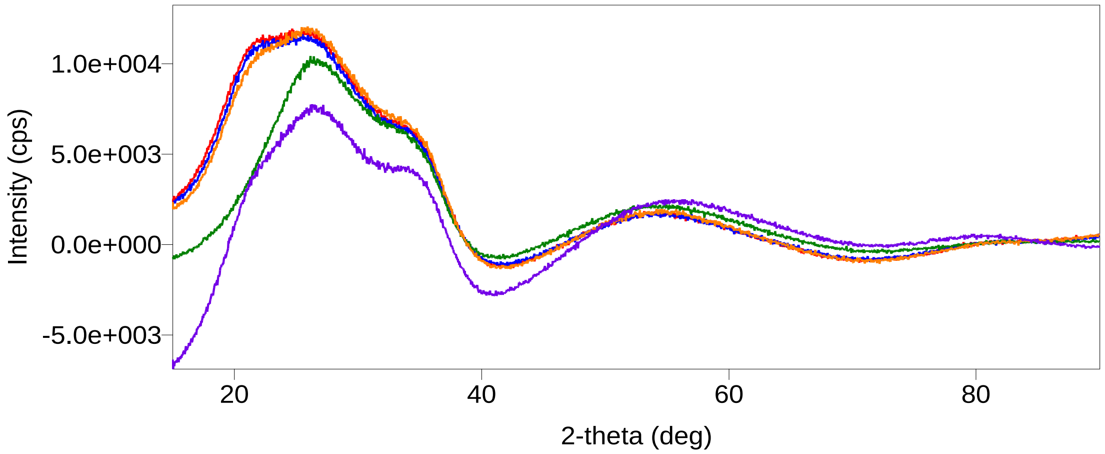

Figure 3.15 Multiple XRD measurements on Ta_2O_5 samples of different thickness. Each colour represents a measurement on a Ta_2O_5 sample.

3.5 Maximisation of coupling light into thin film Ta_2O_5 waveguides

Light must be launched efficiently into the Ta_2O_5 waveguide to allow it to propagate in one of the waveguide modes and interact with the substance to be measured on the waveguide surface. There are generally three methods used to couple light into a waveguide, which are end-firing, grating coupling and prism coupling. The end-firing method is to directly launch the light into a polished edge of the waveguide by either focussing a laser beam through a lens or butting a fiber up closely to the edge. When the beam profile of the laser beam matches that of the waveguide, a maximum coupling efficiency can be achieved. From the previous description in Section 3.2, the optimum thickness for maximum waveguide Raman excitation is around few hundred nanometres depending on the excitation wavelength, and the spot size of the waveguide beam is less than one micro-meter. For an example, a Ta_2O_5 waveguide with core thickness of 150 nm has spot size of ~380 nm at excitation wavelength of 632.8 nm. The beam waist diameter of the Gaussian beam after a focussing lens can be calculated by Equation 3.58, where λ is the beam wavelength and $f/\#$ is the f-number of

$$2w_0 = \left(\frac{4\lambda}{\pi}\right) \cdot f/\# \qquad \text{Equation 3.58}$$

the focussing lens. The relationship between the f-number and numerical aperture (NA) of a focussing lens is given by $f/\# = \frac{1}{2NA}$. By substituting different values of NA, a range of values of beam waist diameter can be obtained, as summarised in table 3.4.

Table 3.4 A set of f-number and their corresponding beam waist diameter

NA	Beam waist diameter ($2w_0$)
0.10	4.0 µm
0.25	1.6 µm
0.40	1.0 µm
0.65	0.62 µm
0.85	0.47 µm

The closest beam waist diameter is still 25% larger than the waveguide spot size, which puts a theoretical limit to the maximum coupling efficiency that can be achieved. Also, the relative small dimension can make it really difficult to align properly hence put realistic obstacles in order to coupling light efficiently into the waveguide. The same issue will happen for the case of fiber optics butted to the waveguide edge surface. Therefore, it can be concluded that end-firing technique may not be suitable for thin-film waveguide coupling.

Grating coupling allows light to be input through a grating region on the waveguide surface, and by striking a laser beam to this region at certain angle so that phase matching can be achieved between the laser beam and the waveguide propagation mode, the laser beam is then coupled into the waveguide. Grating coupling method does not have the small dimension alignment issue imposed by thin Ta_2O_5. However, for different waveguide thickness, different gratings need to be designed and fabricated, therefore not convenient for experimental investigations involving in multiple waveguide designs.

The prism coupling method has already been described in Section 3.4. The thickness of the waveguide does not affect its coupling efficiency in a dramatic fashion as end-coupling method does. For a certain prism, the method is applicable to waveguides with a range of thicknesses if and only if the phase matching condition is met. The coupling efficiency is determined by the pressure asserted to the sample substrate as well as the position that the laser beam strikes at the prism base.

3.5.1 Prism coupling set up

The prism coupling set up is not only utilised to couple light into the waveguide but also facilitate the Raman collection, which requires the flexibilities of putting the collection optics at various locations around the waveguide sample. The requirement put by the latter purpose provides the motivation of self-building a prism coupler. A standalone prism coupler was established to allow experimental flexibility in excitation and collection of Raman signals.

Figure 3.16 shows a self-built prism coupler, which comprises a coupling prism unit, a two-axis translational stage sit on a rotational stage, and a set up mount that connects the stages and the coupling prism unit. The working principle of prism coupler has been explained already, thus in the next it just highlights the key components and their functions. The coupling prism unit is the same type as the Metricon prism coupler used, where each one has a unique code that indicates its refractive index and measurement range of effective index. The rotation stage provides the capability of forming a wide range of incident angles between the laser beam and the prism base. The movements provided by the two-axis translational stage enable further improvement on the coupling efficiency, as the relative position of the laser spot at the prism base and the pressure spot asserted to the sample substrate is critical. A nylon screw is used to provide the necessary pressure in order to squeeze the air gap between the coupling prism and the sample down to few hundred nanometers. Lastly, a set up mount is designed to integrate every part described above into a working unit. The mount provides room for both small and large samples (e.g. 6 inch wafer) to be fit in the set up.

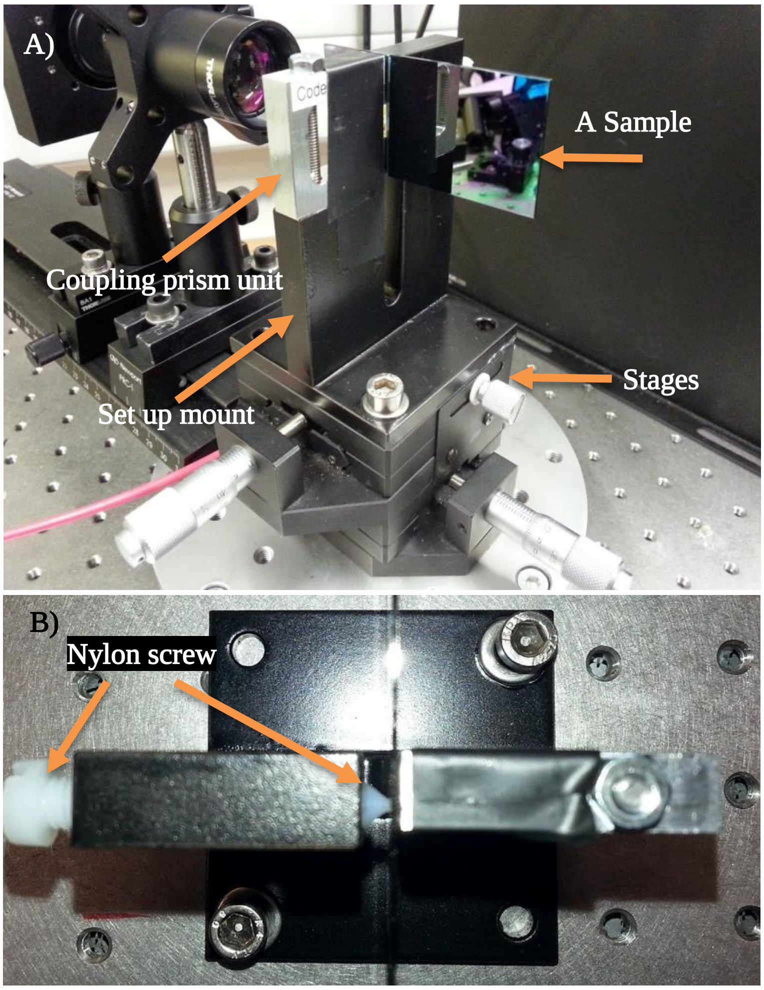

Figure 3.16 Self-built prism coupler. A) 45 degree view and B) top view of the mount for the coupling prism unit.

3.5.2 Performance

The primary goal of the self-built prism coupler is to couple laser light into waveguide samples. Successful couplings have been observed for various samples with thicknesses ranging from 67 nm up to 450 nm. An example is given below. The clear streak of light propagating in waveguide confined mode indicates the success of prism coupling.

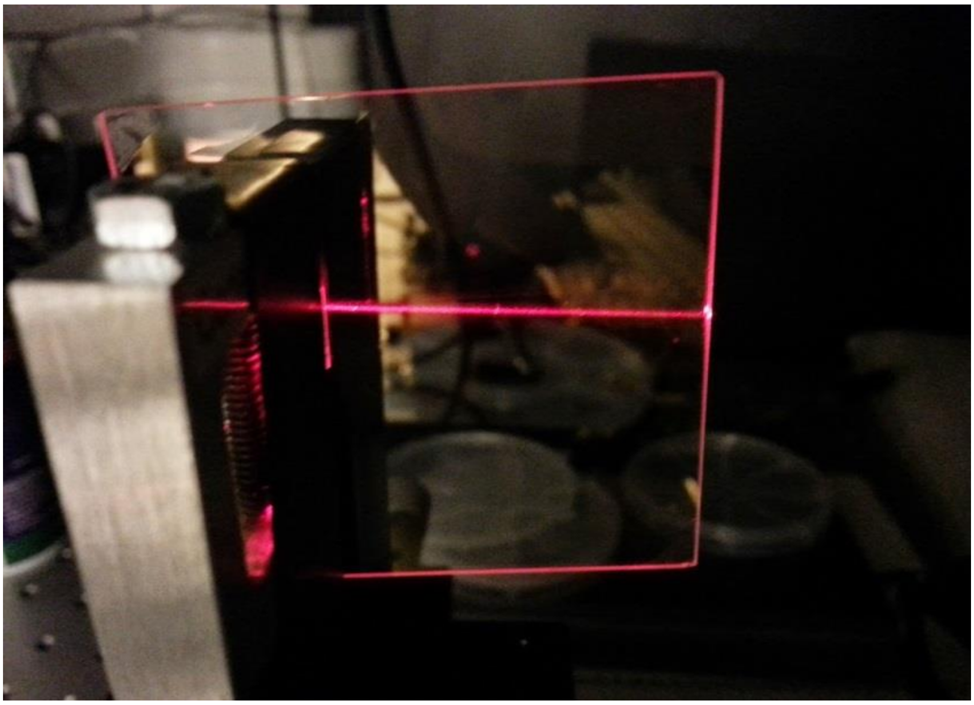

Figure 3.17 Coupling laser light into the fabricated Ta_2O_5 waveguide sample. The deposited Ta_2O_5 film thickness is 130 nm. Waveguide loss was 3 ± 0.3 dB/cm for TM polarisation.

3.6 Conclusion

In order to achieve the maximum waveguide Raman excitation, the design, fabrication and characterisation aspects have been discussed in this chapter. The primary design metric of the waveguide for maximum Raman excitation has been established as its surface intensity.

A thorough investigation of the relationship between the waveguide surface intensity and waveguide design parameters requires the knowledge of waveguide modes. A full electromagnetic model has been established and successfully validated for formulating the eigenvalue equation of the multilayer slab waveguide and numerically solving for its modes. The waveguide design has been optimised against four parameters: index contrast, excitation wavelength, core thickness and medium index. It has been found out that high index contrast can significantly increase the maximum surface intensity. Core material made of high refractive index Ta_2O_5 has been chosen for convenience. As for excitation wavelength, simulation result shows that shorter excitation wavelength provides higher maximum surface intensity. Moreover, the Raman cross-section is inversely proportional to fourth-order of the excitation wavelength, which means shorter excitation wavelength is preferable for maximising the surface intensity. However, shorter excitation wavelength also excites more fluorescence, which is far stronger than the Raman signals. Therefore, a compromise has to be made, which has led the choice of 632.8 nm. During the investigation of the waveguide surface intensity against index contrast and excitation wavelength, it has been found that core thickness plays important roles in achieving the maximum surface intensity at each design scenario. Plots of the surface intensity against core thickness show the optimum values. The refractive index of the medium where the molecules are in can have a significant impact on the waveguide surface intensity. Two most commonly used medium air and water have been simulated and the results show that medium with higher index such as water leads to higher maximum surface intensity. Overall, an optimised waveguide design has been discussed for achieving the maximum surface intensity.

Many fabrication techniques among Physical Vapour Deposition (PVD) and Chemical Vapour Deposition (CVD) can be utilised to deposit thin film Ta_2O_5 on fused silica substrate. Magnetron sputtering technique was chosen due to its ease of use, availability and good performance of achieving dense and smooth films, which results in low loss slab waveguides. It has been found that a good substrate preparation procedure is one of the key factors in achieving the low loss slab waveguides.

The thickness and refractive index of deposited film Ta_2O_5 have been measured using a Metricon prism coupler. The differences are negligible between the measured values and designed values, which indicate successful depositions. The waveguide loss is around 3-4 dB/cm and 6-7 dB for TM and TE, respectively. The crystallinity of the film has been measured to be amorphous by XRD, as expected.

A prism coupler has been built in order to couple light into different waveguide sample and carry out Raman collection at different sites around the sample. A clean and clear streak of light can be observed on the waveguide at certain incident angle, which indicates a successful coupling.

Overall, an optimised Ta_2O_5 three layer dielectric waveguide has been designed, fabricated and characterised. The electromagnetic model established for solving modes of multilayer dielectric waveguides provides flexibilities of making adapted design according to each scenario and giving in-depth analysis, which are the foundations of analysis demonstrated in later chapters. Samples can be fabricated with repeatable quality and consistent results, which can always be checked reliably in the characterisation tool. The prism coupler set up has been intensely used and has provided the experimental platform for investigations that will be shown and discussed in later chapters.

3.7 References

[1] D. Marcuse, “Theory of dielectric optical waveguides.” Academic Press, New York, San Francisco, London, 1974.

[2] M. J. Adams, *An Introduction to Optical Waveguides*. New Jersey: John Wiley & Sons, 1981.

[3] P. Yeh, *Optical Waves in Layered Media*. New Jersey: John Wiley & Sons, Inc., 2006.

[4] W. H. Press, S. A. Teukolsky, W. T. Vetterling, and B. P. Flannery, *Numerical recipes in C—The art of scientific computing*, 3rd ed. New York, USA: Cambridge University Press, 1988.

[5] S. D. Conte and C. De Boor, *Elementary numerical analysis : an algorithmic approach*, 3rd ed. McGraw-Hill Higher Education, 1980.

[6] E. Anemogiannis and E. N. Glytsis, “Multilayer Waveguides: Efficient Numerical Analysis of General Structures,” *J. Light. Technol.*, vol. 10, no. 10, pp. 1344–1351, 1992.

[7] E. Anemogiannis, E. N. Glytsis, and T. K. Gaylord, “Determination of guided and leaky modes in lossless and lossy planar multilayer optical waveguides: reflection pole method and wavevector density method,” *J. Light. Technol.*, vol. 17, no. 5, pp. 929–941, 1999.

[8] E. Ziegel, W. Press, B. Flannery, S. Teukolsky, and W. Vetterling, “Numerical Recipes: The Art of Scientific Computing,” *Technometrics*, vol. 29, no. 4, p. 501, Nov. 1987.

[9] J. S. Kanger, C. Otto, M. Slotboom, and J. Greve, “Waveguide Raman spectroscopy of thin polymer layers and monolayers of biomolecules using high refractive index waveguides,” *J. Phys. Chem.*, vol. 100, no. 8, pp. 3288–3292, Jan. 1996.

[10] K. Schmitt, K. Oehse, G. Sulz, and C. Hoffmann, “Evanescent field Sensors Based on Tantalum Pentoxide Waveguides – A Review,” *Sensors*, vol. 8, no. 2, pp. 711–738, Jan. 2008.

[11] R. Bernini, N. Cennamo, A. Minardo, and L. Zeni, “Planar waveguides for fluorescence-based biosensing: Optimisation and analysis,” *IEEE Sens. J.*, vol. 6, no. 5, pp. 1218–1225, 2006.

[12] M. J. Madou, “Fundamentals of Microfabrication: The Science of Miniaturization,” in *Fundamentals of Microfabrication: The Science of Miniaturization*, 2nd ed., CRC Press, 2002, p. 49.

[13] A. Z. Subramanian, C. J. Oton, J. S. Wilkinson, and R. Greef, “Waveguiding and photoluminescence in Er^{3}+-doped Ta_2O_5 planar waveguides,” *J. Lumin.*, vol. 129, no. 8, pp. 812–816, Aug. 2009.

[14] Z. Yi Yin and B. K. Garside, “Low-loss GeO_2 optical waveguide fabrication using low deposition rate RF sputtering,” *Appl. Opt.*, vol. 21, no. 23, p. 4324, Dec. 1982.

[15] L. Gao, F. Lemarchand, and M. Lequime, “Exploitation of multiple incidences spectrometric measurements for thin film reverse engineering,” *Opt. Express*, vol. 20, no. 14, pp. 15734–15751, 2012.

[16] T. J. Bright, J. I. Watjen, Z. M. Zhang, C. Muratore, A. A. Voevodin, D. I. Koukis, D. B. Tanner, and D. J. Arenas, “Infrared optical properties of amorphous and nanocrystalline Ta_2O_5 thin films,” *J. Appl. Phys.*, vol. 114, no. 8, p. 83515, 2013.

CHAPTER 4 WERS I: surface measurement and power budget analysis

4.1 Introduction

While Chapter 3 explains how the waveguide for waveguide-enhanced Raman spectroscopy has been designed, fabricated and characterised, the following three chapters will explain the use of waveguide for Raman spectra measurement. Specifically in this Chapter, the surface collection of WERS will be demonstrated and compared with that from the conventional Raman microscopy. Through explaining the basic principles of conventional Raman microscopy and the design of WERS for maximum Raman excitation, the advantages of WERS will be revealed compared to the conventional Raman microscopy.

Waveguides were firstly used to study Raman scattering of thin films where the film being studied formed the guiding core of the waveguide [1]–[5]. These were followed by several studies of resonance Raman scattering from monolayers on low index contrast glass or polymer waveguides [6]. While optimisation of waveguides for surface enhancement was not directly addressed, it was observed that enhancement of Raman excitation for thin films resulted from maintaining a high excitation intensity over an increased scattering volume of analyte [4]. Subsequently, an analysis of the intensity of the evanescent field at the surface of an optical waveguide emphasised that thin high-index waveguides yielded the greatest field enhancement for Raman excitation and this was demonstrated experimentally for both a 8 nm thick polystyrene film and a protein monolayer on an optimised high index contrast ZnO waveguide on SiO_2 [7]. The enhancement achieved by WERS may not be sufficient for single molecule detection [8] unless combined with other enhancement mechanisms such as plasmonics in nanostructured gold [9], [10], but is very promising for analytical applications where more modest, but repeatable, surface average enhancements are required, such as biosensors employing surface reactions in ultrathin films.

There is renewed interest in utilising dielectric waveguides [11], [12], silicon waveguides [13] or waveguides combined with plasmonic structures [9], [14], [15] for enhanced Raman spectroscopy, driven primarily by the need for large enhancement factors combined with improved repeatability. Comparison of these approaches would be aided by rigorous quantification of the power conversion efficiency from the laser pump to the Raman signal and of the enhancement of Raman signal compared to a conventional configuration. In this chapter, the waveguide surface collection and a power budget analysis will be addressed to relate the received power in a single Raman emission line to the incident pump laser power, using waveguide surface intensity and Raman cross-section. This approach allows straightforward WERS optimisation and a clear comparison of surface-enhanced techniques.

4.2 Confocal Raman microscopy

This section will introduce a widely used analytical tool – confocal Raman microscopy for: 1) its basic principles and 2) reference Raman measurements of analyte. Both of them will be made as a comparison to WERS in terms of their theoretical performance and measured spectra in later sections.

4.2.1 Basic principles

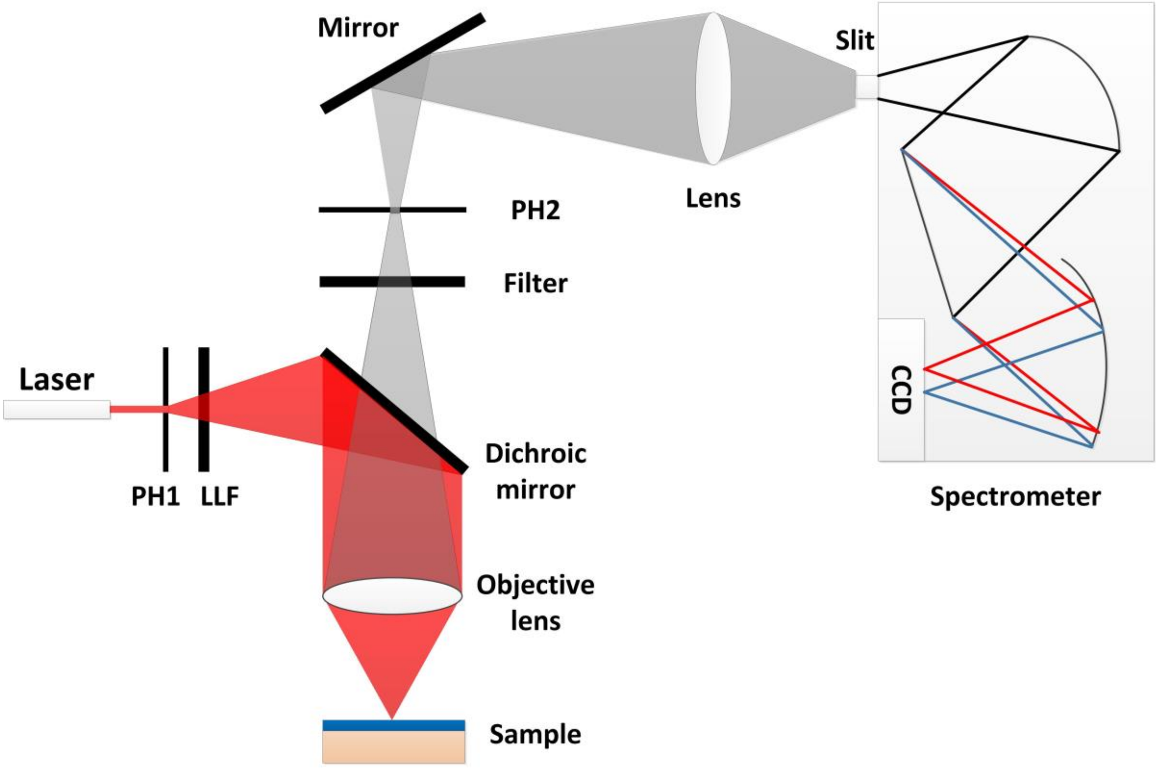

Figure 4.1 Conventional Raman microscopy. PH1: pinhole 1, LLF: laser line filter, PH2: pinhole 2

Despite the vast developments that have been made, the design of a Raman instrument remains substantially unchanged in the sense that it needs a monochromatic light source to excite the sample, collection optics, optics to filter the Rayleigh scattering, a spectrometer, and a detector. Since the Raman spectrum is a spread of features across a wavelength range, the central function of a Raman instrument is to separate these wavelengths. There are two major means of achieving these, either dispersive or interferometric. However, most of the instruments are dispersive due to their robustness, excitation wavelength flexibility and high sensitivity [16]–[18]. The dispersive element is usually a diffraction grating; and the corresponding detector is a Charge-Coupled Device (CCD) array. For many applications, spectra of samples must be obtained from selected micro-meter sized regions which operators can select using a microscope. To suit this purpose, an incorporation of microscope within Raman spectrometer has been made. On top of that, confocal Raman microscopy gives further control of sampling volume both horizontally and vertically, which makes it widely used in many different applications. The key to eliminate out-of-focus light from the background therefore increasing spatial resolution is placing a pinhole at the confocal plane as illustrated in Figure 4.1. Light emerging from laser is focussed into the sample by an objective lens. To regulate the spot size and remove unwanted excitation background light, a pinhole is put in the front of laser. Sometimes there are sidebands or noise in the laser light that can interfere with the Raman signals by appearing as peaks or bumps in the Raman spectrum. A laser line filter that passes through only the wanted narrow band of laser light can effectively remove those noise. A dichroic mirror reflects the excitation light into the sample side and transmits the collection light. On the collection side, either a long pass or notch filter is used to remove the dominantly strong stray light at the laser wavelength. The second pinhole is put in the image plane of the objective to reject any light coming from the out-of-focus region. Collected light is focussed into the spectrometer where light is firstly collimated, then diffracted by the grating, and finally focussed into the CCD. The CCD then converts the photons into electrons and digitises the signal before it is displayed on the software panel of a Personal Computer (PC).

4.2.2 Spectrum measurement

In this work, the purpose of bulk analyte measurements with conventional Raman spectroscopy is to obtain reference spectra with great signal-to-noise ratio and spectral resolution, which can then be used for comparison with waveguide Raman spectra. Toluene has been chosen as a targeted molecule for proof-of-principle experiments due to its Raman active breathing mode at around 1,000 cm^{-1} with strong and known Raman cross-section. However, it is volatile and toxic therefore experiments with it should be operated under an extraction hood. Isopropyl alcohol (IPA) as a standard laboratory cleaning solvent is much less toxic than toluene. Therefore, it is ideal for system calibration and repeated measurements under normal laboratory set up, as an alternative of toluene. As for their spectral measurements, 632.8 nm Raman microscopy (Renishaw 2000) was operated by Yung-Chin Lin in Prof. Philip N Bartlett’s group at University of Southampton. Both of these two substance were held in UV fused Quartz cuvettes (Thorlabs) with laser focussing spot located inside. While it is relatively easy to handle in conventional measurement, volatile solvents (toluene and IPA) can be troublesome when it is put on top of the waveguide and held up for the duration of measurement as they will evaporate fast. Polystyrene film spin coated on top of waveguide can solve this issue brilliantly. Moreover, it has the flexibility of achieving a series of film thickness that is desirable in the process of optimising the waveguide Raman system by gradually decreasing the film thickness, i.e. sample volume. The conventional Raman measurement of polystyrene was taken from its pellet (molecular weight~280,000) supplied by Sigma-Aldrich.

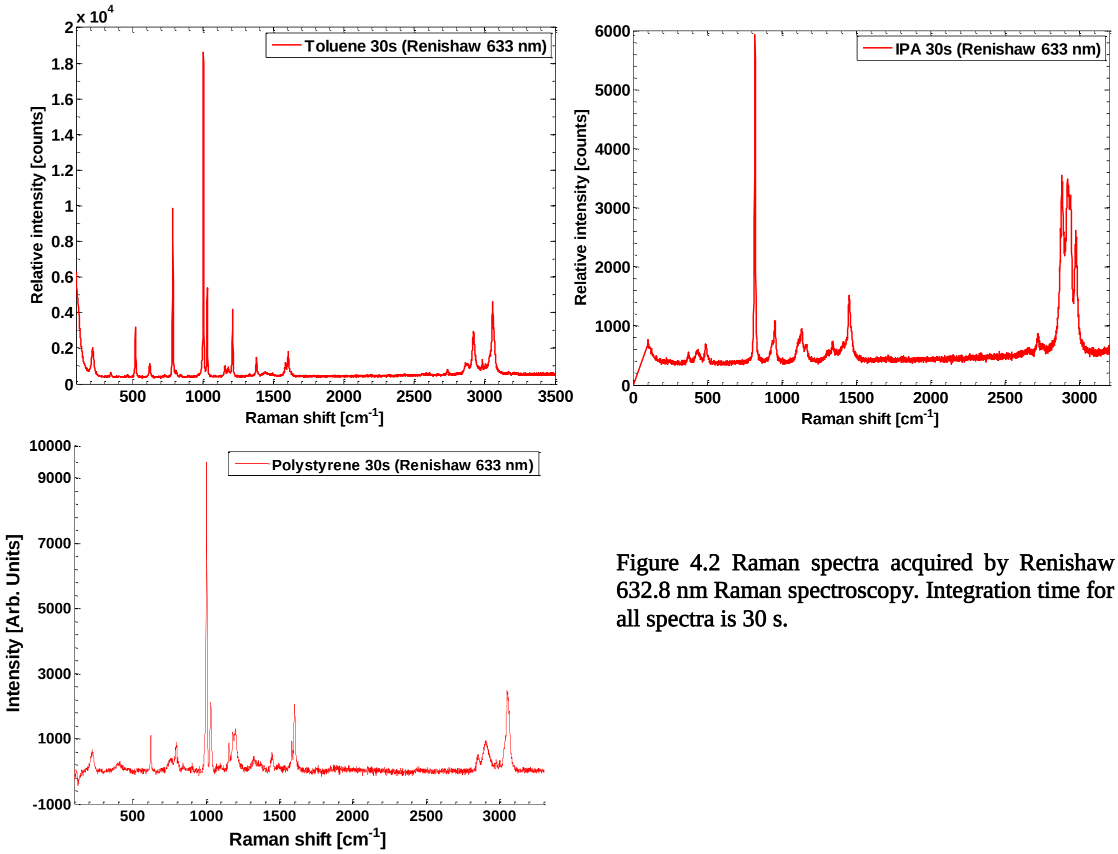

Figure 4.2 Raman spectra acquired by Renishaw 632.8 nm Raman spectroscopy. Integration time for all spectra is 30 s.

As shown in Figure 4.2, the spectra of toluene, IPA and polystyrene taken from the Renishaw 632.8 nm Raman system (Renishaw 2000) give sharp spectral features with great resolution. For instance, two closely spaced toluene Raman spectral features at 1,002 cm^{-1} and 1,027 cm^{-1} have been resolved well. Depending on the objective lens use, the Renishaw 632.8 nm Raman system has its depth of field usually in few tens of micro-meters and minimum laser focused spot size is usually in few micro-meters. The total illuminated volume as well as collected volume can be estimated. If the illuminated volume has been fully filled up with targeted molecules, which is true for the above three cases, then the background contribution can be negligible therefore a relatively large signal-to-noise ratio is achieved. This was further proved by measuring from a sub-μm polystyrene film spin-coated on top of glass sample, in which part of collected signals were contributed from the thin polystyrene film and the rest were from background. For the film thickness down to 100nm, the signal-to-noise ratio dropped significantly so that Renishaw 632.8 nm Raman system could not show any polystyrene Raman feature at all. This is in a contrast to WERS of thin film, which will be showed in Chapter 7.

4.3 Design and simulation of maximum WERS excitation

In common with SERS, waveguide excitation of Raman scattering is determined by the magnitude of the electric field experienced by the Raman medium, so that the optimisation of devices for surface excitation consists of maximising the electric field from the laser “pump” at the location of the species of interest for a given pump power over a certain surface area. In SERS and waveguide collection configurations, the enhancement of Raman emission and the signal collection efficiency are also determined by the local electric field distributions, but this may be strongly dependent upon the frequency (Stokes) shift of the Raman line [19]. For availability and convenience of the laser use, a pump wavelength of 637 nm has been chosen, which strikes a great compromise between low fluorescence and the ability to detect large Stokes' shifts using a silicon CCD spectrometer. Also it benefits comparison with a conventional Raman instrument at a similar wavelength of 632.8 nm.

4.3.1.1 Waveguide surface intensity

For Raman spectroscopy of very thin layers, the key advantage of waveguide surface excitation over conventional excitation with a focussed beam perpendicular to the layer is that the surface intensity is independent of the total excited surface area. In the case of conventional perpendicular excitation, the product of surface intensity and area is fixed (and approximately equal to the incident power). As a result, for thin layers the product of intensity and irradiated area can be much greater in the waveguide excitation case. While the product of intensity and irradiated volume should be optimised for sensitive analysis of bulk media, this reduces to maximising the product of intensity and area for very thin films, which is where waveguide excitation provides a significant advantage. To illustrate this, the intensity at the surface of a 2D (slab) dielectric waveguide, normalised to 1 W modal power per metre waveguide width, I_n, has been calculated using a similar approach to Kanger *et al.* [10], and has units of m^{-1} due to the normalisation. Examples for the TE and TM polarised fundamental modes are plotted in Figure 4.3a against waveguide core thickness for a wavelength of 637 nm, substrate refractive index of $n_2 = 1.46$ (silica), superstrate refractive index of $n_3 = 1.33$ (water), for two core refractive indices $n_1 = 2.1$ (similar to Ta_2O_5 and Si_3N_4 [11]) and $n_1 = 1.53$ (Corning 7059 glass [6]). Ta_2O_5 and Si_3N_4 are both silicon process compatible dielectric materials transparent in the visible and near-infrared parts of the electromagnetic spectrum.

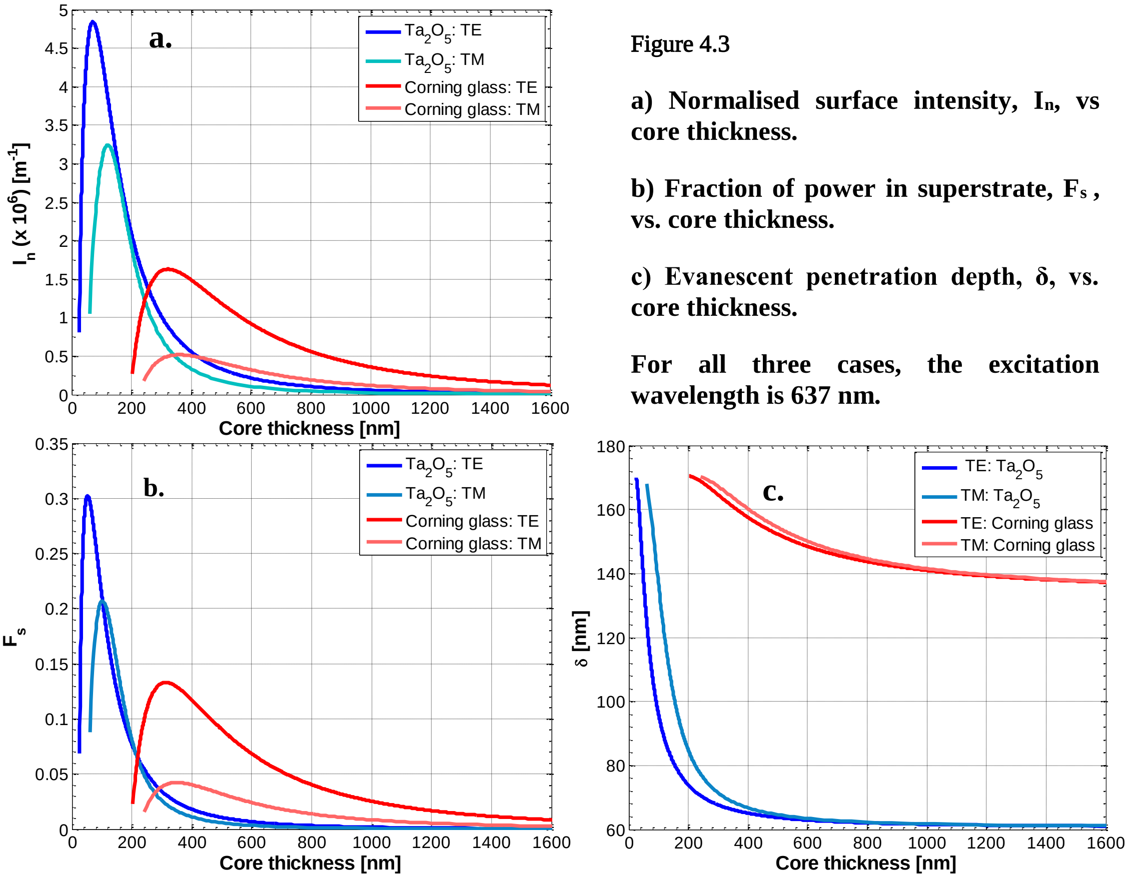

Figure 4.3

a) Normalised surface intensity, I_n, vs core thickness.

b) Fraction of power in superstrate, F_s , vs. core thickness.

c) Evanescent penetration depth, δ, vs. core thickness.

For all three cases, the excitation wavelength is 637 nm.

The maximum normalised surface intensity, I_n, of ~ 4.8×10^6 m^{-1} occurs for the fundamental mode in the TE polarisation for the high index waveguide, as expected [7]. Assuming negligible waveguide loss and negligible pump depletion, for the same pump power, the resultant Raman excitation (the product of intensity and area) is I_n times greater than conventional excitation perpendicular to the thin film *per meter length of waveguide*. The maximum useful waveguide length is then defined by the collection configuration. This assumes insignificant pump depletion along the length of the waveguide, which is reasonable for lengths up to 1cm with losses typically of order 1 dB/cm for high contrast waveguides. Figure 4.3b shows the evanescent penetration depth (1/e intensity) vs. waveguide core thickness, which for a Ta_2O_5 waveguide takes the range 60 nm – 170 nm, corresponding to a mode far from and near to cut-off, respectively. Surface films with thickness of a few nm may thus be assumed to experience the surface intensity shown in Figure 4.3a. Figure 4.3c shows the fraction of power carried in the bulk superstrate (in this case water) by the waveguide mode, F_s, for the same waveguide designs, showing similar behaviour to the surface intensity, modified slightly by the changing penetration depth. Waveguide Raman analysis of bulk media should be optimised using this parameter. For future comparisons with composite plasmonic structures, the TM polarisation was chosen for this study, and so a tantalum pentoxide film of thickness 110 nm was selected to be optimum.

4.3.1.2 Surface collection of Raman emission.

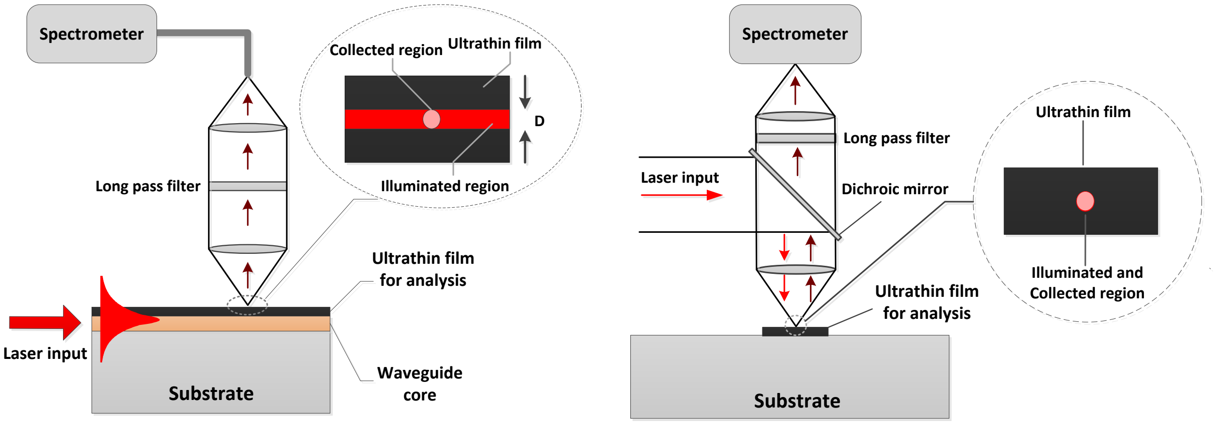

Figure 4.4 a. Waveguide Raman excitation configuration with surface collection **b. Conventional Raman configuration**

A conventional Raman microscope system focuses pump light onto the sample using a microscope objective lens and collects the emitted Raman signal through the same lens and directs it through filters to a spectrometer, as shown in Figure 4.4b. Increasing the numerical aperture (NA) of the lens reduces the spot-size of the incident power allowing higher spatial resolution but, for a uniform film under study, does not change the emitted Raman power (ignoring saturation effects). However, the increased NA does increase the efficiency of collection of the emitted power and, for an isotropic emission, this follows:

$$\eta_c = \frac{1}{2}[1 - cos(sin^{-1}NA)] \qquad \textbf{Equation 4.1}$$

In the case of waveguide excitation with surface normal collection, shown in Figure 4.4a, the collection optics can be optimised independently of the excitation optics, so that even if the surface intensity is no higher than for conventional Raman illumination, the emission can be collected over a larger area. For a low-cost system, where ultimate spectral resolution is not a requirement, the most practical configuration is to use a compact fiber-coupled CCD spectrometer. In this case the maximum collection efficiency is obtained with the collecting end of the fiber as close as possible to the emissive surface [20], using the NA of the fiber in Equation 4.1. The maximum total collected power is then obtained by summing the contributions from all emitting molecules within the area of the fiber core. Thus the maximum efficiency is obtained by using the highest NA fiber with a core that covers the maximum length of the waveguide possible, while ensuring the width of the waveguide illumination, D, is confined to the width of the fiber core. In practice, a lens system imaging a region of the emissive surface onto the end of the collection fiber allows collection without contact between the fiber and surface and the placing of pump filters before the collection fiber will only marginally affect the collection efficiency due to additional reflections etc. For this study, we used a highly multimode 1 mm core diameter fiber with an NA of 0.48. Assuming isotropic emission, this is expected to yield a collection efficiency for an individual emitter of ~6.1%. To compare excitation using an optimised tantalum pentoxide waveguide to a conventional Raman instrument having a similar NA, if the waveguide illumination width is narrower than the fiber core then, from Figure 4.3a, the collected power is expected to be ~4,800 times larger, due to the 1 mm collection length. However, there will be a trade-off between spectral resolution and signal power at the fiber/spectrometer interface due to the use of a large high NA multimode fiber.

4.4 Methods for WERS measurements

Raman emission from bulk toluene (C_7H_8, n = 1.489) was chosen for this study and prism-coupling was used to excite the waveguide mode. While Raman spectroscopy from an ultrathin film would show the most advantage for WERS, the Raman cross-section of toluene is large and well known [22] and a robust comparison of theory and experiment can be readily performed by assuming that the evanescent field is filled with toluene. Validating the theory with a bulk medium also eliminates potential errors due to thickness tolerances and molecular alignment. A reference spectrum for the toluene (Sigma-Aldrich, anhydrous, 99.8%) in a quartz cuvette was first taken with the Renishaw Raman microscopy (Renishaw 2000) operating at 632.8 nm.

Light from a 637nm fiber-coupled semiconductor laser (Thorlabs LP637-SF70) was coupled into the waveguide sample by a high-index prism (Metricon 200-P-2) as shown in Figure 4.5. The laser had a output in TM polarisation, and 44 mW power was incident on the prism in this polarisation.

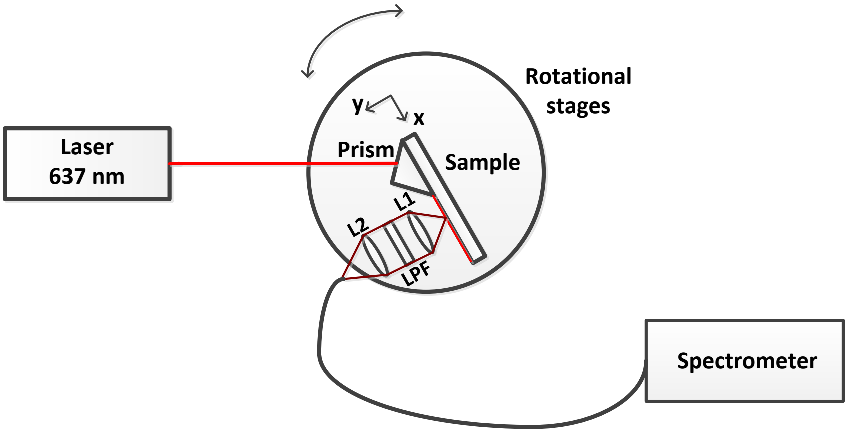

Figure 4.5 Apparatus for waveguide Raman measurements. L1: convex lens with f=25.4 mm, diameter is inch. L2: achromatic lens with f=30 mm, diameter is 1 inch. LPF: long pass filter for laser wavelength between 635 nm and 642 nm and the edge wavelength is 655 nm. The acquisition time is 60 s.

The Raman collection optics consisted of two 1 inch diameter lenses (L1: f=25.4 mm, L2: f=30 mm) coupling through a multimode fiber (NA: 0.48, Core diameter: 1 mm) into a compact spectrometer (Ocean Optics QE65000 Pro) with a 200 μm entrance slit. A long-pass filter (LPF, FELH0650 Thorlabs) with a band edge at 648 nm was placed between the lenses to suppress scattered pump radiation, cutting out signals with Stokes' shifts below 300 cm^{-1}. The spectrometer was USB interfaced to a PC and SpectraSuite software was used to control the spectrometer and process the data.

Depending on the interest of sensing, the sample preparation technique can be different from one to another. For example, a thin solid polystyrene film can be formed on top of waveguide by spin coating, for which the recipe can be found from [23]. Once it is coated on the waveguide surface, it is very durable for repeatable and long period measurement providing that it is handled with care by not scratching it. For liquid, however, it adds some experimental difficulties to hold the liquid on waveguide surface for the duration of measurement, e.g. 60 s. This is particularly true for volatile solvents, such as IPA and toluene. It was found to be repeatable and robust for the duration of measurements by placing a small drop of toluene onto the waveguide surface and locating a coverslip on top to reduce evaporation. A streak of light could be seen going through the toluene covered region as seen in Figure 4.6. The penetration depth of the evanescent field into the toluene is approximately 120 nm and the resulting toluene layer fills this region, resulting in effectively a ‘bulk’ analyte above the waveguide surface rather than the very thin film as encountered in biosensing. Nonetheless, this is sufficient to validate the design and confirm the power budget. The collection system was focussed onto the waveguide surface approximately 2.5 cm away from the prism coupling position and spectra were recorded with an integration time of 60 s.

Figure 4.6 Toluene covered waveguide sample.

4.5 Spectrum acquisition and signal processing

In this section, the purpose is to 1) show the Raman spectrum of toluene measured by WERS and 2) validate the result by comparing with the reference spectrum measured by conventional Raman microscopy.

The ‘raw’ Raman spectrum of toluene collected from waveguide surface is shown in Figure 4.7iA. The Raman spectrum of toluene is interfered with noise and background (baseline). In order to make a better comparison to Renishaw 632.8 nm reference measurement, necessary signal processing needs to be performed.

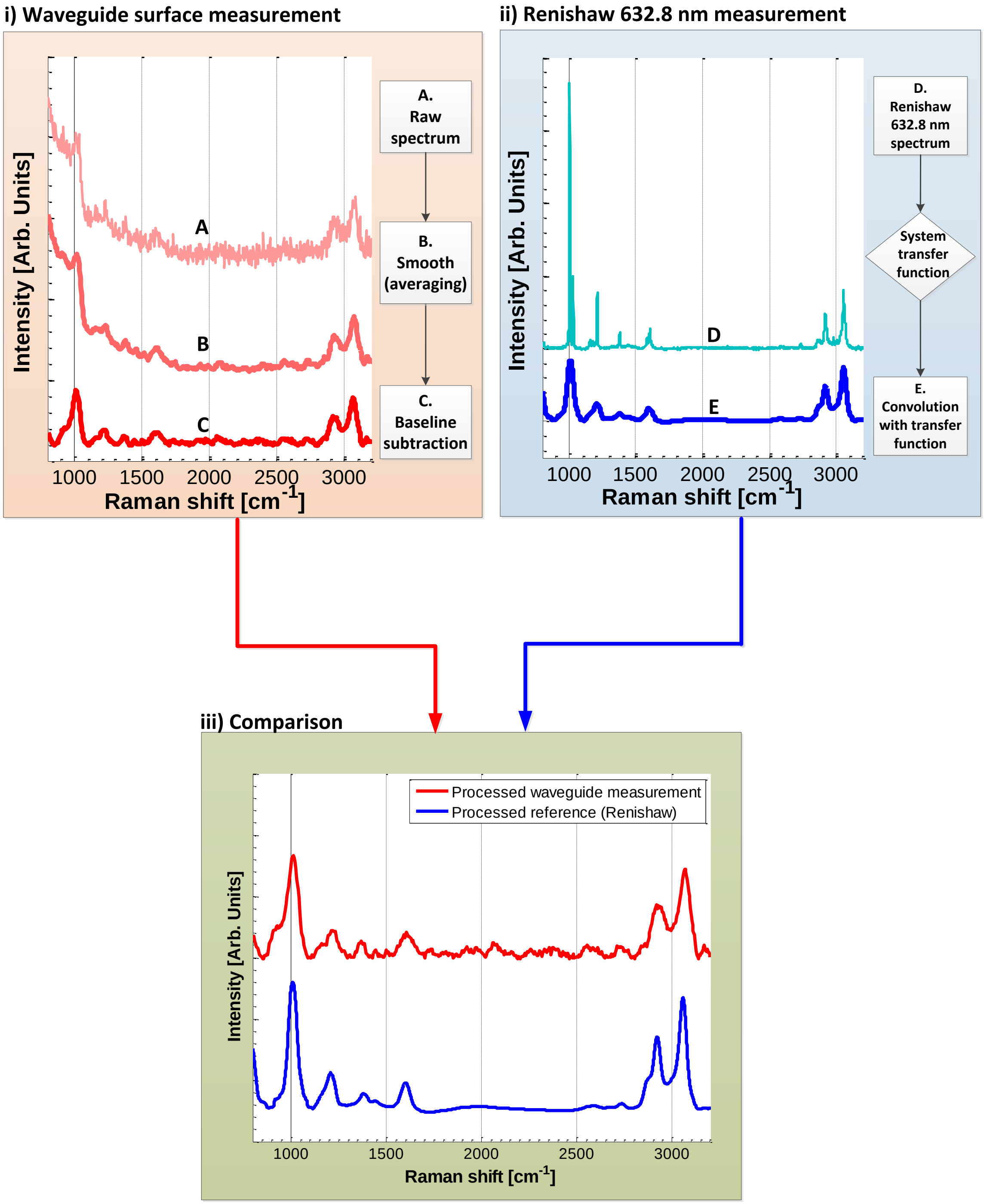

Figure 4.7 Toluene Raman spectrum processing for waveguide measurement and Renishaw 632.8 nm reference measurement, respectively. i) waveguide measurement. Integration time is 60 s; ii) Renishaw 632.8 nm measurement; and iii) comparison between these two.

Two signal processing steps have been performed, one is to smooth the spectrum and the other is to subtract the baseline. The spectrum was smoothed by moving average method, which essentially functioned as a low pass filter to remove high frequency noise. The cut-off frequency was tuned by adjusting the window size, which determined the number of elements to be averaged in a ‘window’. There is an optimum cut-off frequency in which most of high frequency noise will be removed without noticeably compromising signal-to-background ratio. This sweet point was easily found by conducting multiple trials with a series of window sizes, and choosing the window size that gave smooth spectrum and good signal-to-background ratio. Figure 4.7iB shows the toluene spectrum processed by moving average with a window size of eight. As for baseline subtraction, the background can be problematic when determining the relative power between Raman features. For example, Raman feature at around 1,000 cm^{-1} in Figure 4.7iB has its left shoulder merged with the background. In some other measurements, it has been found that both shoulders of this feature could be merged with the background, which made the signal-to-background ratio much smaller compared to features with much weaker background such as feature at around 3,000 cm^{-1} in Figure 4.7iB. However, it does not necessarily reflect the real signal power as strong background merged the signal in the spectrum. Therefore, it is crucial to subtract the background (baseline) before making such a comparison. The background (baseline) subtraction was performed in software Origin by firstly user defined a baseline based upon WERS background measurement that was without the analyte, and then software would generate the spectrum after baseline subtraction, as shown in Figure 4.7iC.

The reference spectrum for toluene with baseline correction, taken using the conventional instrument Renishaw 632.8 nm Raman system, is shown in Figure 4.7iiD (cyan trace) for comparison with the waveguide spectrum. The Raman emission peak at 1,002 cm^{-1} has a published differential Raman cross-section $d\sigma/d\Omega$ of $3.2 \pm 0.3 \times 10^{-30}$ cm^2/sr at a pump wavelength of 633 nm [22]. The processed waveguide Raman spectrum of toluene (Figure 4.7iC) agrees well with the reference spectrum (Figure 4.7iiD), with two main differences. (i) The Raman peaks are broader for the waveguide measurement, due to the lower resolution of the system and (ii) there are additional Raman peaks in the waveguide spectrum at 928 cm^{-1} due to background emission.

The specified resolution of the commercial Raman instrument is ~1 cm^{-1} while the specified resolution of the compact spectrometer is ~5 cm^{-1}. Measurement of the scattered pump signal spectrum in the waveguide configuration shows that the estimated experimental resolution is ~58 cm^{-1}, with the discrepancy being due to bandwidth of the pump laser and the nature of collection by a highly multimode fiber. Specifically, the resolution is not high enough to resolve the two closely spaced peaks at 1,002 cm^{-1} and 1,029 cm^{-1}. However, application to low-cost apparatus for detection and quantification of chemical species does not require ultimate resolution and 58 cm^{-1} may be acceptable for field applications. The reduced spectral resolution of our system causes distortion of the spectra so that while Figure 4.7iiD shows that the reference Raman peak at 1002 cm^{-1} is much higher than the peaks near 3,000 cm^{-1}, Figure 4.7iC shows the opposite for waveguide excitation. The reason for the apparent discrepancy is that the lines near 1,000 cm^{-1} are much narrower than those near 3,000 cm^{-1}, and so carry less power – as the power is proportional to the spectrum feature confined area. To confirm the effect of the reduced resolution upon the measured spectra, the reference spectrum has been convolved with the spectral transfer function of the system (using the part of the collected spectrum corresponding to scattered pump radiation), and the resultant convolved reference spectrum is shown in Figure 4.7iiE. By putting waveguide Raman spectrum and convolved spectrum together in Figure 4.7iii, it is clear that the relative peak heights and linewidths of them are very similar. This emphasises that the power carried by each line is a better measure of cross-section than the peak height.

4.6 Power budget analysis

The emission lines near 1,000 cm^{-1} for toluene were selected for comparison of experimental measurements with the theoretical model and to determine the “power budget” for the system, in terms of power detected in a specific Raman line against pump power launched into the waveguide, as the Raman cross-section for toluene at 1,002 cm^{-1} is well-known [28]. Peaks were fitted to the experimental feature near 1,000 cm^{-1} using the Voigt function [24], as shown in Figure 4.8; the red, green and blue curves represent the toluene Raman peaks at 1,002 cm^{-1} and 1,029 cm^{-1}, and background from the silica substrate respectively. The area confined under the red curve was then used to determine the total number of counts per 60 s due to the Raman line at 1,002 cm^{-1} and then deduce the power in that line to be 2.11×10^{-15} W, with one spectrometer count at this wavelength (675.8 nm) corresponding to 7.2×10^{-18} J [25]. This corresponds to a conversion efficiency of 0.85×10^{-12} mm^{-1} (Watts of Raman power in the 1,002 cm^{-1} line per Watt of pump power per millimeter of waveguide length, assuming that emission from 1 mm waveguide length is collected by the fiber.

A power budget analysis was performed in order to compare the experimental results with the simulations presented in Section 4.3 and to determine where improvements in the waveguide Raman system would provide a significant advantage. Figure 4.9 shows a schematic of the complete system with the major efficiency factors indicated; the product of these efficiency factors results in a total conversion efficiency to compare with the experimental result obtained above. The estimated efficiency factors are given in Table 4.1.

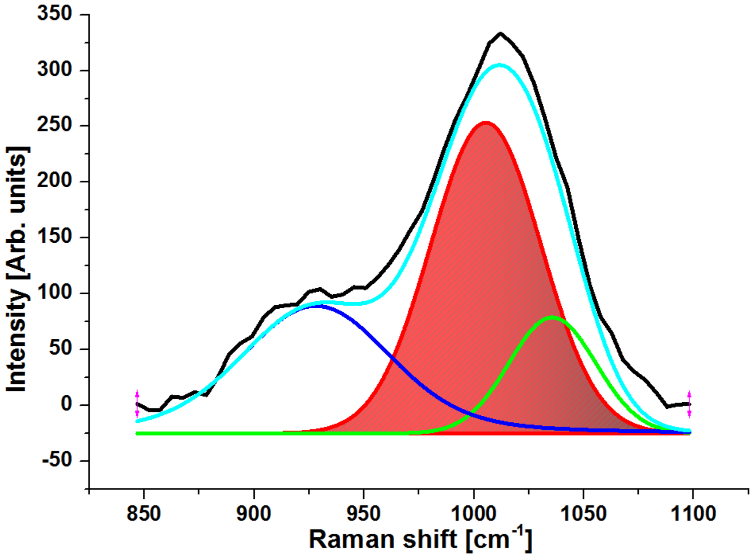

Figure 4.8 Voigt function peak fitting to the spectral features near 1,000 cm^{-1}. The red, green and blue curves represent the toluene Raman peaks at 1,002 cm^{-1} and 1,029 cm^{-1}, and background respectively.

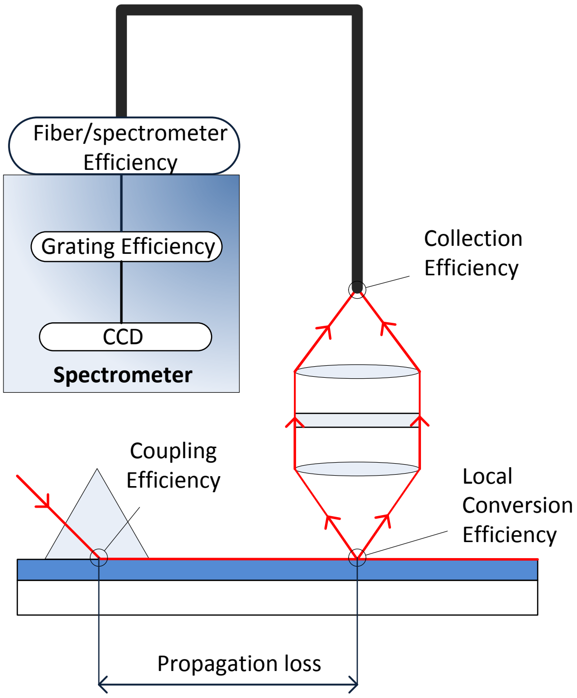

Figure 4.9 Efficiency factors of WERS system

Table 4.1 Summary of efficiencies

Coupling efficiency (η_1)	**0.30 ± 0.1**
Propagation loss factor (η_2)	0.11 ± 0.05
Local conversion efficiency (η_3)	(7.0 ± 0.7) × 10^{-9}
Collection efficiency (η_4)	0.048 ± 0.005
Fiber/spectrometer efficiency (η_5)	0.02 ± 0.01
Grating efficiency (η_6)	0.60 ± 0.02
Total efficiency (η_T)	(1.3 ± 0.8) ×10^{-13}

4.6.1 Coupling efficiency

The proportion of power coupled into the waveguide from the incident beam was estimated to be 30% by subtracting power of all the reflected spots from the pump power, as illustrated in Figure 4.10.

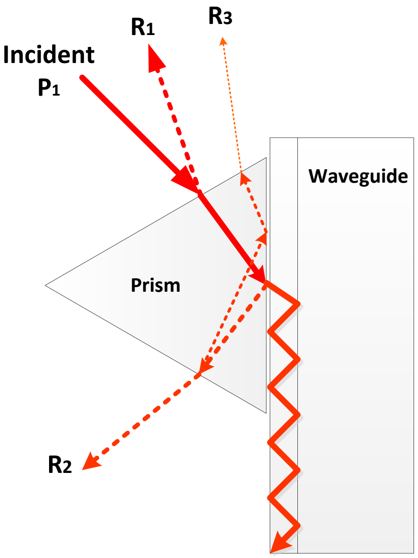

$$\textit{Coupled power} \cong P_1 - R_1 - R_2 - R_3$$

Figure 4.10 Ray traces of light hitting the prism

4.6.2 Propagation loss factor

The propagation loss of the waveguide was measured to be 3.8 dB/cm for TM fundamental mode by Metricon 2010/M Prism Coupler. The Raman spectrum was collected from the waveguide surface at a position 2.5 cm after input coupling and with the measured propagation loss of 3.8 dB/cm, the pump power in the waveguide at this position was estimated to be 5.0 mW, with the propagation loss factor calculated to be 11.2%.

4.6.3 Local conversion efficiency

The local conversion efficiency, η_3, relates the total Raman emission at the waveguide surface to the pump power in the waveguide, over a specific collection area. The power emitted by a Raman line of a bulk material on a waveguide is given by the product of the number density of the emitting molecules, the differential Raman cross-section for that line and the pump intensity, over the excited volume. As only the intensity varies spatially and only in the x-direction (normal to the waveguide surface), this is given by:

$$P_e = \int \rho \cdot N_A/M \cdot \ A \cdot I(x) \cdot 4\pi \cdot d\sigma/d\Omega \cdot dx$$

Equation 4.2

Where ρ and M are the density and molar mass of toluene, respectively, N_A is the Avogadro constant, A is the irradiated waveguide area covered by the bulk medium (approximated as $w \times D$), $I(x)$ is the pump intensity as a function of distance from the surface, $\frac{d\sigma}{d\Omega}$ is the differential Raman cross-section which, for isotropic radiation, yields a total cross-section of $4\pi\frac{d\sigma}{d\Omega}$. The term $\int I(x)\,dx$ is equal to the fractional power plotted in Figure 4.3b, F_s, times the pump power per unit width in the waveguide, P_p/w. The conversion efficiency is then given by:

$$\eta_3 = P_e/P_p = \rho \cdot N_A/M \cdot 4\pi \cdot d\sigma/d\Omega \cdot F_s \cdot D$$ **Equation 4.3**

In the case of our waveguide design for a superstrate medium with the refractive index of toluene, F_s was found to be 0.37, leading to a local conversion efficiency, η_3, of 8.2×10^{-6} per metre length of waveguide. In this experiment, a 0.85mm length of waveguide was imaged onto the 1 mm core of the fiber so that $\eta_3 = 7.0\times10^{-9}$.

4.6.4 Collection efficiency

As described in Section 4.3, the collection efficiency is determined by the numerical aperture of the collection system and the area from which the Raman emission is collected.

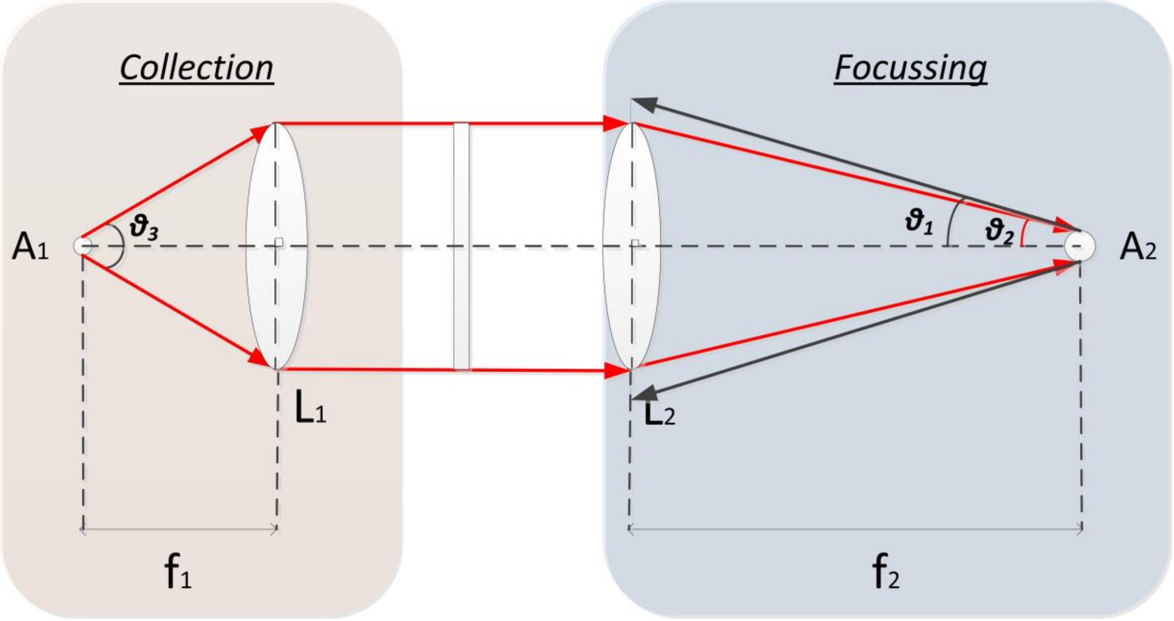

Figure 4.11 Schematic of collection system.

For collection fiber that is at the focussing side of the Figure 4.11, NA=0.48 and diameter is 1,000 um. The half angle of maximum (θ_1) was then calculated to be 28.7^0. For focussing part of the collection system with known parameters such as lens diameter and focal lens, the half angle of maximum (θ_2) can be calculated as below:

$$\theta_2 = \tan^{-1}\frac{D/2}{f_2} = \tan^{-1}\frac{\frac{25.4\,mm}{2}}{30.0\,mm} \approx 23^0$$ **Equation 4.4**

Where D is the lens diameter and f_2 is the focus length of lens 2 (L_2). θ_2 is less than θ_1 means that all of the focussing light is within the collection cone (NA) of the fiber, therefore all light will be collected in theory. By the same way, θ_3 can be calculated with known lens diameter and focus length L$_1$. Hence, the collection solid angle was calculated below as:

$$\Omega = 2\pi \cdot (1 - \sqrt{(1 - sin\theta_3{}^2)}) = 2\pi \cdot (1 - \sqrt{(1 - 0.45^2)}) = 0.672$$ Equation 4.5

The solid angle collection efficiency (η_{angle}) was then calculated as:

$$\eta_{angle} = \frac{\Omega}{4\pi} = \frac{0.672}{4 \times 3.142} = 0.053$$ Equation 4.6

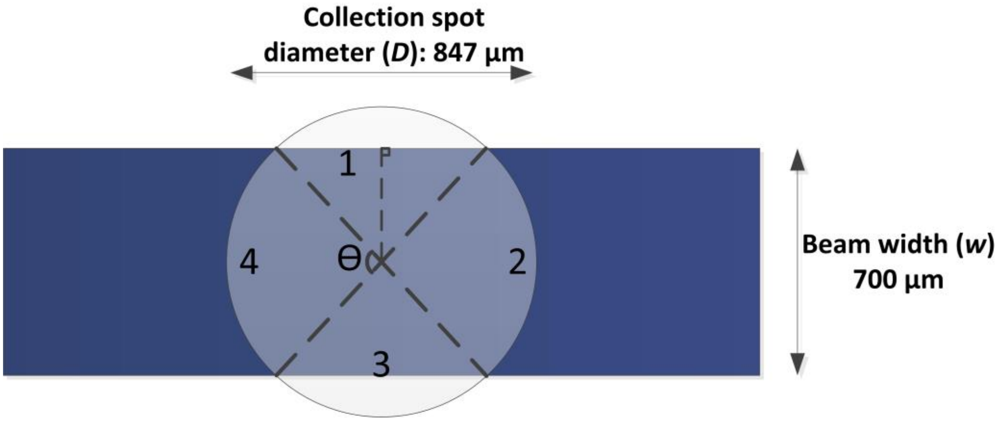

Figure 4.11. Schematic of overlap between beam and collection spot.

The area of excited molecules is in rectangle shape while the collection spot is in circular shape defined by the collection fiber core as illustrated in Figure 4.11. Therefore, there is an area collection efficiency involved in this. The area of light blue is the effective collected area, denoted as A_1. It consists of two triangles 1 and 3 and two sectors 2 and 4. The area of triangle 1 and 3 can be calculated as:

$$A_{1,3} = \sqrt{\left(\frac{D}{2}\right)^2 - \left(\frac{w}{2}\right)^2} \cdot \frac{w}{2} = \sqrt{\left(\frac{847\ \mu m}{2}\right)^2 - \left(\frac{700\ \mu m}{2}\right)^2} \cdot \frac{700\ \mu m}{2}$$ Equation 4.7

$$= 8.4\ \times 10^4\ \mu m^2$$

The area of sector 2 and 4 can be calculated as:

$$\theta = \frac{360^0 - 4 \times \cos^{-1}\frac{w}{D}}{2} = \frac{360^0 - 4 \times \cos^{-1}\frac{700}{847}}{2} = 111^0$$ Equation 4.8

$$A_{2,4} = \pi(\frac{D}{2})^2 \cdot \frac{\theta}{360^0} = \pi\left(\frac{847\ \mu m}{2}\right)^2 \cdot \frac{111^0}{360^0} = 1.7 \times 10^5\ \mu m^2$$ Equation 4.9

The area collection efficiency (η_{area}) was then calculated as:

$$\eta_{area} = \frac{A_{1,3} \times 2 + A_{2,4} \times 2}{\pi(\frac{D}{2})^2} = \frac{8.4\ \times 10^4\ \mu m^2 \times 2 + 1.7 \times 10^5\ \mu m^2 \times 2}{\pi(\frac{847\mu m}{2})^2} = 0.91 \quad \text{Equation 4.10}$$

The total collection efficiency was calculated by taking into account both the solid angle collection efficiency and area collection efficiency:

$$\eta_4 = \eta_{angle} \cdot \eta_{area} = 0.053 \times 0.91 \approx 4.8\% \quad \text{Equation 4.11}$$

4.6.5 Fiber/spectrometer efficiency

The spectrometer has an intrinsic NA of 0.125 and a slit width of 200 µm. Using a similar calculation method demonstrated in Section 4.6.4, the combination of the reduced numerical and physical apertures yield an efficiency factor, $\eta_5 \simeq 2\%$ at the interface between the fiber and the spectrometer.

4.6.6 Grating efficiency

The grating diffract the collected Raman light so that photon of different wavelengths goes into different directions. The selection of grating affects the spectral range and partially determines the optical resolution. Grating H36 provided by Ocean Optics was selected for its excellent balance between wide spectral range in visible to near-infrared and optical resolution. From the manufacturer datasheet, the grating efficiency (η_6) at 675.8 nm that corresponds to 1,002 cm^{-1} is about 60%.

4.6.7 System total efficiency

Equation 4.12 then gives power arriving at the CCD, P$_d$, in terms of the incident pump power in the waveguide

$$P_d = P_i \cdot \eta_T = P_i \cdot \eta_1 \cdot \eta_2 \cdot \eta_3 \cdot \eta_4 \cdot \eta_5 \cdot \eta_6 \quad \text{Equation 4.12}$$

resulting in a predicted power incident on the CCD array in the 1,002 cm^{-1} Raman line of $5.7 \pm 3.5 \times 10^{-15}\ W$ which was in reasonable agreement with the experimental result of $2.1 \times 10^{-15}\ W$ when it was considered that the analysis assumed that isotropic Raman emission and perfect optical alignment and that additional losses such as Fresnel reflections and fiber transmission losses had been ignored.

4.6.8 Discussion

This power budget analysis has verified that the experimental power detected in a single Raman line from a simple bulk liquid analyte compares reasonably well with theoretical predictions, given experimental uncertainties. The efficiency factors which dictate the power budget make clear that the efficiency of transferring the emitted Raman power to the spectrometer CCD array is poor, but this is fundamentally limited by the brightness of the incoherent emission and the numerical and spatial apertures of the spectrometer. Collection of the Raman emission in the waveguide is an attractive alternative as, for low-loss waveguides, collected power can be usefully built up over longer waveguide lengths but collection in a monomode waveguide optimised for excitation by a (coherent) pump is normally poor leading to little advantage despite better aperture matching between the waveguide/spectrometer interface [11], [26]. However, engineering the collection of surface Raman emission at a waveguide surface by exploiting the non-isotropic nature of the emission is a promising avenue to explore [27]. A detailed evaluation of Raman emission in the presence of the waveguide structure should be conducted in order to find out the most effective collection configuration.

4.7 Conclusion

In this chapter, thin film waveguide made of Ta_2O_5 sputtered on top of fused silica has been used for Raman measurement from the waveguide surface. The key advantage of waveguide surface excitation over conventional excitation with a focussed beam perpendicular to the layer is that in one dimension (waveguide thickness), the intensity spot-size can be drastically reduced, and surface intensity thereby significantly increased, without any reduction in the irradiated surface area. Theoretical analysis has demonstrated that both index contrast and core film thickness play important roles in achieving high surface intensity, giving knowledge of excitation wavelength and analyte medium. It also shows that the use of ~100 nm Ta_2O_5 for waveguide Raman measurement for aqueous solution is optimum.

Confocal Raman microscopy has been widely used due to its advantages in spatial resolution over conventional microscopy. In particular, it possesses great SNR and resolution for bulk medium (~µm). Reference Raman spectra of toluene, IPA and polystyrene have been measured in Renishaw 632.8 nm Raman system. These spectra have been processed in an attention for comparison with waveguide Raman measurements.

637 nm light from a semiconductor laser was prism coupled into the thin film waveguide. A two-lens image system was put on top of the waveguide surface for collection. The measured spectra from waveguide system were smoothed and baseline subtracted in order to be ready for comparison with that from the Renishaw Raman microscopy. The Raman spectra features can change dramatically in terms of its relative height as the resolution changes. For comparison purpose, the reference spectra were therefore convolved with the response function of the waveguide Raman system. The resultant spectra show good agreement with each other in terms of feature positions and relative height.

A power budget analysis has been performed by relating the received power in a single Raman emission line to the incident pump laser power. The theoretical value is in reasonable agreement to the experimental value. This approach allows straightforward WERS optimisation and a clear comparison of surface-enhanced techniques. Leading to the next Chapter, discussion of power budget analysis highlights that future improvement in collection efficiency is a very promising venue.

4.8 References

[1] Y. Levy, C. Imbert, J. Cipriani, S. Racine, and R. Dupeyrat, “Raman scattering of thin films as a waveguide,” *Opt. Commun.*, vol. 11, no. 1, pp. 66–69, 1974.

[2] J. Cipriani, S. Racine, R. Dupeyrat, H. Hasmonay, M. Dupeyrat, Y. Levy, and C. Imbert, “Raman scattering of Langmuir-Blodgett barium stearate layers using a total reflection method,” *Opt. Commun.*, vol. 11, no. 1, pp. 70–73, 1974.

[3] J. F. Rabolt, R. Santo, and J. D. Swalen, “Raman spectroscopy of thin polymer films using integrated optical techniques.,” *Appl. Spectrosc.*, vol. 33, no. 6, pp. 549–551, 1979.

[4] J. F. Rabolt, N. E. Schlotter, and J. D. Swalen, “Spectroscopic studies of thin film polymer laminates using Raman spectroscopy and integrated optics,” *J. Phys. Chem.*, vol. 85, no. 26, pp. 4141–4144, Dec. 1981.

[5] N. Schlotter and J. Rabolt, “Raman spectroscopy in polymeric thin film optical waveguides. 1. Polarised measurements and orientational effects in two-dimensional films,” *J. Phys. Chem.*, vol. 16, no. 4, pp. 2062–2067, 1984.

[6] J. F. Rabolt, R. Santo, N. E. Schlotter, and J. D. Swalen, “Integrated optics and Raman scattering: molecular orientation in thin polymer films and Langmuir-Blodgett monolayers,” *IBM J. Res. Dev.*, vol. 26, no. 2, pp. 209–216, 1982.

[7] J. S. Kanger, C. Otto, M. Slotboom, and J. Greve, “Waveguide Raman spectroscopy of thin polymer layers and monolayers of biomolecules using high refractive index waveguides,” *J. Phys. Chem.*, vol. 100, no. 8, pp. 3288–3292, 1996.

[8] S. Ellahi and R. E. Hester, “Enhanced waveguide Raman spectroscopy with thin films. Plenary lecture,” *The Analyst*, vol. 119, no. 4. p. 491, 1994.

[9] Y. Gu, S. Xu, H. Li, S. Wang, M. Cong, J. R. Lombardi, and W. Xu, “Waveguide-enhanced surface plasmons for ultrasensitive SERS detection,” *J. Phys. Chem. Lett.*, vol. 4, no. 18, pp. 3153–3157, 2013.

[10] F. Peyskens, A. Subramanian, A. Dhakal, N. Le Thomas, and R. Baets, “Enhancement of Raman scattering efficiency by a metallic nano-antenna on top of a high index contrast waveguide,” in *CLEO: 2013*, 2013, p. CM2F.5.

[11] A. Dhakal, A. Z. Subramanian, P. Wuytens, F. Peyskens, N. Le Thomas, and R. Baets, “Evanescent excitation and collection of spontaneous Raman spectra using silicon nitride nanophotonic waveguides,” *Opt. Lett.*, vol. 39, no. 13, pp. 4025–4028, 2014.

[12] D. Hu and Z. Qi, “Refractive-index-enhanced Raman spectroscopy and absorptiometry of ultrathin film overlaid on an optical waveguide,” *J. Phys. Chem. C*, vol. 117, no. 31, pp. 16175–16181, Aug. 2013.

[13] X. Jiang, L. Tang, J. Song, M. Li, and J.-J. He, “Integrated Raman spectroscopic sensor based on silicon nanowire waveguides,” in *Proc. of SPIE*, 2014, vol. 9274, p. 92740I.

[14] C. Fu, Y. Gu, Z. Wu, Y. Wang, S. Xu, and W. Xu, “Surface-enhanced Raman scattering (SERS) biosensing based on nanoporous dielectric waveguide resonance,” *Sensors Actuators, B Chem.*, vol. 201, pp. 173–176, 2014.

[15] M. W. Meyer, K. J. McKee, V. H. T. Nguyen, and E. A. Smith, “Scanning angle plasmon waveguide resonance Raman spectroscopy for the analysis of thin polystyrene films,” *J. Phys. Chem. C*, vol. 116, no. 47, pp. 24987–24992, Nov. 2012.

[16] C. Henry, “Product Review: Raman shifts into high gear,” *Anal. Chem.*, vol. 69, no. 9, p. 309A–313A, May 1997.

[17] C. M. Harris, “Product Review: Raman Revisited,” *Anal. Chem.*, vol. 74, no. 15, p. 433 A–438 A, Aug. 2002.

[18] R. L. McCreery, *Raman Spectroscopy for Chemical Analysis*. Hoboken, NJ, USA: John Wiley & Sons, Inc., 2000.

[19] Eric Le Ru and Pablo Etchegoin, *Principles of Surface-Enhanced Raman Spectroscopy and related plasmonic effects*. 1st ed., Elsevier, 2009.

[20] C.A. Burrus, “Small-area high-radiance light-emitting diodes coupled to multimode optical fibers,” in *Topical meeting on integrated optics-guided waves, materials, and devices*, 1972.

[21] K. Schmitt, K. Oehse, G. Sulz, and C. Hoffmann, “Evanescent field Sensors Based on Tantalum Pentoxide Waveguides – A Review,” *Sensors*, vol. 8, no. 2, pp. 711–738, Jan. 2008.

[22] E. C. Le Ru, E. J. Blackie, M. Meyer, and P. G. Etchegoin, “Surface enhanced Raman scattering enhancement factors: a comprehensive study,” *J. Phys. Chem. C*, vol. 111, no. 37, pp. 13794–13803, Sep. 2007.

[23] E. Lock, S. Walton, and R. Fernsler, “Preparation of ultra thin polystyrene, polypropylene and polyethylene films on Si substrate using spin coating technology,” Nav. Res. Labratory. 2008.

[24] M. Bradley, “Curve fitting in Raman and IR spectroscopy : basic theory of line shapes and applications,” *Thermo Fish. Sci. Appl. Note 50733*, pp. 0–3, 2007.

[25] Ocean Optics, “QE65000 and Maya2000 Spectrometers.” [Online]. Available: http://oceanoptics.com/wp-content/uploads/OEM-Data-Sheet-QE65000.pdf.

[26] D. Marcuse, “Launching light into fiber cores from sources located in the cladding,” *J. Light. Technol.*, vol. 6, no. 8, pp. 1273–1279, 1988.

[27] C. Chen, J.-Y. Li, L. Wang, D.-F. Lu, and Z.-M. Qi, “Waveguide-coupled directional Raman radiation for surface analysis,” *Phys. Chem. Chem. Phys.*, vol. 17, no. 33, pp. 21278–21287, 2015.

CHAPTER 5 Theory of waveguide Raman collection

5.1 Introduction

In Chapter 4, WERS with the optimum waveguide design for maximum excitation has been successfully demonstrated for sensing a bulk liquid (toluene) by collection at the waveguide surface. The power budget analysis given highlights that the collection efficiency for waveguide evanescent field excited Raman from collection at above the waveguide surface is very low – 5.3%. This leads to a low sensitivity that renders it extremely difficult to sense a small quantity of sample such as a thin film or monolayer, without using other enhancement mechanisms such as resonance Raman scattering [1]–[5]. However, many biological and chemical applications demand high sensitivities [6], [7]. Therefore, there is a severe performance gap that needs to be filled for WERS. The low collection efficiency of WERS by waveguide surface collection indicates that significant improvements can be made on the aspect of Raman collection. However, the efficient collection of waveguide Raman has not been the focus in the literature.

In Chapter 4, isotropic Raman emission from bulk toluene liquid was assumed in order to theoretically estimate the power received by the spectrometer. However, as Porto pointed out in the angular measurement of Raman emission of benzene liquid, the emission pattern was that of an emitted dipole in free space with two equal lobes, which was determined by the combined effects of the molecule symmetry, polarisation of the excitation light, and the collection direction [8]. In this case, the molecule was treated as a dipole in free space and its emission pattern was calculated to prove the experimental observation. Separately, it had been found that the emission pattern of a dipole near an interface was altered, as extensively studied in the fluorescence community [9], [10]. Raman emission for a molecule evanescently excited by the waveguide requires detailed studies.

In this Chapter, the theory of waveguide effects on an excited molecule will be explained by treating the molecule as a dipole, and studying the behaviour of its excitation and emission under the influence of the waveguide. The modelling and simulation tools will be established for each case, which will be utilised in this Chapter and Chapter 6.

5.2 Waveguide effects on the excited molecule

The waveguide effects on the excited molecule are discussed as compared to that in the free space. The waveguide structure investigated in this project is a three-layer monomode slab waveguide, which can be modelled as a three-layer interface. The simplest structure in the physical model would be a two-layer interface. The effects of an interface on an excited molecule have been extensively studied in the fluorescence community. To summarise the effects, an interface may 1) change the spontaneous emission rate of the excited molecule and 2) alter its spatial power distribution [10]. The former effect is often known as the Purcell effect [11]. For an excited molecule in the cavity, its spontaneous emission can be inhibited if the cavity's characteristic dimensions are small compared to the radiation wavelength, and enhanced if the cavity is resonant. This effect plays an important role in a wide range of applications, such as solar cells [12], light emitting diodes (LEDs), quantum light sources [13], etc. The waveguide, which can be viewed as a cavity, will modify the spontaneous emission rate of the excited molecules within its field [14]. The Purcell enhancement will be determined in the next section for the waveguide structure utilised in the Chapter 4. As for the emission distribution from an excited molecule near an interface, the spatial distribution of the emission will be altered as some of the emission may couple into the non-radiative near-field paths while the others are interfered by the interface and result in a modified far-field radiation pattern compared with that in free space. By tuning the interface design parameters, such as the interface materials, layer thickness, and distance between the excited molecule and the interface, efficient collection of the far-field radiation was achieved by the fluorescence community [15]. In a contrast, non-radiative near-field paths were generally considered as losses and therefore avoided [10]. Both near-field radiation patterns into the slab waveguide and far-field radiation patterns for an excited molecule near a three-layer interface will be determined in the following sections.

5.3 Purcell enhancement

In this section, the Purcell enhancement factor will be determined for a specific waveguide design of optimised excitation. The Purcell enhancement factor (F_p) is defined as:

$$F_p = \frac{P_c}{P_{fs}} \qquad \textbf{Equation 5.1}$$

where P_c is the radiated power in the environment, which in this case is with the presence of the waveguide, P_{fs} is the radiated power for the emitted molecule in free space. Since most of modelled cases are for an excited molecule or atom in a cavity, there is a specific expression for this [14]:

$$F_p = \frac{3}{4\pi^2} \cdot (\frac{\lambda}{n})^3 \cdot \frac{Q}{V} \qquad \textbf{Equation 5.2}$$

Where λ is the emission wavelength, n is the refractive index of the environment around the molecule, Q is the quality factor of the cavity, and V is the mode volume. Equation 5.2 is difficult to calculate especially for a structured surface, therefore in this Chapter the Purcell factor was found numerically. Software Lumerical FDTD solutions was utilised to model the structure and numerically determine the Purcell enhancement factor by using Equation 5.1. The specific waveguide design with optimised Raman excitation as utilised in Chapter 4 was modelled. The modelled structure, as shown in Figure 5.1, has a fused silica (SiO_2) substrate, 110 nm tantalum pentoxide (Ta_2O_5) core, and a bulk toluene background that was set to have the index of 1.49 corresponding to the emission wavelength at 685 nm, which referred to the 1,002 cm^{-1} vibrational mode for an excitation wavelength of 637 nm. A dipole source was added at exactly the interface between the core and the toluene. The dipole angle with respect to the waveguide surface was set at either 90^0 (perpendicular) or 0^0 (parallel) to the interface. The FDTD simulation region utilised in this Chapter had a span of 9 μm in the *x*-direction and 2.5 μm in the *y*-direction, which provided enough space for simulations to be performed without suffering from interferences of multiple reflections of the region boundaries. The mesh accuracy of the FDTD region was set to provide a good trade-off between accuracy, memory requirements and simulation time. The mesh refinement method was chosen to be Conformal variant 1, which provided much better convergence for many simulations involving calculations such as Mie scattering, or reflection and transmission from multilayer stacks, which are essential for this calculation [16]. The nature of a very thin 110 nm core layer poses a threat to the simulation accuracy. To tackle this, a finer mesh region is added covering the whole core region, and expanding 50 nm into the substrate and top layer to cover the two interfaces. For this finer mesh region, the mesh size is 10 nm in the vertical *y* direction and 30 nm in the *x* direction. The boundary of the FDTD simulation region sets to perfectly matched layer (PML), in order to avoid reflection interferences from the boundary. Other simulation parameters: simulation time is 500 fs after convergence test, simulation temperature is 300K (room temperature). 3D simulation, rather than full 3D simulation, was chosen as a good compromise between simulation time and precision, and was appropriate for an essentially 2D slab waveguide.

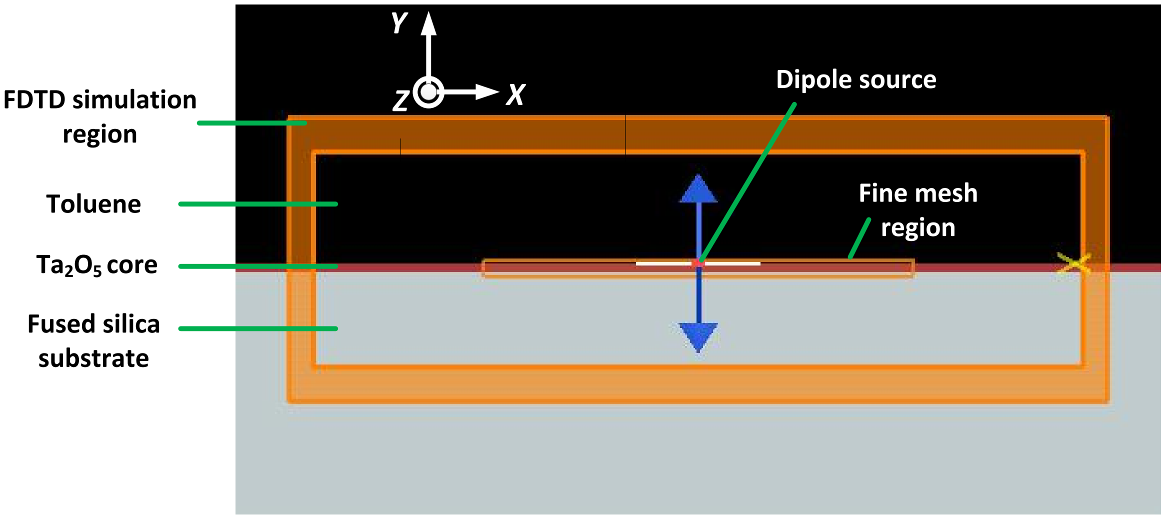

Figure 5.1 Illustration of FDTD model schematic. The dipole source is *y*-oriented in the above schematic. The simulation region is within the rectangular boundary.

After the simulation completion, the Purcell enhancement factor can be obtained from the dipole source results. For the above waveguide design, the Purcell enhancement factors are 1.4 and 2.5 for parallel and perpendicular dipoles located at the interface, respectively. This confirms that spontaneous emission rate is modified for a dipole located "at the interface" of the proposed waveguide.

5.4 Emission routes: near field and far field radiation

There are two emission routes for a dipole near the waveguide. One is through near field radiation that involves emission that is either absorbed or coupled into the waveguide guided mode(s), which are usually inhibited from far field observation. The other is through far field radiation that is either directly emitted from the dipole position or emitted radiation that is reflected by the interfaces, which can reach the far field. The name of these two emission routes suggests where the emission will be in terms of the dipole location; as near field radiations are often contained within the waveguide structure, whereas far field radiations reach out in far field. Depending on the collection configuration, the contribution of these routes to the total collection into a collection system with defined NA can be very different. Therefore, for efficient collection, it is important to figure out the spatial distribution of the emitted power by studying each emission route.

5.4.1 Near field radiations for a dipole near a slab waveguide

The purpose of this section is to determine the proportion of power coupled into the waveguide guided mode(s) as well as its angular emission pattern. Dipoles of different orientations will be discussed. The modelling and simulation were performed by using the Lumerical model discussed in Section 5.3.

The emission pattern of any linearly polarised dipole can be obtained by linearly summing the contribution of x, y and z oriented dipoles, respectively. For a two-dimensional (xy plane) confined slab waveguide structure, there are in effect only two different cases of the dipole orientation: parallel to the interface (x- or z-oriented) and perpendicular to the interface (y-oriented). The case of dipole located at the surface will be modelled to illustrate. For excitation light at a wavelength of 637 nm, the breathing mode of toluene Raman at around 1,000 cm^{-1} corresponds to a Raman emission wavelength of 685 nm, corresponding to a dipole oscillating at 438.0 THz (685 nm). Again, for all cases in this chapter, the waveguide structure has a Ta_2O_5 core thickness of 110 nm on top of a fused silica substrate, with bulk toluene liquid as the top cladding.

Firstly, the near field radiation of a dipole parallel to the interface (x-oriented dipole) is shown in Figure 5.2. The proportion of power coupled into the waveguide was calculated by summing the power transmission of each side of the enclosed structure, with each side plane (two xy planes and two yz planes) having the same distance of 2.5 µm to the dipole. The distance was chosen after convergence tests so that the power transmission to each side was stabilized. For an x-oriented dipole, the proportion of power coupled into the waveguide to the total emitted power is 62%. As for the near field radiation pattern, the power is mostly coupled in the direction (z) perpendicular to the dipole orientation (*x*). The *xz* plane radiation pattern is very similar to that of the cross-section of a dipole in free space, which is governed by $\sin^2\theta$ [8].

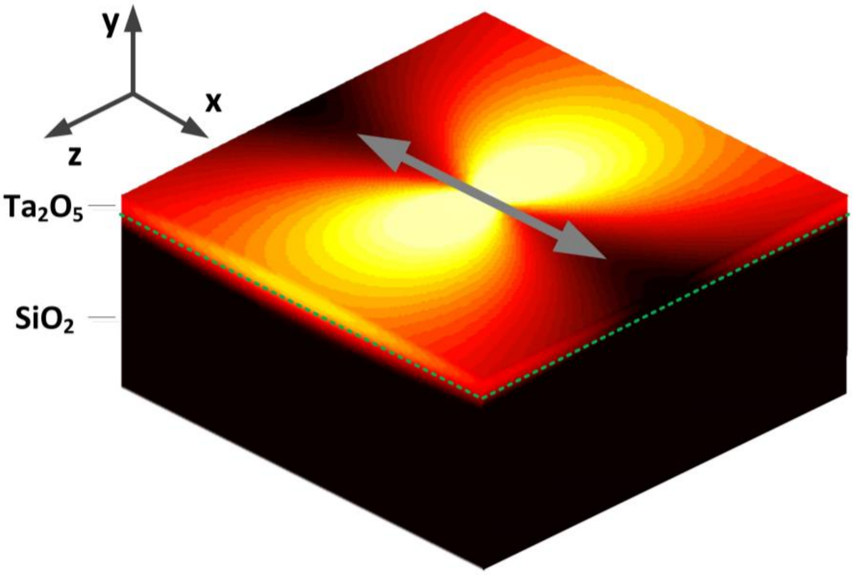

Figure 5.2 Power diagram of near-field coupling from parallel dipole (*x*-oriented) located at the waveguide surface. Arrow indicates the orientation of the emitted dipole. Dotted line indicates the interface between SiO_2 and Ta_2O_5. Higher brightness indicates larger power density.

For a dipole perpendicular to the interfaces, shown in Figure 5.3, 76% of the total emitted power is coupled into the waveguide guided mode(s). The radiation is uniformly distributed in all directions of the *xz* plane. This is expected as the orientation of the emitted dipole is parallel to the symmetrical axis of the plane.

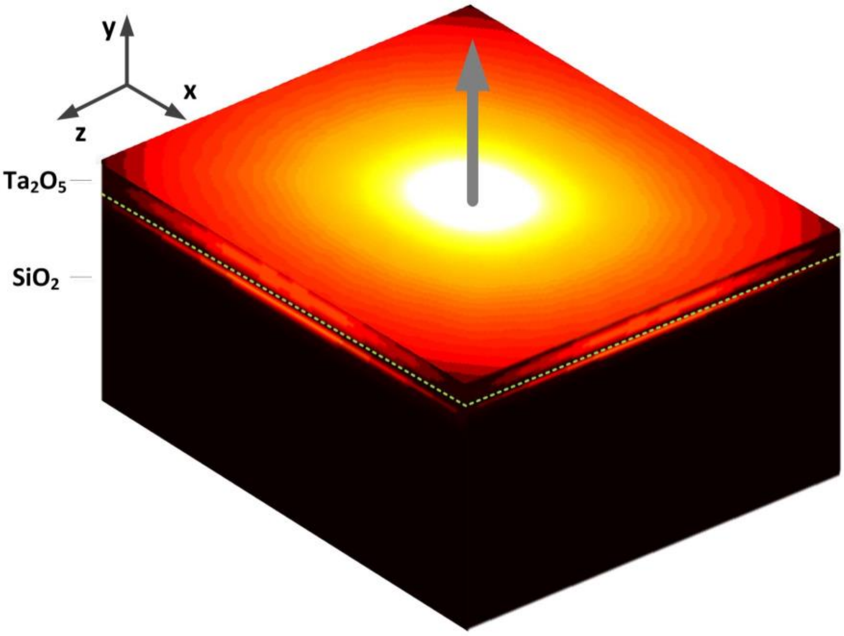

Figure 5.3 Power diagram of near-field coupling from perpendicular dipole (*y*-oriented) located at the waveguide surface. Arrow indicates the emitted dipole orientation. Dotted line indicates the interface between SiO_2 and Ta_2O_5. Higher brightness indicates larger power density.

To summarise, for both parallel (*x*- or *z*-oriented) and perpendicular (*y*-oriented) dipoles located at the waveguide surface, the majority of the emitted power is coupled into the waveguide guided mode(s) for this waveguide design. In terms of the radiation pattern, parallel dipoles have characteristic of in-plane (*xz* plane) angular emission, for which the majority of the emission is in the direction perpendicular to the dipole orientation; whereas for perpendicular dipoles, the in-plane emission has a uniform power distribution. Putting these into perspective of the collection, the majority of the Raman emission for a dipole sitting at the waveguide surface cannot be collected from above the waveguide surface, as it is contained by the waveguide structure. In order to collect these near field emissions, collection from the waveguide periphery should be employed.

5.4.2 Far field radiation for a dipole near a slab waveguide

For the case of a dipole located at the waveguide surface, while the majority of the emitted power is distributed to near field radiation, the rest of the emitted power goes to the far field radiation. Knowing how much power the near field radiation has as a proportion of the total emission, the proportion of power going to far field radiation can be easily calculated as 38% and 24%, for an *x*(*z*)-oriented dipole and an *y*-oriented dipole, respectively.

The purpose of this section is to determine the far field emission pattern of a dipole located at the waveguide surface. In free space, in the absence of a waveguide structure, the dipole emission pattern in the far field has two equal lobes, as shown in Figure 5.4, as experimentally verified by Porto for the 994 cm^{-1} vibrational mode of liquid benzene [8]. However, when a waveguide is placed in the vicinity of the molecule, the far field emission distribution will change due to the influence of the waveguide structure.

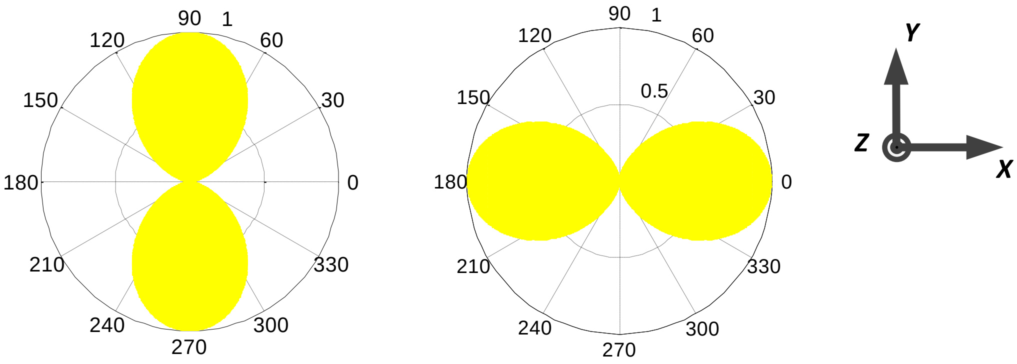

***x*-oriented** ***y*-oriented**

Figure 5.4 Far-field angular emission diagram of *x*- and *y*- oriented dipoles in free space.

5.4.2.1 Theory of far-field emission of a dipole at around interfaces

Analytical expressions for far-field emission into the cladding (upward) and substrate (downward) can be obtained by applying the optical reciprocity theorem [17]. The optical reciprocity theorem generally states that the source and detector of electromagnetic fields can be interchanged without affecting the physical situation [18]. For example, in order to know the angular power distribution of emission to the substrate, only the transmission coefficient of light traveling from the substrate to the position of excitation at each angle needs to be known. The same apples to the case of calculating the angular power distribution for the upward emission. Analytical expressions of far field emission for a dipole located on top of a multilayer structure will now be given. Then they will be utilised to calculate far field emission for oriented dipoles located on top of the waveguide structure as described earlier.

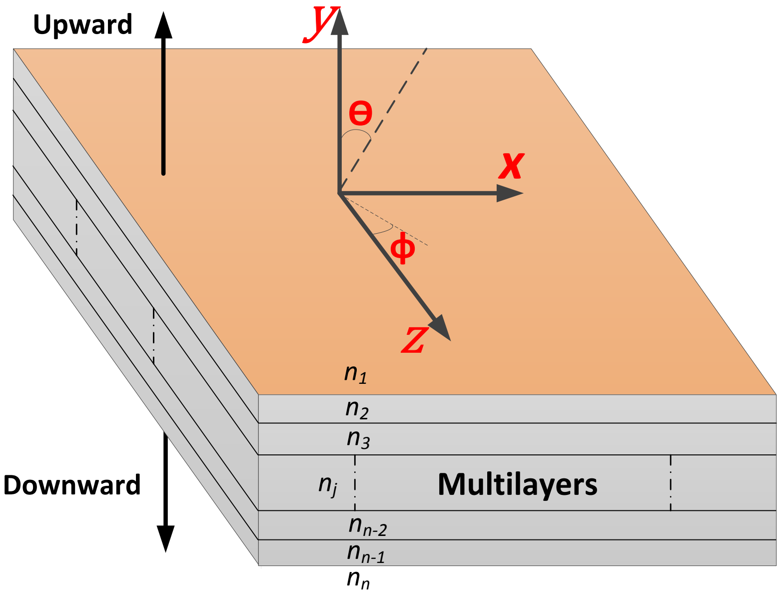

Figure 5.5 Cartesian system of a dipole on top of a multilayer structure.

The analytical expression for normalised three dimensional radiation patterns of an arbitrary dipole on top of a two dimensional multilayer system, as shown in Figure 5.5, is given by [18] as:

$$\frac{p(\theta,\phi)}{P_0} \propto \frac{n_n}{n_1} \cdot \{\mathbb{A} + \mathbb{B} + \mathbb{C} + \mathbb{D}\}$$

Equation 5.3

$\mathbb{A}$: $p_y^2 \sin^2\theta \left\|\Phi_j^1\right\|^2$	*z*-oriented contribution
$\mathbb{B}$: $\|p_z \cos\phi + p_x \sin\phi\,\|^2 \cos^2\theta \left\|\Phi_j^2\right\|^2$	*x*-oriented contribution
$\mathbb{C}$: $\|\sin\phi - p_x \cos\phi\,\|^2 \left\|\Phi_j^3\right\|^2$	*y*-oriented contribution
$\mathbb{D}$: $-\sin\theta\cos\theta$ $\times [p_y (p_z{}^* \cos\phi$ $+ p_x{}^* \sin\phi)\Phi_j^{*(1)}\Phi_j^{(2)}$ $+ p_y{}^* (p_z \cos\phi$ $+ p_x \sin\phi)\Phi_j^{(1)}\Phi_j^{*(2)}]$	Interference contribution from horizontally and vertically oriented dipole

where $p(\theta,\phi)$ is defined as the radiation pattern without normalization, P_0 is the radiation power of the dipole in a homogeneous medium (n_a), n_n and n_1 is the refractive index of the substrate and analyte (or air) respectively. p_i is the dipole moment in $i = x, y, z$ direction and ${p_i}^*$ represents the complex conjugate of the p_i with $i = x, y, z$. Φ_j^n ($n = 1{,}2{,}3; j = 1, n$) is defined as follows:

$$\Phi_1^{(1)} = \left[e^{-ik_1 y_0 \cos\theta} + r^p(\theta) e^{-ik_1 y_0 \cos\theta}\right] \qquad \text{Equation 5.4}$$

$$\Phi_1^{(2)} = \left[e^{-ik_1 y_0 \cos\theta} - r^p(\theta) e^{-ik_1 y_0 \cos\theta}\right] \qquad \text{Equation 5.5}$$

$$\Phi_1^{(3)} = \left[e^{-ik_1 y_0 \cos\theta} - r^s(\theta) e^{-ik_1 y_0 \cos\theta}\right] \qquad \text{Equation 5.6}$$

$$\Phi_n^{(1)} = \frac{n_n \cos\theta}{n_1 \cos\theta_r} t^p(\theta) e^{ik_n[y_0 \cos\theta_r + \delta\cos\theta]} \qquad \text{Equation 5.7}$$

$$\Phi_n^{(2)} = -\frac{n_n}{n_1} t^p(\theta) e^{ik_n[y_0 \cos\theta_r + \delta\cos\theta]} \qquad \text{Equation 5.8}$$

$$\Phi_n^{(3)} = \frac{\cos\theta}{\cos\theta_r} t^s(\theta) e^{ik_n[y_0 \cos\theta_r + \delta\cos\theta]} \qquad \text{Equation 5.9}$$

with $\cos\theta_r = \frac{k_{y1}}{k_n} = \sqrt{(\frac{n_1}{n_n})^2 - \sin^2\theta}$ whereas $\cos\theta = \frac{k_{y1}}{k_1}$, k_i is the propagation constant of ith layer, defined as $k_i = \frac{2\pi}{\lambda} \cdot n_i$, y_0 is the distance of the dipole to the interface, δ is the total height of the layered interface, $r^{p,s}$ and $t^{p,s}$ are the Fresnel coefficients of reflection and transmission respectively, with p and s representing TM and TE polarisation respectively. The upward ($+y$) and downward (-y) emission can be calculated by substituting $j = 1$ and $j = n$ into Equation 5.3. Noting that the upward emission starts at the dipole position whereas the downward emission starts at the interface between layer n_{n-1} and n_n.

5.4.2.2 Far field emission pattern of an x-oriented dipole located at the waveguide surface

The case to be modelled is a parallel (x-oriented) dipole located at the surface of the waveguide having the structure described in section 5.3. The far field radiation pattern for both upward and downward emission were calculated by substituting $p_x = 1, p_y = 0, p_z = 0$ into Equation 5.3. Figure 5.6 demonstrates the simulation result. First of all, the 3D radiation pattern (Figure 5.6a) shows that the power is not evenly distributed between the upward and downward emission, as there is much more downward emission into the substrate. Secondly, the emission pattern clearly shows that the directivity as upward emission favours yz plane more than xy plane. This is in a contrast with the near field emission of an x-oriented dipole, for which the emission is maximum in the direction perpendicular to the dipole orientation. These two features reveal that the radiation pattern of a parallel dipole located at the waveguide surface is very different to that of a dipole in free space, which confirms that the presence of the waveguide modifies the directivity of the far-field radiation.

Considering only a single parallel dipole (*x*-oriented) implies that collection of far-field radiation from either top surface or substrate (perpendicular to the interfaces) is more efficient than collection at any waveguide edge.

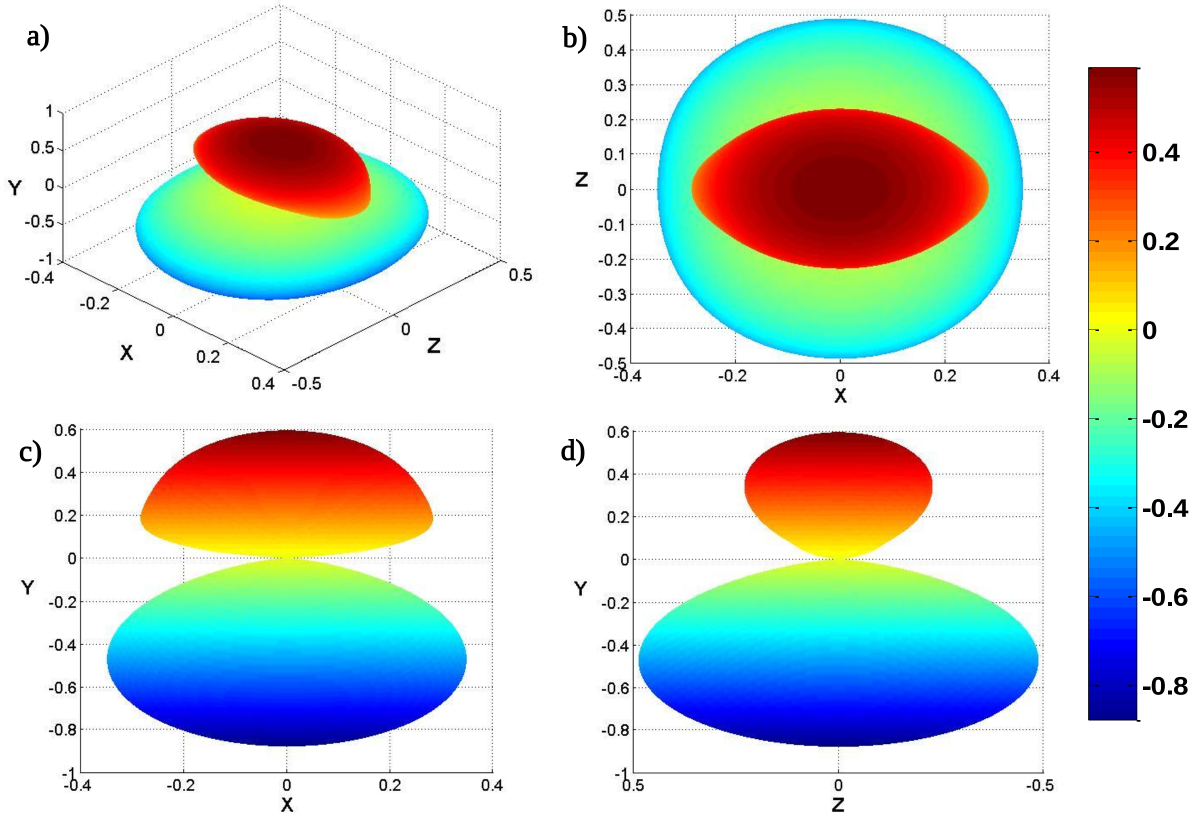

Figure 5.6 Far field spatial radiation pattern of *x*-oriented dipole. a) 3D radiation pattern; b) top view at plane XZ; c) side view at plane XY; d) side view at plane YZ.

As for perpendicular dipole (*y*-oriented) located at the waveguide surface, the far field radiation pattern was calculated by substituting $p_x = 0, p_y = 1, p_z = 0$ into Equation 5.3. Figure 5.7 shows that the emission pattern is symmetrical with all planes at dipole position that are perpendicular to the interfaces. In particular, it shows an angular characteristic so that the maximum emission is at an angle of approximately 50^0 and the minimum emission is in the *y*-direction. Unlike the parallel dipole (*x*-oriented), for a single *y*-oriented dipole this clearly indicates that collection of far field radiation with typical NA at either the top surface or the substrate is inefficient.

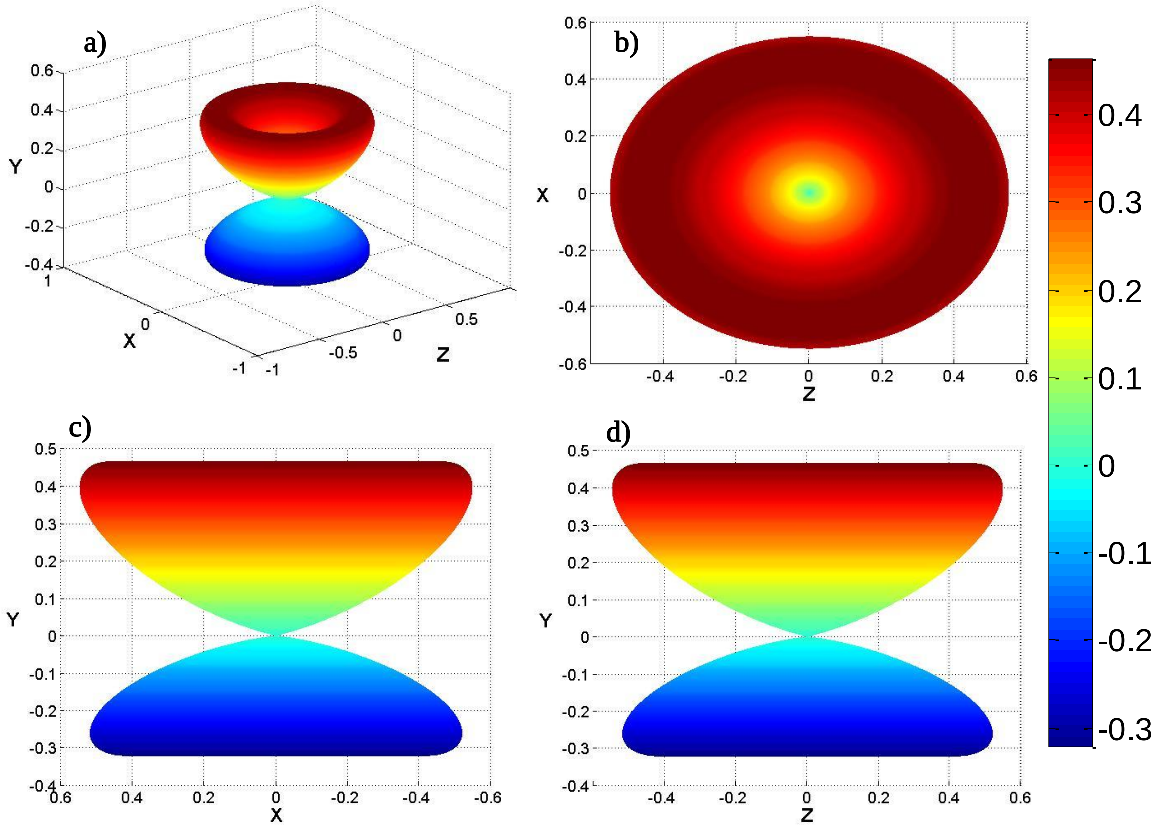

Figure 5.7 Far field spatial radiation pattern of *y*-oriented (vertical) dipole. a) 3D radiation pattern; b) top view at plane XZ; c) side view at plane XY; d) side view at plane YZ.

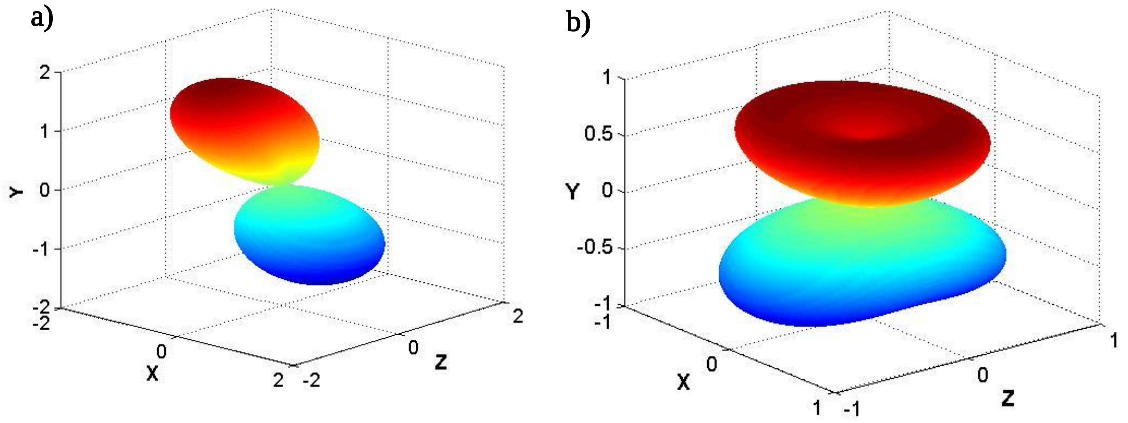

Figure 5.8 3D radiation pattern of XY linearly polarised dipole with p_x=1 and p_y=1. a) With interference term; b) without interference term.

The far field radiation pattern of a linearly polarised dipole is not simply the superposition of corresponding components contributed by *x*-oriented and *y*-oriented dipole, but also includes addition of an interference component between *x*-oriented and *y*-oriented dipole as governed by Equation 5.3 $\mathbb{D}$. In order to reveal the effect of this interference term, the far field radiation pattern of a linearly polarised dipole with $p_x = 1, p_y = 1, p_z = 0$ is shown in Figure 5.8 with (a) and without (b) taking into account of the interference term.

With interference term, radiation pattern of XY linearly polarised dipole shows strong directional behaviour, with the maximum emission in the direction $(-1,1,0)$ perpendicular to the dipole orientation $(1,1,0)$. Whereas for the case without the interference term, characteristics of both x-oriented and y-oriented dipole can be clearly seen, as the overall pattern is similar to that of the y-oriented dipole with more directional emission along the x direction for upward emission. It is dramatic to see how the interference between x and y oriented dipoles nearly suppresses all emission along the (1,1,0) direction. As far as collection is concerned, the strong directivity of far-field radiation shown for the linearly polarised dipole ($p_x = 1, p_y = 1, p_z = 0$) indicates that collection at an angle to the interface normal is more efficient than collection at the normal, from either the waveguide surface or the waveguide substrate. Unlike cases of x-oriented and y-oriented dipoles, the maximum emission only occurs along one vector direction for XY linearly polarised dipole.

Above all, as far as Raman collection is concerned, both near-field and far-field radiation patterns of oriented dipoles show apparent angular characteristics of emission directivity, which clearly indicates that the collection configuration is crucial for efficient collection.

5.5 Conclusion

In this chapter, the role a 2D slab waveguide plays on emission from a molecule has been discussed. The waveguide structure can change the spontaneous emission rate and the directional emission pattern of an emitted molecule, modelled as an oriented dipole. The spontaneous emission rate is characterised by the Purcell factor and was simulated by using the Lumerical FDTD package. The dipole emission is split into near field radiation and far field radiation. Dipoles of different orientations have been modelled. Both the proportion of power coupled into the near field waveguide guided mode(s) and its radiation pattern was calculated by using the Lumerical FDTD package. This has revealed that the majority of emission is coupled into the waveguide guided mode(s). This clearly indicates that collection from the waveguide surface is inefficient as the near field emission does not contribute to the surface collection. The near field radiation patterns of parallel (x-oriented) and perpendicular (y-oriented) dipoles show different characteristics of directivity, which provide insights into efficient collection of the near field emission. As for the far field radiation, the 3D radiation pattern was calculated analytically for parallel (x-oriented), perpendicular (y-oriented) and XY oriented dipoles. Each one of them shows altered direction of emission due to interference. The important role played by the interference between the x- and y- oriented dipole on the directionality for a XY oriented dipole has been discussed. This analysis has made clear that a proper collection configuration can potentially greatly enhance the collection efficiency due to the directivity of the emission from a molecule near a slab waveguide structure. The theoretical models developed in this chapter will be used to compare with experimental results in Chapter 6.

5.6 References

[1] J. S. Kanger and C. Otto, “Orientation effects in waveguide resonance Raman spectroscopy of monolayers,” *Appl. Spectrosc.*, vol. 57, no. 12, pp. 1487–1493, Dec. 2003.

[2] S. B. Ellahi and R. E. Hester, “Waveguide surface-enhanced resonance Raman spectroscopy of Ru(bpy)$_3$^{2}+,” *Ananlytical Chem.*, vol. 67, no. 1, pp. 108–113, 1995.

[3] S. Ellahi and R. E. Hester, “Enhanced waveguide Raman spectroscopy with thin films. Plenary lecture,” *The Analyst*, vol. 119, no. 4. pp. 491–495, 1994.

[4] J. S. Kanger, C. Otto, M. Slotboom, and J. Greve, “Waveguide Raman spectroscopy of thin polymer layers and monolayers of biomolecules using high refractive index waveguides,” *J. Phys. Chem.*, vol. 100, no. 8, pp. 3288–3292, 1996.

[5] D. Walker, H. Hellinga, S. Saavedra, and W. Reichert, “Integrated optical waveguide attenuated total reflection spectrometry and resonance Raman spectroscopy of adsorbed cytochrome c,” *J. Phys. Chem.*, vol. 97, no. Number 39, p. 10217, 1993.

[6] R. L. McCreery, *Raman Spectroscopy for Chemical Analysis*. Hoboken, NJ, USA: John Wiley & Sons, Inc., 2000.

[7] R. A. Potyrailo, S. E. Hobbs, and G. M. Hieftje, “Optical waveguide sensors in analytical chemistry: today’s instrumentation, applications and trends for future development,” *Fresenius. J. Anal. Chem.*, vol. 362, no. 4, pp. 349–373, 1998.

[8] T. C. Damen, R. C. C. Leite, and S. P. S. Porto, “Angular dependence of the raman scattering from benzene excited by the He-Ne cw laser,” *Phys. Rev. Lett.*, vol. 14, no. 1, pp. 9–11, 1965.

[9] R. R. Chance, A. Prock, and R. Silbey, “Molecular fluorescence and energy transfer near interfaces,” in *Advances in Chemical Physics*, vol. 37, I. Prigogine and S. A. Rice, Eds. Hoboken, NJ, USA: John Wiley & Sons, Inc., 1978, pp. 1–65.

[10] W. L. Barnes, “Fluorescence near interfaces: the role of photonic mode density,” *J. Mod. Opt.*, vol. 45, no. 4, pp. 661–699, 1998.

[11] E. M. Purcell, “Spontaneous emission probabliities at radio frquencies,” *Phys. Rev.*, vol. 69, pp. 674–674, 1946.

[12] E. Yablonovitch, “Inhibited spontaneous emission in solid-state physics and electronics,” *Phys. Rev. Lett.*, vol. 58, no. 20, pp. 2059–2062, May 1987.

[13] A. J. Shields, “Semiconductor quantum light sources,” *Nat. Photonics*, vol. 1, no. 4, pp. 215–223, 2007.

[14] D. Kleppner, “Inhibited spontaneous emission,” *Phys. Rev. Lett.*, vol. 47, no. 4, pp. 233–236, 1981.

[15] E. H. Hellen and D. Axelrod, “Fluorescence emission at dielectric and metal-film interfaces,” *J. Opt. Soc. Am. B*, vol. 4, no. 3, p. 337, 1987.

[16] “Mesh refinement options.” [Online] Available: https://kb.lumerical.com/en/index.html?ref_sim_obj_mesh_refinement_options.html. [Accessed: 15-Aug-2016].

[17] C. Chen, J.-Y. Li, L. Wang, D.-F. Lu, and Z.-M. Qi, “Waveguide-coupled directional Raman radiation for surface analysis,” *Phys. Chem. Chem. Phys.*, vol. 17, no. 33, pp. 21278–21287, 2015.

[18] L. Novotny, *Principles of Nano-Optics*, 2nd ed. New York, USA: Cambridge University Press, 2006.

CHAPTER 6 WERS II: waveguide front edge collection

6.1 Introduction

In Chapter 4, waveguide Raman spectroscopy for sensing a bulk liquid on surface collection (see Figure 4.6) has been successfully demonstrated with collection from above the surface in the far field, using an optimum waveguide design for maximum excitation. The power budget analysis given highlights that the collection efficiency from above the waveguide surface is very low at ~ 5.3%. This leads to a sensitivity that renders it not easy in practice to sense a small quantity of samples such as a thin film or monolayer, without using other enhancement mechanisms such as resonance Raman scattering. Meanwhile, high sensitivity is highly desirable in many biological and chemical applications. So the low sensitivity of WERS with surface collection becomes the limitation on expanding the use of waveguide enhanced Raman spectroscopy. In Chapter 5, the emission pattern of an excited molecule located at the waveguide surface was discussed. The total emission of the molecule was broken down into near-field radiation and far-field radiation. The former radiation component accounts for what is coupled into the waveguide guided mode(s) while the latter is what is emitted into free space. Simulation results show that the majority of radiation is coupled into the near-field, which is not accessible to the surface collection. This explains the main reason for the low efficiency of the surface collection. In addition, the radiation patterns of both near-field and far-field emission clearly show characteristics of directivity, which in many cases does not favour surface collection. All of those analyses in Chapter 5 indicate that collection direction and configuration is crucial for efficient Raman collection of WERS. In this chapter, orders of 1-2 enhancement will be shown to be achievable without introducing any complex nanostructures or noble metals, simply by collecting the Raman scattering signals from the slab waveguide front edge, which not only significantly increases the sensitivity for WERS but also clarifies the understanding of the field and has appeal for a broader community such as in the field of optical antennas.

In the past, nearly all work demonstrated in WERS utilised ‘the default’ surface collection [1]–[19] with few relying on substrate collection [20], [21]. Both surface and substrate collection configuration were oriented normal to the waveguide layer interfaces, and the specific reason of using one over another was not discussed in those studies. However, as it was made clear in Chapter 5, the intrinsic collection efficiency from these two configurations can be different. Thus, here they are treated as separate collection configurations. Only recently, collection from the waveguide front edge has been demonstrated for WERS [22].

The idea of collecting Raman signals from the end of planar waveguide has been utilised to observe the forward and backward Raman scattering in developing the silicon Raman amplifier for example

[23], [24]. The Raman scattering efficiency (excitation) and effective collection efficiency (collection) can be calculated based on the measured power out of the waveguide facet. From this engineering approach, the physical picture of how emitted Raman light is collected by the waveguide is omitted. In these cases, the Raman medium is in the waveguide core whereas in our case the Raman active sensing medium is located in the waveguide cladding. Recently, the front end collection of bulk IPA Raman from monomode silicon-nitride (SiN_4) strip waveguides was experimentally demonstrated [22]. The semi-classical approach developed by [25] was adopted to theoretically predict how much light will be collected and guided to the waveguide front edge by knowing the pump light power, analyte and waveguide parameters. However, the emission pattern of the emitted molecule as a dipole near the waveguide structure was not revealed. Moreover, there was no direct comparison between the waveguide end collection and surface collection. In this chapter, a direct comparison between the waveguide edge and above-surface collection will be made both experimentally and theoretically. The physical picture of an emitted molecule near the waveguide structure developed in Chapter 5 will be utilised to analyse the experimental results.

In the following, the experimental results on Raman power of bulk liquid toluene and thin polystyrene film emitted from the waveguide front edge will be described first, and compared to that from the surface. Then, the origins of this difference will be discussed. Finally, bulk liquid toluene will be taken as an example to compare the theoretical and experimental values.

6.2 Experiment: waveguide front edge collection of Raman spectra

In this section, the experiment set up utilised for the waveguide front edge collection of Raman spectra will be described, clearly showing the difference between the surface and the front edge collection. Then, the Raman spectra obtained from these two configurations will be shown and discussed.

6.2.1 Experimental apparatus and procedures

As shown in Figure 6.1, waveguide front edge collection was simply achieved by moving the collection system from imaging the waveguide surface to imaging the front edge. In the former case, emission from a ~1mm diameter area on the surface is collected; whereas in the latter case, emission from the waveguide front edge, that including both the waveguide core and a large part of the substrate region (1 mm thick), is collected.

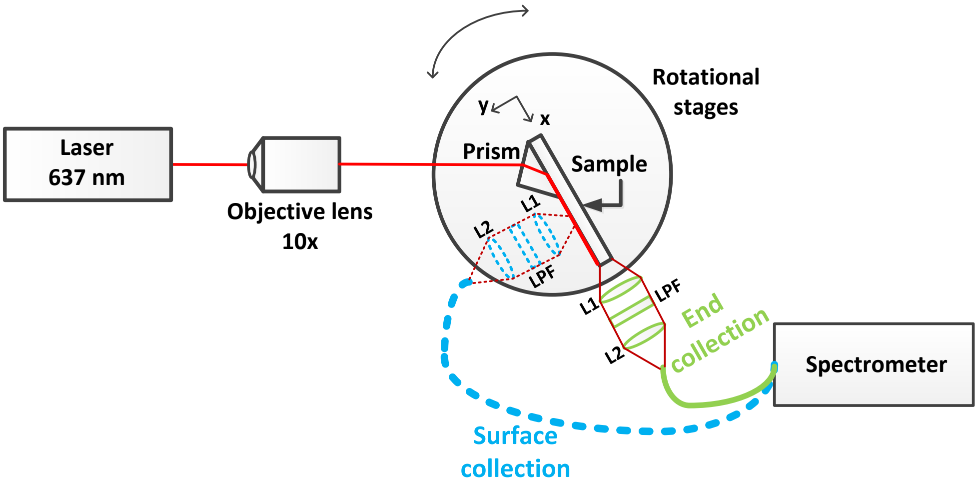

Figure 6.1 Illustration of front edge collection and surface collection in experimental apparatus. Broken blue lines: waveguide surface collection configuration; Solid green lines: waveguide front edge collection configuration. L1 and L2 are convex lenses. LPF: low pass filter. The relative dimensions have been adjusted for clarity.

TM polarisation was utilised for the measurement due to the fact that the laser with the experimental set-up only supported this polarisation. The waveguide sample utilised was approximately 110 nm thick, optimised for maximum TM excitation with bulk sample index around 1.49. Both bulk liquid and solid films were measured in this investigation. Specifically, toluene was chosen as the liquid sample and a thin polystyrene film was chosen as the solid, as in the previous cases of waveguide surface collection. In the case of toluene, a small drop (<0.15 ml) of toluene was placed on the waveguide surface and a coverslip located on top to reduce evaporation. The penetration depth of the evanescent field into the toluene was approximately 120 nm and the resulting toluene layer filled this region, in effect resulting in a bulk analyte above the waveguide surface. The polystyrene film was fabricated by spin-coating following the procedure given in [26]. Polystyrene pellets (molecular weight 280,000) were dissolved in anhydrous toluene (99.8%) at 4% (w/v). The sample was uniformly covered with the solution. Then the film was spin coated at 3000 rotation-per-minute

(RPM) for 60 s. The film thickness was measured to be ~340 nm by using KLA Tencor P-16 Stylus Profiler.

The collection system was focused onto the waveguide surface and the waveguide front edge in turn, at approximately 2.5 cm and 3 cm away from the prism coupling position, respectively. The integration times were 60 s and 5 s for waveguide surface and front edge collection, respectively. The shorter integration time was necessary for the front edge measurement to prevent saturation of the spectrometer.

6.2.2 Experimental Results

The recorded spectra were baseline subtracted by method described in Section 4.5, and then transformed to units of power spectral density using the corresponding integration time and spectrometer resolution parameter (0.25 nm/pixel). The resultant spectra are shown in Figure 6.2, giving the toluene Raman emission bands from 700 cm^{-1} to 3200 cm^{-1}, covering most of the biologically-relevant Raman window (500 cm^{-1} – 3500 cm^{-1}) [27]. The region below 700 cm^{-1} is dominated by background emission from the fused silica substrate and the coupling prism, masking the toluene Raman feature at around 622 cm^{-1}. In applications where spectral information below 700 cm^{-1} is needed, another material such as CaF_2 could be used as the substrate as it exhibits no Raman features above 322 cm^{-1} and the use of grating coupler would eliminate the unwanted emission from the prism at around 600 cm^{-1}. Figure 6.2 clearly shows that the power in the Raman emission lines collected from the waveguide front edge is approximately 40 times higher than that from the waveguide surface. The phenyl ring breathing mode at around 792 cm^{-1} can be easily distinguished using front edge collection but is completely submerged under the background using surface collection, emphasising the improved signal from this approach.

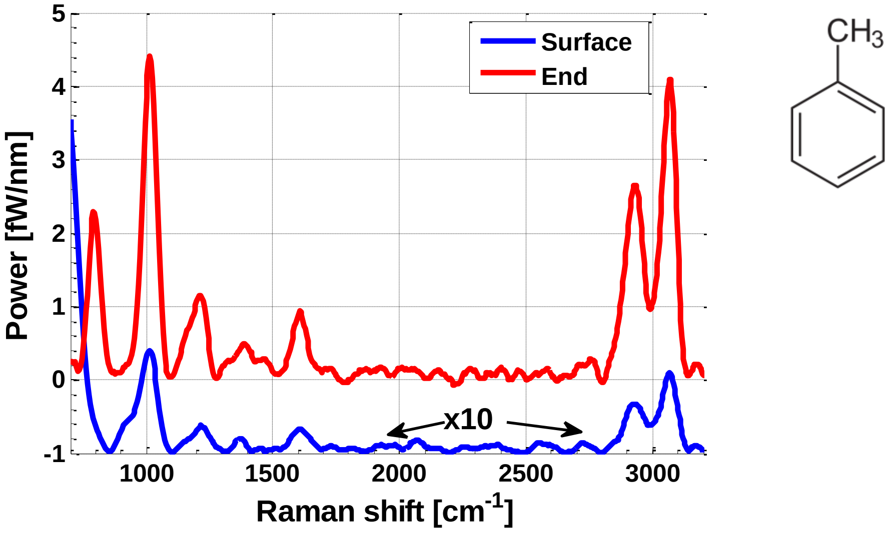

Figure 6.2 Raman spectra of toluene from the waveguide front edge (end) and surface. TM polarised excitation light.

Figure 6.3 shows the waveguide surface and front edge collection comparison of Raman spectra obtained from the polystyrene film. The spectra cover the spectral region from 500 cm^{-1} up to 3200 cm^{-1}, in which all Raman peaks of polystyrene are shown except for the one at 600 cm^{-1} that is overlaid by the background Raman emission of the coupling prism. Spectrum recorded from the waveguide front edge shows a much better signal-to-noise performance, e.g. in between 1300 cm^{-1} to 1600 cm^{-1} despite in a much shorter integration time (5 s vs. 60 s). Comparing with the reference spectrum obtained from Renishaw confocal Raman spectroscopy, the relative difference of the power within each feature is the same for the end collection while there are some noticeable changes for the surface collection, e.g. comparing features at 1000 cm^{-1} and 1200 cm^{-1}. The average enhancement of the Raman power collected from the front edge collection was calculated to be a factor of approximately 140 over to that from the surface collection.

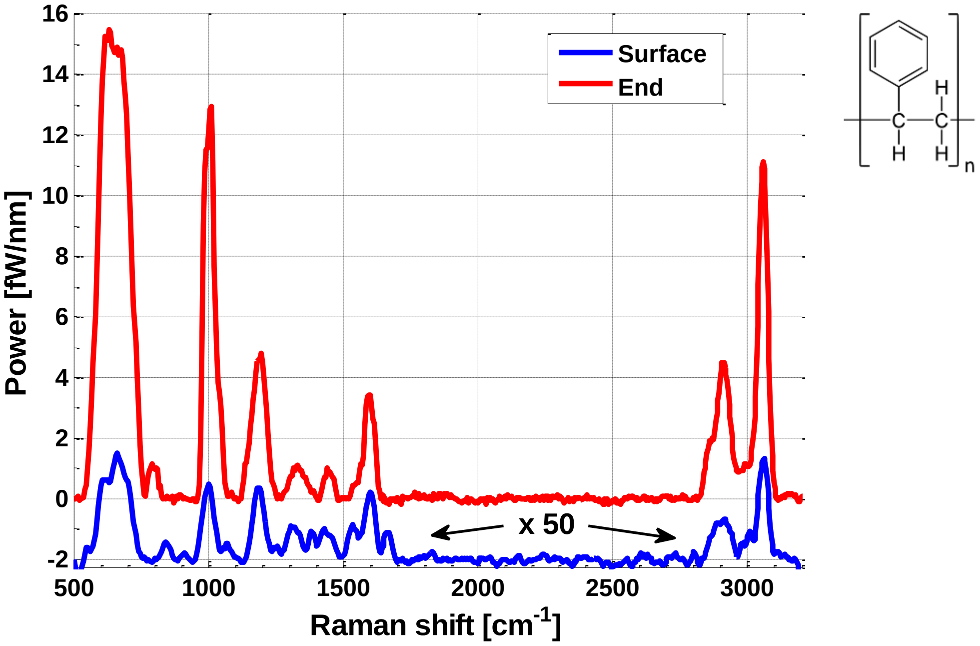

Figure 6.3 Raman spectra of polystyrene from the waveguide surface and front edge (end). TM polarised excitation light.

To summarise, collection at the waveguide front edge shows a significant enhancement over that obtained from the waveguide surface. There is an enhancement of 40 for bulk liquid toluene (index 1.49) and average enhancement of 140 for solid polystyrene (index 1.59). The large enhancement with the front edge collection also means that a much shorter integration time is needed and at the same time a much cleaned spectrum is obtained. Noting that this waveguide design is only optimised with consideration of the excitation. The origin of the enhancement observed from the experiment will be described in the next section.

6.3 Enhancement for waveguide front edge collection

6.3.1 Enhancement origins

First, it is important to clarify the difference between the surface collection and the front edge collection. Figure 6.1 clearly shows the difference between the two - the collection system (image system) was focussed onto a 1mm diameter circle at the surface and end facet, respectively. The observation was that there was more Raman emission from the collection region at the end facet, including both core and substrate region, than that from the surface. It was predicted in Chapter 5 that a large part of the Raman emission at the surface couples into the waveguide guided mode(s), so that by measuring at the waveguide front edge all excited molecules along the propagation path contribute, whereas surface collection only receives contributions from molecules in the 1mm diameter collection circle. This explanation is essentially what Dhakal *et al.* relied on to theoretically predict their measured Raman power from the waveguide front edge [22]. However, several experimental observations have indicated that this physical picture is incomplete. For example, it has been found that a significant amount of emission comes out of the waveguide ‘substrate’ region in addition to that from the core region (see Appendix B). Moreover, emission is directional despite it being assumed that Raman emission is isotropic as in Chapter 4. Therefore, the effect of the change in collection from the surface to the front edge will also be influenced by the directional nature of the Raman emission. These two hypotheses will be verified in the next section. While there is little discussion of the above phenomena in the waveguide Raman community, these emission characteristics have been thoroughly well studied by the fluorescence community [28], [29].

As has been discussed in Chapter 5, the existence of a waveguide in the vicinity of an excited molecule modifies its emission in the spontaneous emission rate and radiation pattern. In the current context, the former is the same for both collection configurations, whereas the latter that essentially governs the spatial distribution of the emitted power can lead to different observed power at different collection ‘directions’, as will be described for different collection configurations in the next sections.

6.3.2 Emission routes

The substrate (SiO_2), waveguide (Ta_2O_5), toluene layer and coverslip form a composite waveguide structure, bounded by the upper air-glass and lower air-silica interfaces, as shown in Figure 6.4. The near-field and far-field radiation mentioned below referred to the case of a bulk toluene layer, waveguide, and the substrate. For far-field emission, emitted light travelling within the critical angle at the corresponding interfaces will be trapped by the composite structure and will propagate to its periphery (right rays). In addition, non-radiative emission coupled into the thin-film waveguide mode will propagate to the waveguide end. Thus Raman emission at the Ta_2O_5 surface can follow three alternative routes: 1) coupling into the waveguide guided mode(s), 2) trapping by the composite structure, or 3) escaping the composite structure into the half-space above or below (yellow rays).

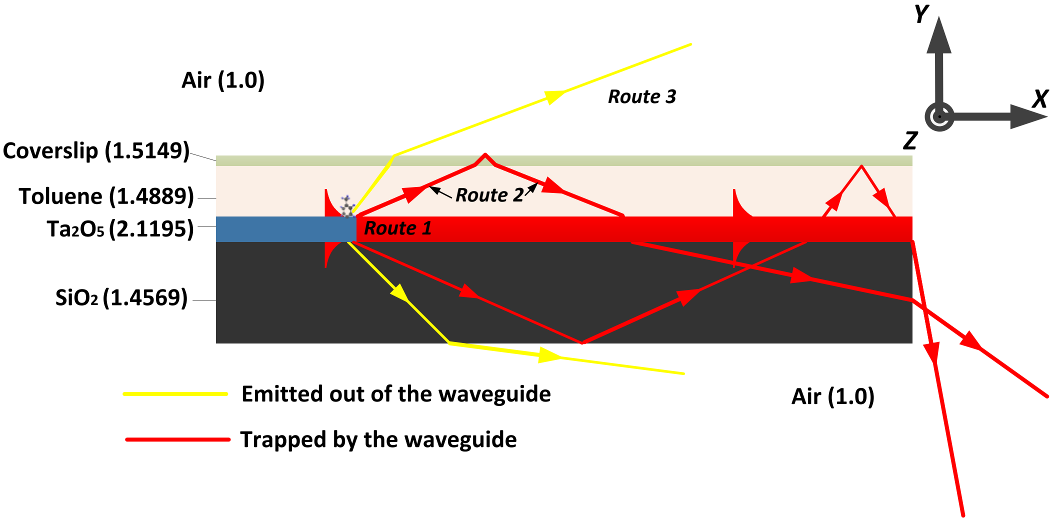

Figure 6.4 Illustration of Raman emission based upon whether they are trapped by the structure.

Raman collection from the waveguide surface results from only route 3, while Raman collection from the end of the structure receives contributions from routes 1 and 2. The relative power collected from the waveguide surface and from the composite waveguide front edge by the collection fiber will be theoretically estimated next by (i) determining the proportion of total Raman emitted light for a single emitter (excited molecule) into each of the three routes, followed by (ii) integration of the power incident on the collection fiber end within its NA from a uniform distribution of Raman emitters on the Ta_2O_5 surface, filling the entire evanescent field. For all the following analysis, the emission of an excited molecule can be determined from the corresponding induced (Raman) dipole. For toluene liquid, the orientation of the emitted dipoles are assumed to be the same as the polarisation of the excitation light. For liquid benzene, which possesses nearly the same Raman characteristics as the toluene, Porto *et al.* have experimentally verified this for the 994 cm^{-1} vibrational mode [30]. So, for toluene molecule excited in TE polarisation, the orientation of the emitted dipole is parallel to the interface. Note that this relationship between the emitted dipole orientation and excitation light polarisation is not always equal for all materials, as the reason will be explained in Chapter 8.

6.3.3 Route 1: near-field emission into waveguide guided mode(s)

The case to be modelled for all the following analyses is an emitting molecule located at the surface of a slab waveguide with the structure: bulk toluene, waveguide (110 nm Ta_2O_5), and fused silica substrate. The molecule is evanescently excited by the fundamental TM mode of the waveguide. The emission wavelength of the molecule is 685 nm, corresponding to ~1000 cm^{-1} for an excitation wavelength of 637 nm. The excited molecule can be modelled as an oriented dipole, and it is assumed to have the same orientation as the excitation polarisation.

The proportion of emitted power coupled into the waveguide guided mode and its angular emission pattern will be discussed in this section. It is modelled and numerically calculated using a commercial FDTD package (Lumerical Solutions, Inc.) as explained in Chapter 5.

One fundamental but often overlooked fact is that the evanescent fields of TM modes are 'elliptically' polarised, which originates from the π/2 phase difference between the electric field components that are perpendicular and parallel to the interfaces [31]. The implication of this for near field coupling has only recently been discussed in [32], which shows unidirectional excitation of guided modes by the resultant elliptically polarised dipole emitters. This has not yet been discussed or demonstrated to date in the field of WERS. This effect and its contribution to the waveguide front edge collection will be described below.

Figure 6.5 shows the near-field coupled power distribution of emission from the elliptically polarised dipole at the waveguide structure. The relative strength of dipole moment in each direction ($p_x = -j, p_y = 2.74, p_z = 0$) is equal to the relative strength of the electric field (E) of the excitation in each direction, with the latter determined by using Equation 6.1:

$$\frac{|p_y|}{|p_x|} = \frac{|E_y|}{|E_x|} = \frac{n_{eff}}{\sqrt{n^2{}_{eff} - n^2{}_t}} \qquad \text{Equation 6.1}$$

where n_{eff} is the effective index of the waveguide guided mode; and n_{eff} can be determined by the waveguide design tool explained in Chapter 3. Therefore, under the TM excitation, the dipole amplitudes (dipole moment strength) in x and y direction were calculated by using the above method after setting $|p_x| = 1$.

The introduction of imaginary number j indicates that there is a phase lag between the x and y components. Compared to p_x, p_y is the dominant component, therefore the power distribution is similar to that from a y-oriented dipole (Figure 5.3). Despite this similarity, more power propagates along the forward direction of the x-axis. In order to calculate the proportion of power travelling toward the front and back edge of the waveguide, a 2D power monitor, called 'Frequency-domain field and power', was put at each side of the waveguide to form an enclosed structure, capturing all near-field emission. The distance between each monitor to the dipole is 2.5 µm. The power monitors show that about 23.0% and 13.4% of the total emitted power flow out of the front (+*x*) and back (-*x*) end facet of the structure shown in Figure 6.5, with a total of 62.8% of light coupling into the waveguide guided mode. Due to this asymmetrical coupling, the dominant front end has 71.6% more power propagating out of it than that at the opposite back end.

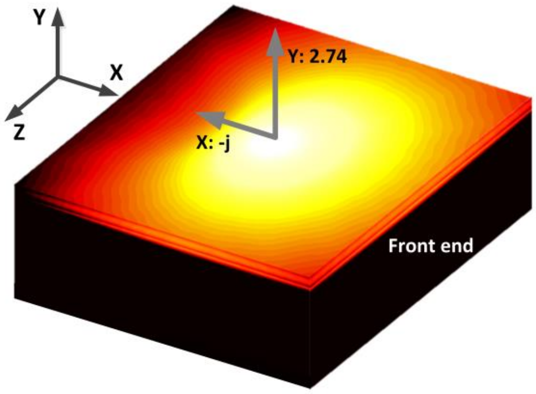

Figure 6.5 Power diagram of near-field coupling from elliptically polarised dipole located at the waveguide surface. X and Y indicate the vectorized dipole orientation with value indicating the dipole moment strength. j implies the π/2 phase difference between the two components.

To summarise, for liquid toluene molecules excited by the fundamental TM mode of a 110 nm Ta_2O_5 waveguide, 62.8% of the total emitted power couples into the waveguide guided mode(s) – the non-radiative emission, which is not captured by the collection from the waveguide surface. This confirms that collection from the waveguide surface is very inefficient in this case. Moreover, the asymmetrical coupling resulting from the elliptically polarised Raman dipole leads to a dominant power flow in the positive x direction, due to the near-field interference of the two dipole components. The two dipole components add up destructively in the negative x direction, whereas they reinforce each other in the positive x direction [32]. This adds further advantage to collect on the waveguide front edge. In the next section, the focus will be on accounting for the remaining 37.2% of emitted light into the far field, which gives insights into collection from above the waveguide surface as well as from its front edge.

6.3.4 Routes 2 and 3: far-field emission into the substrate and cladding

The far-field dipole emission of the modelled case was calculated by using Equation 5.3. Again, the relative dipole moment strengths are $p_x = -j, p_y = 2.74, p_z = 0$. The spatial radiation pattern of the far-field was plotted in Figure 6.6. From the 3D radiation pattern shown in Figure 6.6a, it looks very similar to that from the XY polarised dipole ($p_x = 1, p_y = 1, p_z = 0$) without the interference term (Figure 5.8 b). However, the far field emission pattern of this elliptically polarised dipole shows asymmetrical upward emission ($+y$). On the other hand, the downward emission tends to be strong in the yz-plane, where the maximum is at an angle to the interface normal.

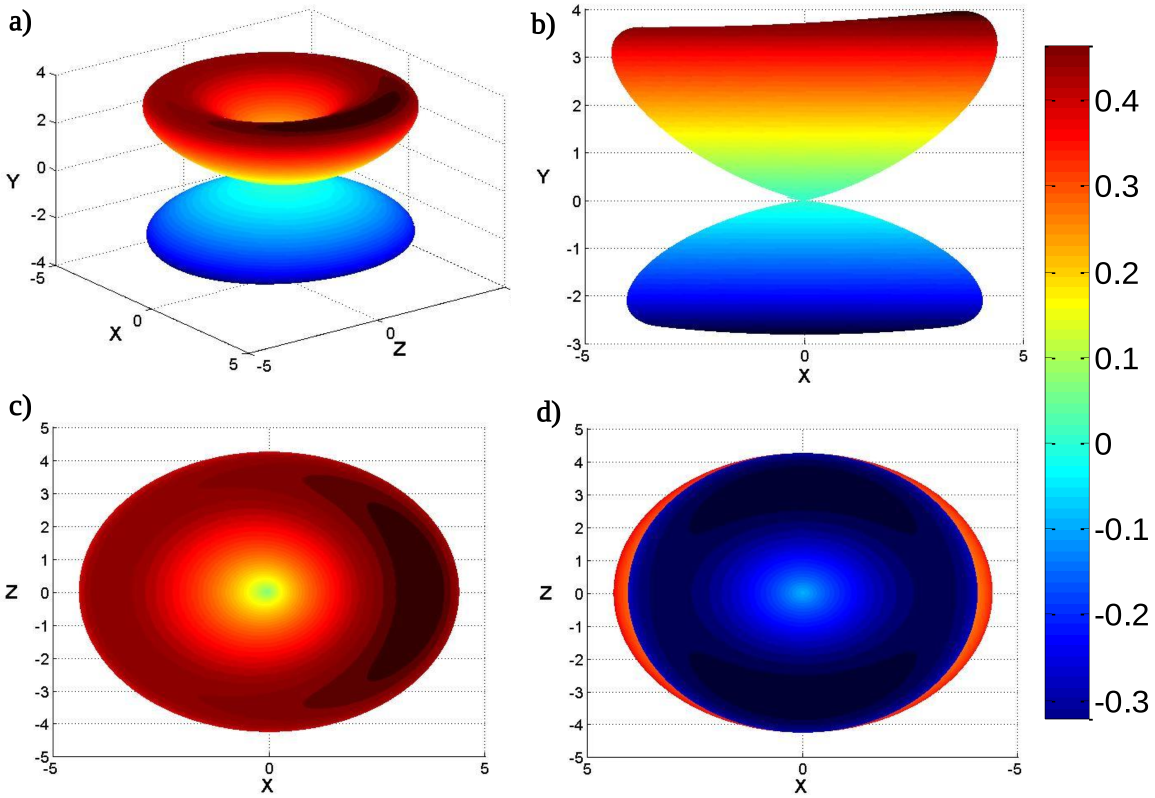

Figure 6.6 Far field spatial radiation pattern of an elliptically polarised dipole ($p_x = -j, p_y = 2.74, p_z = 0$). a) 3D radiation pattern; b) side view at plane XY; c) top view at plane XZ; d) bottom view at plane XZ.

Having determined the far-field radiation pattern, the next step is to determine quantitatively the proportion of light that is trapped by the composite waveguide structure and carried to the waveguide edge, and then to determine the proportion of power that is emitted into the upper half-space above the composite structure.

Figure 6.7 shows the angular diagram of far-field radiation for an elliptically polarised dipole ($p_x = -j$; $p_y = 2.74$) at xy plane. Emission at an angle above the critical angle at the toluene/air and substrate/air interfaces will be trapped by the waveguide, which are indicated by the red region in Figure 6.7; whereas yellow regions indicate power that is emitted out of the waveguide structure. The proportion of power trapped by the composite waveguide to the total far-field emission is calculated firstly by integrating the emission power over angles of the red region, then divided by the integration over whole angle range. 60.5% of the total far field emission (at xy plane) is trapped by the waveguide while 23% of the total far field emission is emitted upwards without trapping. To put this into perspective, the collection from the waveguide surface only receives contributions from this 23% while collection at the waveguide front edge receives contributions from the total available 30.3% (one side), which shows the advantage of edge collection at the first place. Note that this is for the case of a single dipole only. The number of dipoles contributed to each collection configuration will be discussed in a later section. One interesting point is that the observed asymmetrical emission in the far-field has negligible impact as there is only 0.02% difference between the left upwards emission and right upwards emission power for this particular waveguide design.

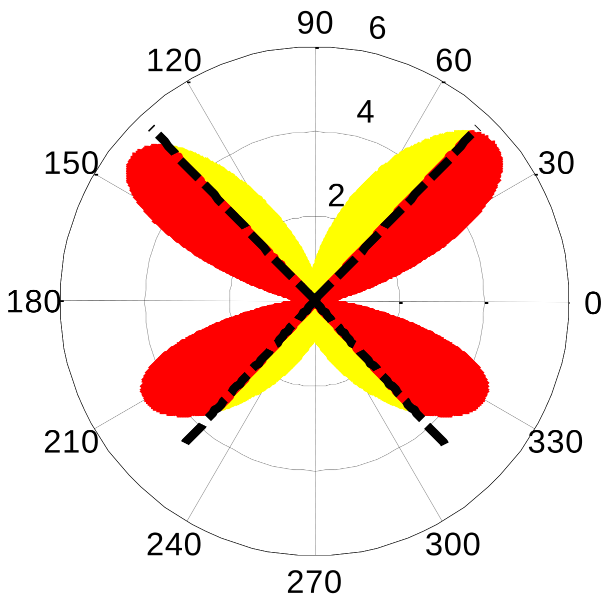

Figure 6.7 Angular diagram of far field radiation of an elliptically polarised dipole (P_x: -1j; P_y: 2.74) at *xy* plane. Red region: trapped by the waveguide; yellow region: emitted out of the waveguide

6.3.5 Summary

For an emitted Raman dipole, there are two types of emission: near field and far field. The former emission couples into the waveguide guided modes, while the latter emission can either be trapped by the composite waveguide, or emitted out upwards and downwards. This physical picture is crucial for understanding and theoretically determining the difference between the top surface collection and the waveguide end collection.

Table 6.1 Proportion of Raman dipole power emitting into each route of each emission type

Emission type	Emission routes		Ratio to the total emitted power	
			Elliptically polarised dipole (Px=-1j; Py=2.74)	
Near field	Coupled into Ta_2O_5 waveguide		Back: 20.8%	Forward: 44.3%
Far field	Trapped by the substrate/cover		Back: 10.6%	Forward: 10.6%
	Emitted out	Upward (+y)	8.0%	
		Downward (-y)	5.7%	

Based on the analyses above, Table 6.1 summarises the calculated proportion of power emitted into each route of near field and far field emission. The proportion of power coupled into each route for both near-field and far-field radiation, was calculated from the 2D emission pattern of the *xy* plane, which takes an approximation that the 3D emission pattern can be obtained by rotating this *xy* plane continuously 180^0. The proportion coupled into the thin-film Ta_2O_5 waveguide was calculated by using the Lumerical FDTD, as described above, by integrating around the waveguide periphery. The proportions of power emitted into the composite structure and into free-space were calculated using the far field distribution governed by Equation 5.3 and the air-glass and air-silica critical angles.

65.1% of the total emitted power is collected in the Ta_2O_5 waveguide. In particular, 44.3% of the total emitted power is coupled into the forward direction, which is more than doubled to its counterpart – backward direction. In terms of far-field radiation, emitted power is nearly evenly distributed between the half-plane in the forward and backward direction. 61% of the far field emission (21.2% of the total) is trapped by the composite waveguide, while the rest is either emitted out upward or downward, carrying 8% and 5.7% of the total emission power, respectively.

Surface collection (normal to the interface) only receives contributions from the 8% upward out-of-the-waveguide emission, whereas front edge collection (normal to the end facet) receives contributions from a total 54.9% of the total emitted power from both the near-field coupled emission and the far-field trapped emission, for which the former is more than 4 times of the other. As a result, a factor of 6.9 greater power is collected in the composite waveguide (including the Ta_2O_5 core) compared with emission through the top cover-slip. This is referred to as the *radiative enhancement factor*, which combines alteration in the angular emission pattern and the total radiated power of the dipole due to the dielectric structure (including evanescent tunnelling). To conclude, the proportion of power emitted by one Raman dipole coupled into each route has been calculated. In the next section, the power of the 1,002 cm^{-1} emission line after going through these routes collected by the fiber and ultimately the power detected in the spectrometer will be theoretically determined for the case above.

6.4 Power coupled into the collection fiber

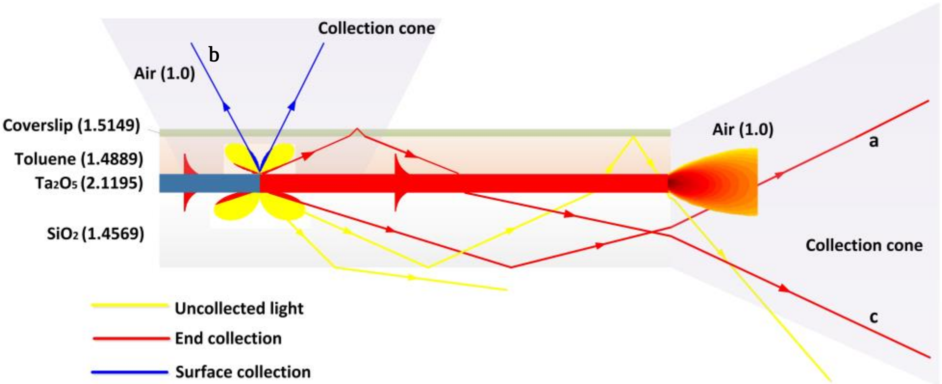

Figure 6.8 Composite waveguide structure and ray diagrams indicating paths for dipole emission. The dipole emission shown is for an *y*-orientated dipole. a) Downward emitted light trapped by the structure falls into the end-fiber collection cone; b) upward emitted light escapes the composite structure and falls into the surface fiber collection cone; c) upward emitted light trapped by the structure falls into the end fiber collection cone.

In this section, the total power collected by the fiber at the waveguide surface or front edge is determined by integration over the spatial and numerical aperture of the collection system, for a uniform distribution of Raman emitters on the Ta_2O_5 surface. The collection cone of a multimode fiber with 1mm diameter and NA of 0.48 is imaged onto the structure. For surface collection, emission from only those molecules within the imaged area and fiber NA will be collected as shown in Figure 6.8; this portion of power within the NA is shown in blue shaded region in Figure 6.9, and for the configuration here, corresponds to 3.6% collection efficiency (wrt total dipole emission).

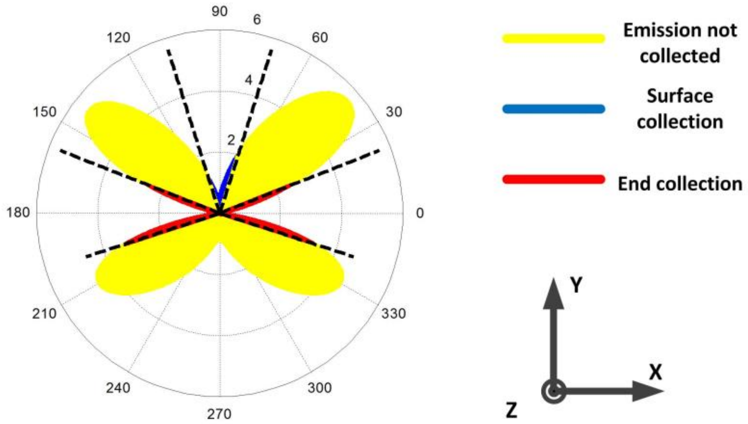

Figure 6.9 Far field radiation pattern of emitted dipole under collection.

For edge collection, the red regions in Figure 6.9 represent the angles over which light collected by the substrate and cover emerges from the end of the composite waveguide and falls within the collection system NA. By integrating the radiation power over its region angles, the proportion of far-field emission power contributed to the waveguide front edge collection (right half) was calculated. As for the near-field radiation, it was assumed that the waveguide had no propagation loss therefore all power coupled into the waveguide guided mode(s) carried to the waveguide edge. The collection efficiency of power emitted out of the waveguide front edge by the collection system was calculated by using Lumerical. As a result, the near-field contribution to the waveguide front edge collection was calculated. The total collection efficiency at the waveguide front edge for an emitted dipole located at the waveguide surface is 25.9% comprising 3.7% far field contribution and 22.2% near field contribution. Thus, the radiative enhancement factor is 7.2 for a single emitted dipole under the present 2D analysis.

For front edge collection, in addition, ‘all’ excited molecules within a surface area defined by the fiber NA will contribute, though their contributions will vary depending on their distance from the waveguide edge, as illustrated in Figure 6.9. Thus, edge-collection potentially provides a further enhancement factor due to Raman collection over a larger surface area of the waveguide than the 1mm diameter imaged spot used for surface collection; this is referred to as the *area enhancement factor*. Assuming the waveguide propagation loss is 3 dB/cm, integrating the emitted power over the full depth of the waveguide evanescent field and the full length of the relevant waveguide excited region yields a predicted area enhancement of a factor of ~7.7, resulting in a total theoretical enhancement factor of 55.4. The detailed calculation is given in Appendix C.

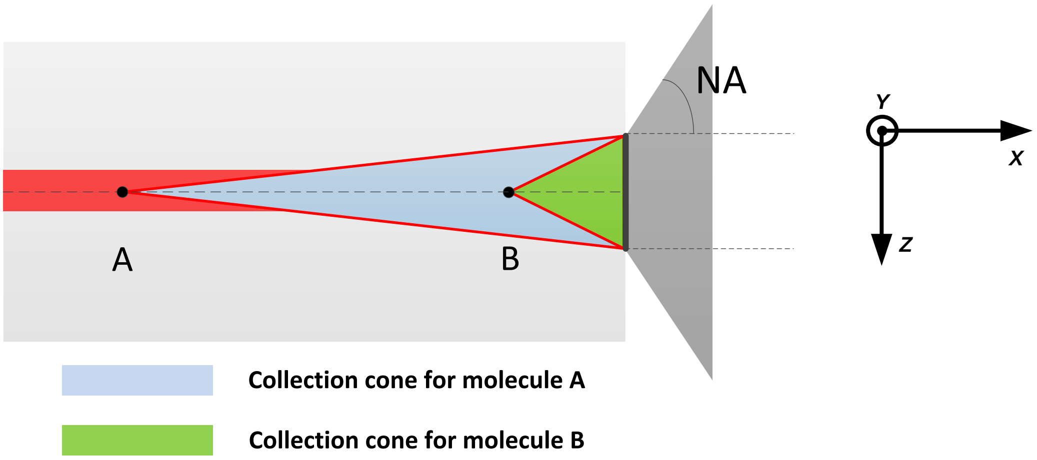

Figure 6.10 Emitted molecule at different positions contribute differently to the front edge collection.

The discrepancy between this and the experimentally-measured enhancement factor of ~40 can originate from the following factors. Firstly, there are a number of assumptions made in achieving the final result. For example, for integrating contributions from different positions at the propagation path, it is assumed that for any excited molecule along *z*-direction at a fixed position *x*, their collection cone is the same as the one at the center of *z*-direction, as shown in Figure 6.9, which may slightly over-estimate fiber collection. Secondly, for molecules at a distance away from the surface, near-field coupling efficiency is assumed to be proportional to exponentially decaying evanescent field intensity, which may over-estimate the result. Apart from these, the waveguide propagation loss is assumed to be 3 dB/cm based upon the measurement (3-4 dB/cm) with air as the top cladding, as that replacing air with toluene of higher refractive index can reduce the waveguide propagation loss. It is believed to be a reasonable assumption but the variation between the real value and the assumed one cause the error, which might add to the final discrepancy. Nevertheless, a good agreement between the theory and the experiment has been obtained.

6.5 Conclusion

Overall, it has been found that waveguide front edge measurement of Raman leads to 1-2 orders of enhancement compared to that from the waveguide surface. This is significant as it can result in much better sensitivity, which is required for a wide range of applications. The mechanisms of this enhancement for an emitted toluene molecule near the waveguide have been given as an example by 1) describing the total emission as a combination of near-field and far-field emission; 2) showing the emission pattern of each type of emission; 3) dividing the total emission into different routes that leads to either waveguide surface (substrate) or front edge collection; and 4) determining the theoretical maximum collection efficiency of each collection configuration (wrt total emission) by summing corresponding contributions from each route. For a single emitter, without and with consideration of the NA of the collection optics, they show radiative enhancement factors of 6.9 and 7.2, respectively. In addition, collection from the waveguide front edge receives contributions from all emitted molecules along the propagation region since their emissions are trapped and guided to the waveguide edge, which results in an area enhancement factor of 7.7 considering the NA of the collection optics. In total, the theory predicts a total enhancement factor of 55.4 giving good agreement with the experimentally measured value of ~40. The discrepancy between the two has also been discussed.

The analyses given in this chapter target solely on one specific waveguide design that is optimised for the waveguide excitation. The response of emission rate and directivity to different waveguide designs need to be found out in order to determine the maximum collection efficiency, hence optimised design for considering both the excitation and collection.

6.6 References

[1] A. Pope, A. Schulte, Y. Guo, L. K. Ono, B. R. Cuenya, C. Lopez, K. Richardson, K. Kitanovski, and T. Winningham, “Chalcogenide waveguide structures as substrates and guiding layers for evanescent wave Raman spectroscopy of bacteriorhodopsin,” *Vib. Spectrosc.*, vol. 42, no. 2, pp. 249–253, 2006.

[2] B. M. Beam, A. Simmonds, P. A. Veneman, E. Ratcliff, S. B. Mendes, S. S. Saavedra, and R. Armstrong, “Waveguide-based chemical and spectroelectrochemical sensor platforms,” in *ECS Transactions*, 2009, vol. 19, no. 6, pp. 109–117.

[3] S. O. Konorov, D. A. Akimov, A. N. Naumov, A. B. Fedotov, R. B. Miles, J. W. Haus, and A. M. Zheltikov, “Bragg resonance-enhanced coherent anti-Stokes Raman scattering in a planar photonic band-gap waveguide,” *J. Raman Spectrosc.*, vol. 33, no. 11–12, pp. 955–961, 2002.

[4] J. S. Kanger and C. Otto, “Orientation Effects in Waveguide Resonance Raman Spectroscopy of Monolayers,” *Appl. Spectrosc.*, vol. 57, no. 12, pp. 1487–1493, Dec. 2003.

[5] J. Mugnier, C. Urlacher, J. C. Plenet, and B. Champagnon, “Waveguide Raman microspectroscopy used for local investigation of very thin films,” *J. Raman Spectrosc.*, vol. 28, no. 12, pp. 989–993, 1997.

[6] T. E. Plowman, S. S. Saavedra, and W. M. Reichert, “Planar integrated optical methods for examining thin films and their surface adlayers,” *Biomaterials*, vol. 19, no. 4–5, pp. 341–355, Mar. 1998.

[7] J. S. Kanger, C. Otto, M. Slotboom, and J. Greve, “Waveguide Raman spectroscopy of thin polymer layers and monolayers of biomolecules using high refractive index waveguides,” *J. Phys. Chem.*, vol. 100, no. 8, pp. 3288–3292, 1996.

[8] Y. Levy, C. Imbert, J. Cipriani, S. Racine, and R. Dupeyrat, “Raman scattering of thin films as a waveguide,” *Opt. Commun.*, vol. 11, no. 1, pp. 66–69, 1974.

[9] J. F. Rabolt, R. Santo, and J. D. Swalen, “Raman spectroscopy of thin polymer films using integrated optical techniques.,” *Appl. Spectrosc.*, vol. 33, no. 6, pp. 549–551, 1979.

[10] J. F. Rabolt, R. Santo, and J. D. Swalen, “Raman measurements on thin polymer films and organic monolayers.,” *Appl. Spectrosc.*, vol. 34, no. 5, pp. 517–521, 1980.

[11] J. F. Rabolt, N. E. Schlotter, and J. D. Swalen, “Spectroscopic studies of thin film polymer laminates using Raman spectroscopy and integrated optics,” *J. Phys. Chem.*, vol. 85, no. 26, pp. 4141–4144, Dec. 1981.

[12] I. Chabay, “Optical Waveguides,” *Anal. Chem.*, vol. 54, no. 9, p. 1071A–1080A, 1982.

[13] J. F. Rabolt, R. Santo, N. E. Schlotter, and J. D. Swalen, “Integrated optics and Raman scattering: molecular orientation in thin polymer films and Langmuir-Blodgett monolayers,” *IBM J. Res. Dev.*, vol. 26, no. 2, pp. 209–216, 1982.

[14] W. M. Hetherington, G. I. Stegeman, R. M. Fortenberry, N. E. Van Wyck, and E. W. Koenig, “Observation of coherent Raman scattering in thin-film optical waveguides,” *Opt. Lett.*, vol. 9, no. 3, p. 88, Mar. 1984.

[15] N. E. Schlotter and J. F. Rabolt, “Raman spectroscopy in polymeric thin film optical waveguides. 1. Polarised measurements and orientational effects in two-dimensional films,” *J. Phys. Chem.*, vol. 16, no. 4, pp. 2062–2067, 1984.

[16] J. Rabe, J. Swalen, and J. Rabolt, “Order-disorder transitions in Langmuir-Blodgett films. III. Polarised Raman studies of cadmium arachidate usign integrated optical techniques,” *J. Chem. Phys.*, vol. 86, no. May 2015, p. 1601, 1987.

[17] D. R. Tallant, K. L. Higgins, and A. F. Stewart, “Application of waveguide Raman spectroscopy to high-index dielectric films.,” *Appl. Spectrosc.*, vol. 42, no. 2, pp. 326–330, 1988.

[18] N. E. Schlotter, “Diffusion of small molecules in glassy polymer thin films studied by waveguide Raman techniques,” *J. Phys. Chem.*, vol. 94, no. 4, pp. 1692–1699, 1990.

[19] J. K. F. Tait, N. M. Dixon, N. Everall, G. Davies, R. McIntyre, and J. Yarwood, “Waveguide Raman spectroscopy of polymers and polymer laminates,” *J. Raman Spectrosc.*, vol. 24, no. 8, pp. 511–518, Aug. 1993.

[20] S. Ellahi and R. E. Hester, “Enhanced waveguide Raman spectroscopy with thin films. Plenary lecture,” *The Analyst*, vol. 119, no. 4. pp. 491–495, 1994.

[21] D. Hu and Z. Qi, “Refractive-index-enhanced Raman spectroscopy and absorptiometry of ultrathin film overlaid on an optical waveguide,” *J. Phys. Chem. C*, vol. 117, no. 31, pp. 16175–16181, Aug. 2013.

[22] A. Dhakal, A. Z. Subramanian, P. Wuytens, F. Peyskens, N. Le Thomas, and R. Baets, “Evanescent excitation and collection of spontaneous Raman spectra using silicon nitride nanophotonic waveguides,” *Opt. Lett.*, vol. 39, no. 13, pp. 4025–4028, 2014.

[23] R. Claps, D. Dimitropoulos, Y. Han, and B. Jalali, “Observation of Raman emission in silicon waveguides at 1.54 microm.,” *Opt. Express*, vol. 10, no. 22, pp. 1305–1313, 2002.

[24] H. Oda, K. Inoue, N. Ikeda, Y. Sugimoto, and K. Asakawa, “Observation of Raman scattering in GaAs photonic-crystal slab waveguides.,” *Opt. Express*, vol. 14, no. 15, pp. 6659–6667, 2006.

[25] Y. C. Jun, R. D. Kekatpure, J. S. White, and M. L. Brongersma, “Nonresonant enhancement of spontaneous emission in metal-dielectric-metal plasmon waveguide structures,” *Phys. Rev. B - Condens. Matter Mater. Phys.*, vol. 78, no. 15, pp. 1–4, 2008.

[26] M. W. Meyer, V. H. T. Nguyen, and E. A. Smith, “Scanning angle Raman spectroscopy measurements of thin polymer films for thickness and composition analyses,” *Vib. Spectrosc.*, vol. 65, pp. 94–100, 2013.

[27] C. H. Camp Jr, Y. J. Lee, J. M. Heddleston, C. M. Hartshorn, A. R. H. Walker, J. N. Rich, J. D. Lathia, and M. T. Cicerone, “High-speed coherent Raman fingerprint imaging of biological tissues,” *Nat. Photonics*, vol. 8, no. 8, pp. 627–634, 2014.

[28] W. L. Barnes, “Fluorescence near interfaces: the role of photonic mode density,” *J. Mod. Opt.*, vol. 45, no. 4, pp. 661–699, 1998.

[29] R. R. Chance, A. Prock, and R. Silbey, “Molecular Fluorescence and Energy Transfer Near Interfaces,” in *Advances in Chemical Physics*, vol. 37, I. Prigogine and S. A. Rice, Eds. Hoboken, NJ, USA: John Wiley & Sons, Inc., 1978, pp. 1–65.

[30] T. C. Damen, R. C. C. Leite, and S. P. S. Porto, “Angular dependence of the raman scattering from benzene excited by the He-Ne cw laser,” *Phys. Rev. Lett.*, vol. 14, no. 1, pp. 9–11, 1965.

[31] L. Józefowski, J. Fiutowski, T. Kawalec, and H.-G. Rubahn, “Direct measurement of the evanescent-wave polarisation state,” *J. Opt. Soc. Am. B*, vol. 24, no. 3, p. 624, 2007.

[32] F. J. Rodríguez-fortuño, G. Marino, P. Ginzburg, D. O’Connor, A. Martínez, G. A Wurtz, and A. V Zayats, “Near-field Interference for the Unidirectional Excitation of Electromagnetic Guided Modes,” *Science*, vol. 340, no. February, pp. 328–330, 2013.

CHAPTER 7 Applications of WERS: self-assembled monolayer (SAM) detection

7.1 Introduction

In the previous chapters, WERS of bulk media and thin films have been successfully demonstrated. With efficient collection from the waveguide front edge, 2-3 orders of magnitude additional enhancement can be achieved compared to the collection from the waveguide surface. This leads to a much better sensitivity that is required for many applications. In this chapter, the motivation is to demonstrate the capability of WERS through self-assembled monolayer (SAM) detection.

Monolayer detection represents the ultimate test for WERS of thin films. The monolayer itself has been an attractive research venue. Although monolayer films are extremely thin (typically ca. 2 nm), they can completely change the surface properties, such as wettability and friction, corrosion protection, patterning, etc. Moreover, SAMs display superior stability due to the covalent bonding to the surface, which makes them suitable for extensive handling and further modification steps without deterioration [1]. This is very attractive for biosensing applications, and indeed applications of SAMs for miniaturised biosensors, especially for diagnostic applications, have become one of the main driving forces in the monolayer research activities [2]. By careful selection of monolayer molecules and tuning its functional groups, desired optical, electrical, and chemical properties can be introduced in order to meet the requirement of each specific application [3]. In these applications, monolayer molecules are often utilised as ligands to selectively bind target molecules. In addition, monitoring of the interactions between analyte and SAMs attracts a lot of interest for DNA and protein study [4], [5]. All these applications require a sensitivity that is capable of monolayer detection. Fluorescence spectroscopy has been used for detection and characterisation of monolayer films [4], [6]. Despite the desired sensitivity provided by the fluorescence technique, the sample preparation involved with synthesis of fluorescent molecules is complex and the structural information of the targeted molecule is missing. Raman spectroscopy offers non-destructive sampling and provides rich structural information, and should be a more advanced technique provided that the required sensitivity is met. Apart from this, Raman spectroscopy offers more information about molecular orientation, molecular conformation and interactions between a substrate and the first layer [7]. WERS delivers these benefits offered by the Raman spectroscopy as well as offering low cost and miniaturised system for monolayer detection and investigation. Several reports of WERS of monolayers through surface collection have been demonstrated, nearly all using resonance Raman scattering to provide the necessary enhancement in order to overcome the low Raman signal issue. The only exception is the work of Kanger *et al.*, where the Raman signal from the protein bovine albumin and Langmuir-Blodgett layers were obtained from a monomode high index contrast slab waveguide with optimised excitation design [8]–[12]. However, only one Raman feature group was shown in Kanger's case whereas molecule differentiation often requires a group of Raman bands. In addition, the success was at the expense of using a high power laser and a bulky expensive spectrometer, which is not ideal for low cost and miniaturised applications. With the newly revealed enhancement from measuring at the waveguide front edge, low cost and miniaturised WERS of monolayers can be achieved.

Trichloro(phenyl)silane (PTCS) and *p*-tolyltrichlorosilane (TTCS) were chosen as the monolayer test systems for the following reasons: 1) as silanes they are compatible with the metal oxide substrate such as SiO_2 and Ta_2O_5, as demonstrated in the literature [13]; 2) the resultant SAMs are chemically and mechanically robust, due to an irreversible covalent cross-linking step involved in the growth process [14]; 3) the molecular structures of the two are very similar to that of toluene and polystyrene, implying that very similar spectral characteristics can be observed.

The chapter will be structured as follow: firstly the fabrication and characterisation of trichloro(phenyl)silane (PTCS) and *p*-tolyltrichlorosilane (TTCS) monolayers on Ta_2O_5 will be explained, then waveguide Raman spectra of these monolayers will be shown and discussed, after that polarised Raman collection of TTCS under TE excitation will be demonstrated and depolarisation ratios calculated, Density Function Theory (DFT) will then be introduced to theoretically calculate the relationship between the depolarisation ratio and monolayer tilt angle, finally the monolayer tilt angle is estimated based on the results.

7.2 Fabrication of silane self-assembled monolayers (SAMs) on Ta_2O_5

The concept of a monolayer and its fabrication were firstly introduced by Langmuir in 1917, and later developed by Blodgett, nowadays known as Langmuir-Blodgett (LB) films. LB films were vulnerable to temperature changes or exposure to solvents; they are thermodynamically unstable. The adsorption from solution onto a platinum substrate was firstly demonstrated by Zismal *et al.* in 1946 [3], [15]. The versatility of these monolayers was not realised until Sagiv *et al.* demonstrated the formation of trichlorosilane monolayers with controllable in-plane molecular organization on SiO_2 along with the discoveries of other SAMs on gold, other glasses, and metal oxides [1], [3], [16].

The selection of monolayers has to be considered in view of the substrate to be used, for example thiol molecules are often selected for gold substrates [14]. Trichlorosilane SAMs were often selected for SiO_2 substrates since the first work by Sagiv *et al.* [16]. The same fabrication approach has been successfully applied to Ta_2O_5 substrates [13]. Trichlorosilane-based SAMs are chemically and mechanically robust, which are desirable for sensor applications. In addition, SAM properties are often modified through introducing different functional groups. Trichlorosilane-based SAMs have a family of molecules with different functional groups, making them very attractive. Like toluene and polystyrene, both of them have phenyl rings in their molecular structure, which result in strong Raman cross-section and characteristic vibration modes. Therefore, phenyltrichlorosilane (PTCS) and *p*-tolyltrichlorosilane (TTCS) are selected for the SAM test systems in this work. The latter has one more functional methyl group than the former, allowing proof of discrimination.

7.2.1 Fabrication of PTCS and TTCS SAMs on Ta_2O_5

7.2.1.1 Principle of monolayer formation

The selected trichlorosilane molecules are chemically bounded onto the substrate through reaction with the surface hydroxyl (–OH) groups. Therefore, the substrate needs to be hydroxylated firstly, commonly either by using piranha solution or plasma treatment [13], [17]. This step also removes organic contaminates. The resultant surface after this step is hydrophilic. After the hydroxylation, the activated surface can react with the selected silane molecules with the help of trace amounts of water, a step known as hydrolysis, where the Si-Cl bonds of the silane molecules react with the hydroxyl groups of the substrate surface to form new –O–Si bonds. The above procedures are illustrated in the Figure 7.1. Though these procedures are very commonly practiced to fabricate more and more sophisticated molecular structures on SiO_2, it is noted that the actual mechanism of the monolayer formation remained a subject of debate at least until the early 2000s [1], [13]. Several factors such as substrate cleanliness and crystallinity, water content, pH, and temperature are known to affect the SAMs formation, among which an appropriate amount of water is the key for the formation of well-packed monolayers [13], [14], [18]. A more in-depth explanations of SAM growth and formation can be found in Ulman and Schwartz's reviews [14], [19].

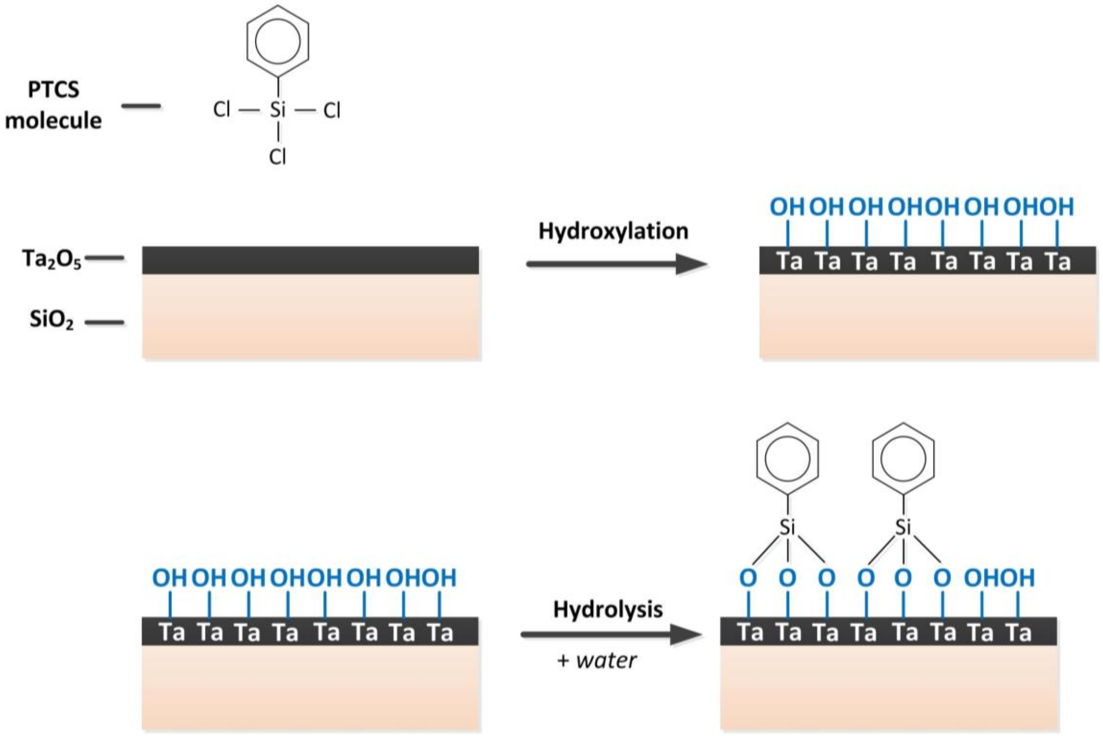

Figure 7.1 Schematic procedure for trichlorosilane (PTCS) SAM fabrication. The relative dimensions have been adjusted for better visual demonstration.

7.2.1.2 Fabrication procedures

The fabrication process started with the sample preparation. The end-polished 110 nm thick Ta_2O_5 on 1 mm thick fused silica sample was firstly chemically cleaned with acetone, IPA and a large quantity of deionised (DI) water, then dried by a nitrogen gun. The cleaned sample was immediately put into the plasma asher with plasma power 100 W and O_2 flow of 600 μL/min for 2 min. This process hydroxylated the Ta_2O_5 surface by generating –OH groups. The resultant surface was hydrophilic and prone to form a thin physisorbed water layer [13]. The sample was then put in a covered petri-dish and transported to an N_2 filled glove box, where the monolayer fabrication process was carried out.

The use of the N_2 filled glove box is necessary to control water exposure, as 1) PTCS reacts violently with water, and 2) the amount of water in the immersion solution has a significant role in the monolayer assembly process [13], [14], [20], [21]. 5 times 125 μL 97% PTCS solvent (from Sigma Ald-rich) was added by pipette into 12.5 mL of anhydrous 99.8% toluene (from Sigma-Aldrich) and mixed in a petri-dish, resulting in a concentration of 5% (volume by volume or v/v) in a range that agreed with the literature [20]. The sample was immersed in the solution at room temperature overnight. The variation in concentration as well as immersion time have been found not to affect the resultant PTCS or TTCS SAMs [20]. After the immersion, the sample was rinsed with toluene, then taken out of the N_2 filled glove box and rinsed with acetone and IPA to remove the loosely attached residues.

7.3 Characterisation of PTCS/TTCS SAMs

The nature of small quantities of molecules in monolayers makes it impossible to get a complete picture of the monolayer without the utilisation of a variety of analytical tools. The common characterisation methods are contact angle or wettability measurements, IR spectroscopy, ellipsometry, X-ray Photoelectron Spectroscopy (XPS), Atomic Force Microscopy (AFM), and cyclic voltammetry, which in sequence provides the SAM information of hydrophobicity, molecular structure and orientation, layer thickness, elemental composition, molecular packing, layer thickness and defects, respectively. A more complete summary of the common analytical techniques for SAMs can be found in the literature [3]. Each of these analytical tools reveals certain but not all structural information about the SAM. Therefore, it is essential to determine what the purpose of characterisation is before selecting a method. Availability and practicality have also to be taken into account.

The primary purpose of the characterisation was to determine whether PTCS/TTCS SAMs were formed on Ta_2O_5. If so, then to what order (how densely) the SAMs were packed. Contact angle measurements can conveniently and effectively give information about these two. Through measuring the contact angle of a droplet of water (probe liquid) on the target surface, the hydrophobicity of the surface can be determined. After cleaning, the Ta_2O_5 surface is expected to show a good degree of wetting, indicated by a contact angle around 50^0. After the hydroxylation step, the Ta_2O_5 surface should be ultra-hydrophilic, which means that the contact angle is close to zero. After the formation of a densely packed SAM, the Ta_2O_5 surface should be very hydrophobic, indicated by a contact angle much higher than that of the Ta_2O_5 surface without any treatment. The contact angle increases with the increase of immersion time as gradually more and more SAM molecules adsorb onto the surface. The increase of the contact angle will reach saturation when the reaction equilibrium is reached and the maximum contact angle is achieved. Therefore, the contact angle provides a good knowledge of 1) whether a SAM is formed on the surface; 2) how densely packed the SAM is.

After SAM fabrication the sample was put onto the stage of the drop shape analyzer (Krüss DSA100). After translational adjustments of the stage, the sample image was captured by the equipment camera and displayed in live mode in the software panel on a PC. The injection needle of the probe liquid was carefully moved to above the sample surface until it appeared in the camera image. Then, it was crucial to adjust the focus of the camera so that the needle appeared at the focal plane. Next, the droplet volume was set to 3 µL. After that, the needle with the droplet was carefully moved with the finest step size towards the sample surface until the droplet touched the surface. Then the needle was moved away from the sample, and the droplet formed on the surface. The camera captured the image and the software analysed it to give the contact angle. The above process was repeated at five different locations of the sample. Finally, the averaged contact angle was obtained for the SAM coated sample.

Figure 7.2 clearly shows examples of the contact angle measured at each stage of the PTCS SAM fabrication. The contact angle was around $54^0\pm3^0$ for the cleaned Ta_2O_5 surface. After the hydroxylation step, the contact angle was approximatly zero, which indicated that the Ta_2O_5 surface was contamination free and closely packed with –OH groups. After immersion in the trichlorosilane solution, the Ta_2O_5 surface became hydrophobic with a contact angle of $\sim87^0\pm3^0$, which agreed well with the $\sim85^0$ value from the literature [22]. The result indicated that a closely packed PTCS SAM was successfully formed onto the Ta_2O_5 surface. The corresponding contact angle for the TTCS SAM coated Ta_2O_5 surface was $\sim93^0\pm3^0$, which was lower than the maximum of 110^0 in the literature [20]. This suggests that the TTCS SAM was formed but that it was not ‘fully’ closely packed. The reason could be due to the water content difference during the fabrication of these two monolayers, which might be affected by the atmospheric humidity during the sample transportation. Overall, contact angle measurements clearly revealed that well-defined SAMs of PTCS and TTCS were formed on the Ta_2O_5 surfaces.

a. Cleaned Ta_2O_5 surface b. Hydroxylated Ta_2O_5 surface c. PTCS SAM coated Ta_2O_5 surface

Figure 7.2 Camera images captured from contact angle measurements of the substrate at each stage of the PTCS SAM fabrication. The probe liquid is DI water and droplet volume is 3 µL.

7.4 WERS of the monolayers

While contact angle measurements conveniently confirm the formation of closely packed SAMs, they provide little structural information for the monolayer molecules. Raman spectroscopy that provides structural molecular information can be used to tell exactly what the monolayer is. As far as sensor applications concerned, SAMs often serve as the binding layers to attract target molecules. Therefore, successfully detecting these SAM molecules can prove adequate sensitivities that are favoured for the detection of other target molecules. Moreover, fundamental studies of the interactions between SAM and target molecules, SAM and the substrate, or any other changes that involve changes in molecule structure can benefit from Raman spectroscopy, as it reveals rich molecular information that is not available from conventional techniques such as fluorescence spectroscopy. For all these, the successful detection of monolayer Raman is the key. While conventional Raman spectroscopy cannot provide enough sensitivity for monolayer detection, the goal here is to demonstrate monolayer Raman detection by WERS.

The basic procedure for WERS monolayer measurements is as follows. After SAM fabrication on waveguide samples, they were put into the waveguide end measurement configuration shown in Figure 6.1. The laser was a collimated, polarised, and narrow-line 633 nm diode laser (RO-633-PLR-75) from Ondax. The maximum power is 75 mW. TE and TM polarisations were selected by rotating the laser head. The laser light was prism coupled into the SAM-coated waveguide sample. The monolayer was evanescently excited by the guided light and the resultant Raman signals were collected by the composite waveguide, as explained in the Chapters 5 and 6. These signals were guided through to the composite waveguide front edge, and were collected by a multimode fiber (core diameter: 400 µm; NA=0.39) with the help of an image system (magnification ≈ 1). The other end of the fiber was connected to an Ocean Optics spectrometer (QE65000). The spectrometer then measured the Raman signals and sent them to a connected PC. For better Raman yield, droplets of water (higher index than the air) were added on top of the surface to cover the whole active region. The same waveguide sample but with a higher index superstrate is expected to increase the surface intensity, thereby enhancing both the Raman excitation and collection efficiency.

Both raw Raman spectra measured from the waveguide sample with and without PTCS SAM are displayed in Figure 7.3. The distinguishable peak features in the shaded regions b and d are background signals since they appear in both cases; whereas features in shaded region a and c are Raman signals from the PTCS SAM since they only appear in Raman spectrum of PTCS SAM coated waveguide sample.

For analysis purposes, baselines were subtracted for all the following SAM spectra. The procedures of baseline subtraction again were practised by using the 'baseline subtraction' function in the Origin software, as described in Section 4.5. Anchor points were firstly user-generated after spotting the baseline trend by comparing the Raman spectra with and without the monolayer. The 'Spline' method provided by the software was used to generate the baseline based on those anchor points. After that, the processed spectrum could be obtained by subtracting the baseline using the software.

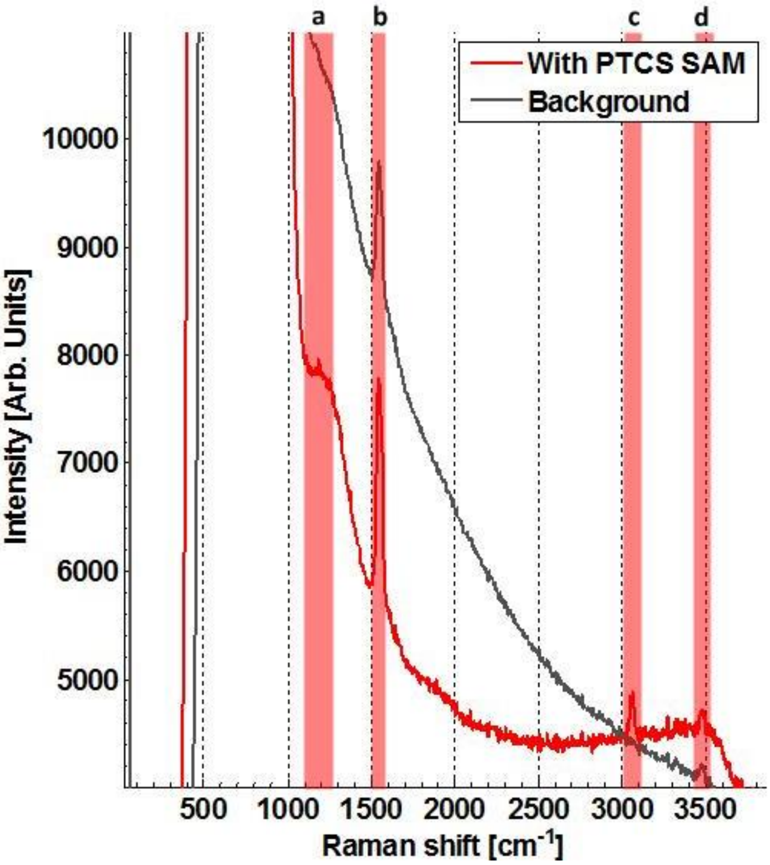

Figure 7.3 Raw waveguide Raman spectra with and without PTCS SAM. Shaded regions a and c highlight Raman signals of PTCS, whereas b and d highlight background signals that are not PTCS Raman. The excitation is in TE polarisation. Integration time is 60 s.

Figure 7.3 shows baseline subtracted Raman spectra of PTCS SAM under both TE and TM excitation from the 110 nm Ta_2O_5 waveguide sample. The spectral range plotted spans from 1050 cm^{-1} to 3200 cm^{-1}, covering most of the fingerprint region; the lower range wavenumber from 500 cm^{-1} to 1000 cm^{-1} is overwhelmingly superimposed by the prism Raman signals, and is therefore not shown.

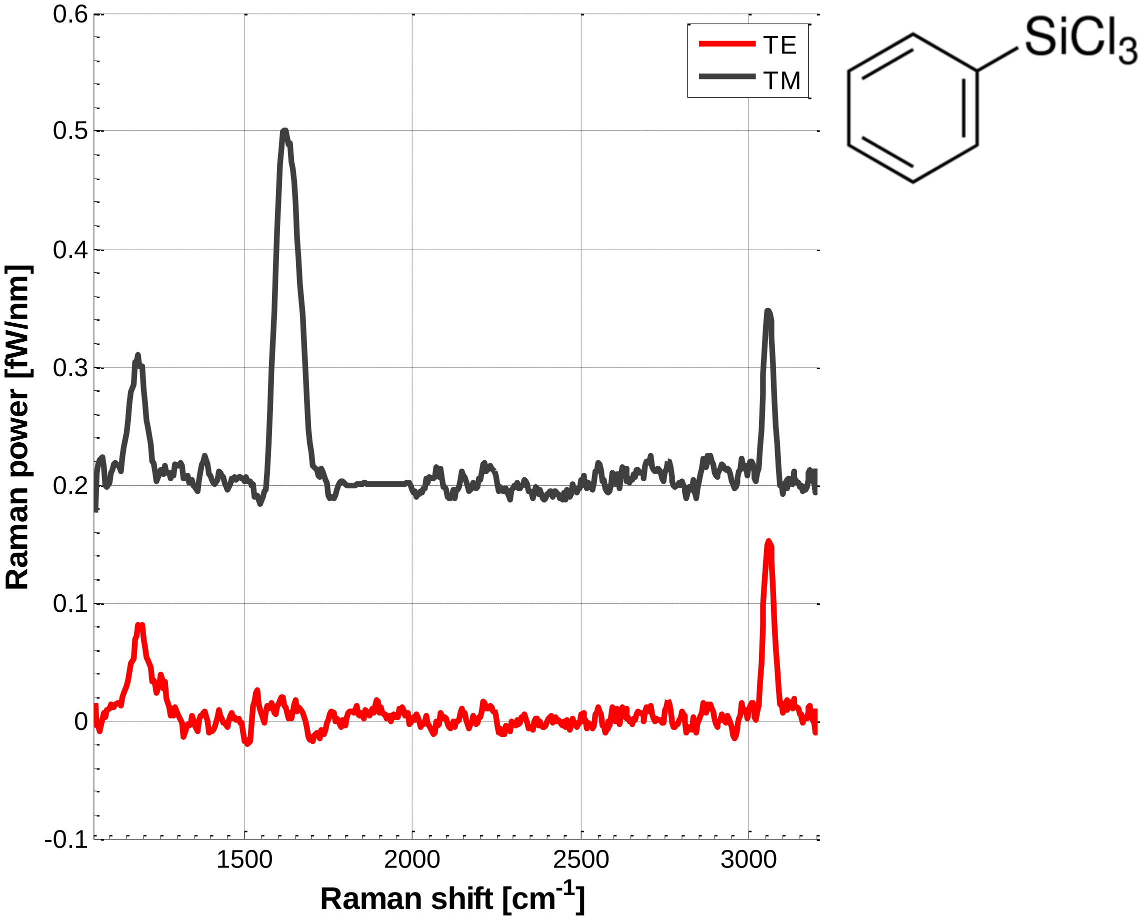

Figure 7.4 Baseline subtracted Raman spectra of PTCS SAM coated waveguide samples under TE and TM excitation, respectively. The integration time is 60 s. Spectrum for TM is translated 0.2 fW/nm for visual purposes. Top right corner shows the PTCS molecule.

First of all, Raman features of the PTCS monolayer are clearly visible in the WERS measured spectra. For both polarisations, PTCS Raman features at ~1184 cm^{-1} and 3058 cm^{-1}, corresponding to ring vibration and aromatic C-H stretching respectively, are clearly seen. Only under TM excitation, a strong ring vibration at ~1615 cm^{-1} was observed. The appearance of this 1615 cm^{-1} band for the TM polarisation is very likely because the SAM molecules are ‘oriented’ at the surface. The tensor nature of the Raman scattering process requires a polarisation to match with the molecule orientation in order to excite the mode efficiently. The implications of this are the relative amplitude changes of the Raman features of oriented monolayer molecules under different polarisations (excitation and collection). This will be explored in the next section. Compared to the reference of PTCS Raman, only the feature at around 1425 - 1480 cm^{-1} is not shown in the WERS measured spectrum, which is because the Raman yield was too low to be detected.

As a matter of confirmation, the TTCS SAM Raman spectrum measured by WERS is also demonstrated by plotting together with the PTCS SAM Raman spectrum, as shown in Figure 7.5. Both of them are under TE excitation. The waveguide samples have 110 nm Ta_2O_5 and 100 nm Ta_2O_5 film, for PTCS and TTCS respectively. The differences in Ta_2O_5 thickness are due to the sample availability rather than purposeful design, but the small difference is expected to have little impact on the results.

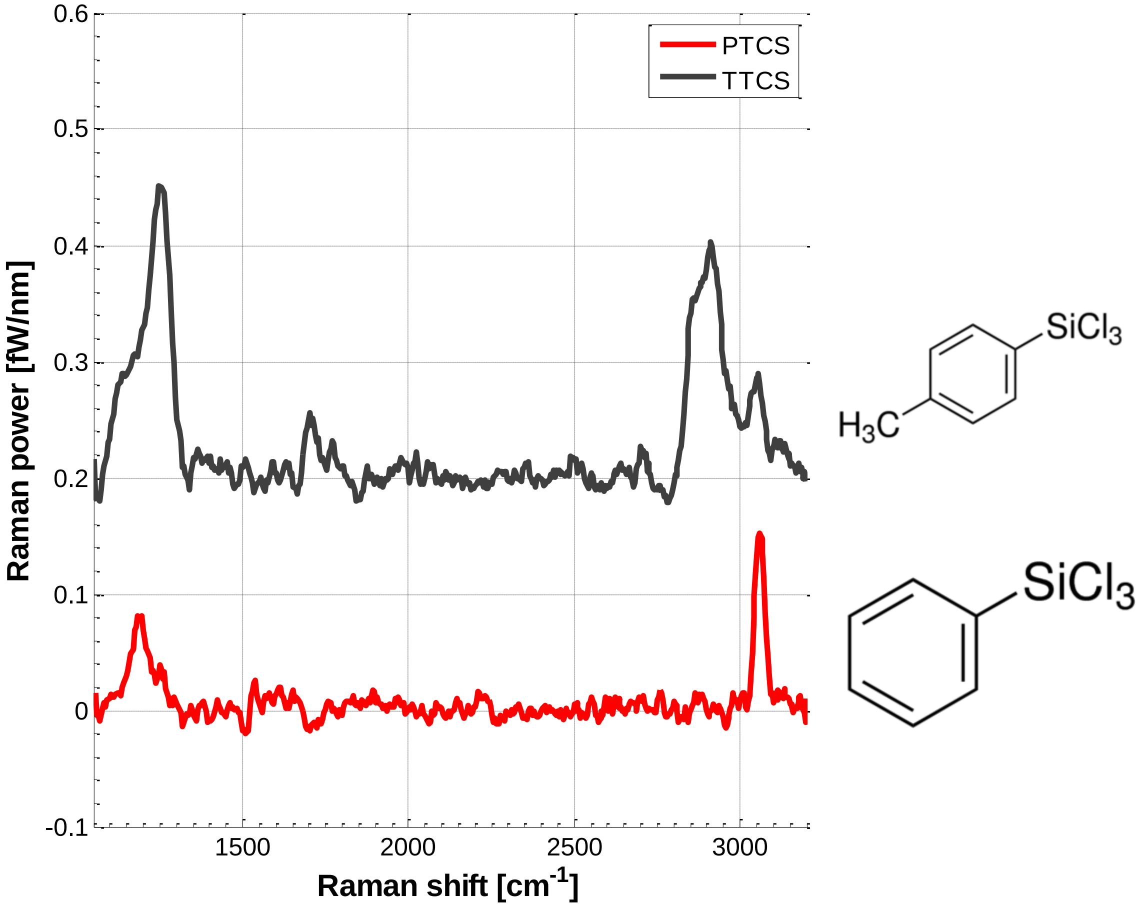

Figure 7.5 PTCS and TTCS SAM waveguide Raman spectra. Integration time are 60 s and 90 s for PTCS and TTCS, respectively. The Ta_2O_5 sample thicknesses are 110 nm and 100 nm, respectively for PTCS and TTCS measurements.

Due to the similarity of the molecular structure, waveguide Raman spectra of PTCS and TTCS SAM show very similar Raman features. For example, two major Raman features at around 1200 cm^{-1} and 3058 cm^{-1} are clearly shown. However, the TTCS spectrum uniquely shows significant Raman features at 2856 cm^{-1} to 2913 cm^{-1}, which is due to the aliphatic C-H stretching from the methyl group ($-CH_3$) of TTCS. This is clear evidence adding to the validity of WERS monolayer measurements. Also, the successful differentiation of two types of molecule with very similar molecular structures demonstrates a strong WERS performance, which can inspire many applications.

In addition, it is noticeable that there are relative amplitude changes among the Raman feature groups at around 1184 cm^{-1} to 1253 cm^{-1} comparing PTCS and TTCS spectra. The molecule orientation difference between the two monolayers is thought to be the reason behind this.

To conclude, these results are very significant as this is the first time (to the author's knowledge) that monolayer Raman spectra with 'multiple' Raman features have been successfully demonstrated using only the low cost monomode slab waveguide that has the simplest structure in the waveguide family. Previous work on WERS monolayer Raman either only demonstrated a single Raman feature due to the sensitivity issue [12] or were only achieved by relying on SERS that however had more fabrication complexities [23], or resonance Raman scattering that however put constraints on applications [8], [24], or both [10]. This successful demonstration of monolayer Raman detection by slab WERS with front edge collection opens up a huge venue for both sensor applications and fundamental studies.

7.5 Polarised WERS: monolayer orientation studies

The molecular orientation of a SAM has significant impact on the realisation of many applications. Many fabrication factors of a SAM can influence its molecular orientation. Therefore, the characterisation of the molecular orientation is a prerequisite for a better understanding of well-controlled SAM formation, and the selection of SAMs which possesses desired properties for a wide range of applications. Vibrational spectroscopy, such as Raman spectroscopy and infrared absorption spectroscopy, can be employed to characterise the molecular orientation of SAMs.

The Raman signal P obtained from a molecular vibration υ can be expressed as a function of molecular orientation and polarisation geometry [24], [25] as follows:

$$P \propto |e_i \cdot \alpha_\upsilon \cdot e_s|^2 \qquad \text{Equation 7.1}$$

where e_i and e_s are the unit polarisation vectors of the electric field for the incident and scattered laser beams, respectively, and α_υ represents the Raman scattering tensor for a molecular vibration υ, which is a function of the molecular orientation. By selecting different combinations of incident (e_i) and scattered (e_s) polarisation vectors, corresponding Raman measurements allow the Raman scattering tensor determined based on Equation 7.1, and hence the molecular orientation. This is the principle of characterising monolayer molecular orientation by using polarised Raman spectroscopy.

For polarised WERS studies of the SAMs, the measurement procedure was to 1) choose an input polarisation e_i; 2) establish and maintain incident light and sample position once the light coupling condition is met; and 3) rotate a polariser at the waveguide front edge to selectively measure scattered light under different polarisation states e_s. Rotation of only the output polariser ensured the very same experimental conditions for the polarised Raman emission measurements. Due to the tensor nature of the physical process, the laboratory coordinate system was established and measurement geometry was specified according to that. The laboratory coordinate system and the measurement concept are illustrated in Figure 7.6.

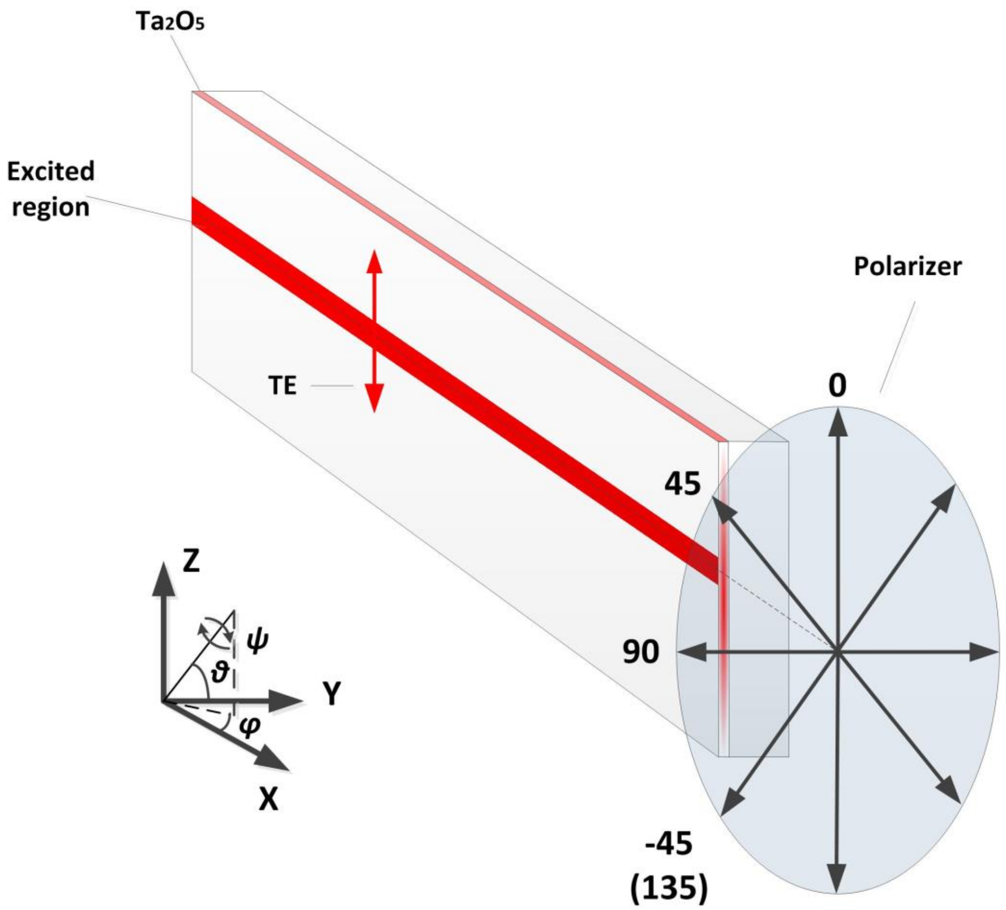

Figure 7.6 Illustration of polarised Raman emission measurements. Arrow lines in the polariser represent the transmission axis.

Both the light propagation direction and polarisation states need to be specified for each measurement geometry. The following convention was utilised for specifying these two types of geometry: *i(jk)l* with *i, j, k,* and *l* being *x, y,* or *z* in the coordinate system established in Figure 7.6. In this notation, *i* and *l* refer to the polarisation states of the incident light and scattered light, respectively; and *j* and *k* refer to the light propagation direction of the incident light and collected light, respectively [24]. For example, in Figure 7.6 the TE polarised (*i=z*) incident light propagates in the direction *x* (*j=x*), and the scattered light is collected in direction x (*k=x*) after transmission through the output polariser at zero degrees (*l=z*). The measurement geometry is then denoted as *z(xx)z.*

The polarised Raman emission measurements were carried out by rotating the output polariser for the measurement geometry *z(xx)z*. The rotation was started from 0^0, which corresponded to *l=z* in 45^0 incrementing steps in an anti-clockwise direction. A reference measurement was taken for the same measurement geometry *z(xx)* but without the output polariser. The measured polarised Raman emission spectra of TTCS are plotted in Figure 7.7 with experimental conditions explained in the figure caption.

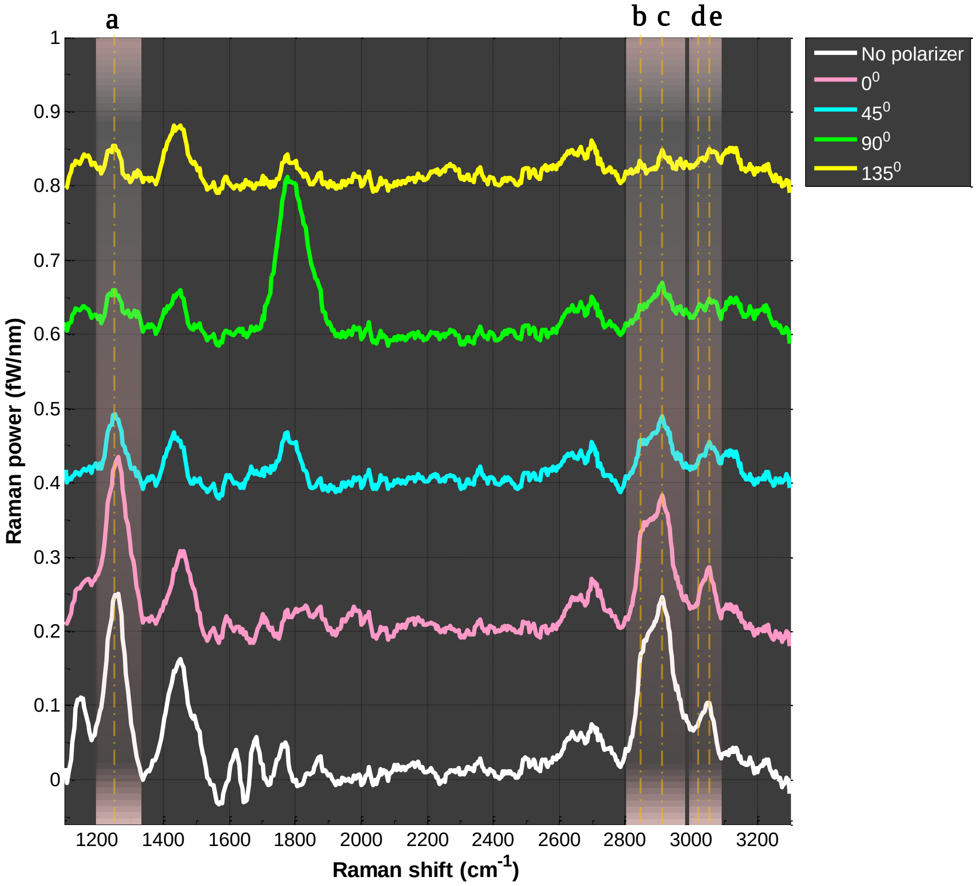

Figure 7.7 Polarised Raman collection at the waveguide front edge (end) for TTCS monolayer. The shaded regions indicate Raman feature groups of TTCS to be investigated with dotted lines a, b, c, d, and e indicating the spectral position of the Raman features. The waveguide sample had 100 nm thick Ta_2O_5 on 0.5 mm thick fused silica glass slab waveguide. All spectra were acquired with 90 s integration time. The collection fiber has core diameter 400 µm and NA of 0.38. The spectra were all baseline subtracted, followed by smoothing using moving average method with window size of 5 CCD pixels.

Five Raman features of TTCS were specifically analysed in the current investigation. They are at around 1253 cm^{-1} (a), 2856 cm^{-1} (b), 2913 cm^{-1} (c), 3027 cm^{-1} (d) and 3056 cm^{-1} (e). The resolution was not high enough to perfectly distinguish between each feature in the same group, for the reasons explained in Chapter 4. Therefore, the Raman feature group was decomposed by fitting a Voigt function at each feature's spectral position, which was performed by using commercially available software (Origin 9.1). The confined areas under these features, which are proportional to the Raman power, are summarised in Table 7.1. The errors on the results were primarily from baseline subtraction and peak-fitting, and were estimated for all features.

Table 7.1 Summary of relative Raman power measured from polarised Raman emission measurements

	1253 cm^{-1}	2860 cm^{-1}	2913 cm^{-1}	3034 cm^{-1}	3056 cm^{-1}
No polariser	41.7 ± 3.0	8.4 ± 0.8	18.4 ± 0.8	2.1 ± 0.3	2.7 ± 0.3
0^0	28.8 ± 3.0	6.3 ± 0.8	15.5 ± 0.8	1.0 ± 0.3	3.0 ± 0.3
45^0	8.1 ± 1.0	1.4 ± 0.3	11.5 ± 0.3	0.5 ± 0.2	0.7 ± 0.2
90^0	3.0 ± 0.3	0.8 ± 0.3	4.5 ± 0.3	0.4 ± 0.2	0.6 ± 0.2
135^0	1.9 ± 0.5	0.9 ± 0.4	1.0 ± 0.4	0.2 ± 0.1	0.4 ± 0.2
ρ	0.10 ± 0.01	0.14 ± 0.07	0.29 ± 0.03	0.40 ± 0.32	0.18 ± 0.08
ρ (corrected)	0.08 ± 0.01	0.11 ± 0.06	0.23 ± 0.03	0.31 ± 0.25	0.14 ± 0.06

As shown in Table 7.1, the Raman power of each feature generally decreases, but does not fall to zero, as the polariser rotates from 0^0 to 90^0. This confirms the tensor nature of the Raman scattering of the TTCS monolayer. It is noticeable that the degree of power variation between each Raman feature varies as the angle changes, which indicates the differences between the Raman tensor of each vibration. The Raman depolarisation ratio (ρ), defined as the ratio of Raman power polarised perpendicular to the incident light (90^0) and Raman power polarised parallel to the incident light (0^0), contains information about the symmetry of the vibrational mode [26] and also the orientation of the molecule on the surface. Each will be addressed in the following discussion. The Raman depolarisation ratio for each feature was calculated and is presented in the penultimate row of Table 7.1. The ratio values span from the minimum close to null to a maximum of 0.4. A Raman depolarisation ratio equal to zero occurs when the Raman tensor is isotropic, which means that the scattered light preserves the polarisation of the incident light. In this case, Raman tensors for the vibrational modes at 1253 cm^{-1} and 2860 cm^{-1} are close to isotropic. For the others, there is a considerable amount of 're-distribution' of Raman intensity from one polarisation to the other with the magnitude of the depolarisation ratio determining the amount. Here a higher depolarisation value indicates that a greater amount of the intensity was transferred to the polarisation that is perpendicular to that of the incident light. Unlike waveguide surface collection as described by [24], [25], the collection efficiency of the scattered Raman power of polarisation parallel with the incident ($P_{\parallel}$) and that of perpendicular polarisation ($P_{\perp}$) is different. For example, the waveguide collection efficiency of y and z oriented dipoles are about 27% and 21% respectively, for the current sample parameters. Therefore, $P_{\perp}$ is more efficiently collected than $P_{\parallel}$ in the waveguide and guided to the waveguide front edge, hence a higher measured depolarisation ratio ρ than the real value. The corrected values of ρ are recorded in the last row of Table 7.1.

The Raman tensor determines the depolarisation ratio of each vibrational mode, which is variant of the molecule orientation. Consider the Raman tensor (α_v) which takes the form:

$$\alpha_v = \begin{pmatrix} \alpha_{xx} & \alpha_{xy} & \alpha_{xz} \\ \alpha_{yx} & \alpha_{yy} & \alpha_{yz} \\ \alpha_{zx} & \alpha_{zy} & \alpha_{zz} \end{pmatrix}$$ Equation 7.2

The power of Raman scattered light with polarisation perpendicular ($P_\perp$) and parallel ($P_\parallel$) to that of the incident light are then given as:

$$P_\perp \propto \left|e_z{}' \cdot \alpha_v \cdot e_y\right|^2$$ Equation 7.3

$$P_\parallel \propto |e_z{}' \cdot \alpha_v \cdot e_z|^2$$ Equation 7.4

where $e_z = [0; 0; 1]$ and $e_y = [0; 1; 0]$. In order to determine the tilt angle, the functional relationship between the depolarisation ratio and the tilt angle (θ) is now described, assuming that the molecules are randomly oriented over azimuthal angle (φ) and rotation angle (ψ). Firstly, the reference case of completely randomly oriented molecules is considered. The depolarisation ratio for the measurement geometry *z(xx)* is given as:

$$\rho = \frac{\int_0^{2\pi}\int_0^{2\pi}\int_0^{\pi}\left|e_z \cdot R(\psi\theta\phi) \cdot a_v \cdot R(\psi\theta\phi)' \cdot e_y\right|^2 d\phi d\theta d\psi}{\int_0^{2\pi}\int_0^{2\pi}\int_0^{\pi}|e_z \cdot R(\psi\theta\phi) \cdot a_v \cdot R(\psi\theta\phi)' \cdot e_z|^2 d\phi d\theta d\psi}$$ Equation 7.5

where $e_z = [0; 0; 1]$ and $e_y = [0; 1; 0]$. $R(\psi\theta\phi)$ represents the rotation matrix after rotating ψ, θ, and ϕ respectively. $R(\psi\theta\phi)$ can be calculated by:

$$R(\psi\theta\phi) = R(\psi) \cdot R(\theta) \cdot R(\phi)$$ Equation 7.6

$$R(\psi) = \begin{pmatrix} \cos\psi & -\sin\psi & 0 \\ \sin\psi & \cos\psi & 0 \\ 0 & 0 & 1 \end{pmatrix}$$ Equation 7.7

$$R(\theta) = \begin{pmatrix} \cos\theta & 0 & \sin\theta \\ 0 & 1 & 0 \\ -\sin\theta & 0 & \cos\theta \end{pmatrix}$$ Equation 7.8

$$R(\phi) = \begin{pmatrix} 1 & 0 & 0 \\ 0 & \cos\phi & -\sin\phi \\ 0 & \sin\phi & \cos\phi \end{pmatrix}$$ Equation 7.9

The Raman tensor (a_v) of TTCS molecule was theoretically calculated by using Density Function Theory (DFT), which computes the electronic structure of a molecule with known geometry [26]. The calculation was performed using the commercially available software (Gaussian) with the choice of the default DFT method of B3LYP and the basis set of 6-311++G(d,p). After a sequence of computations following the procedure exemplified in Ref [26], the Gaussian output produced the Raman vibrational frequency, linear polarisability derivatives, normalized displacements and reduced mass. This DFT calculation was performed by Dr. Christopher Cave-Ayland in Prof. Jonathan W Essex's group at University of Southampton. The Gaussian outputs were then used to calculate the Raman polarisability tensor of each vibrational mode. The Matlab code is provided in Appendix D for this calculation.

Based upon the Raman polarisability tensor produced by calculation using Gaussian, the depolarisation ratios (ρ_r) for completely randomly oriented TTCS molecules were calculated using Equation 7.5. The results for the modes currently being considering are listed in Table 7.2.

Table 7.2 Depolarisation ratios for calculated randomly oriented molecules ρ_r and experimental values ρ (corrected)

	1253 cm^{-1}	2860 cm^{-1}	2913 cm^{-1}	3034 cm^{-1}	3056 cm^{-1}
ρ_r	0.07	0.10	0.62	0.52	0.11
ρ (corrected)	0.08	0.11	0.23	0.31	0.14

It can be seen that the measured depolarisation ratios differ from that of the randomly oriented case, especially for the bands at 2913 cm^{-1} and 3034 cm^{-1}. This further implies that the monolayer molecules are oriented. Assuming that the TTCS monolayer sits on a smooth surface, free rotation about the Si-phenyl bond will average out the rotation angle (ψ), and random orientation of attachment will average out azimuthal angle (φ) but a tilt angle (θ) can be formed. To estimate the molecule tilt angle, the relationship between the depolarisation ratio (ρ) and the tilt angle (θ) was plotted for each vibrational mode in Figure 7.8. For each measured ρ, the tilt angle was read from the curve. The tilt angles are 36^0, 31^0, 20^0, 41^0 from the $\rho - \theta$ curve of the vibrational mode at 1253 cm^{-1}, 2860 cm^{-1}, 3034 cm^{-1} and 3056 cm^{-1}, respectively. The measured depolarisation ratio of the mode 2913 cm^{-1} is below the smallest point in the curve, therefore the tilt angle cannot be read. Apart from this outlier, all the others are well within the range of 20^0 – 40^0, the average is around 30^0 ($\pm 3^0$). Therefore, the tilt angle for TTCS monolayer molecules on Ta_2O_5 was estimated to be around 30^0 ($\pm 3^0$) by polarised WERS.

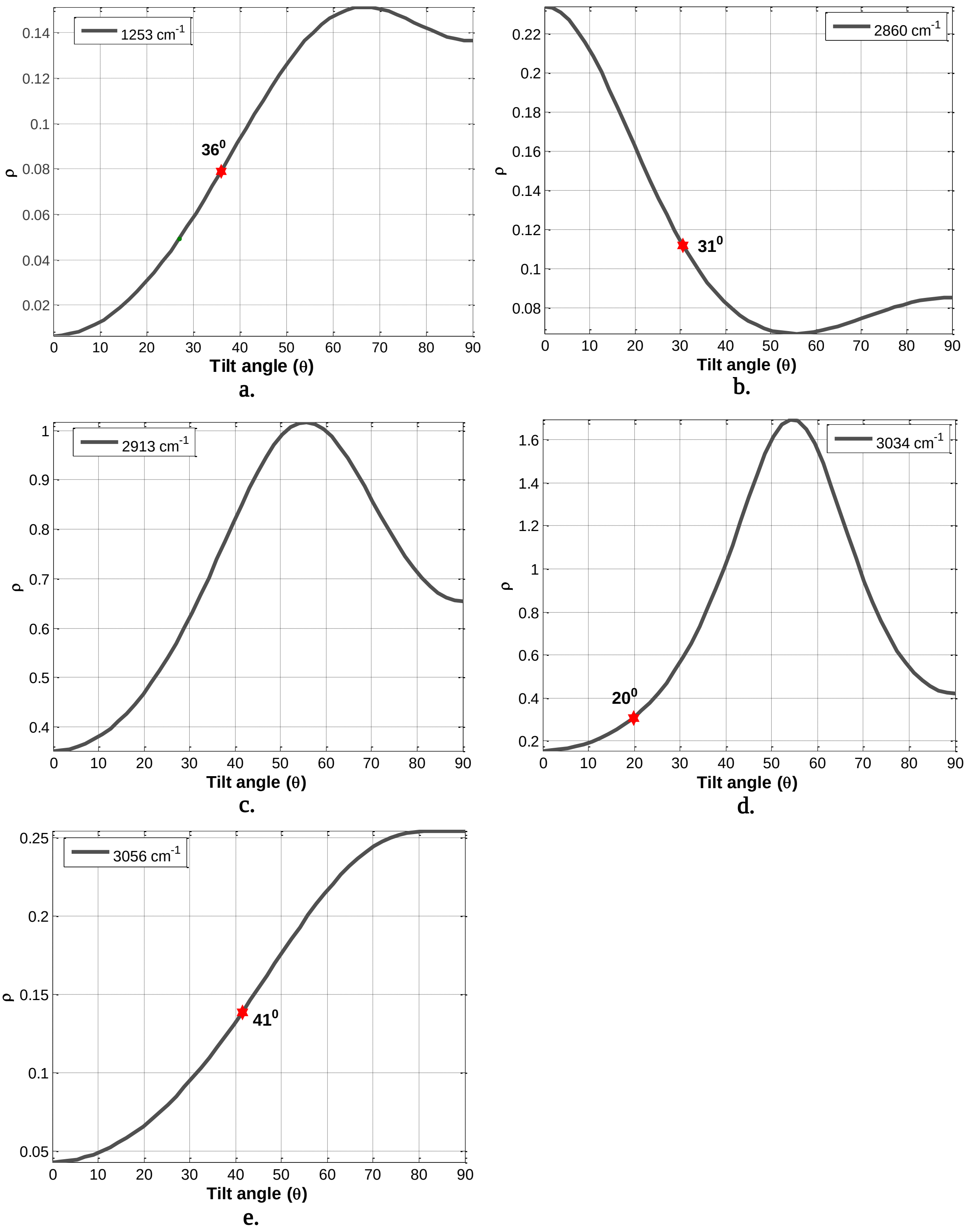

Figure 7.8 Theoretical curves of depolarisation ratios and tile angle.

Figure 7.9 shows different orientations of a TTCS molecule attached to the waveguide surface. Ideally, the TTCS molecule should stand perpendicular to the surface, which corresponds to a tilt angle of 90^0. A tilt angle of 30^0 suggests that only two or even one of the three Si-O bonds has formed, allowing the molecule to tilt.

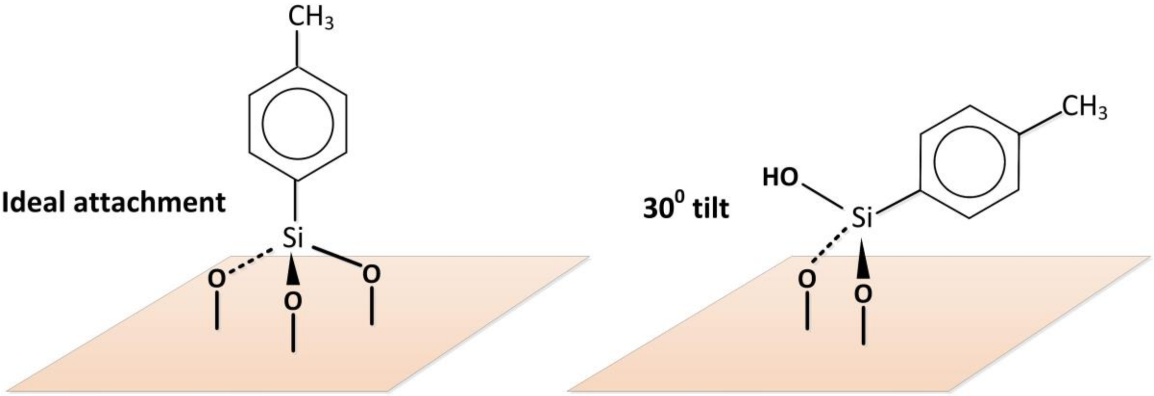

Figure 7.9 Illustrations of TTCS molecule attached to the waveguide surface.

These are the preliminary results for measurement of SAMs orientation. It will be interesting to further develop this technique in order to establish a fuller understanding of the molecular orientation of SAMs on WERS platform. Further improvements can be made in order to more accurately estimate the tilt angle. While the above example is a demonstration for TE excitation, the result can be further confirmed by using TM excitation. However, it was found that in the TM polarisation this particular waveguide was too lossy to allow successfully measurement at the waveguide front edge. As explained in the literature [14], the silane monolayer tends to form islands, for which the periodicity of the islands might favour one polarisation over another in terms of the transmission. In addition, further improvements on the sensitivity will help to better resolve the Raman features, which could then lead to more accurate results for calculation of tilt angles.

7.6 Conclusions

The sensitivity of waveguide enhanced Raman spectroscopy was tested on a Ta_2O_5 monomode slab waveguide sample by measuring monolayers. Two kinds of monolayer molecules from the silane family, phenyltrichlorosilane (PTCS) and *p*-tolyltrichlorosilane (TTCS), were chosen as the test systems due to their chemical, mechanical robustness, compatibility with the Ta_2O_5 surface, and their Raman features. The contact angle measurements after fabrication showed that a monolayer or a submonolayer was formed. The Raman signals of these monolayers were successfully measured with multiple spectral features detected. The spectral difference between the two monolayers due to the methyl group clearly confirmed the validity of the measurement. The success in measuring monolayer Raman with multiple Raman features is significant as this was previously only achieved by using resonant Raman scattering or SERS, compared to which the WERS approach with collection at the waveguide front edge enables low cost and miniaturised solutions to many applications.

Monolayer detection is of great importance for many applications. Raman measurements of monolayers can provide molecular structural information of the monolayer forming molecule. One featured application is to measure the monolayer orientation by using polarised Raman spectroscopy. Having selected the incident polarisation as TE, collecting the Raman signals at the waveguide front edge with a polariser inserted in between to select the scattered light parallel and perpendiculars to the incident polarisation, led to the calculated depolarisation ratio based on the measurement data. In addition, Density Function Theory (DFT) performed using the commercial software (Gaussian) gave the Raman polarisability tensor of each vibrational mode, which then was utilised to generate the relationship between the depolarisation ratio and the molecular tilt angle, with the assumption that the molecules were randomly oriented in the azimuthal and rotational plane. The tilt angle was calculated to be around 30^0. Further improvements on sensitivity and utilisation of all TE and TM polarisations will allow greater accuracy in tilt angle determination.

7.7 References

[1] S. Onclin, B. J. Ravoo, and D. N. Reinhoudt, “Engineering silicon oxide surfaces using self-assembled monolayers,” *Angew. Chemie - Int. Ed.*, vol. 44, no. 39, pp. 6282–6304, 2005.

[2] N. K. Chaki and K. Vijayamohanan, “Self-assembled monolayers as a tunable platform for biosensor applications,” *Biosens. Bioelectron.*, vol. 17, no. 1–2, pp. 1–12, Jan. 2002.

[3] S. Flink, F. C. J. M. Van Veggel, and D. N. Reinhoudt, “Sensor functionalities in self-assembled monolayers,” *Adv. Mater.*, vol. 12, no. 18, pp. 1315–1328, 2000.

[4] C.-C. You, O. R. Miranda, B. Gider, P. S. Ghosh, I.-B. Kim, B. Erdogan, S. A. Krovi, U. H. F. Bunz, and V. M. Rotello, “Detection and identification of proteins using nanoparticle-fluorescent polymer ‘chemical nose’ sensors.,” *Nat. Nanotechnol.*, vol. 2, no. 5, pp. 318–323, 2007.

[5] R. A. Dluhy, S. M. Stephens, S. Widayati, and A. D. Williams, “Vibrational spectroscopy of biophysical monolayers. Applications of IR and Raman spectroscopy to biomembrane model systems at interfaces,” *Spectrochim. Acta Part A Mol. Biomol. Spectrosc.*, vol. 51, no. 8, pp. 1413–1447, Jul. 1995.

[6] L. Li, P. Gao, K. C. Schuermann, S. Ostendorp, W. Wang, C. Du, Y. Lei, H. Fuchs, L. De Cola, K. Müllen, and L. Chi, “Controllable growth and field-effect property of monolayer to multilayer microstripes of an organic semiconductor,” *J. Am. Chem. Soc.*, vol. 132, no. 26, pp. 8807–8809, 2010.

[7] Y. Ozaki, S. Morita, Y. Hirano, and X. Li, “Chapter 12 Monolayers on Air/Solid Interfaces: Vibrational Spectroscopy and Atomic Force Microscopy Studies,” in *Advanced chemistry of*

monolayers at interfaces: trends in methodology and technology, T. Imae, Ed. 2007, pp. 309–359.

[8] R. Santo, N. E. Schlotter, and J. D. Swalen, “Integrated optics and Raman scattering : molecular orientation in thin polymer films and Langmuir-Blodgett monolayers,” *IBM J. Res. Dev.*, vol. 26, no. 2, 1982.

[9] J. Rabe, J. Swalen, and J. Rabolt, “Order-disorder transitions in Langmuir-Blodgett films. III. Polarised Raman studies of cadmium arachidate usign integrated optical techniques,” *J. Chem. Phys.*, vol. 86, no. May 2015, p. 1601, 1987.

[10] S. Ellahi and R. E. Hester, “Enhanced waveguide Raman spectroscopy with thin films. Plenary lecture,” *The Analyst*, vol. 119, no. 4. p. 491, 1994.

[11] J. F. Rabolt, R. Santo, and J. D. Swalen, “Raman measurements on thin polymer films and organic monolayers,” *Appl. Spectrosc.*, vol. 34, no. 5, pp. 517–521, 1980.

[12] J. S. Kanger, C. Otto, M. Slotboom, and J. Greve, “Waveguide Raman spectroscopy of thin polymer layers and monolayers of biomolecules using high refractive index waveguides,” *J. Phys. Chem.*, vol. 100, no. 8, pp. 3288–3292, Jan. 1996.

[13] R. De Palma, W. Laureyn, F. Frederix, K. Bonroy, J. J. Pireaux, G. Borghs, and G. Maes, “Formation of dense self-assembled monolayers of (n-decyl)trichlorosilanes on Ta/Ta_2O_5,” *Langmuir*, vol. 23, no. 2, pp. 443–451, 2007.

[14] D. D. K. Schwartz, “Mechanisms and kinetics of self-assembled monolayer formation,” *Annu. Rev. Phys. Chem.*, vol. 52, pp. 107–137, 2001.

[15] W. C. Bigelow, D. L. Pickett, and W. a. Zisman, “Oleophobic monolayers. Films Adsorbed From Solution In Non-Polar Liquids,” *J. Colloid Sci.*, vol. 1, no. 6, pp. 513–538, 1946.

[16] J. Sagiv, “Organized monolayers by adsorption. 1. Formation and structure of oleophobic mixed monolayers on solid surfaces,” *J. Am. Chem. Soc.*, vol. 399, no. 1976, pp. 92–98, Jan. 1980.

[17] S. J. Lee, B. G. Paik, G. B. Kim, and Y. G. Jang, “Self-cleaning features of plasma-treated surfaces with self-assembled monolayer coating,” *Japanese J. Appl. Physics, Part 1 Regul. Pap. Short Notes Rev. Pap.*, vol. 45, no. 2 A, pp. 912–918, Feb. 2006.

[18] N. K. Chaki and K. Vijayamohanan, “Self-assembled monolayers as a tunable platform for biosensor applications,” *Biosens. Bioelectron.*, vol. 17, no. 1–2, pp. 1–12, 2002.

[19] A. Ulman, “Formation and Structure of Self-Assembled Monolayers,” *Chem. Rev.*, vol. 96,

no. 4, pp. 1533–1554, 1996.

[20] J. Xiang, P. Zhu, Y. Masuda, and K. Koumoto, “Fabrication of self-assembled monolayers (SAMs) and inorganic micropattern on flexible polymer substrate.,” *Langmuir*, vol. 20, no. 8, pp. 3278–83, 2004.

[21] Y. Wang and M. Lieberman, “Growth of ultrasmooth octadecyltrichlorosilane self-assembled monolayers on SiO2,” *Langmuir*, vol. 19, no. 4, pp. 1159–1167, 2003.

[22] Z. Liu, A. A. Bol, and W. Haensch, “Large-scale graphene transistors with enhanced performance and reliability based on interface engineering by phenylsilane self-assembled monolayers,” *Nano Lett.*, vol. 11, no. 2, pp. 523–528, Feb. 2011.

[23] F. Peyskens, A. Dhakal, P. Van Dorpe, N. Le Thomas, and R. Baets, “Surface enhanced Raman spectroscopy using a single mode nanophotonic-plasmonic platform,” *ACS Photonics*, vol. 3, no. 1, pp. 102–108, Jan. 2016.

[24] J. S. Kanger and C. Otto, “Orientation effects in waveguide resonance Raman spectroscopy of monolayers,” *Appl. Spectrosc.*, vol. 57, no. 12, pp. 1487–1493, Dec. 2003.

[25] V. Presser, B. E. Schuster, M. B. Casu, U. Heinemeyer, F. Schreiber, K. G. Nickel, and T. Chassé, “Raman polarisation studies of highly oriented organic thin films,” *J. Raman Spectrosc.*, vol. 40, no. 12, pp. 2015–2022, Dec. 2009.

[26] P. E. Le Ru and P. G. Etchegoin, *Principles of Surface-Enhanced Raman Spectroscopy: and Related Plasmonic Effects*, 1st editio. Elsevier, 2009.

CHAPTER 8 Conclusions and future possibilities

8.1 Conclusions

The challenges of having better environment and healthcare for Homo sapiens living in the early twenty-first century demand miniaturised, low-cost, automated yet powerful analytical instruments for obtaining chemical or biochemical information. Integrated optics is set to revolutionise the translation of laboratory based bulky and expensive spectroscopy instruments to mass-producible chips, with the help of optical waveguide technologies. The goal of this project is to significantly improve the WERS performance in terms of Raman yield while minimising costly materials, components and techniques.

The principle of Raman spectroscopy has been explained in Chapter 2. Compared to fluorescence spectroscopy, Raman spectroscopy provides more molecular specificity and is suitable for multiplexing applications. Unlike fluorescence spectroscopy, Raman spectroscopy does not require costly and complicated labelling or tagging, and no or trivial sample preparation of the analyte is needed. Compared to IR spectroscopy, Raman spectroscopy is suitable for aqueous measurements. For these advantages, Raman spectroscopy has been selected as the analytical technique over others.

Despite these advantages, Raman spectroscopy has suffered from low sensitivity due to inherently low efficiency of the Raman scattering. Many methods have been developed in order to tackle this issue, such as RR, SRS, CARS, SERS, WERS, TERS, etc. Among all of these, WERS realised by incorporating Raman spectroscopy on waveguide platform, has unique advantages for achieving a miniaturised, mass-producible, yet powerful spectroscopy-on-a-chip.

By replacing bulky free-space optical components, the waveguide as the fundamental component of integrated optics is utilised to transport light, excite Raman scattering of the sample, and collect the Raman emission. In principle, guided light in waveguide is squeezed in a scale of dimension similar to its wavelength, which results in a large optical intensity over a long propagation range. Analyte molecules close to the waveguide surface interact with the evanescent field of the waveguide to be Raman excited and their emission collected.

A systematic approach has been taken to achieve the project goal. In the first stage of the project, the necessary ‘building blocks’ for completing a successful WERS measurement were established in Chapter 3, including electromagnetic models for waveguide design tool, a fabrication protocol, characterisation practices, and experimental apparatus. A matrix method was utilised to model multilayer waveguide structures with user-defined number of layers, layer index, layer thickness and excitation wavelength; and Muller’s method was applied to numerically solve for their modes. This developed mode-solving tool has been checked successfully against literature examples, including a six-layer dielectric waveguide structure and a five-layer metal-clad waveguide. Based on these modes, the field distribution inside the waveguide structure was able to be calculated. With this model tool, a waveguide design for maximising Raman excitation was then obtained. Surface intensity was defined and justified to be the figure-of-merit for waveguide Raman excitation. With pre-assumptions that the substrate is fused silica (SiO_2), simulations were run against design parameters, such as index contrast between the core and the substrate, excitation wavelength, core thickness, and refractive index of the analyte environment. Results showed that surface intensity was maximised when the index contrast was high, hence the high-index material Ta_2O_5 was chosen as the core after comparing with other common glass materials. The excitation wavelength was chosen to be red light at around 633 nm for a compromise between maximising surface intensity, Raman cross-section and minimising background fluorescence. Depending on the selected analyte, the waveguide core thickness can be selected for maximising waveguide surface intensity. Compared to free-space illumination (unfocussed), Raman excitation by waveguide in general has a surface intensity enhancement of more than 10^6 (Figure 4.3A).

Waveguides were fabricated by using RF sputtering. The resultant samples were well-guided, with a loss around 3-4 dB/cm and 6-7 dB/cm for TM and TE polarisation, respectively. Prism coupler was selected for coupling light into the thin film waveguide for simplicity. A prism coupler was designed and constructed with successful test runs.

WERS measurements of bulk analyte were taken with Raman collection from the waveguide surface (in Chapter 4). Toluene liquid and polystyrene film were chosen for their easy-to-observe Raman features due to strong phenyl ring vibrations. The optimised waveguide with a Ta_2O_5 core thickness of 110 nm was utilised for the experiment under TM excitation. Raman spectra for both toluene and polystyrene were successfully measured with distinguished Raman features. A power budget analysis was then applied to the system, resulting in a total conversion efficiency of $\sim 0.5 \times 10^{-12}$ from the pump power in the waveguide to the collected Raman power in the 1002 cm^{-1} Raman line of toluene, in comparison with a calculated efficiency of 3.9×10^{-12}. The discrepancy is primarily originated from the assumptions that Raman emission was isotropic around the waveguide, which in Chapter 5 would be proved to be not accurate. Collection efficiency, dictated by the collection configuration and the numerical and physical apertures of the spectral detection system, was found to be very small.

Theoretical analysis of spatial emission distribution of an excited molecule on waveguide surface was then given in Chapter 5, in which the excited molecule was modelled as a radiating dipole. Waveguide structure was found to modify the spontaneous emission rate and emission pattern of the dipole. The change of spontaneous emission rate was characterised by Purcell factor, which was calculated by using the Lumerical FDTD package. For the dipole excited by the TM mode on the waveguide surface, Purcell factor was calculated to be 2.5, which indicated an enhanced spontaneous emission rate. In terms of spatial emission distribution, the dipole emission is split into near-field radiation and far-field radiation. The near-field radiation was calculated by using the Lumerical FDTD package, which showed that the majority of emission was coupled into the waveguide guided mode(s). As the near-field emission does not contribute to the collection from the waveguide surface, this clearly indicated that collection from the waveguide surface was inefficient, which also partly explained the discrepancy of conversion efficiency between the theory and the experiment in Chapter 4. The 3D far-field emission pattern was calculated analytically for different oriented dipoles, which showed altered emission pattern than that in free space. These findings provide guidelines to accurately account for emission collection at different locations. Most importantly, it indicated that collection at the waveguide front edge would improve the collection efficiency, compared with that from the waveguide surface.

In experiments shown in Chapter 6, Raman collection from the waveguide front edge was found to have 2-3 orders of enhancement compared to that from the waveguide surface for TM excitation. Bulk toluene measurement was taken as an example to explain the enhancement mechanism. Spatial distributions of both near-field and far-field radiation were generated for an emitted dipole located at the waveguide surface. Very interestingly, asymmetrical radiations were observed for both near-field and far-field radiation due to elliptically polarised dipole under TM excitaiton. Notably, the waveguide front edge has received 71.6% more near-field emission than that at the back edge. By summing up the contributions received from near-field and far-field radiation of the emitted dipole, radiative enhancement factor for collection at the waveguide front edge was calculated to be 7.2. In addition, collection from the waveguide front edge received contributions from all emitted molecules along the propagation region, which resulted in an area enhancement factor of 7.7. In total, the theory predicted a total enhancement factor of 55 in good agreement with the experimental result of ~40. The discrepancy is believed to have originated from assumptions made in the theoretical calculations.

With the much improved sensitivity provided by the enhancement from the waveguide front edge collection, WERS was utilised for monolayer detection. Two silane molecules, trichloro(phenyl)silane (PTCS) and *p*-tolyltrichlorosilane (TTCS), were chosen for their chemical and mechanical robustness, compatibility with the metal-oxide surface, and inclusion of phenyl rings in their molecular structures. Self-assembled monolayers (SAMs) were formed on the waveguide surface, verified through contact angle measurements. The Raman signals of these monolayers were successfully measured with multiple spectral features detected. The spectral difference between the two monolayers due to the methyl group clearly confirmed the validity of the measurement in that the Raman signals were proven to derive from the monolayer. The success of measuring monolayer Raman in all dielectric planar waveguide with multiple Raman features was the first demonstration as this was previously only done by using resonant Raman scattering or surface-enhanced Raman spectroscopy (SERS), compared to which the WERS approach with collection at the waveguide front edge enables low-cost and miniaturised instrumentation for many applications.

An even more performance-demanding measurement was utilised to further test the WERS system. As Raman measurements of monolayers can provide molecular structural information of the monolayer forming molecule, the monolayer orientation can be predicted by using polarised Raman spectroscopy. Having selected the incident polarisation as TE, collecting the Raman signals at the waveguide front edge with a polariser put in between to select the scattered light parallel and perpendicular to the incident polarisation, led to the calculated depolarisation ratio based on the measurement data. The relationship between the depolarisation ratio and the molecular tilt angle was calculated with DFT generated Raman polarisability tensor of each mode. With the assumption that the molecules were randomly oriented in the azimuthal and rotational plane, the title angle was calculated to be around 30^0. Results were preliminary as more measurements based on different combinations of polarisations are needed to give more confidence. The main limitation to achieving this was the requirements for even higher WERS sesnitivity. A fully optimised WERS for both excitation and collection would be the next step to improve the sensitivity. Nevertheless, the results were demonstrations of state-of-the-art WERS performance, which are expected to inspire other applications.

Overall, 1-2 orders of enhancement was obtained for WERS with collection at the waveguide front edge compared to the conventional of collection at the waveguide surface, which achieved the project goal. Theoretical analysis of Raman collection from an emitting molecule on the waveguide surface allowed clarification of physical and quantitative understanding, which will also be useful for waveguide-enhanced fluorescence spectroscopy, waveguide-enhanced absorption spectroscopy, etc. Monolayer detection and the subsequent polarised WERS measurements significantly showed the great capabilities offered by WERS with simple, cheap, all-dielectric slab waveguide structures.

8.2 Future possibilities

It is suggested that the highest priority for future work will be to obtain a fully optimised WERS device for both waveguide excitation and waveguide collection with the theories and simulation tools provided in this thesis. One important observation in this project was the collection of far-field radiation by the composite waveguide structure, which should have lower propagation loss than the near-field coupled waveguide mode(s). However, the relationship between the far-field radiation and waveguide design parameters has not been explored before, and further investigation is worthful. In addition, far-field radiation can be emitted in a very narrow angle band by tailoring the waveguide design, which leads to very efficient far-field radiation collection.

The slab waveguides utilised in this project are the simplest structures in the waveguide family, which provides 2D confinement. As the optical confinement is the source of enhancement offered by waveguide structures, rib or channel waveguides that provide 3D confinement are expected to further enhance the waveguide excitation and collection performance. In fact, recent works from Dhakal *et al.* have focussed on rib and channel waveguides on WERS [1], [2]. However, a direct comparison of conversion efficiency (pump power to measured Raman power) between his works and the works demonstrated in this project shows that to date the slab waveguide has a slightly better performance. To remove different experimental factors, it would be novel to compare the performance between slab and channel waveguides made of the same materials in the same experimental condition. The decision to choose channel or rib waveguide should also be taken into account the increased fabrication complexity and cost.

With the improved WERS performance, polarised measurements of monolayers under full set of polarisations can be pursued in order to accurately and reliably measure the molecular orientation and other related effects. Moreover, WERS can be applied to detection of DNA or pollutants immobilised on waveguide surface, in order to deliver the promises of WERS in healthcare and environmental monitoring. Protocols of immobilizing DNA or pollutant molecules on waveguide surface need to be developed by collaborators in chemistry.

To realise the vision of spectrometer-on-a-chip or lab-on-a-chip, the integration of WERS with on-chip laser or spectrometer will be a fascinating work to do, similarly for integration of flow cytometry and WERS. To further reduce the cost, plastic substrates can be explored to replace fused silica glass.

8.3 References

[1] A. Dhakal, A. Raza, F. Peyskens, A. Z. Subramanian, S. Clemmen, N. Le Thomas, and R. Baets, “Efficiency of evanescent excitation and collection of spontaneous Raman scattering near high index contrast channel waveguides.,” *Opt. Express*, vol. 23, no. 21, pp. 27391–404, 2015.

[2] A. Dhakal, A. Z. Subramanian, P. Wuytens, F. Peyskens, N. Le Thomas, and R. Baets, “Evanescent excitation and collection of spontaneous Raman spectra using silicon nitride nanophotonic waveguides,” *Opt. Lett.*, vol. 39, no. 13, pp. 4025–4028, 2014.

Appendix A Matlab code for Muller's method

```
%**********************************************************************
**
%                            Muller's method
%used to solve for eigenvalues of the mode equation determined by the
%waveguide structure.This method can be used to solve for complex
%solutions. The efficacy and accuracy of this numerical method can be
%adjusted by tuning parameters e1 and e2. One needs to give three initial
%guesses of the effective index. Depending on structures, sometimes it
may
%need some trials to figure out three 'good' initial guesses, which then
%give all the solutions or one particular solution. This is especially
true
%for metal involved structures.
%
%                            Input parameters:
%Mode equation in analytical form: mode
%Three initial guesses: x(1),x(2),x(3)
%Number of solutions need to be solved: N
%
%                            Output parameter:
%                                 zero
%Author:Zilong Wang
%Contact detail:michaelwang9053@gmail.com
%**********************************************************************
**

%Input parameters
e1 = 1e-50;  %minimum step portion
e2 = 1e-20;  %closeness to zero
N =2;  %number of solutions

%step 1 - Three approximations of zeros ofi fi(x) and compute fi
x(1)=(1.7 )*(2*pi/(lamda)); %x_i-2
x(2)=(1.56)*(2*pi/(lamda)); %x_i-1
x(3)=(1.8)*(2*pi/(lamda));   %x_i
%**********************************************************************
**
syms beta
f=mode;
digits(10);

m = 3;
z = 1;  %indicate num of zeros

count=0;


Ite=0;

while (count<N)
    fi = @(m) vpa(subs(mode, x(m)),10);     %This returns a double number

    %step 2 - compute h and lamda
    h(m) = x(m) - x(m-1);
    lmd(m) = h(m) / (x(m-1) - x(m-2));
```

```
    %Two Criterias
    while ((abs(x(m)-x(m-1))/abs(x(m))>=e1 && abs(fi(m)) >= e2)...
            &&~(isnan(abs(x(m)-x(m-1))/abs(x(m)))...
            ||isnan(abs(fi(m))))&&(Ite<=100))


        %step 3 - compute gi
        g(m) = (1 + 2*lmd(m))*(fi(m) - fi(m-1)) - lmd(m)^2 * (fi(m-1) -
fi(m-2));

        %Step 4 - compute lamda_i+1
        if (abs(g(m) + sqrt(g(m)^2-4*fi(m)*(1+lmd(m))*lmd(m)*(fi(m) -
fi(m-1) - lmd(m)*(fi(m-1)-fi(m-2))))))>...
                abs(g(m) - sqrt(g(m)^2-4*fi(m)*(1+lmd(m))*lmd(m)*(fi(m) -
fi(m-1) - lmd(m)*(fi(m-1)-fi(m-2))))))
            lmd(m+1) =  -2 * fi(m) *(1+lmd(m))/(g(m) + sqrt(g(m)^2-
4*fi(m)*(1+lmd(m))*lmd(m)*(fi(m) - fi(m-1) -lmd(m)*(fi(m-1)-fi(m-2)))));
        else
            lmd(m+1) = -2 * fi(m) *(1+lmd(m))/(g(m) - sqrt(g(m)^2-
4*fi(m)*(1+lmd(m))*lmd(m)*(fi(m) - fi(m-1) - lmd(m)*(fi(m-1)-fi(m-2)))));
        end

        %step 5 - compute x(i+1), h(i+1)
        x(m+1) = x(m) + h(m)*lmd(m+1);
        fi = @(m) vpa(subs(f, x(m)),10);
        h(m+1) = h(m) * lmd(m+1);
        lmd(m+1) = h(m) / (x(m-1)-x(m-2));

        %Display the iteration information in text
        Ite = m-3;
        x_m = double(vpa(x(m)/(2*pi/(lamda)),5));
        % x_m = double(vpa(x(m),5));
        OuFunc = double(vpa(abs(fi(m)),5));
        Step = double(vpa(abs(x(m)-x(m-1))/abs(x(m)),5));
        X=[num2str(Ite),'                 ', num2str(x_m),'      ',
num2str(OuFunc),'            ', num2str(Step)];
        disp('Iteration         Neff                    Output Func
Step size');
        disp(X);

        m = m+1;
    end

    %store zero
    zero(z) = x(m-1)/(2*pi/(lamda));
    beta_value(z)=x(m-1);
    % zero(z)=x(m-1);
    z = z+1;
    count=count+1;

    f = f/(beta - x(m-1));
    m=3;
end
```

Appendix B Investigations of spatial distribution of WERS emission at the waveguide front edge

Two investigations of collections at waveguide front edge have been carried out. One investigation is about angular measurements by changing the angle between collection optics and the waveguide in the incident plane. The other investigation is about translational measurements by scanning the waveguide front edge.

Polystyrene coating was utilised instead of IPA or Toluene (solvent) for three reasons:

- Thickness controlled and measurable
- No coverslip effect
- No evaporation

The thickness of spin-coated polystyrene film is determined by the concentration of solution, which is made by dissolving polystyrene pellets (Mw ~280,000) in 98% anhydrous toluene [1]. The polystyrene film can be easily measured by using Stylus Profiler. This measured thickness is useful for theoretical quantification of Raman excitation. Unlike in the case of IPA or toluene, where a coverslip needs to be put on top of the waveguide surface to reduce the evaporation speed of the solvent, polystyrene film is stable on waveguide surface, hence avoid the use of coverslip. 30 nm polystyrene film was coated on a 110 nm Ta_2O_5 waveguide.

For angular measurements at the waveguide front edge, collection optics was put at an angle to the waveguide +*x* axis for each measurement of Raman collection, as shown in Figure B. 1. The integration time for collection was 30s. The collection optics comprised of an image system and a collection fiber with NA of 0.38 and core diameter 400 µm.

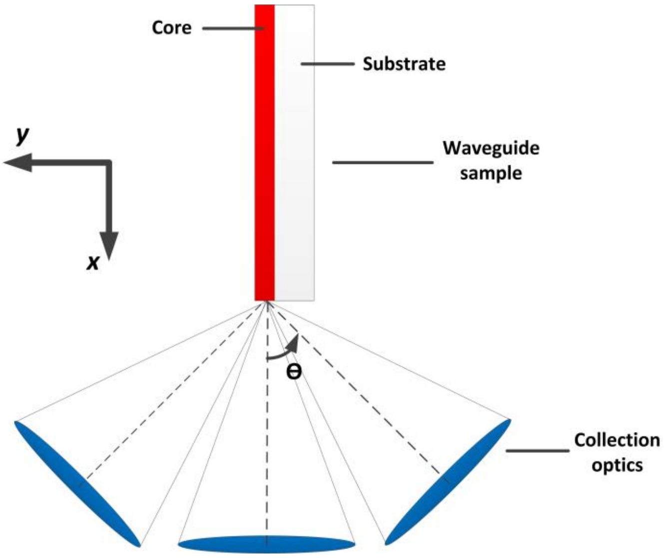

Figure B. 1 Illustration of angular measurements at the waveguide front edge.

After Raman spectra acquisitions, power of the Raman band at around 3100 cm^{-1} was calculated by integrating the power confined by that band in the spectral axis. This Raman band served as a representative of the total Raman power measured at each collection angle. Figure B. 2 shows angular measurements at waveguide front edge in TM and TE polarisations. For both, a substantial Raman power have been collected at an angle to $+x$ axis located at the substrate side. Specifically, the maximum Raman collection was achieved at an angle of 30 degrees for TM, and 0 degree for TE. The latter maximum was at 0 degree, yet Raman signals were within the error ±0.5 of the maximum across the angles from 0 degree to 30 degree. Similarly, the Raman signal remained within the error of the maximum from 15 degrees to 30 degrees. If Raman signals were all emitted out of the waveguide core, a symmetric power distribution of Raman collection about the $+x$ axis should be expected. This dominant behaviour of Raman signals emitting towards the substrate half-plane indicates that far-field radiation to the substrate plays a role. A hypothesis is that the far-field radiation from the excited region close to the front edge of the waveguide emits to the substrate, and reaches to the waveguide front edge without reflections at the substrate – air interface, which contributes significantly to the front edge collection.

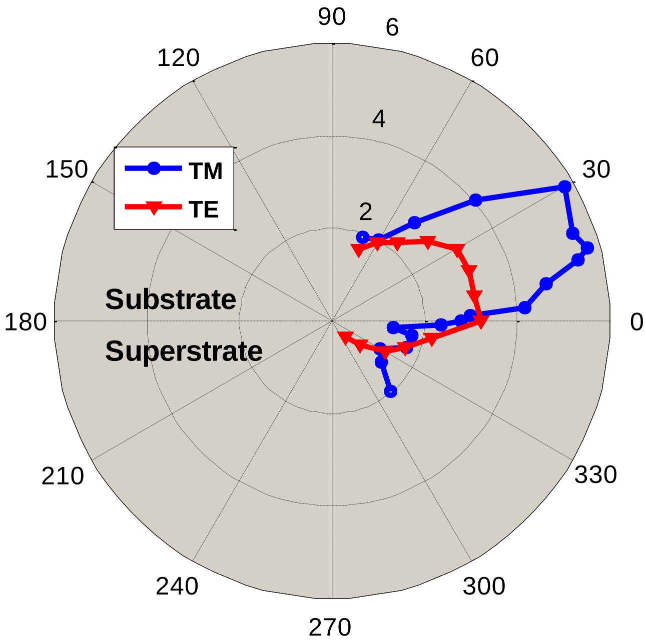

Figure B. 2 Angular measurements at waveguide front edge in TM and TE polarisations. The magnitude unit of the Raman intensity are arbitrary, and the error is ± 0.5 units.

In order to verify the hypothesis that a significant amount of Raman front edge collection is contributed by far-field radiations into the substrate, waveguide front edge was scanned through by collection optics. The fused silica substrate had a thickness of 1000 µm. Figure B. 3 shows the result of translational measurements at the waveguide front edge with collection optics tilted at 20 degrees to the substrate (in *xy*-plane). For each measurement, Raman power was calculated by integrating power confined by the Raman band at ~3100 cm^{-1}. The maximum Raman power was measured when the collection optics focussing on the waveguide core edge. As the collection optics scanned towards the substrate, the received Raman power decreased in half within 100 µm to the waveguide core edge. Then, the received Raman power maintained steadily at the same level from 100 µm to 950 µm, before it decreased sharply after 950 µm. Near-field radiations of emitted molecules reach the waveguide front edge by waveguide core; while the far-field radiations of emitted molecules that are trapped by the composite waveguide reach the waveguide front edge 'uniformly' (excluding the region close to the core) distributed for the majority of the substrate edge. Collection by focussing at the waveguide core edge receives contributions from both near-field radiations and far-field radiations, hence the maximum. As the collection optics moves towards the substrate region, the contribution from near-field radiations sharply decreases to null and solely the far-field radiations contribute to the measured Raman power at the waveguide front edge, thus a steady Raman power received from the region 100 µm to 950 µm. As the collection optics moves out of the substrate region, the power sharply reduces towards null, as expected. These results provide clear evidence that far-field radiations trapped in the waveguide substrate is substantial, which to date haven't been exploited in the field of waveguide-enhanced spectroscopy to achieve optimum collection of emission. Note that, the collection optics was at a tilt angle of 20 degrees to the substrate, therefore near-field radiations emitted out of the waveguide core was not collected at the maximum.

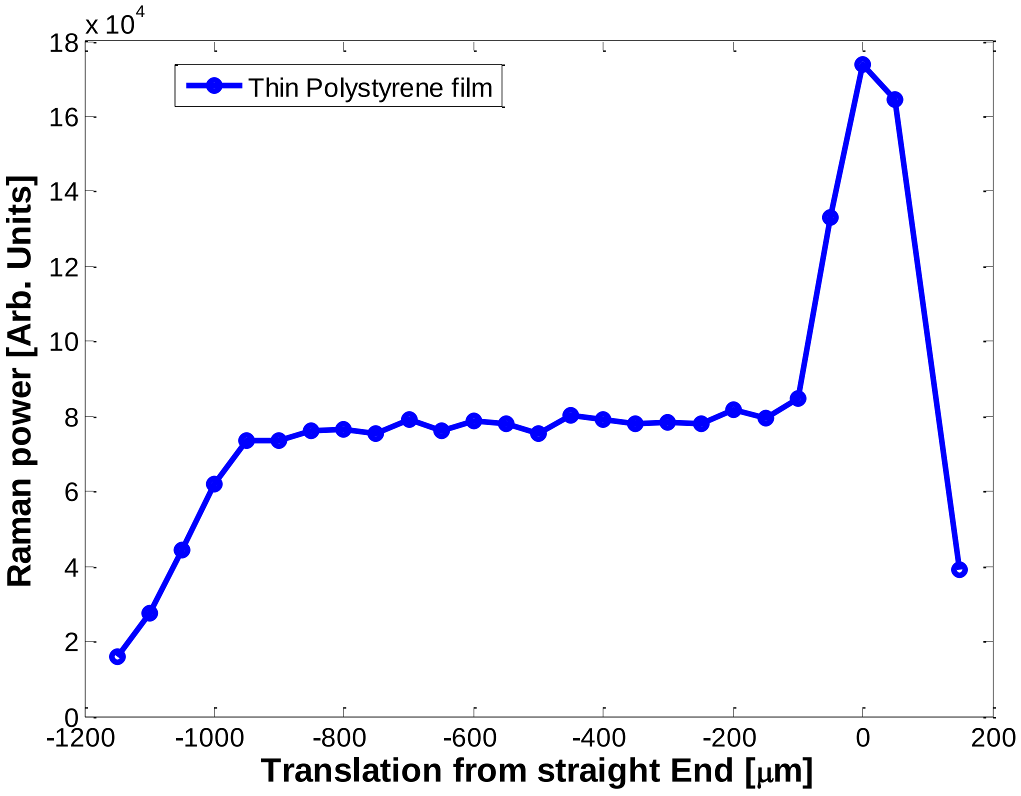

Figure B. 3 Translational measurements at waveguide front edge with collection optics at 20 degree tilted to the substrate. The waveguide was coated with 30 nm polystyrene film. The translational step was 50 µm and the fiber utilised was 200 µm in diameter and NA was 0.39. The integration time was 30s. The error was estimated to be ± 0.5 × 10^4.

Appendix C Calculation for waveguide front edge collection

Front edge collection gets contributions from near-field emission guided by the waveguide mode and far-field emission trapped by the composite waveguide, as explained in section 6.3. In this section, the calculation method will be demonstrated here.

For the near-field emission, emitted light is confined in the X-Y plane but not bounded in the X-Z plane, as illustrated in the Figure C. 1. The collection system, comprised of an image system and a multimode collection fiber, determines the numerical aperture (NA) and detection cone diameter (*D*) of the detection region at the waveguide end surface. And these two parameters determine the effective collection cone of each emitted molecule. In *Z*-direction (waveguide width), it is assumed that every emitted molecule at the same x_0 will be collected equally in power. Along the propagation length (x-direction), an emitted molecule located far away (B') from the waveguide end reaches the detection region in a small emitted angle (θ) that is within the NA. As the emitted molecule gets closer and closer to the waveguide end facet, the maximum emitted angle becomes larger and larger until at critical point B where the emitted angle reaches its maximum. Any point closer to the waveguide end will have the same collection NA.

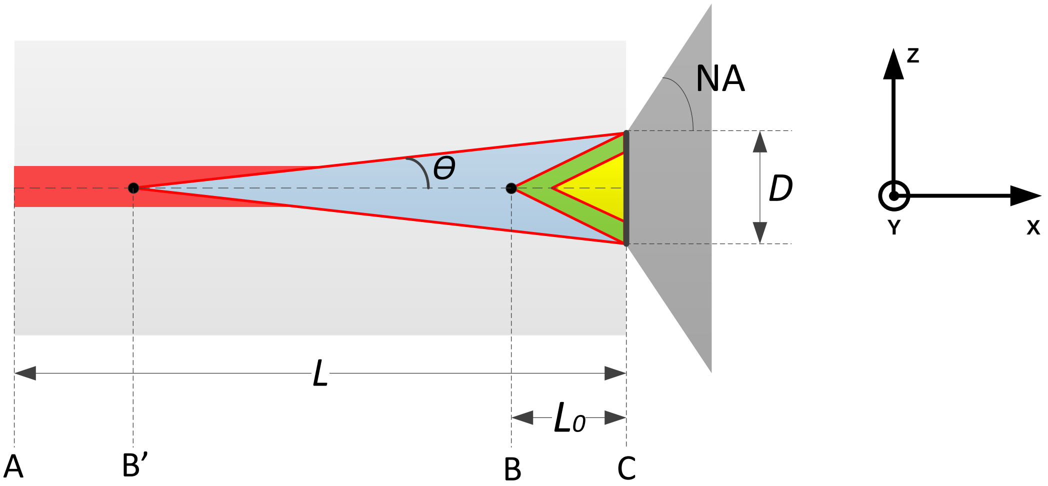

Figure C. 1 Illustration of collection cone of each point at the excited region.

Assuming that the coupling efficiency (η) of emitted light into the waveguide mode is the same in all directions within the plane X-Z, the collected power of each point at the waveguide end is proportional to the maximum emitted angle (θ) so that:

$$P_{Rc}(x) = P_{Re}(x) \cdot \eta_{cw}(y) \cdot \frac{\theta(x)}{\pi} \qquad \textbf{Equation C. 1}$$

where

$P_{Rc}(x)$	Waveguide end collected power of an emitted molecule at position$x$, where x is the relative distance to the coupling spot.
$P_{Re}(x)$	Total emitted Raman power of an molecule at position x $P_{Re}(x) = \int_0^{+\infty} I(y)dy$
$\eta_{cw}(y)$	Coupling efficiency of the Raman emission into the waveguide guided mode in +x direction, which is y dependent and in a relationship of $\eta_{cw}(y) = \eta_{cw}(0) \cdot e^{-2k_{1y} \cdot y}$. $y = 0$ corresponding to the position at the surface. $k_{1y} = \frac{2\pi}{\lambda} \cdot \sqrt{{n_{eff}}^2 - {n_1}^2}$, where n_{eff} is the effective index of the waveguide mode and n_1 is the refractive index of the top layer.
$\theta(x)$	The maximum emitted angle at position x

$P_{Re}(x)$ is x depended as the Raman excitation intensity drops along the propagation length as a result of propagation loss (α_{pl}). The total collected Raman power (at the waveguide end) by guided mode is then calculated as:

$$P_{R_{End}} = \int_0^L \frac{\theta(x)}{\pi} \cdot e^{-\alpha_{pl} \cdot (L-x)} \int_0^{+\infty} P_{Re}(x) \cdot \eta_{cw}(y)\, dy \cdot dx \cdot \eta_{dfr} \qquad \text{Equation C. 2}$$

Where

$$P_{Re}(x) = e^{-\alpha_{pl} \cdot x} \cdot \int_0^{+\infty} I(y) \cdot \frac{d\sigma}{d\Omega} \cdot 4\pi \cdot N \cdot dy \qquad \text{Equation C. 3}$$

Substituting $P_{Rc}(x)$ into the $P_{R_{End}}(x)$:

$$P_{R_{End}} = e^{-\alpha_{pl} \cdot L} \cdot W_Z \cdot \eta_{dfr} \cdot \int_0^L \frac{\theta(x)}{\pi} \cdot [\int_0^{+\infty} I(y) \cdot \frac{d\sigma}{d\Omega} \cdot 4\pi \cdot N \cdot \eta_{cw}(y) \cdot dy] \cdot dx \qquad \text{Equation C. 4}$$

where

P_{R_End}	Total collected power at the waveguide end
α_{pl}	Waveguide propagation loss (assuming this loss is relatively the same for excitation and stoke wavelength)
W_Z	Width of excited area
$I(y)$	Evanescent field intensity along the direction y
$\frac{d\sigma}{d\Omega}$	Differential Raman cross-section of toluene
N	Total number of excited molecule per unit volume
η_{dfr}	The collection efficiency of power out of the waveguide end by the fiber.

To summarise all the assumptions made in arriving at the above expression:

1. The coupling efficiency of the emitted light into the guide mode is equal at all directions in the plane X-Z.
2. Assuming the coupling efficiencies of all the emitted dipole located along the y-direction are governed by $\eta_{cw}(y) = \eta_{cw}(0) \cdot e^{-2k_{1y} \cdot y}$.
3. Assuming the loss difference is negligible due to the path length difference of emission at different angle so that the power arriving at the collection cone are equal.
4. Assuming the loss are equal for excitation wavelength and stoke wavelengths.

In terms of far-field emission trapped by the composite waveguide, the efficiency can be calculated as followed expressions below:

$\eta_{cl} = 1 - 2 \cdot \eta_{cw}$	Portion of power emitted to the far field (cladding)
$\eta_{col} = (\frac{P_{colour}}{P_{cl}})/2$	Efficiency of those power emitted to the cladding get collected at one waveguide edge, P_{colour} corresponds to the power represented by the red region of figure 3b in the main text of the paper.
$\eta_y = \frac{{n_{eff}}^2}{{n_{eff}}^2 - {n_1}^2}$	Efficiency of y-oriented molecules get excited. n_{eff} – the effective index of the waveguide excitation mode n_1 – the refractive index of the top layer, which is toluene in this case.
$\eta_x = 1 - \eta_y$	Efficiency of x-oriented molecules get excited
$\eta_{clad} = \eta_{x(y)} \cdot \eta_{cl} \cdot \eta_{col}$	The collection efficiency of an emitted dipole.

The waveguide end collected power of an emitted molecule at position x can be calculated as:

$$P_{Rc2}(x) = P_{Re}(x) \cdot \eta_{clad} \cdot \frac{\theta(x)}{\pi} \qquad \text{Equation C. 5}$$

with assumptions

(1) Raman emission pattern is the same across azimuthal plane.
(2) The collection efficiencies are equal for emitted molecules along the y-direction.

The total collected power, through the emissions to the claddings, can be calculated as:

$$P_{R_{End}} = W_Z \cdot \int_0^L \eta_{clad} \cdot \frac{\theta(x)}{\pi} \cdot e^{-\alpha_{pl} \cdot x} [\int_0^{+\infty} I(y) \cdot \frac{d\sigma}{d\Omega} \cdot 4\pi \cdot N \cdot dy] \cdot dx \qquad \text{Equation C. 6}$$

Appendix D Matlab code for calculating Raman polarisability tensors based upon Gaussian output

```
%Raman polarisability tensors calculation from Gaussian output

%*********************************************************************
%1st step: formulate the 'linear polarisability tensors' - lpt in A^2
%*********************************************************************
N=18;   %Number of atoms
% mode = 3*N-5;  %total number of modes 3*N-6 for CO2
mode = 3*N-6;  %total number of modes 3*N-6

h = 6.626e-34;  %Plank's const.  [m^2*kg/s]
c=3e8;  %velocity of light in vacuum [m/s]
e0 = 8.854e-12; %permittivity of free space
theta = 30; %x-y plane rotation angle (clockwise)
theta = theta*2*pi/360; %unit in radians
alpha = 0;  %x-z plane rotation angle (clockwise)
alpha = alpha*2*pi/360; %unit in radians
beta = 0;   %y-z plane rotation angle (clockwise)
beta = beta*2*pi/360; %unit in radians

%Unit conversion to SI unit
amu = 1.66e-27; %one atomic mass units (amu) in SI unit [kg]
B = 0.529;  %Distances are expressed in Angstroms A from Bohr B: 1B =
0.529 A
A=1e-10;    % 1 A = 10^-10 m
SI = 4*pi*e0*1e-30; %1A^3 = .... SI[e0*m^3]

%Initialization
lpt=zeros(3,3,3*N);  %Important step: create an all zero matrix to store
values
Rt_1=zeros(3,3);
Rt_2=0;
Rt=zeros(3,3,mode);
Rpt=zeros(3,3,mode);
% freqs=str2num(freqs);

D_xy=[cos(theta),-sin(theta),0;sin(theta),cos(theta),0;0,0,1]; %Transform
matrix
D_xz=[cos(alpha),0,sin(alpha);0,1,0;-sin(alpha),0,cos(alpha)]; %Transform
matrix
D_yz=[1,0,0;0,cos(beta),-sin(beta);0,sin(beta),cos(beta)]; %Transform
matrix

lpt_1=[lpds(:,1,1),lpds(:,2,1),lpds(:,3,1)];
lpt_2=[lpds(:,1,2),lpds(:,2,2),lpds(:,3,2)];
lpt_3=[lpds(:,1,3),lpds(:,2,3),lpds(:,3,3)];

for i=1:(3*N)
    lpt(:,:,i)=[lpt_1(i,:);lpt_2(i,:);lpt_3(i,:)];
end

lpt = lpt*B^2;  %Transform the unit for B^2 to A^2

%*********************************************************************
%2nd step: calculate Raman tensors - Rt in [A^2*amu^-1/2]
```

```
%**********************************************************************
for j=1:mode
    Rt_1=zeros(3,3);
    for i=1:(3*N)
        Rt_1=Rt_1+1/sqrt(masses(j))*rdps(j,i)*lpt(:,:,i);
    end



    Rt_1=D_xy*Rt_1*D_xy.';    %Transform to co-ordinate system based on
the surface
    %If the benzene ring is rotating about its molecular axis, then in
    %averaging
    Rt_1=D_xz*Rt_1*D_xz.';
    Rt_1=D_yz*Rt_1*D_yz.';

    Rt(:,:,j)=Rt_1;
end

%**********************************************************************
%3nd step: calculate Raman polarisability tensors - alpha
%**********************************************************************
bk=sqrt(h./(8*pi^2*c.*freqs.*1e2));   %zero-point amplitude or the normal
vibrational mode (P102)
bk = bk*2.44e23;    %Based on example given in p484 E Le Ru's book

for i=1:length(bk)
    Rpt(:,:,i)=Rt(:,:,i)*bk(i);
end

Rpt_SI = Rpt*SI;

%**********************************************************************
%Optional - calculate isotropic depolarisation ratio z(xx) case
%**********************************************************************
for i=1:length(Rpt)
trace = 1/3*(Rpt(1,1,i)+Rpt(2,2,i)+Rpt(3,3,i));
aniso = 1/2*((Rpt(1,1,i)-Rpt(2,2,i)).^2+(Rpt(2,2,i)-
Rpt(3,3,i)).^2+(Rpt(3,3,i)-
Rpt(1,1,i)).^2)+3*(Rpt(1,2,i)^2+Rpt(1,3,i)^2+Rpt(2,3,i)^2);
anti_aniso=3/4*(abs(Rpt(1,2,i)-Rpt(2,1,i))^2+abs(Rpt(2,3,i)-
Rpt(3,2,i))^2+abs(Rpt(3,1,i)-Rpt(1,3,i))^2);
rau(i)=(3*aniso+5*anti_aniso)/(45*trace^2+4*aniso);
end
```